Experiment and Computational Characterization of Strong Vent Flow Enclosure Fires - Dissertation

NIST GCR 12-968

Experimental and Computational Characterization of Strong Vent Flow Enclosure Fires - Dissertation

Craig George Weinschenk
The University of Texas at Austin
1 University Station
Austin, TX 78712

April 2012

Notice

This report was prepared for the Engineering Laboratory of the National Institute of Standards and Technology under Grant number 60NANB7D6122. The PI on this Grant is Ofodike A. Ezekoye. The statement and conclusions contained in this report are those of the authors and do not necessarily reflect the views of the National Institute of Standards and Technology or the Engineering Laboratory.

The Dissertation Committee for Craig George Weinschenk Certifies that this is the approved version of the following dissertation:

EXPERIMENTAL AND COMPUTATIONAL CHARACTERIZATION OF STRONG VENT FLOW ENCLOSURE FIRES

Committee:

Ofodike A, Ezekoye, Supervisor

Alexandre K. Da Silva

Michael D, Engelhardt

John R, Howell

Venkatramanan Raman

Robert Nicks

EXPERIMENTAL AND COMPUTATIONAL CHARACTERIZATION OF STRONG VENT FLOW ENCLOSURE FIRES

by

Craig George Weinschenk, B.S.; M.S.E.

Dissertation

Presented to the Faculty of the Graduate School of

The University of Texas at Austin

in Partial Fulfillment

of the Requirements

for the Degree of

Doctor of Philosophy

The University of Texas at Austin

August 2011

Dedication

This dissertation is dedicated to my friends and family for all of their support. Specifically this is dedicated to my parents who have taught me the value of commitment and hard work. This is also dedicated to my brother who taught me to never be satisfied with average if excellence can be achieved.

Acknowledgements

I would first like to thank my advisor, Dr. Ofodike Ezekoye, for both his encouragement and advice throughout my graduate study. Dr. Ezekoye's guidance was integral to my academic growth and I cannot recognize or praise his efforts enough.

I must also acknowledge the work of Dr. Rochan Upadhyay, whose expertise in the quadrature method of moments and development of the libMOM library were essential to the stochastic work in this dissertation. Dr. Upadhyay is also a co-author of a conference paper, "Comparison of a partially stirred reactor model and a perfectly stirred reactor model for large vent flow fires.," which is included in this dissertation.

I would also like to thank the sponsor of this research, the National Institute of Standards and Technology (NIST). The work was funded by the NIST Department of Commerce Grant No. 60NANB7D6122. The Engineered Fire Research Group provided funding, instrumentation, and advice that were vital to both the experimental and computational work presented in this dissertation. Specifically, I would like to thank Steven Kerber, Dan Madrzykowski, Kevin McGratten, and Randall McDermott.

I would also like to thank fellow students for their assistance in my research. Particularly I would like to thank the members of the UT Fire Research Group. I would like Dr. Colin Beal who was my research partner for the construction of the experimental test facility and non-reacting flow experiments. Colin Beal is also a co-author on the journal paper, "Modeling fan-driven flows for firefighting tactics using simple analytial models and CFD," which is included in this dissertation. Additionally, I would like to thank Kristopher Overholt and Kevin Carollo whose help was instrumental to the reacting

Experimental and Computational Characterization of Strong Vent Flow Enclosure Fires

Publication No._____

Craig Weinschenk, Ph.D.

The University of Texas at Austin, 2011

Supervisor: Ofodike A. Ezekoye

Firefighters often arrive at structures in which the state of fire progression can be described as ventilation-controlled or under-ventilated. This means that inside the enclosure the pyrolyzed fuel has consumed most, if not all of the available oxygen, resulting in incomplete combustion. Under-ventilated (fuel rich) combustion is particularly dangerous to occupants because of the high yield of toxins such as carbon monoxide and to firefighters because once firefighters enter the structure and introduce oxidizer, the environment can rapidly change into a very dangerous, fast burning condition. The fuel load in many compartment fires would support a several megawatt fire if the fire were not ventilation controlled. In the process of making entrance to the fire compartment, firefighters will likely provide additional ventilation paths for the fire and may initiate firefighting tactics like positive pressure ventilation to push the hot flammable combustion products out of the attack pathway. Forced ventilation creates a strongly mixed flow within the fire compartment. Ventilation creates a complex fluid

mechanics and combustion environment that is generally not analyzed on the scale of compartment fires.

To better understand the complex coupling of these phenomena, compartment scale non-reacting and reacting experiments were conducted. The experiments, which were conducted at The University of Texas at Austin's fire research facility, were designed to gain insight into the effects of ventilation on compartment thermal characteristics. Computational models (low and high order) were used to augment the non-reacting and reacting experimental results. Though computationally expensive, computational fluid dynamics models provided significant detail into the coupling of buoyantly driven fire products with externally applied wind or fan flow. A partially stirred reactor model was used to describe strongly driven fire compartment combustion processes because previously there was not an appropriate low dimensional computational tool applicable to this type of problem.

This dissertation will focus on the experimental and computational characterization of strong vent flows on single room enclosure fires.

Table of Contents

x

List of Tables

List of Figures

xvii

Chapter 1: Introduction and Scope

This dissertation involves computational validation of non-reacting and reacting flow simulations in a modeled room scale burn facility to quantified experiments conducted in the actual room scale facility on The University of Texas-Austin's campus. This chapter provides background and motivation for the work discussed in greater detail in the following chapters.

1.1 OVERVIEW OF POSITIVE PRESSURE VENTILATION

The application of an adequate water supply is often thought of as the only requirement for firefighters to extinguish a fire. While water control plays an important role in firefighting tactics; understanding and manipulating airflow has also become more widely recognized as being an important part of helping firefighters gain control of a fire. Airflows of interest come in two main forms: natural airflow and mechanically induced airflow. Mechanically induced airflows can be used to purge the structure of the hazardous products of combustion that impede the firefighting search, rescue, and suppression activities (Figure 1.1.1). The fan is setup outside of the structure entrance and a window is broken in the fire room. The pressure generated by the fan flow forces combustion gases out of the compartment through the broken window.
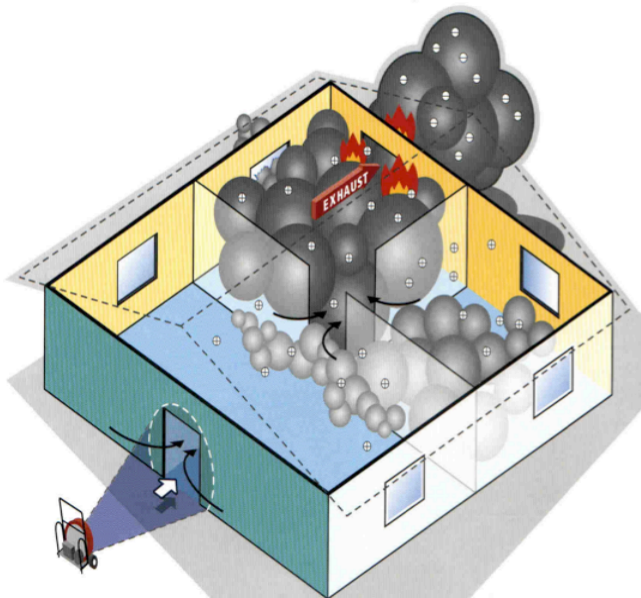
Figure 1.1.1: Schematic showing the application of positive pressure ventilation to a residential structure. (Tempest-Technology, 2010).

Airflow from wind has been implicated in several firefighter line-of-duty-deaths in which a sudden change in the wind direction or magnitude pushed the fire onto firefighters within a structure. There is a long research record of studies evaluating the impact of natural airflow (wind) on structural integrity and ventilation. Burnett et al. in 2004 used computational fluid dynamics to examine the optimal orientation of a residential high-rise building to maximize cross flow ventilation (Burnett, Bojic, & Yik, 2005). The use of wind as a source of natural ventilation/temperature control in residential structures has been characterized through mathematical resistance models as developed by Aynsley (Aynsley, 1997).

In addition to examining the impact of wind ventilation within structures during normal building operating conditions, much more limited research has been conducted to study the impact of wind on fire growth within structures. The most notable studies are from National Institute of Standards and Technology (NIST) experiments conducted by

Kerber and Madryzkowski on laboratory scales, followed by tests in a high-rise building on Governors Island in New York (S. Kerber & Madryzkowski, 2009a, 2009b).

Kerber and Madryzkowski's laboratory experiments found that compared to a baseline (no-wind) test, the wind driven fires had a much faster transition to untenable (hazardous) conditions after ventilation (S. Kerber & Madryzkowski, 2009b). These tests highlight the importance of the airflow direction being aligned with the direction of firefighter attack to reduce overall firefighter exposure to the fire hazard. Kerber and Madryzkowski's experiments in a 7-story building on Governors Island in New York extended the laboratory tests. From these tests, they determined that wind speeds on the order to 10 m/s to 20 m/s are sufficient to create wind driven (hazardous) conditions within a structure (S. Kerber & Madryzkowski, 2009a). Lastly, these test results also stressed the importance of considering wind effects, magnitude and direction, as part of the fire-service initial "size up" of a fire (S. Kerber & Madryzkowski, 2009a). Size-up is a tactic used by the fire-service where firefighters encircle the structure of interest in order to gauge fire severity and location.

Chen et al. also studied the impact of wind on fire growth in high-rise structures (Chen, Lui, & Wanki, 2009). They studied smoke flow variations and temperature changes in a ventilation controlled fire scenario in a high-rise compartment. Similar to the NIST study, a critical wind speed was found where wind was sufficiently strong to overcome the buoyancy of the fire plume and begin to feed the fire oxygen (Chen et al., 2009). Note however, that the critical wind speed to feed oxygen to the fire in such a way as to increase the burning rate is less than the wind speed that adversely affects firefighter progress into the structure.

While wind naturally and uncontrollably drives airflow around and in structures, a controlled mechanical firefighting tactic called positive pressure ventilation (PPV) is also

3

used to drive flows within structures. PPV is a firefighting tactic in which an industrial fan is used to drive hot smoke and combustion products out of a structure to improve interior firefighting conditions. The intent is to push smoke and heat out through open windows and doors nearest the fire location and away from the direction in which firefighters enter. However there are concerns about negative impacts associated with the use of PPV. Svensson showed that while PPV can lower temperature in rooms on the windward side of the fire, it can increase temperature in rooms on the leeward side of the fire (Svensson, 2001). This is important because it may change a firefighter's approach to using PPV if there is a possible victim inside the structure. Kerber and Walton showed that higher temperatures, increased window gas flows, and higher pressures were recorded in their experiments where PPV was used compared to natural ventilation (S. Kerber & Walton, 2005). In addition to the thermal concerns, another potential hazard is that the pressurization associated with PPV can drive fire through holes in the structure's walls or ceiling, spreading fire through void spaces between wall studs or ceiling beams. Research into the application and effectiveness of positive pressure ventilation is an important area of fire research as results can have a direct impact on firefighting tactics. PPV research is generally broken into two separate categories: studying the impact of flow rates through non-reacting flows and studying the impact on the thermal environment through reacting flows.

Despite concerns, when employed properly the use of PPV as a firefighting tactic has demonstrated benefits. Ezekoye et al., found that for their specific test house, the impact of lowering the fire room temperature outweighed the slight increase of temperature in a victim room (Ezekoye, Lakshminarasimhan, Seers, & Nicks, 2005). Kerber and Walton, in the same PPV/natural ventilation comparison experiments discussed above, found that after peak heat release rates were reached for both ventilation

tactics, PPV reduced temperatures faster and more significantly as compared to natural ventilation (S. Kerber & Walton, 2005).

1.2 OVERVIEW OF COMPUTATIONAL MODELS

The use of computational fire models continues to grow in both user base and application. The user base ranges from firefighters to engineers who use the models to examine firefighting tactics, to improve building safety design (e.g. structural fire protection), and to perform post incident investigation. While models can provide insight into the fluid mechanics, heat transfer, and combustion properties of a fire that may not otherwise be available, the responsibility falls on the user to choose an application-appropriate model and to ensure the model results are valid. The current state of fire models ranges from zone models (single or multi) to full computational fluid dynamics (CFD) models. When using a zone model there are assumptions made about the domain. The main assumption in zonal models is that chemical composition and temperature within the zone are uniform. This assumption is fair for fires in compartments with a distinct plume and upper smoke layer (Jones, Peacock, Forney, & Reneke, 2009). This two layer formulation is the basis for the low order zone model called Consolidated Model of Fire and Smoke Transport (CFAST). CFAST is the zone model used in this research. CFAST is zone fire model that determines how smoke, combustions productions, and temperatures evolve during a compartment fire. Inherent to any zone model is the assumption that each compartment is modeled as at least one control volume that is uniform in composition and temperature. In CFAST each compartment is divided into two distinct control volumes or zones. In each zone, CFAST solves what is essentially an initial value problem for a system of ordinary differential equations. The governing equations are conservation of mass and energy, the ideal gas law, and relations

5

for density and energy. These equations are used to predict pressure, layer interface height, and temperature given an accumulation of mass and enthalpy in the control volume. For quantities that cannot be computed from theory, correlations and approximations are used, and it understood that this technique introduces error (Jones, Peacock, Forney, & Reneke, 2009). The separator between the two zones in a CFAST compartment is called the layer interface. The layer interface exists because there is no mixing between the two zones; however there is smearing of computed quantities at the interface. A schematic showing the upper and lower layer as well as orifice flow in CFAST is show in Figure 1.2.1.
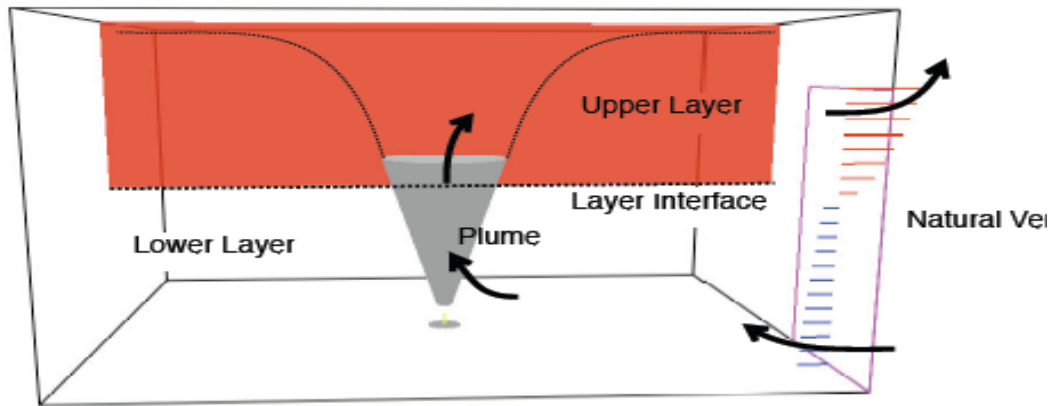
Figure 1.2.1: Schematic showing the two zone model used in CFAST (Jones et al., 2009)

However, a zone model does not simulate systems with local mixing and large spatial variances well. Despite the limitations, an advantage of zonal models is that there is minimal computational expense using these types of models. CFD models can provide more accurate solutions to all ranges of problems as the domain can be dissected into small computational cells based on a user-defined grid. The downside to CFD models is the large computational expense associated with dividing up the domain. In this research,

the CFD model used is the National Institute of Standards and Technology code Fire Dynamics Simulator (FDS) (McGrattan, McDermott, Hostikka, & Floyd, 2010b).

Fire Dynamics Simulator (FDS) is an open source computational fluid dynamics software package that solves a discretized form of the Navier-Stokes equations for low-Mach number, thermally driven flows. The low Mach number form of the Navier-Stokes is obtained as the asymptotic limit of the Mach number approaches zero. For FDS, low speed flows are defined as a Mach number less than 0.3. The low Mach number approximation of the Navier-Stokes equations is beneficial in this application because it filters out high-speed acoustic waves while allowing for large variations in temperature and density; this reduces the computational expenses of integrating the conservation equations since the short time scale acoustic physics are no longer resolved.

The partial differential equations specifying conservation of mass, momentum, and energy are written in conservative forms and are differenced in space using a second-order central difference scheme and in time using an explicit second order predictor-corrector scheme. The computational domain in an FDS simulation must be composed of rectilinear volumes or meshes. The mesh is divided into smaller volumes, grid cells, where the user sets the size of the grid cells. In order to solve complex fire related problems, FDS uses several models. The default combustion model is a single-step global reaction with an empirical local extinction model. The combustion model is a fast chemistry model based on the mixture fraction, which is defined as the mass fraction of the gas mixture that originated from the fuel source. Extinction is determined by the local (cell) temperature and oxygen concentration. Combustion products are found through linear transformations of the mixture fraction. Soot is assumed to be produced like gas phase products with a fractional yield from the carbon in the fuel. There are significant

errors in such an approximation. The combustion model will be discussed in more detail later in this dissertation.

Turbulence is modeled using a large eddy simulation (LES) model. FDS uses the Smagorinsky form of LES, which is a technique used to model dissipative processes that occur on length scales smaller than those resolved by the user defined grid. An LES model is an appropriate choice for FDS as fire plumes are dominated by large scale eddies that can generally be resolved with reasonable grid resolution. Large-scale simulations in FDS have been found to have the best results when the Smagorinsky constant is set at the lowest value that maintains numerical stability, minimizing the damping of resolvable eddies from the addition of artificial viscosity (McGrattan, McDermott, Hostikka, & Floyd, 2010a).

Radiative heat transfer is modeled in FDS as part of the radiation transfer equation (RTE). The RTE is computed using a finite volume method, which is applied to the same grid as the flow solver. Because of the spectral dependency of the terms in the RTE for a participating media, the equation becomes difficult to solve accurately. In large-scale fires, soot is the dominant product affecting gas phase radiation. The radiation spectrum of soot is continuous therefore a fair assumption is to model the gas a gray medium. For simulations with minimal soot production, band models (6 or 9 bands) are used to approximate the spectral dependence. To solve for the source term in the RTE, radiative intensity, two approaches are taken. For the computational cells that resolve the flame sheet, specifically for large grid cells, an empirical model is used because temperature is smeared over the grid. Since intensity goes as temperature to the fourth power, an underprediction in temperature can have a large impact on intensity. For cells away from the flame sheet, radiation intensity is found using discrete ordinates. By default, FDS uses 100 discrete solid angles, however the user can increase this number.

1.3 OVERVIEW OF UNCERTAINTY PROPAGATION AND THE QUADRATURE METHOD OF MOMENTS

Uncertainty propagation is an important part of the analysis and discussion in this work due to the significant use of experimental data and computational models. Often, nominally steady state data may have some time variation. While it is expedient to compute a mean value for the data, it is important to also characterize and use the full statistical behavior of the data in analysis. Too often, computation of some derived quantity $z=f(x,y)$ utilizes only mean values of the input variables (cf. figure 1.3.1). The statistical variation in the input data could be driven by uncertainty in the physical sensor behavior, changing environmental conditions, etc. It is useful to model the statistical behavior of the data (i.e., the uncertainty) using probability density functions (PDFs). To propagate the uncertainty within any given data set into other quantities of interest, Monte Carlo methods are often used to sample values from an input distribution so that an underlying model can compute the output distribution. Though a simple method, a large number of input values are required in order to accurately produce the desired output distribution. Monte Carlo methods can quickly become computationally expensive, especially for multi-variate problems with expensive function calls. For the uncertainty propagation in this work, a much more computationally inexpensive approach known as the method of moments (MOM) will be used.
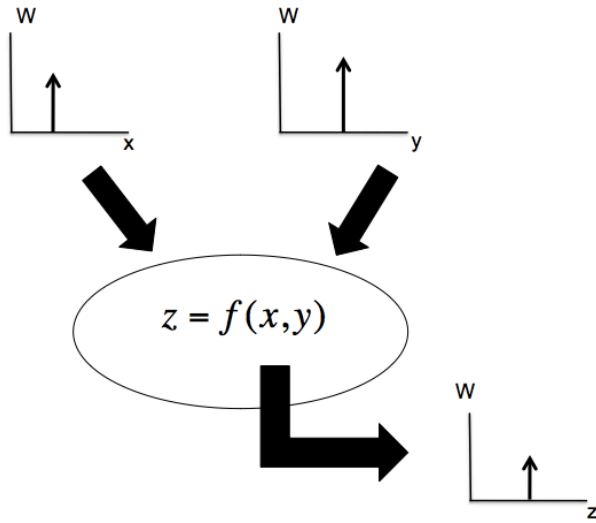
Figure 1.3.1: Illustration of deriving a functional value, z, based on representative mean values, x and y.

The method of moments scheme that allows distributions to be evaluated by their moments, where a moment is a statistical descriptor of the distribution. In terms of statistics the first moment of a distribution is its mean, the second is its variance, etc. While knowing higher order moments allows for a better approximation of the distribution, low order moments (zeroth, first, and second) may be satisfactory, depending on the underlying distribution. Given a PDF, $p(x)$, then the kth moments can be found by:

$$_x M_k = \int x^k p(x) dx \qquad\qquad 1.1$$

Since the moments of the PDF are a compact may of representing the PDF characteristics, it is useful to cast conservation equations and other relationships between variables in this research into PDF formulations that can then be reformulated in terms of moments of the PDF. In general there will be a moment closure problem since the sequence of moments being computed must be truncated to yield tractable computations. To appropriately compute "unclosed" moments, the quadrature method of moments was

developed, which represents the moment integral in equation 1.1 as an n-point sum (McGraw, 1997):

$$_x M_k = \sum_{i=1}^{n} \hat{x}_i^k w_i \qquad\qquad 1.2$$

where $\hat{x}_i^k$ is known at the ith quadrature point, w_i is known as the ith quadrature weight, and n is the number of quadrature points. Anzalone (Anzalone, 2010) provides a summary on the application of QMOM for uncertainty propagation by working through both univariate and multivariate problems.

Evolutions of moment equations using QMOM and DQMOM are completed using the libMoM library developed by Upadhyay (Upadhyay & Ezekoye, 2011). This library has built in functions to generate a set moments from several predetermined types of PDFs, and to solve for quadrature points and weights from the set of moments.

1.4 SCOPE OF THE WORK

This dissertation is organized into 5 chapters. In Chapter 2, the non-reacting flow problem associated with use of positive pressure ventilation fans is presented and analyzed. This work was conducted to understand the fluid mechanics of the problem independent of thermal modifications associated with reacting flows. A series of experiments were conducted to quantify compartment pressure and flow rates for various exhaust path configurations under forced ventilation. CFD simulations and a low order analytical model were then validated using the experimental data. Chapter 3 presents and discusses the reacting flow experiments and develops the computational tools used to model the coupled fluid mechanics, combustion, and heat transfer processes. In Chapter 3, model parameters are calibrated and the models are validated against experimental data. It is shown that models of varying complexity and sophistication are useful in

predicting different aspects of the physics of the system. In Chapter 4, the computational tools are used to model compartment fires under various ventilation tactics. This is done to provide insight into the impact of the ventilation tactics on the thermal environment of the fireground. Finally, conclusions and future work are presented in Chapter 5.

Chapter 2: Modeling Fan Driven Flows for Firefighting Tactics

2.1 OVERVIEW OF FAN DRIVEN FLOW EXPERIMENTS AND MODELING

The work in this chapter is largely based on previously published work by this author in the Journal of Fire Protection Engineering (Weinschenk, Beal, & Ezekoye, 2011).

In general, the combination of experimental and computational results is useful for understanding and characterizing complex engineering problems, especially in fire research. Fire Dynamics Simulator (FDS), developed by the National Institute of Standards and Technology (NIST), is the most widely used fire computational fluid dynamics code. Similar to most CFD tools for complex and large-scale systems, FDS uses models where direct solutions of the governing equations are infeasible. FDS uses the low Mach number approximation, limiting the types of solutions to low speed flows. A predictor-corrector scheme is used for the hydrodynamic model, which is second order in both time and space. Turbulence is modeled using a large eddy simulation (LES) framework in which subgrid scale flow processes are modeled using the Smagorinsky model. A more detailed description of the FDS code is included in Chapter 3.

Since models and submodels are used in this CFD code for the predictions of interest, the code user has the responsibility to validate the computational results. Model validation can sometimes be accomplished using experimentally determined correlations or, more directly, through experimental data. To make the claim that the model is validated, the model must be shown to have an acceptable level of accuracy for that specific situation (McGrattan et al., 2010a).

Modeling ventilation of a fire is challenging due to the complex coupling of fluid mechanics, heat transfer, and combustion equations that govern the system. Relevant information for modeling the fluid mechanics problem includes: the type of structure, impact of the environment on the structure, location and number of open vents, and the source (natural or mechanical) of flow. In addition, these physical processes occur over widely disparate length and time scales. Various levels of approximations and simplified models can be developed to predict aspects of the problem. It is useful to validate these simplified models in decoupled but closely related problems. Non-reacting flow experiments were conducted in a one-room experimental structure. The mechanical flow source was a 6.5 hp (4.85 kW) motor, commercial PPV fan. Experimental pressure and velocity measurements are used as the basis for comparison to the computational simulations. Three cases are investigated: one with no exit vent window and two cases with different exit vent window locations. For the simulations, a fan model was derived based on specifications taken from the manufacturer and then scaled appropriately to match the conditions for the most basic experimental case (*i.e.*, with no exit vent). The resulting fan model and the induced flows along with an analytical model are compared to the data for the more complex cases to evaluate the model predictions. The results show if a simple fan calibration process is used, then simple analytical models are reasonable tools for predicting global flow properties during use of PPV.

2.2 NON-REACTING FLOW EXPERIMENTS

2.2.1 Experimental structure geometry

The experimental structure primarily consists of a single room and an entrance hallway, as shown in Figure 2.2.1. To approximate leakage paths from the interior compartments to the wall spaces, a gypsum failure area was created in the experimental

system. The gypsum failure area is a hole in the gypsum board of a wall in the fire room, and exposes a void space (between the wall studs) to the main room. Understanding the effects of a gypsum failure area is important to firefighters using PPV because there is a concern that pressurizing a compartment can drive hot flammable gases into void spaces in the compartment walls. The void space is designed to resemble structural void spaces in balloon frame construction, which represents a worst-case structural failure system for a pressurized fire compartment. Balloon frame construction utilizes long studs that run from the sill to the eave. Since floors are built off of the studs, if fire stops are not added, this type of construction provides pathways for fire to spread vertically. The structure geometry shown in Figure 2.2.1 was used for the non- reacting flow experiments and the simulations.
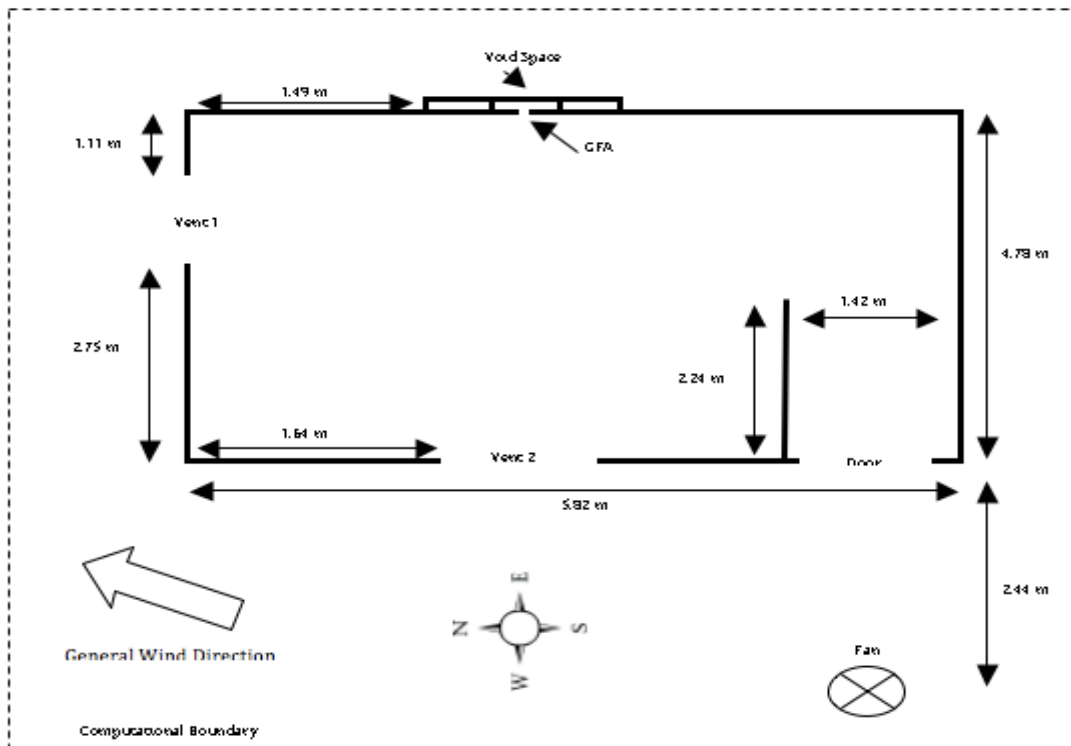
Figure 2.2.1: University of Texas at Austin burn structure geometry. This geometry was used for all of the experiments and simulations in this study.

The ceiling is 2.44 m in height everywhere except within the void space which is 3.05 m tall and open at the top. The experimental structure is 5.82 m in length, 4.78 m wide, and the hallway partition is located 1.42 m from the right wall. The hallway is 2.24 m long and 1.42 m in width. The hallway partition is located 0.10 m from the doorway. Both windows, vent 1 and vent 2, are 0.91 m wide and 1.22 m tall with a sill height of 0.91 m. The door is 0.91 m wide, 2.13 m tall, and is located 0.41 m from the right wall. The test section was constructed with 1.6 cm thick gypsum board fastened to 0.10 m wide studs that are 3.05 m tall. The gypsum failure area was placed through the interior gypsum wallboard of the void space to expose the void space to the main room. The gypsum failure area is 0.023 m^2 for the experiments and all simulations. The studs within the void space are separated by 0.41 m, which results in a void space that is 0.10 m x 0.41 m x 3.05 m. Figure 2.2.2 is a three-dimensional rendering of the structure showing major features.
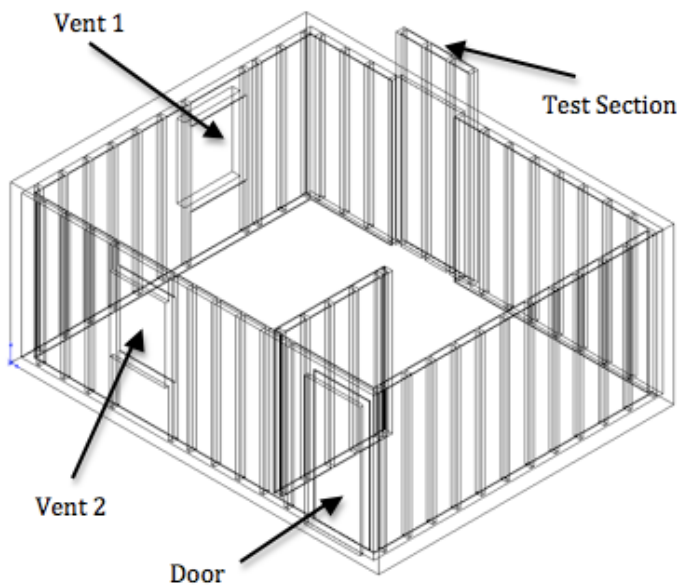
Figure 2.2.2: 3-D rendering of the University of Texas at Austin burn structure.

2.2.2 Fan properties

The experiments used a 6.5 hp (4.85 kW) motor, commercial PPV fan to generate the airflow. The fan has a diameter of 0.61 meters and was operated at full throttle. It was rated to produce 13.12 m^3/s when operated at 3500 rpm. The fan was set 2.44 m from the door based on recommendations from Kerber and Walton that the fan should be placed between 1.82 m and 3.0 m for best effectiveness (S. Kerber & Walton, 2003). 2.44 m was chosen as it falls in the middle of the recommended range. The fan height was adjustable and was set at a centerline height of 0.71 m (the height of the fan with legs extended) so that the jet of air produced from the fan best seals the doorway.

2.2.3 Experimental methods

The PPV flow experiments were performed for three venting configurations: windows closed (no vent), the north window open (vent 1), and the west window open (vent 2) (cf. Figure 2.2.1). Since leakage can significantly affect conditions during the application of PPV (Beal, Fakhreddine, & Ezekoye, 2008), the experimental structure leakage was determined according to the "blower-door" test (Beal, 2008) as described by ASHRAE Standard 119 (ASHRAE, 1988). For this test an impermeable membrane is sealed across the doorway and around the outside shroud of a fan that is located in the doorway, blowing out of the compartment. The flow rate produced by the fan and the resulting compartment pressure were recorded and Sherman provides a standard method for using these data to characterize the leakage (Sherman, 1995). Sherman's method produces an effective leakage area (ELA), which corresponds to the actual leakage area present in a structure and a normalized leakage value (NL), which can be used to compare the leakage of one structure to others. The leakage test was conducted and the ELA and NL values obtained were 0.029 m^2, and 1.02, respectively. In another study, Sherman and Dickerhoff provide an average normalized leakage for a residential

structure to be 1.72 with a standard deviation of 0.84 (Sherman & Dickerhoff, 1998). The leakage in the experimental structure is within one standard deviation of average residential houses.

Bi-directional probes were used to measure the velocities produced during the cold flow experiments. These probes, as first described by McCaffrey and Heskestad, can be used to determine the incident flow velocity by measuring the differential pressure established across the probe (McCaffrey & Heskestad, 1976). Each probe used in the experiments was connected to a differential pressure transducer (Setra model 264). The probes and transducers were calibrated in a wind tunnel (Beal, 2008).

Flow through the structure was measured by placing three probes in the doorway, four probes in the windows (when applicable), and three probes near the top of the void space. The probes in the door were spaced at 0.61 m, 1.22 m, and 1.83 m elevation along the doorway centerline. The four probes in the window were spaced evenly, effectively dividing the window into quadrants. Finally, the probes in the void space were located at an elevation of 2.75 m and evenly spaced across the 0.41 m test section. All of the probes were oriented to measure velocity normal to each of the associated vents.

Ambient wind velocity was measured at an elevation of 2.75 m on the corner of the experimental structure between vent 1 and vent 2 (cf. Figure 2.2.1). The probe used to measure the wind speed was aligned with the wind by using a tuft. In all of the experiments the wind blew in the general direction shown in Figure 2.2.1. During these tests, wind speeds averaged 1.5 m/s with gusts less than 5 m/s. Using the characteristic fan jet speed (an average speed based upon the speed at the fan face and at the doorway) divided by the average wind speed, the velocity ratio for the fan jet in cross flow is approximately 20. For velocity ratios greater than 15, the cross flow has minimal impact on the structure of the jet, though it may cause the jet to become asymmetric downstream

(Higuera & Martinez, 1993). This means that the effects from wind on the fan flow can be neglected in the models.

Finally the compartment gauge pressure was recorded with a differential pressure transducer by running one of the transducer leads into the compartment and leaving the other outside the compartment, open to the atmosphere. The lead exposed to the environment was protected such that wind effects would be negligible. The interior transducer lead was located near the floor in the northwest corner of the experimental structure.

The *No Vent* scenario was conducted by applying PPV with both vents closed and the gypsum failure area open. The *Open Vent* experiment was conducted by applying PPV with vent 1 completely open, vent 2 completely closed, and the gypsum failure area open. Experiments and simulations were also conducted using vent 2 as the exit vent. However, the results with vent 2 open will not be included in this study because they are similar to the results with vent 1 open. Previous studies have evaluated the effect of exit vent location on the application of PPV (Beal, 2008; Beal & Ezekoye, 2008).

The error associated with the bi-direction probe velocity measurements is dominated by the alignment of the probes to the incident flow. Since the probes were aligned normal to all of the associated vents it is reasonable to assume the alignment between the flow and the probes was within 20 degrees. Based on the results presented by Liu et al., a 20 degree flow alignment corresponds to an uncertainty of 15% in the experimental velocity results (Liu, Wong, Chan, & Can, 1990). The pressure transducers used in the experiments were each calibrated with an inclined tube manometer (Beal, 2008).

2.3 ANALYTICAL MODEL OF PPV

Analytical models, even simple ones, can provide insight into experimental and computational results. While a simplified analytical solution can sometimes only provide trends, this can still be important because the relative impact of the assumptions can be determined.

The quasi-analytical model used to analyze the flow through the experimental structure in this study is a standard pressure-driven resistance flow model (Figure 2.3.1). In Figure 2.3.1, P_c is the compartment gage pressure. The underlying methodology is substantially similar to the vast literature on pressure-driven flow models. The basic idea is that for a flow system identified with nodes i and j at which a total pressure can be defined, then the volumetric flow rate between node i and node j is defined by:

$$Q_{ij} = \frac{A_{ij} C_{Dij}}{\rho^{1/2}} \frac{\left(P_i - P_j\right)}{\left|P_i - P_j\right|} \sqrt{2\left|P_i - P_j\right|} \qquad 2.3.1$$

C_d is the orifice coefficient, typically 0.61 for small openings (leaks) and 0.80 for large openings (windows) (Awbi, 2003). P_i and P_j are the pressures measured at the respective i and j orfices. Mass conservation must be satisfied for internal nodes that might represent compartments within a structure. Typically, the challenge in the use of such models is in the description of an external nodal pressure when an external flow (e.g., wind) impacts the structure. The total pressure is specified using a product of a pressure coefficient and the dynamic pressure.

$$P_{i,EXIT} = \frac{1}{2} \rho U_C^2 C_p + P_0 \qquad 2.3.2$$

Here ρ is ambient density, U_C is a characteristic flow velocity, C_p is the pressure coefficient, and P_0 is ambient static pressure. The pressure coefficient is generally tabulated for various wind-structure configurations (Awbi, 2003). For the case of a

mechanical fan impinging on a open vent/door, it is inappropriate to define a pressure coefficient and C_p is set equal to 1.0, since the jet is centered on the opening and is unaffected by the presence of the structure walls. The use of C_p equal to 1.0 for the fan will be discussed in further detail later in the manuscript.
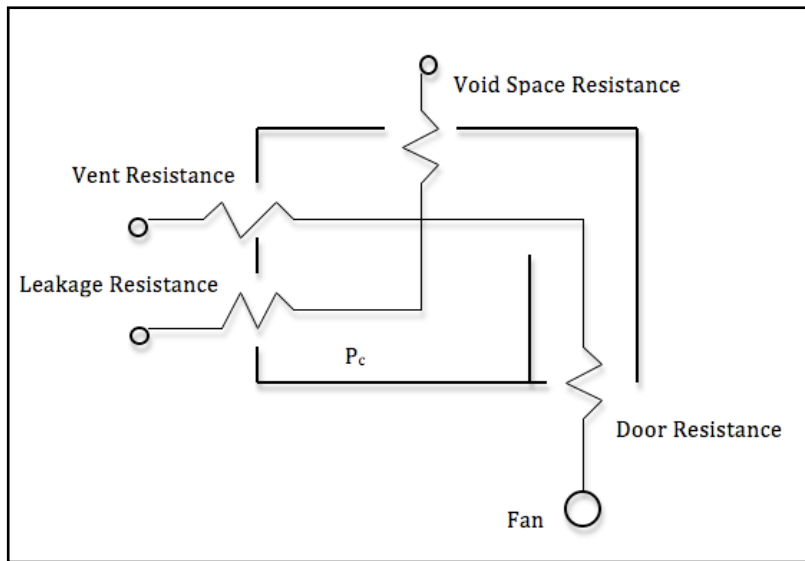
Figure 2.3.1: Resistance diagram of burn structure.

To better understand the impact of fans on flows through structures, Ingason and Fallberg of the Swedish National Testing and Research Institute conducted non-reacting flow research on a single inlet and outlet structure (Ingason & Fallberg, 2002). They stated that to achieve best performance from PPV, there is an optimal ratio for exit to entrance vents. Their result is obtained using relatively simple equations for volume flow rate through an exit vent and the static positive pressure inside a structure developed by a fixed source. The model assumes the fan is placed at the appropriate distance away from the inlet vent so that the air cone produced by the fan completely seals the vent. The fan is considered to be centered with respect to the inlet vent (e.g., the door through which

firefighters enter the structure). Ingason and Fallberg write that the volume flow rate of exhaust gases, Q_{Exit}, is

$$Q_{EXIT} = \frac{2.44}{\pi\sqrt{\xi}} \frac{BQ_{FAN}}{D_{Fan}} \left(\frac{S}{S^2+1} \right)$$
2.3.3

where B is the width of the entrance opening, Q_{Fan} is a characteristic airflow from the fan, ξ is the static pressure loss coefficient, D_{Fan} is the fan diameter, and S is the ratio of exit to inlet vent areas (A_{Exit}/A_{Inlet}). They define the "positive pressure", ΔP, as

$$\Delta P = 8\rho \left(\frac{Q_{FAN}}{\pi D_{FAN}H} \right)^2 \frac{1}{S^2+1}$$
2.3.4

where Q_{Fan} is the flow rate generated at the fan face, ρ is ambient air density, and H is the height of the opening. The positive pressure is essentially the overall driving potential across the structure. Eqn 2.3.1 is a more general version of their result. We can show that the most general case can be reduced to a form more consistent with theirs.

Based upon their work, when holding all other parameters constant, an increase in the exit-to-entrance vent area ratio, S, will increase the exit flow rate as defined by equation 2.3.3. However, the exit flow rate asymptotically approaches a limiting value as S continues to increase. Additionally as S increases, the positive pressure, as defined by equation 2.3.4, drops. In practice, as the pressure, or driving potential, drops, the flow through the compartment becomes more sensitive to changes in the wind speed. For "best" performance, Ingason and Fallberg suggest that the ratio of exit-to-inlet vent areas should be between 1.5 and 2 (Ingason & Fallberg, 2002).

The resistance model that is developed in this work is somewhat different from the Ingason and Fallberg model (Ingason & Fallberg, 2002) since multiple outlet vents are being analyzed as compared to a single outlet and because the fan flow-door model is more complex. The inclusion of multiple vents is particularly relevant to the way that the

door flow is modeled. Both inflow and outflow areas are allowed though the door. Experiments in fan flows clearly show that backflow often occurs in doors subjected to a PPV fan flow.

As previously noted, characteristic external velocities are required to define the pressure driving potential. For the fan driven flow, a round jet flow model is used to specify the characteristic velocity and volumetric flow rate. This is the simplest level description of a PPV fan and it neglects several features of actual PPV fan flows. First, it neglects the asymmetry in the fan flow associated with the ground. Interestingly, some fans, including the one that used in these tests have legs to limit the ground flow effects. The model also neglects the effects of swirl and the annular flow generated because of the fan hub. Because annular jets are known to develop much more rapidly than round jets (x/D ~ 2) and because they reach the same self-preserving state (Ko & Chan, 1978) it seems that the assumption of a round jet is reasonable. It will be shown in the results section that not explicitly accounting for the ground flow and swirling-annular flow has negligible effects on predicting global quantities.

Downstream of the fan/source, the jet entrains air, thus increasing the mass flow rate. The jet area increases and average velocity decreases. The velocity decrease and entrainment are modeled using simple jet growth model equations where a virtual origin displacement is used (Awbi, 2003):

$$\frac{U(x)}{U_{Fan}} = \frac{0.48}{a\left(\dfrac{x}{D_{Fan}}\right) + 0.145} \qquad\qquad 2.3.5$$

$$\frac{Q(x)}{Q_{Fan}} = 0.32\left(\frac{x}{D_{Fan}}\right) \qquad\qquad 2.3.6$$

In equation 2.3.5, $U(x)$ is the centerline velocity of the jet, U_{Fan} is the supply velocity, x is the downstream distance, D is the supply diameter, and *a* is a circular jet constant which for this fan is 0.24 (Awbi, 2003). In equation 2.3.6, Q_{Fan} is the supply volume flow rate, x and D are the same parameters used in equation 2.3.7, and $Q(x)$ is volume flow at a position x downstream. The constants in equations 2.3.5 and 2.3.6 both arise since both equations were developed empirically (Awbi, 2003). The downstream velocity, assumed to be uniform with a magnitude of $U(x)$, is divided into the volume flow rate, Q, to find the area, $A_{d,in}$, of the jet at the downstream position x. This area is used to determine how much of the structure doorway is sealed by the jet. For this model, it is assumed that mass is flowing into the structure over the area, $A_{d,in,}$ and mass can exit the structure across the remaining unsealed (door) area. The door is approximately 4 diameters downstream of the PPV fan, so the top-hat profile is not a bad assumption.

The "true" fan face flow rate is unknown. An initial solution set is found by solving the system of mass flow equations at each orifice using the manufacturer's volumetric flow rate specifications (13.1 m^3/s) at the face of the fan. The flow rate was then iteratively scaled until the analytically calculated structure pressure was within 10% of the experimentally measured pressure for the *No Vent* case. The best analytical fan flow rate that predicts the structure pressure with no windows open is 12.5 m^3/s. Holding the fan parameters constant, the venting conditions were changed to reflect the *Open Vent* experiment to examine the model predictions for that case.

While both the Ingason and Fallberg model and resistance model shown above were developed from flow conservation equations, several differences exist between them. The first difference is the fan model. For the Ingason and Fallberg model, an assumption is made that the fan is placed at a distance away from the structure so that cone of air from the jet completely seals the door. The resistance model is similar to real

applications of PPV where the fan is set at some distance (e.g., 2.44 m) from the door and the amount of sealing area at the doorway is based on the fan parameters. The choice of fan placement would impact the mass flow rate through the doorway due to the differences in air entrainment. As previously noted, the second difference is that the Ingason and Fallberg model only accounts for one exit path through the structure compared to the resistance model, which does not limit the number of exits. This factor is important because as discussed earlier, in addition to major flow paths such as vents, structures are not completely sealed so leakage needs to be accounted for.

For a case in which the compartment has only two vents and a fan is placed to exactly seal one of the vents, equations 2.3.5 and 2.3.6 can be used to determine the nondimensional downstream distance at which the fan needs to be placed to seal the door. The flowrate at a position downstream, $Q(x)$, is equal to the velocity times the area, $U(x)A$. Equations 2.3.5 and 2.3.6 are plugged into the flow rate equation, which is then solved for $\dfrac{x}{D_{Fan}}$. The nondimensional distance is found from the quadratic equation:

$$\left(\frac{x}{D_{Fan}}\right)^2 + 0.077\left(\frac{x}{D_{Fan}}\right) - 6.23\left(\frac{H}{D_{Fan}}\right)^2 = 0 \qquad\qquad 2.3.7$$

Solution results in a sealed fan to door distance of 5.1 meters for the 0.61 meter diameter fan. This result is not believable and is limited by the various assumptions made in simplifying the jet flow model. Here, it is possible that the ground effect and the subsequent modification to jet entrainment would have a considerable effect. However, it is useful to compare the predictions of this simplified case with equation 2.3.2 derived by Ingason and Fallberg. Interestingly, since the linear term in equation 2.3.7 does not contribute significantly, a simplified relationship is that x=2.5H for a fully sealed door.

From equation 2.3.7, the positive pressure in the structure reduces to a form similar to equation 2.3.2.

$$\Delta P = 8\rho\left(\frac{Q_{Fan}}{\pi D_{Fan}H}\right)^2 \frac{1}{S^2+1}\left(\frac{0.32x}{H}\right)^2 \qquad\qquad 2.3.8$$

The resistance model has an additional multiplicative term compared to the Ingason and Fallberg expression (cf. equation 2.3.2) that is approximately equal to 0.6. It is possible that the primary difference in the two models for a single inlet and single outlet problem is the description of the jet entrainment. Ingason and Fallberg do not explicitly discuss the entrainment model, so further discussion about the reasons for the differences would be speculative.

2.4 COMPUTATIONAL SIMULATION OF NON-REACTNG PPV

The experiments conducted at the UT burn structure were used for model validation. Combining experimental and computational results has been proven to be an effective way to understand the phenomena associated with PPV (Beal et al., 2008; S. Kerber & Walton, 2003; Vettori, Madryzkowski, & Walton, 2002; Weinschenk, 2007; Zeisler, Gunnerson, & Williams, 1994). The geometry, vent sizes, and vent locations used in all simulations were specified to be the same as the actual structure (cf. Figure 2.1). Examination of the experimental results reveals several issues that must be accurately considered to adequately model positive pressure ventilation. These issues include appropriately resolving the structure on the computational grid, modeling the PPV fan, and characterizing the leakage properties of the structure.

2.4.1 Grid resolution and parallelization

The governing fluid mechanics equations for the CFD model were solved using the parallel processing methodology within FDS. The computational simulations were

completed using 24 meshes of equal volume (7.26 m^3) and equal resolution (194,400 cubic 4-cm mesh cells). The simulations were completed using FDS 5.4.0 SVN 4629 Parallel running on the *Lonestar* Linux Cluster, which is part of the Texas Advanced Computing Center (TACC). To ensure load balancing and optimal efficiency the number of processors was chosen to be a multiple of 4, since the hardware in this cluster: two Xeon Intel Duo-Core 64-bit processors per compute node, has 4 cores per compute node.

The resources of *Lonestar* allow the number of processors to be set equal to the number of meshes, up to 256 processors. Increasing the number of processors in a parallel simulation is advantageous because if resolution is held constant, the number of cells each processor has to perform calculations on is reduced. As the computational demand of a processor decreases, performance increases. However, there is a finite limit to the number of processors a parallel code can utilize before the benefits are negated by the communication costs between the processors. More work is being conducted to examine this limit in this calculation.

Uniform meshes were chosen to maximize parallel efficiency by ensuring each processor was active during the entire simulation. Additionally, two abutting meshes should meet such that the number of cells in adjoining meshes are in integer ratios. Otherwise, numerical inaccuracies and instabilities can develop if cell boundaries do not match. Figure 2.4.1 illustrates this issue. Therefore, based on the domain for the non-reacting simulation, resolution requirements of the rotational fan model, and the goal to have small uniform meshes, 24 cubic meshes of 4 cm resolution were used. 4 cm resolution was chosen based on the overall domain size, location of the fan and structural elements within the domain, location of experimental measurement devices, and resolving both the leakage area and gypsum failure area.
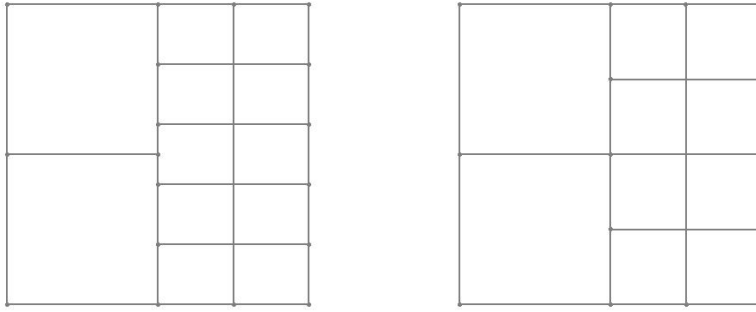
Figure 2.4.1: Abutment of meshes in FDS. The left image shows non-integer abutment
while the right shows the proper integer abutment.

2.4.2 Fan characterization model

Kerber and Walton also conducted non-reacting flow experiments of PPV, focusing on computationally characterizing a positive pressure ventilation fan (S. Kerber & Walton, 2003). The fan model that they developed was accurate in predicting average exit velocities from a vent in a 1-room structure to within 17% of experimental values. For that level of accuracy, the model appears to have required a considerable amount of geometric complexity in describing the fan. Since computational expense scales with geometric complexity, it would be useful to develop fan models that are of comparable accuracy but with significantly less detail.

The fan model used for the simulations in this work is a rotational flow model developed by Weinschenk (Weinschenk, 2007). The rotational flow fan model features four "blades" arranged in a cross-like configuration (cf. Figure 2.4.2) with normal and tangential velocities (indicated with X's and arrows, respectively). The fan flow rate and rotation were modeled based on cubic feet per minute rating and revolutions per minute specifications provided by Kerber and Walton (S. Kerber & Walton, 2003). This model was subsequently compared to a series of non-reacting PPV experiments using a mesh element size of cubic 5-cm (Weinschenk, 2007). The primary source for fan model

validation was experimental work conducted by Kerber and Walton at NIST (S. Kerber & Walton, 2003). These experiments examined velocities downstream of the fan at 1.83 m, 2.44 m, and 3.05 m and compared them to a computational model developed at NIST. Table 2.4.1 shows the comparison between the rotational flow model to Kerber and Walton's model as well as the experimental data.

Table 2.4.1: Comparison of Experimental and FDS Model Average Velocities at three different distances downstream of the fan.

	Average Velocities [m/s]					
	1.83m	% Diff.	2.44m	% Diff.	3.05m	% Diff.
Experimental Data (S. Kerber & Walton, 2003)	2.42	--	2.72	--	3.35	--
Kerber/Walton Model (S. Kerber & Walton, 2003)	2.65	8.68	3.19	14.73	3.25	3.08
Rotational Flow Model	2.95	17.97	2.81	3.20	2.54	31.89

The rotational model compares well to the experimental data set, though not as well as the Kerber and Walton model. The main benefit to rotational model is computational cost. The Kerber and Walton model requires grid resolution of 16.4 cm^3 compared to 125 cm^3 that has been used for the rotational model. The rotational model also compares very well at 2.44 m, the distance the fan is set from the door for the experiments. Overall, the computational savings balance the maximum 30% error in average velocity for near field conditions.
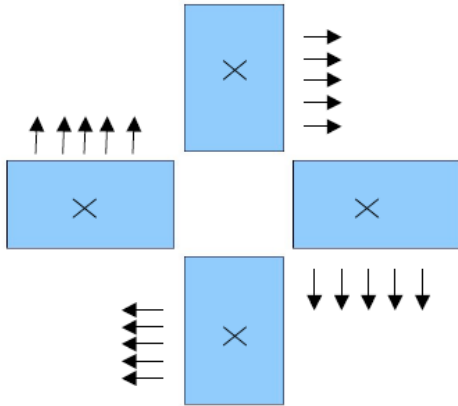
Figure 2.4.2: Schematic of rotational flow PPV fan model. The X's represent normal
velocities while the arrows represent tangential velocities.

In addition to comparing near field velocities downstream of the fan, validation of
the fan model also examined far field properties. Since annular jets (e.g., a PPV fan flow)
in the far field are similar to a round jet, the velocity profile far downstream of the fan
should be self-similar (i.e., the scaled velocity is independent of downstream position x).
This means that if scaled plots are created for different distances, the plots should
collapse into a single curve (cf Figure 2.4.3). For the fan simulations, the average axial
velocity, $<U_j>$, normalized by the centerline velocity, U_0, shows self-similar scaling when
plotted against the radial position, r, normalized by the half maximum distance, $r_{1/2}$ (cf.
Figure 2.4.3).
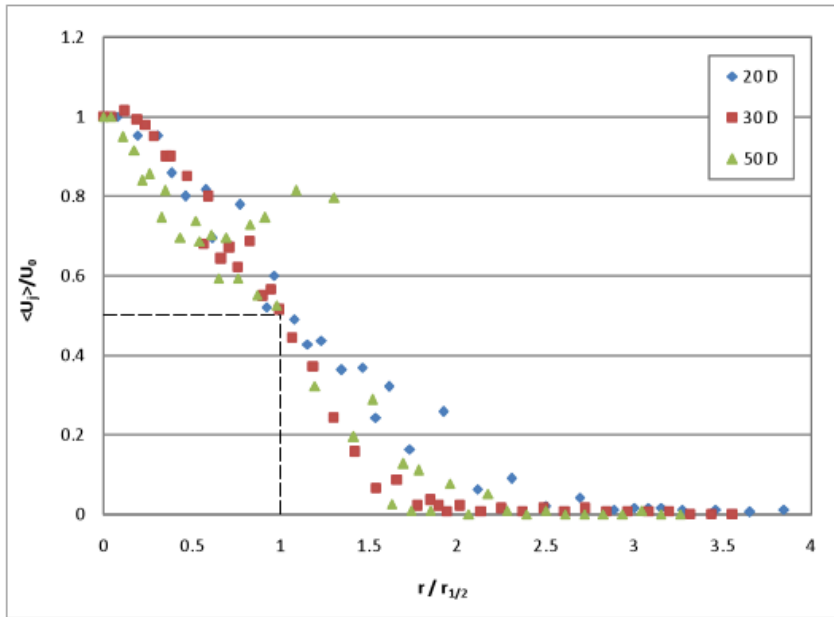
Figure 2.4.3: Self-similarity plot for 20D, 30D, and 50D downstream of the fan.

Figure 2.4.3 shows that at 20, 30, and 50 diameters downstream of the fan, the scaled profiles collapse into a single curve. The results show a core region ($r/r_{1/2} < 0.2$) where the velocity is essentially the centerline value. As $r/r_{1/2}$ increases, there is a transition into a linear region with a constant slope. The scaled velocities reach zero around an $r/r_{1/2}$ value of about 2. The plot showing the self-similarity of the rotational flow model in FDS compares well to round jet profiles found in literature (Awbi, 2003; Weinschenk, 2007). Based on these data, the rotational flow fan model was determined to be a reasonable representation of the actual fan flows, and was used for all simulations in this study.

The computational model of the PPV fan is the most significant source of error in the simulations. While this model was shown to compare reasonably well to Kerber's data, it was done so using a specific fan for which the actual flows rates were well characterized. The same characterization was not used for the fan in the experiments. To

characterize the fan, 8 critical velocity locations on the fan face and an additional 4 locations were used to calculate the fan's average flow rate in m^3/s (Casey et al., 2008). These velocity measurements were averaged and converted to a flow rate based on the area of the fan face. This experimentally measured fan flow rate, 6.2 m^3/s. Recall that the manufacturer specifies the fan flow rate to be 13.1 m^3/s.

Ideally, experimental determination of the fan flow rate is the best way to determine model parameters for any given fan since each fan is slightly different and the testing conditions under which the manufacturer parameters were determined are unknown. Since the experimental flow rate was approximately half of the manufacturer specifications and initial simulations under-predicted pressure, simulations were instead based off the manufacturer specifications. The volumetric flow rate of the model fan was then modified so that the gauge pressure inside the structure during the *No Vent* simulation was with 10% of the experimental results. This was accomplished by iteratively reducing the model fan flow rate from the manufacturer's specifications until the *No Vent* simulation gauge pressure converged to the experimentally measured pressure to within 10%. The fan flow rate setting needed to match the experimental pressure is 11.7 m^3/s, or 89% of the manufacturer specifications of the experimental fan. The second parameter changed was fan height to make sure the model fan sealed the door similar to the actual fan. Using experimental data from the bi-directional probes, the centerline height of the model fan was lowered to be 0.45 m so that the computational flow sealed the door in a manner similar to what was observed in the experiments.

2.4.3 Structure flow models

Accurately modeling the effective leakage area and the gypsum failure area is a concern because of uncertainty about the required grid resolution. For the simulations, a

leakage hole of area 0.029 m², resolved by 18 grid cells, was included in the structure, located along the north wall, 1.2 m from the west wall and 0.6 m above the floor. To determine the impact of resolution on flow through small orifices, test simulations were created to calculate the mass flow and pressure drop associated with low speed flows moving normal to, and through a small opening. The hole area studied in these simulations was 0.026 m² (0.16 m by 0.16 m). This area was chosen because it represents the effective leakage. The goal of these simulations was to see how the orifice discharge coefficient varied as a function of resolution and computation time.

The discharge coefficient equation was developed by applying conservation of energy to points on a streamline in addition to continuity. The equation for discharge coefficient is a function of mass flow rate, pressure drop, and geometric parameters:

$$C_d = \frac{m\sqrt{1 - \left(\frac{D_2}{D_1}\right)^4}}{A_2\sqrt{2\rho(P_1 - P_2)}} \qquad\qquad 2.4.1$$

where D_1 is the inlet diameter, D_2 is the exit diameter and A_2 is the exit area. Pressure drop and mass flow rate were recorded during the simulations. Figure 2.4.4 shows plane view of the simulation geometry that was used. Table 2.4.2 shows the results from the simulations.
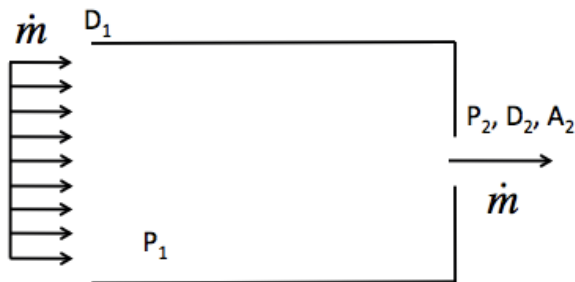
Figure 2.4.4: Plane view of geometry used to test grid cell impact on discharge coefficient.

33

Table 2.4.2 shows that for the 2, 4, and 8 cm resolutions the orifice coefficients, pressure drop and mass flow rates are similar. Despite the fast computation time, 10 cm resolution returns poor results. Due the way FDS models obstructions/holes – if the boundary of an obstruction does not align with a mesh boundary, FDS moves the obstruction to align with the nearest mesh element. Therefore, 10 cm resolution for a 0.16 m by 0.16 m hole becomes a 0.2 m by 0.2 m hole. As a result, when modeling small holes in FDS it important use to a mesh size that allows the hole to be accurately resolved. The differences between the results for the 2, 4, and 8 cm simulations are insignificant relative to the overall error in an FDS simulation.

Table 2.4.2: Comparison of orifice coefficient and computation time for varying grid resolution.

Resolution [cm]	Pressure Drop [Pa]	Mass Flow [kg/s]	Orifice Coeff.	Comp. Time [min]
2	33.3	0.181	0.536	345.6
4	32.8	0.181	0.541	33.05
8	34.2	0.184	0.539	2.18
10	13.2	0.17	0.521	0.4

The shape and location of the leakage hole was also examined as part of this study. Beal et al. show that leakage location affects results for reacting flows, as temperature is a function of height (Beal et al., 2008). For a non-reacting flow, where temperature is assumed to be spatially uniform, location should not play a significant role. Analysis showed that the discharge coefficient changed due to the geometric changes of the hole, since C_d is a function of exit diameter and exit area. Overall, for non-reacting flows the proper pressure drop and mass flow rates can be determined if the grid resolution used can accurately resolve the dimensions of the hole. Using a resolution at

least as fine as recommended by use of the rotational fan model, the ability to simulate flow through the leakage area should be a minimal cause of error.

In addition to modeling structure leakage and flow through the gypsum failure area, a secondary area of concern was accurately characterizing the flow through the void space. The test section is designed to replicate balloon-frame construction but can be thought of as a channel with a footprint of 0.16 m by 0.28 m and a length of 3.05 m. Due to the small area within the channel, it was necessary to compare FDS' model for wall flows to an analytical model. If the channel flow is modeled incorrectly, the simulation results can be adversely impacted.

Using standard equations for flow through a noncircular duct, a model for the pressure drop through the test section can be developed. Based on the experimental results, the flow was found to be turbulent with a Reynolds number of approximately 26,000 (Beal, 2008). Approximating the test section as parallel plates, the friction factor can be determined by

$$\frac{1}{f^{\frac{1}{2}}} \approx 2.0 \log\left(\text{Re}_{D_h} f^{\frac{1}{2}}\right) - 1.19 \qquad\qquad 2.4.2$$

where f is the friction factor and Re_{Dh} is the Reynolds number based on hydraulic diameter. Head loss can be calculated using the friction factor by

$$h_f \approx f \frac{L}{D_h} \frac{U^2}{2g} \qquad\qquad 2.4.3$$

where f is the friction factor calculated in equation 2.4.2, L is the length of the test section, U is the velocity of the flow, g is the acceleration due to gravity, and D_h is the hydraulic diameter. Finally the pressure loss can be determined by using head loss:

$$\Delta P = \rho g h_f \qquad\qquad 2.4.4$$

Using this pressure loss calculation, the flow through the test section was modeled analytically to compare to FDS. The results from the analytical calculations show that the pressure drop along the test section channel from the gypsum failure area to the top of the channel is 2.07 Pascal. The computational result for pressure losses over the same length of channel is 2.23 Pascal. This good comparison between the two predictions provides confidence in the FDS wall model. Additionally, since the pressure loss due to channel flow is less than 4% of the pressure loss through the gypsum failure area, it can be neglected in the analytical flow model.

2.5 VALIDATING STRUCTURE FLOW MODELS

2.5.1 No vent

Validation for the PPV experiments began with the *No Vent* test case. As previously noted, the fan model volumetric flow rate at the fan face was set at 11.7 m^3/s (or 89% of the manufacturer specifications) so that the simulated structure pressure matched that of the experiments for the no vent case. Pressure was chosen as the parameter to match since it is the driving potential for flow exiting the structure. Once the pressures were matched between the data sets, flow rates through the test section and doorway were analyzed.

The experimental pressure was recorded using a differential pressure transducer located in the northwest corner of the structure, as described in the *Experimental methods* section. The computational pressure was calculated as an average of 13 simulated pressure transducers inside the structure. The first transducer was located at the approximate position of the experimental tap, while the remaining 12 were evenly spaced in 3 rows of 4 at a height of 1.22 m (4 ft). While the pressure was expected to be uniform,

the large number of pressure transducers was used in the simulation to ensure that the structure pressure did not abruptly change between meshes.

The experimental and simulation data obtained in this study have minimal time variation. Therefore, the data sets will be time averaged and presented in a table format. The experimental data included the uncertainty associated with the use of bi-directional probes. Mass flow rates through vent openings were compared, in addition to structure pressure. The measured velocities were used to calculate average mass flow rates through the vents. From the experiments, the test section flows were assumed to be plug flow (Beal, 2008). Based on entrance length calculations, this flow is still developing, so using a single point measurement in the test section to characterize the entire flow is insufficient. Assuming the test section is well-sealed, mass flow is a better characterizing parameter, because it is constant throughout the length of the test section compared to changing velocities. The results for the *No Vent* test case are included in Table 2.5.1. Two FDS simulations are listed: one with leakage and one without.

Table 2.5.1: Average mass flow rates entering the structure and through the void space and structure pressure comparison for *No Vent* experiment, computational simulation, and analytical model.

	Net Flow Rate at Door (kg/s)	**Avg. Void Space Flow Rate (kg/s)**	**Gage Structure Pressure (Pa)**
No Vent Experiment	----*	0.19±0.052	51.6±0.25
No Vent Simulation	0.52	0.24	54.2
No Vent Simulation (no leakage)	0.27	0.27	60.5
Resistance Analytical Model	0.35	0.16	53.4
Ingason Analytical Model [9]	0.26	N/A	54.7

* Due to lack of bidirectional probe resolution at the doorway, an accurate measurement as to the total mass flow rate entering the structure could not be determined.

The simulation with leakage matched the structure pressure to within 5% of the experimental value. This pressure resulted in a simulated mass flow through the test section (0.24 kg/s) with a 26% error as compared to the mean experimental mass flow rate (0.19 kg/s). While the FDS simulated mass flow rate through the void space has a fairly large percentage error relative to mean experimental value, it is at the upper bound of the experimental value when incorporating measurement uncertainty. Note that the void space mass flow rates are typically a small percentage of the flow rates through the structure when a window is open. Additionally, even for the no vent (sealed case), the uncertainty in the void space flow rate (0.05 kg/s) is less than 10% of the predicted mass flow entering the structure (0.52 kg/s). Recognize that in both Tables 2.5.1 and 2.5.2, the mass flow rate through the door generally does not equal the mass flow rate through the void or through the void and window. This is because a model for an additional leakage

path was incorporated into both the CFD simulation and the analytical model. To understand the impact of leakage on results, the FDS simulation was run without leakage. For the no-leakage simulation, the structure pressure increased by 12.5% while the void space mass flow rate increased by 11.6%. In addition, without leakage, the mass flow rate into the structure decreased to 0.27 kg/s from 0.52 kg/s when there is leakage; this is expected as the total exit area is approximately halved when leakage is omitted. This shows that despite the small leakage area, its presence impacts conditions within the structure.

A second comparison of the leakage and no leakage cases was to examine velocity flow fields and pressure contours between the two tests. Figures 2.5.1 and 2.5.2 are vector plots of the velocity at a height of 0.72 m for the leakage and no leakage cases respectively (both for the *No Vent* case). The height of 0.72 m was chosen because it is the middle of the leakage area used in the simulations. When examining the flow patterns of the structure for the two cases, the results show similar patterns indicating that the presence and location of the leakage does not have a significant impact on airflow within the structure. This is important because leakage is represented by a single hole with the size of the total leakage in the structure. In reality, the ELA is the sum of all the small holes throughout the structure, which cannot be modeled accurately since they are sub-grid.
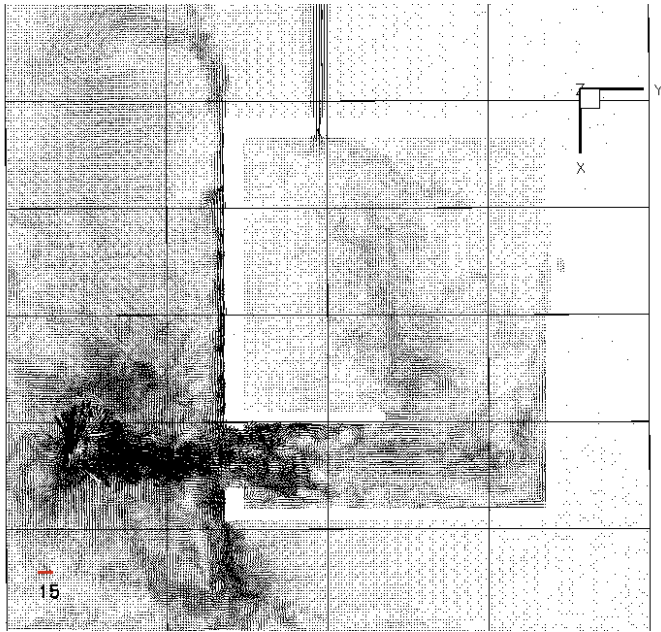
Figure 2.5.1: Velocity vector plot of *No Vent* with leakage at an elevation of 0.72 m.
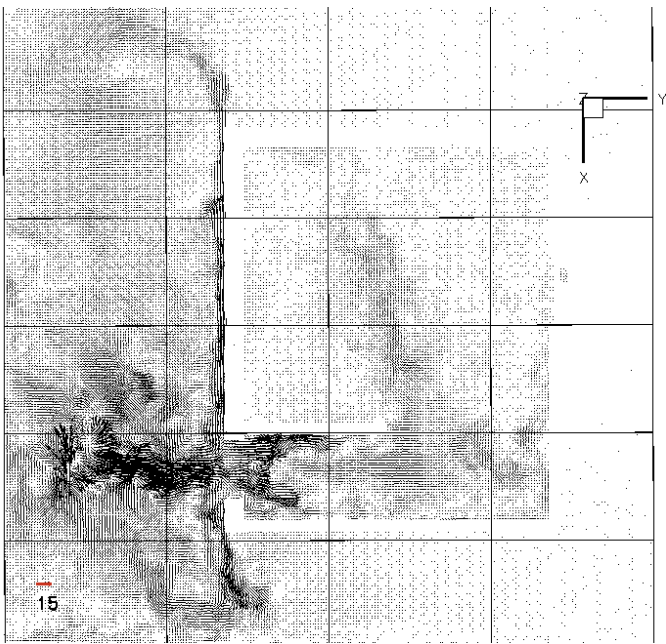
Figure 2.5.2: Velocity vector plot of *No Vent* without leakage at an elevation of 0.72 m.

The last comparison is to examine pressure contour plots to see the variability in the pressure distribution between the two cases. Figures 2.5.3 and 2.5.4 are contour plots at 0.72 m high of the leakage and no leakage cases respectively. Similar to the velocity vector plots, the pressure contours do not show significant variation throughout the structure. This again shows that the presence of leakage did not impact the flow pattern yet affected the average pressure within the structure. The plots similarly show that there is not an abrupt change at the doorway from ambient pressure to room pressure. The jet velocity slows upon entering the structure, resulting in an increase in pressure. The structure pressure increases until the velocity is approximately zero, resulting in the final room pressure.
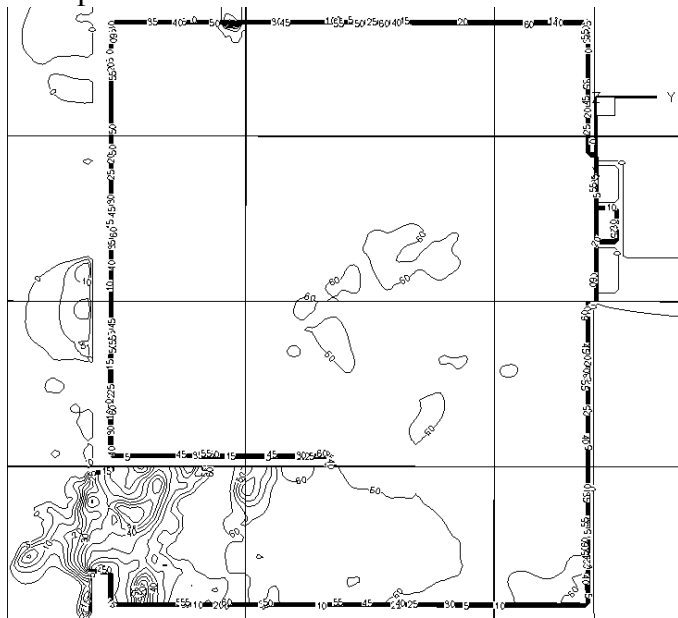
Figure 2.5.3: Pressure contour plots of *No Vent* with leakage at an elevation of 0.72 m.
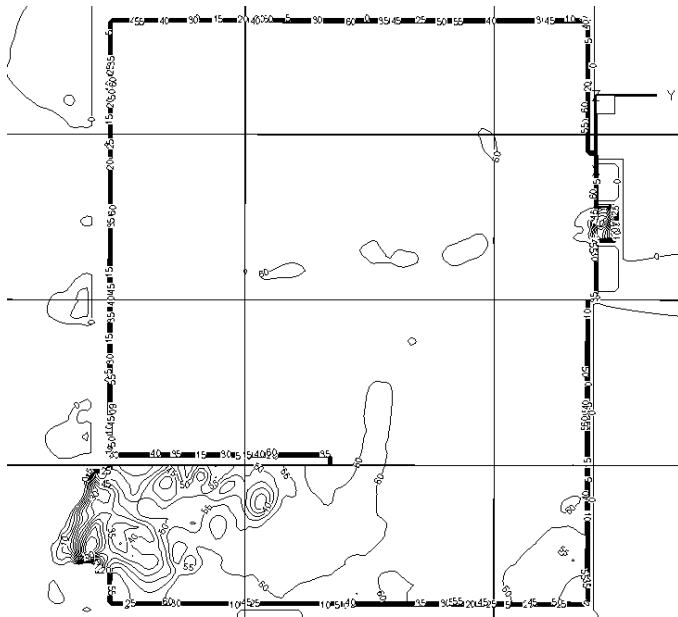
Figure 2.5.4: Pressure contour plots of *No Vent* without leakage at an elevation of 0.72 m.

For the *No Vent* test case, the resistance model and the Ingason and Fallberg model match pressure to within 3.4% and 6% respectively. This good agreement was expected since the fan face flow rate was iteratively changed such that the predicted pressure was within 10% of the experimental pressure. The interesting result is that while the analytical pressures are almost the same, the fan flow rates for the two models are somewhat different. The matched resistance model fan flow rate is 12.5 m^3/s or 95% of the manufacturer settings while the Ingason and Fallberg (I&F) model flow rate is 10 m^3/s or 76% of the manufacturer settings. The difference in fan flow rates is likely a result of the differences in the entrainment model. Since the I&F model is set farther away, more mass is entrained in the cone, so a lower initial flow rate would be required to achieve the same conditions at the doorway. A second difference in the models is that the I&F model cannot differentiate between flow leaving through the void space or through leakage. Since these are two different areas, not one lumped large area, this could

42

also be the cause for the 25% difference in the net mass flow rate through the door. The resistance model predicts the mass flow rate through the void space to be within 15.8% of the experimental value, which is closer than the FDS model.

2.5.2 Open vent

After calibrating the fan model to match pressure for the *No Vent* case, predictions were issued for the *Open Vent* condition. The *Open Vent* simulation includes leakage and the results are shown in Table 4 along with the experimental and analytical results.

Table 2.5.2 shows that the simulation pressure (23.3 Pa) has 2.5% error compared to the experimentally measured pressure (23.9 Pa). The test section mass flow rate (0.13 m^3/s) has an error of 18.2% relative to the experimental value of 0.11 m^3/s. The window mass flow rate (5.81 m^3/s) has an error of 9.9% relative to the experimental value of 6.45 m^3/s. Both the test section and window mass flow rate values are within the experimental error of the measurements. On the surface, compared to the experimental results, the FDS predictions for the *Open Vent* case are more accurate than the FDS predictions for the *No Vent* case. The simple explanation is that overall flow rates are much larger for the *Open Vent* case and small discrepancies are not magnified. For the *Open Vent* case, the computational challenge is significantly reduced because flow through the window is the dominant exit path. FDS accurately models flow through highly resolved large orifices where the effects of the boundary on the flow are minimal. As discussed earlier there is a 7% difference in pressure drop through the test section channel. In the *No Vent* case where the channel flow has a larger influence on total exit flow, the error in the wall model would be more evident.

Table 2.5.2: Average mass flow rates entering the structure and through the void space and structure pressure comparison for *Open Vent* experiment, computational simulation, and analytical model.

	Net Flow Rate at Door (kg/s)	Average Flow Rate (kg/s)		Average Gage Structure Pressure (Pa)
		Window	Void Space	
Open Vent Experiment	----*	6.45 ±1.46	0.11±0.052	23.9±0.12
Open Vent Simulation	6.13	5.81	0.13	23.3
Resistance Analytical Model	6.31	6.10	0.10	20.5
Ingason Analytical Model [9]	6.04	N/A	N/A	44.2

* - Due to lack of bidirectional probe resolution at the doorway, an accurate measurement as to the total mass flow rate entering the structure could not be determined.

In order to test the appropriateness of using $C_p = 1.0$ for the pressure generated by the fan in the analytical model, which was discussed in an earlier section, the resistance model was compared to experimental and computational data sets (three of these experimental data sets are from Ingason and Fallberg (Ingason & Fallberg, 2002) and the experimental and simulation data sets discussed in this paper). Figure 2.5.5 shows the predicted structure pressure from the analytical model compared to the experimental and computational pressures as a function of exit to inlet area ratio. The area ratio is a measure of the resistance to flow; the smaller the area ratio, the more flow resistance there is. The structure is completely sealed for an area ration of zero.
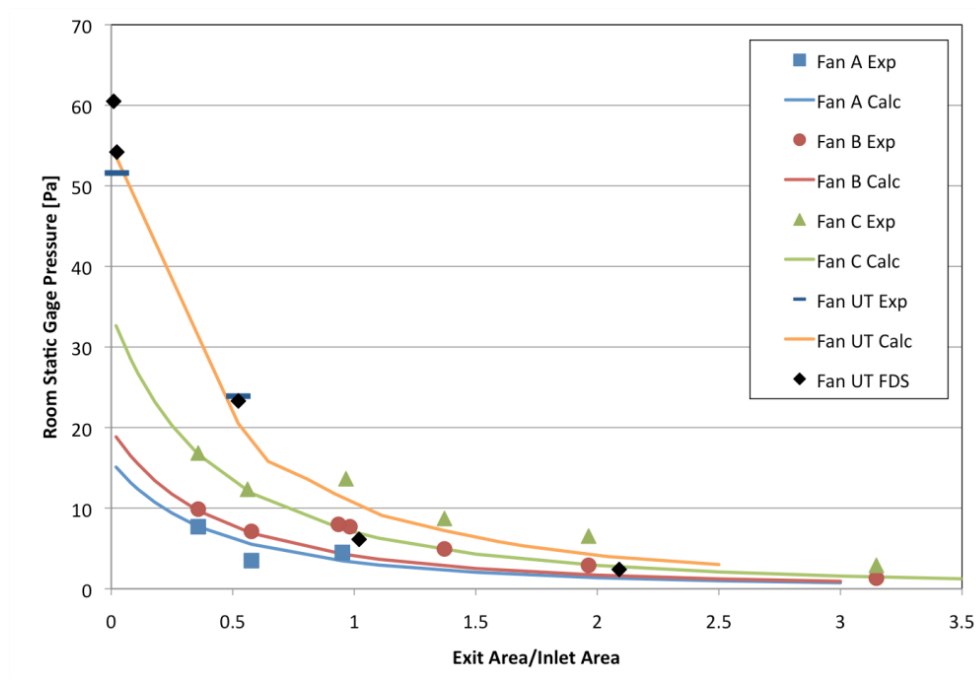
Figure 2.5.5: Comparison of analytical resistance model to experimental and computational data for a variety of positive pressure ventilation fans.

The analytical model compared well to data for each of the 4 fans. The FDS simulation modeled the same fan as the in-house experiment to extrapolate to area ratio data that could not be achieved during experiments. The analytical model was able to predict structure pressure for varying sources (fans) and structure configurations (1 exit vent for Ingason & Falberg tests (Ingason & Fallberg, 2002) and multiple exit vents for The University of Texas at Austin's tests). These results show that the pressure coefficient that is often used for determining the driving pressure for wind driven flows remains at 1.0 for fan driven flows over a wide range of exit to inlet area ratios. Wind effects can be included in the resistance model by adding a pressure equation for wind at applicable vents over which the wind acts. Pressure coefficient data for wind acting on an exposed rectangle structure with a flat roof was taken from Awbi (Awbi, 2003). For wind in blowing south, into vent 1 (cf. Figure 2.2.1) the C_p value is 0.6 and for wind blowing

45

north, putting vent 1 in a wake, the C_p value is -0.35 (Awbi, 2003). The sign convention for this analysis is that wind blowing into vent 1 is positive while wind blowing away from vent 1 is negative.

Figure 2.5.6 shows the impact of wind magnitude and direction on both mass flow-rate through the structure and pressure. Figure 2.5.6 shows that for wind speeds +/- 5 m/s there is minimal impact on mass flow rate and structure pressure from the case with no wind. In this range of wind speeds, wind can generally be neglected from calculations due to the small impact on large-scale flow conditions. As the wind speed directed at vent 1 gets large, it can overcome the presence of the fan and reverse the flow through the structure and cause air to flow into vent 1 and out of the doorway. Under these conditions, the hazard associated with this improper use of positive pressure ventilation is significant, as combustion products from the fire are pushed by the wind towards firefighters.
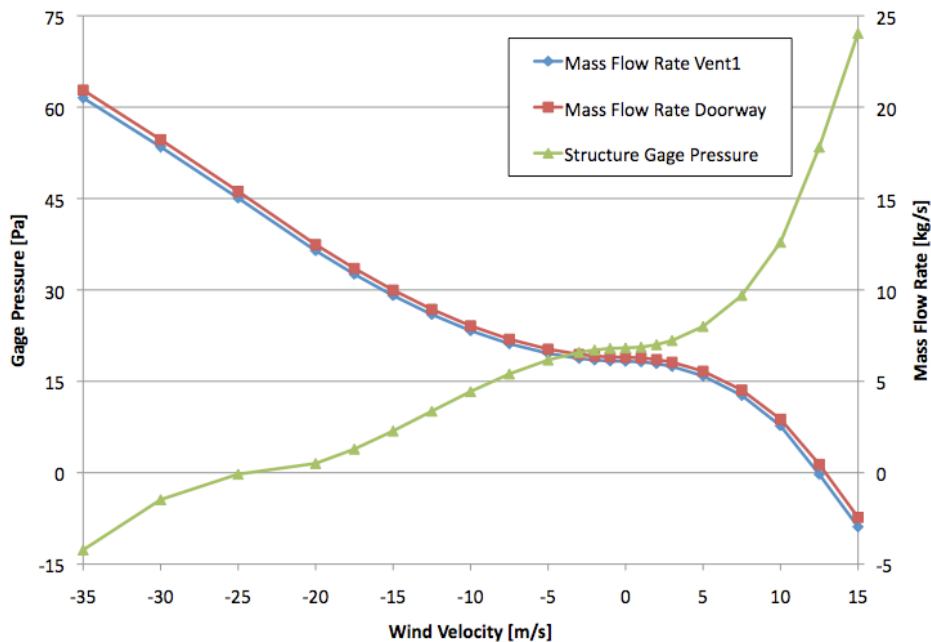
Figure 2.5.6: Examination of wind effects (speed and direction) on mass flow rate through the structure and resulting structure gage pressure.

46

For the case where vent 1 is in a wake due to the presence of the structure, the negative C_p value decreases resistance for flow exiting the vent. As Figure 2.5.6 shows, with the wind blowing away from vent 1, the pressure in the structure drops and mass flow rate out of the window increases. This would be a favorable condition for positive pressure ventilation as airflow through the structure is increased by the presence of the wind.

While both analytical models show good agreement with the experimental pressure for the *No Vent* case (cf. Table 2.3), the I&F model by itself does not predict the pressure as well for the *Open Vent* case as seen in Table 2.5.2. The I&F model predicts the gage pressure to be 44.2 Pa, 85% higher than the experimental gage pressure. Comparing the two models shows that their total mass flow rates through the structure are within 5% of each other, however the resistance model more accurately predicts gage pressure to be 20.5 Pa, which is only a 14.2% error. The resistance model predicts the vent mass flow to a 5.4% error and the void space mass flow rate to a 9% error. The resistance model slightly better predicts the global experimental results than FDS, although both models seem to work equally well.

2.6 CONCLUSIONS

Although there are some differences between analytical model, FDS simulation, and experiments, this effort demonstrates a significant improvement in understanding the relevant factors when simulating non-reacting, mechanically driven flows. The two relevant factors for obtaining valid results are the accurate characterization of the flow source (PPV fan) and accurate quantification of the effective leakage area in the structure. The computational model of PPV simulates mass flow rates through exit vents within the experimental uncertainty for the non-reacting flow results. The pressure within the

47

structure was matched within 5% for the two ventilation cases studied. FDS was shown to adequately model complex flows, and varying venting parameters did not have a significant impact on the accuracy. A validated fan model and calibration of the specific fan used in the experiments are the primary reasons for the accurate simulations. Thus, this study demonstrates the importance of specifying, and subsequently verifying an accurate fan model in simulations of PPV. A second parameter, which affects simulation accuracy, is accounting for the presence of structure leakage. The lack of leakage in the *No Vent* simulations resulted in a 12.5% increase in pressure and an approximately 50% decrease in net mass flow rate through the door. If similar results exist in reacting flow experiments, the differences in mass flow rates could have consequences in the fire dynamics. As an example, the difference in mass flow rate of 0.25 kg/s could affect the heat release rate for a ventilation-controlled fire. A simple order of magnitude estimate of the increase in heat release rate assuming that the heat of combustion on an oxygen basis is 13 MJ/kg is approximately 750 kW. As such, leakage should be considered in simulations of real structures.

The resistance model produced pressure and bulk flows through structure outlets to within 16% of the experimental results for both venting conditions. The resistance model also showed the initial fan flow rate and inclusion of leakage are important in developing accurate predictions. For steady-state calculations the resistance model is a good tool for macroscopic predictions, as the model requires solving only a system of equations. The analytical model is computationally less expensive than the full CFD solution and as future work improves wind modeling, it can be better choice for predicting bulk flow rates. Therefore choosing the correct model based on required level of flow detail is important because the most complex model is not always needed.

The framework presented in this study for evaluating PPV can be used to include wind effects. As a result, this approach can potentially enable a complete characterization of non-reacting airflow on a structure, including natural (*i.e.*, wind) and mechanical (*i.e.*, PPV) sources.

Chapter 3: Compartment Fire Characterization

When firefighters enter an active compartment fire they assume a degree of risk for injury. The simple act of opening a door to make entry into a home filled with hot products of combustion can cause a sudden increase in the heat release rate in the entry compartment and injure any firefighters making entry. To better understand this issue, compartment-scale reacting flow experiments were conducted to measure how the thermal environment changes as a compartment is vented in order to make entry. To help explain the experimental results different types of computational fire models are used. Fire models can vary significantly in the level of physical approximations embodied in the models and computational expense. Both a zone fire model (relatively low order and inexpensive) and a field/CFD model (more detailed and more expensive) are explored for predicting the evolution of the thermal environment during an enclosure fire. To model the thermal and species evolution in the compartment when there is significant ventilation by a fan or by the wind, a stochastic low order model, parameterized by the CFD model, is used.

3.1 EXPERIMENTAL METHODS

3.1.1 Experimental structure

The experimental steel structure with dimensions 4.88 m by 6.09 m by 2.44 m that was used for the non-reacting flow experiments was used for the reacting experiments. The structure is located on the J.J. Pickle Research Campus of The University of Texas at Austin. For a plan view of the structure, refer to Figure 2.2.1. Additional details on the construction of the burn facility can be found in Beal (Beal, 2008).

3.1.2 Fire protection

To minimize damage to the external structure, the interior was fire protected. The interior walls and ceiling were framed with 5 cm (2 in) by 10 cm (4 in) dimensioned lumber spaced 40 cm (16in) on center. In between the studs, R-13 fiberglass insulation was used. The walls were then enclosed with 1.6 cm (5/8 in) fire rated gypsum board. The floor was also protected using gypsum board. Gypsum board was chosen to be the primary material use for fire protection because it is an effective and inexpensive insulator. Insulation was added behind the gypsum board to best approximate the resistance to heat losses of typical residential structures.

3.1.3 Experimental burners and HRR

Two 30 cm (12 in) by 30 cm (12 in) by 20 cm (8 in) sand burners were chosen as the burner system for the compartment. Propane enters the bottom of each burner and flows vertically through the porous sand and disperses radially in the sand. This process increases the burning area by approximately 72 times compared to if it simply flowed out of the supply pipe. The sand burner design was based on ASTM Standard E2257, a standard for room fire tests (ASTM, 2008). A rotameter was installed inline between the propane source tank and sand burners to regulate the fuel flow rate. The heat release rate, $\dot{Q}_{DESIRED}$, is found by multiplying the fuel mass flow rate, $\dot{m}_{fuel}$, by the heat of combustion of the fuel, $h_{c,fuel}$ (43.7 kJ/kg). The burners were found to have a critical mass flow rate, above which point the gas would fluidize the sand instead of percolating through it. This critical flow rate is equivalent to a heat release rate (HRR) of 250 kW. Therefore, for safety reasons, experimental heat release rates were limited to 200 kW per burner.

Safety was a governing factor which both limited the size of the test fires (max total HRR) and the ignition process. Due do the dangers associated with manually igniting the propane gas at the burners and the experiments requiring all vents to initially

be closed, a passive method for ignition needed to be developed. The initial plan was to ignite a flammable condensed phase material (e.g., crumpled paper) that would be placed on top of the sand burner. While the material was burning, the person who ignited it could leave the compartment. Once safely outside the compartment, the gas could be turned on. The burning item would provide sufficient energy to ignite the flowing propane gas. The problem with this procedure was that it was hard to control the burn-out time of the material relative to the flow time to the burner. This was dangerous, as non-combusted propane could fill the compartment if the ignition source extinguished before the propane gas was ignited. To remedy this problem, candles were chosen as the pilot flame source because they provided a sustained source for ignition and met the repeatability demands.

3.1.4 Instrumentation

Reacting flow experiments used the same instrumentation to measure velocity as the non-reacting flow experiments: 10 bi-directional probes to measure velocity through orifices, a bi-directional probe mounted externally to measure wind speed, and a pressure tap to measure structure pressure. Additional instrumentation included 32 thermocouples to measure temperature at 4 elevations over 8 spatial locations. For these experiments, thermocouple trees are fixed at 8 distinct spatial locations. Figure 3.1.1 shows the location of each of the thermocouple trees as well as the location for the burners discussed in *Section 3.1.3*.
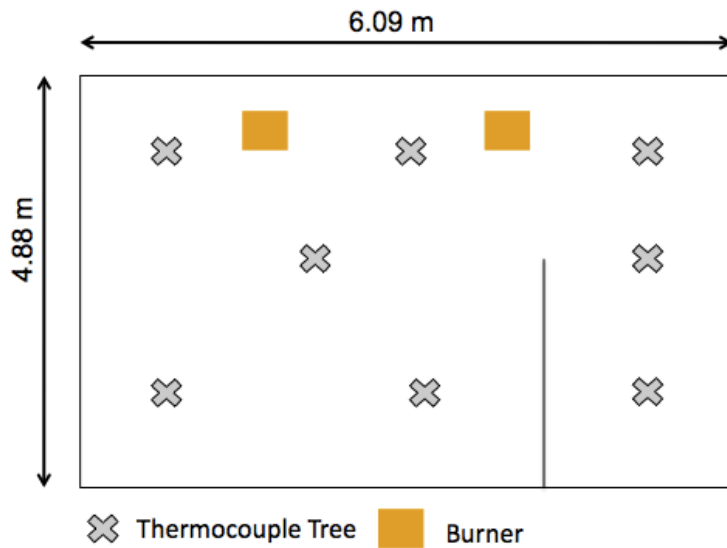
Figure 3.1.1: Plan view of burn structure showing burner and thermocouple locations.

Thermocouples were also attached to each of the 10 bi-directional probes in order to correct the velocity measurements for temperature effects. Two thermocouples were used to measure temperature at each side the gypsum failure area and two were used to measure temperature at various heights in the test section.

In addition to temperature measurements, a directional flame thermometer (DFT) was used to measure incident heat flux (Kokel, 2008). In the experiments, the DFT was positioned at different locations throughout the structure to measure how ventilation tactics influenced heat flux.

Lastly, two video cameras were installed to provide real time visual observation into the compartment during testing. The videos proved to be a valuable qualitative tool during fire testing. One camera was positioned inside the compartment to provide footage of the burners while the second camera was external to the compartment but designed to capture possible flame spread into the test section. Over the course of testing, the internal

camera proved to be more valuable as it allowed us to visualize ignition, the effects of airflow on flame structure, and extinction effects due to oxygen consumption.

3.1.5 Data acquisition

An Agilent Technologies data acquisition system was used during the reacting flow experiments. The system has 70 total channels: 48 channels designated for Type T thermocouples (used for thermocouples in the structure), 10 channels designated for Type K thermocouple (used for directional flame thermometers) and 12 channels designated for differential voltage (bi-directional probes and pressure). The system samples all 70 channels at a rate of 1 Hertz.

3.2 REACTING FLOW EXPERIMENTS

3.2.1 Ventilation experiments

The nomenclature used to describe the tests is the same as that used for the non-reacting flow experiments. *No Vent* represents both windows closed and *Open Vent* represents the north window, Vent 1, open. A total of 57 ventilation experiments have been conducted at The University of Texas-Austin burn structure. There have been 30 positive pressure ventilation tests and 27 natural ventilation tests. For the PPV tests, the fan and its configuration were identical to the non-reacting cases. For natural ventilation tests, the door was opened and the fan remained off. Of the 30 PPV tests, there were 23 *No Vent* tests and 7 *Open Vent* tests. For the natural ventilation tests, all 27 tests were *No Vent* tests. There were significantly more *No Vent* experiments conducted because minimal ventilation is the perceived worst-case for applying PPV (Weinschenk, 2007). The *No Vent* natural ventilation tests were conducted to develop a baseline to quantify the impact of PPV.

Typically, when fire fighters begin suppression actions the fire size in the room of origin can range between 1.1 MW to 2.1 MW (Averill et al., 2010). The use of contemporary furnishings in residential structures have led to fires that transition to flashover and subsequently become ventilation controlled in approximately 4 minutes (S Kerber, 2010), faster than times typical for firefighter suppression to occur (~10-14 minutes) (Averill et al., 2010). In the experiments discussed in this work, heat release rates (HRRs) ranged from 1 burner at 150 kW to 2 burners at 400 kW. The low heat release rates were driven primarily by the safety concerns, which were discussed in Section 3.1.3. These heat releases, however, were sufficient to raise the compartment temperature to high enough values such that the effects of ventilation were still observable.

For each test, the compartment remained sealed (windows and door closed) until the temperatures reached steady state and then the appropriate ventilation tactic (natural or PPV) was applied. The pre-ventilation time varied between 6 minutes to 9 minutes depending on the HRR of the particular test. Larger HRRs took longer to reach steady state. In some cases, ventilation had to be applied before steady state was reached because video inside the compartment indicated that the flame was starting to die from a lack of oxygen. This was done to avoid the flame extinguishing due to a lack of oxygen for safety reasons.

Ventilation, PPV or natural, was applied until a new steady state temperature was reached; typically this was between 3 to 5 minutes. The burner supported flames remained ignited through ventilation. The commercial PPV fan used in the non-reacting experiments (discussed in Chapter 2) was also used for the reacting PPV tests. Similar to the non-reacting flow experiments, the fan was set 2.44 m from the doorway and run at

full throttle. The air cone from the fan was found to not completely seal the doorway as smoke still exited the structure (cf. Figure 3.2.1).

Figure 3.2.1 Post-PPV application for a *No Vent* test case with fan centerline height set at 0.32 m.

3.2.2 Experimental uncertainty

For any series of experiments it is essential to recognize that there will be uncertainty in the scenario of interest and also in the measurement data. The focus of this section is on discussing the uncertainties in the scenario and in the compartment temperature measurements. The bias in the temperature sensors is a source of uncertainty that affects the accuracy of the measurements. The thermocouples are accurate to the maximum of 1 °C or 0.75% of the measured temperature. This bias is constant for all of the experiments. Additional sources of error are that the sensors specify thermocouple temperature, not the actual gas temperature and that the thermocouples vibrate and move once the fan is turned on. Effort was made to ensure that the thermocouple junctions were

at the same locations between the start of each test, but there are likely errors in this positioning.

Sources of uncertainty in the scenario (i.e. the thermal fluid environment) include the variations in the ambient conditions (temperature, pressure, wind speed), the heat transfer characteristics of the structure, the leakage characteristics of the structure, and the prescribed fuel mass flow rate used to supper the fire. The dominant source of scenario uncertainty is the fuel mass flow rate. A rotameter was used to regulate the mass flow rate of fuel to the burners. Error in the rotameter would lead to uncertainty in energy released during experiments. A Dwyer RMC 122 SSV rotameter was used which has a flow rate range between 2.4×10^{-3} m^3/s to 7.1×10^{-3} m^3/s for air. According to their documentation (Dwyer Instruments, 2011) this rotameter has a ±2% error in flow rate at full scale (maximum flow rate). This 2% error is reflected in the actual mass flow through the rotameter compared to the expected mass flow. As discussed in section 3.1.3, heat release rate is tied directly to the mass flow rate of fuel. Additionally the physical difference in actual versus expected mass flow at the full scale is constant over the range of the device (Dwyer Instruments, 2011). This means that the percentage error increases as flow rate decreases. Converting the mass flow rate error in propane to a heat release rate indicates that a ± 15 kW error should be expected. For the low heat release rate tests of 150 kW there could be as much as a 10% error due to our flow controller.

The structure is located outside and is therefore susceptible to environmental influences. The majority of testing occurred in the summer where the environmental temperature fluctuated from 27°C at the start of testing to 38°C at the end of testing. Another issue is that tests were conducted consecutively, resulting in variations in starting temperature for the tests (despite our best efforts to cool the compartment). This

is another source of uncertainty affecting the thermal conditions inside the compartment during testing.

To quantify experimental repeatability, temperature evolutions are examined for the 8 400 kW experiments that were conducted. The focus is on pre-ventilation data as these were conducted under nominally similar conditions. Since ignition time varied between the tests an ignition criterion needed to be used to align the data sets. The criterion was defined to be a 1% increase in upper layer temperature between time steps. Ignition times were confirmed by comparing the 1% increase criterion to videos taken during the experiments. The next step was to determine a ventilation time. This criterion was a 0.1% decrease in temperature over consecutive measurements. These times were also compared to the video and showed good agreement. Note that these criteria were applied to the experimental data after measurement noise had been filtered out using a 40-point Hanning window. This was necessary, as the high frequency fluctuations of the raw data could have led to false ignition/ventilation times. Figure 3.2.2 shows a comparison between the raw experimental data and the filtered experimental data.
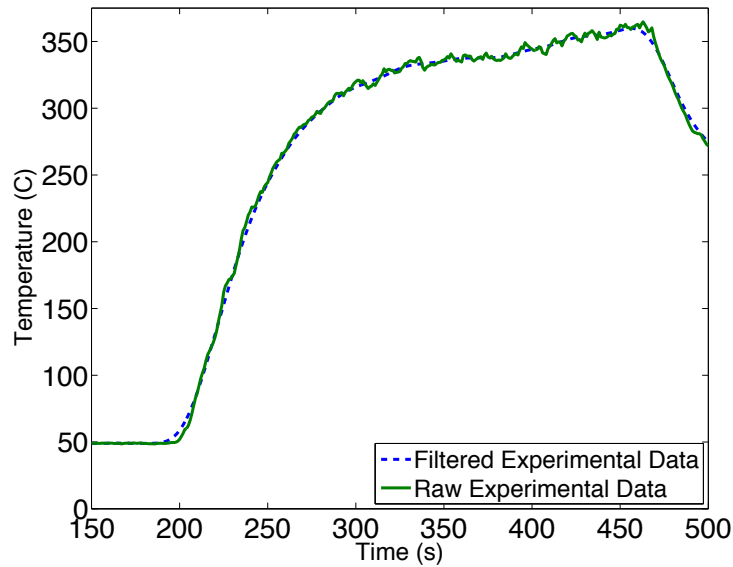
Figure 3.2.2: Comparison of filtered experimental data using a 40-point Hanning window to the raw experimental data.

Figure 3.2.2 shows that the pre-ignition data is smooth. As the experiment progresses, however, there is more noise in data. This starts around 300 seconds and last until ventilation occurs. Some of the fluctuations are significant enough to trigger the -0.1% ventilation criterion creating a false ventilation time. As a result the filtered experimental data were used.

The final step was to truncate the experimental data sets based on the test that had the shortest ignition to ventilation time. This was done to prevent post ventilation cooling from skewing the data for longer tests. This process left 8 time-temperature curves that begin with the ignition time and end at the ventilation time of the shortest test.

These 8 curves are different from one another because of the experimental uncertainties discussed above. The amount of variation in the temperature curves is dependent on how significant the sources of uncertainty are on the thermal conditions

within the enclosure. The remainder of this section will focus on the statistical characterization of the experimental uncertainty.

Inside the compartment 32 thermocouples are used to measure gas temperature. One approach would be to look at the variation of the data at each of the sensors over the 8 tests. While eight samples at each device and each time step could be enough data points to generate statistics (mean and standard deviation), a characteristic of compartment fires is utilized that allows the grouping of thermocouples as a function of elevation. In non-vented compartment fires (natural leakage only) the thermal environment is stratified because the hot, buoyant combustion gasses fill the compartment from the top down and cool as they descend. Only six of the thermocouple trees were considered; the two trees closest to the door were neglected. Due to leakage around the doorway (and resulting wind effects) those two trees have consistently lower temperatures at all elevations, not characteristic of the rest of the compartment. Using the 6 trees, there are 48 temperature samples at each elevation (8 tests x 6 thermocouples per test) at each time. The larger number of samples improves the statistical significance. At each elevation and time there is now a distribution of temperature values. Figure 3.2.3 shows the experimental temperature variation for one 400 kW experiment at the highest elevation, 2.08 m.
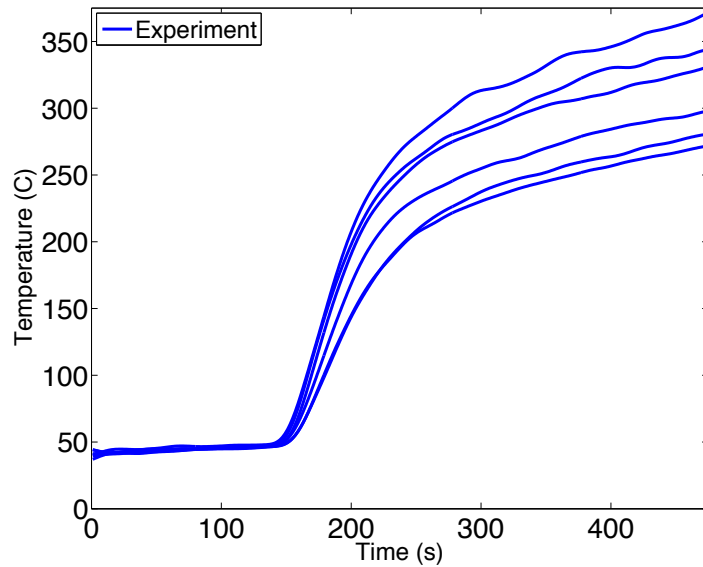
Figure 3.2.3: Experimental time-temperature curve for a 400 kW test showing temperature variation at the 2.08 m elevation. Ignition occurs at 150 seconds.

The temperature distribution (like the one shown in Figure 3.2.3) is described using a probability density function (PDF). The PDF is the normalized frequency/density of a random variable taking on a particular value. For this exercise, we want to know the probability of a particular temperature occurring at a specific elevation and time. The importance of knowing the PDF is that it provides statistical information about the population. Some important statistical information about the distribution is available in the moments of the distribution. A moment can be thought of as a functional that quantifies the shape of a distribution. These functionals can be used to describe the distribution; the more moments that are known results in a better description of the distribution. The first moment of a distribution is the mean; the second moment centered on the mean is the variance, etc. For this problem, if the PDF is known, then the moments of the temperature distribution can calculated by:

61

$$M_n(t) = \int T^n(t) n\big(T(t)\big) dT \qquad\qquad\qquad 3.2.1$$

where n is the index of the particular moment, T is the temperature value, and $n\big(T(t)\big)dT$ is the probability of the occurrence.

One issue for this problem is that a continuous function that describes the temperature distribution is unknown. However, a discrete PDF can be constructed by building a histogram of the data. A temperature range can be found which bounds the values in each group and each time. This range can be discretized into small intervals or bins. The size of the bin affects how well resolved the numerical approximation is (i.e. as the bins becomes small enough such that no bin has more than sample the analytical solution is approached). For this analysis a bin size of 5 °C is used. With larger bin sizes (10 °C) too much information about the distribution was lost. Smaller bins (1 °C) provided a more accurate representation, however, the computational cost to generate the histograms was not worth the nominal gain in accuracy.

The bins are populated by assigning each temperature sample to the bin/interval in which it belongs. The number of samples in each bin can be thought of as the frequency of occurrence of values in that interval or bin. If the number of samples in each bin is divided by the total number of samples, then the count is known as the relative frequency or the density. Example histograms displaying relative frequencies are shown in Figure 3.2.4 for 48 total samples.
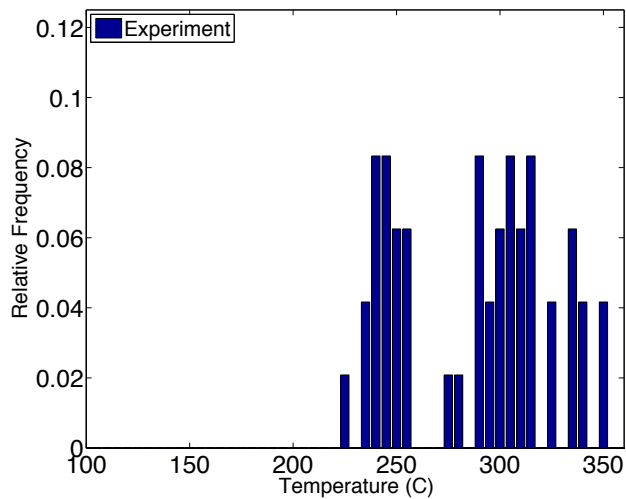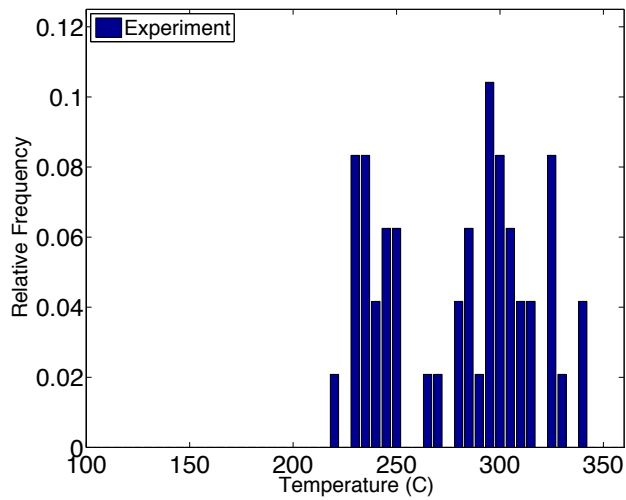
Figure 3.2.4: Histograms, with a bin size of 5 °C showing the relative frequency of temperature measurements occurring at different temperature intervals, 200 seconds (top) and 225 seconds (bottom) after ignition at the 2.08 m thermocouple elevation.

The histograms in Figure 3.2.4 show the scatter in temperature measurements at the 2.08 m elevation, 200 and 225 seconds after ignition. Over the 48 temperature samples, there is a range of approximately 120 °C with two peaks indicating that this distribution is bimodal. The time-temperature curves in Figure 3.2.3 show that there are

two separate groups of three temperatures. This could be a result of burner placement with respect to the thermocouple trees (cf. Figure 3.1.1) as the three trees closest to the burners had higher temperatures. Another factor could be that leakage within the structure results in uneven cooling of the thermocouples. From the information presented in the histograms, as shown in Figure 3.2.4, the moments can be determined following equation 3.2.2.

$$M^n(t) = \sum_{i=1}^{\#\,bins} T_i^n f(T_i) \qquad\qquad 3.2.2$$

where T_i^n is the value along the x-axis in Figure 3.2.4 and $f(T_i)$ is the relative frequency (i.e., the corresponding value on the y-axis). For analyzing the repeatability in the test data standard deviation of temperature, $\sqrt{M_2(t) - M_1(t)^2}$ is examined. Figure 3.2.5 is a plot of the standard deviation of thermocouple temperature at each elevation for the 400 kW tests.
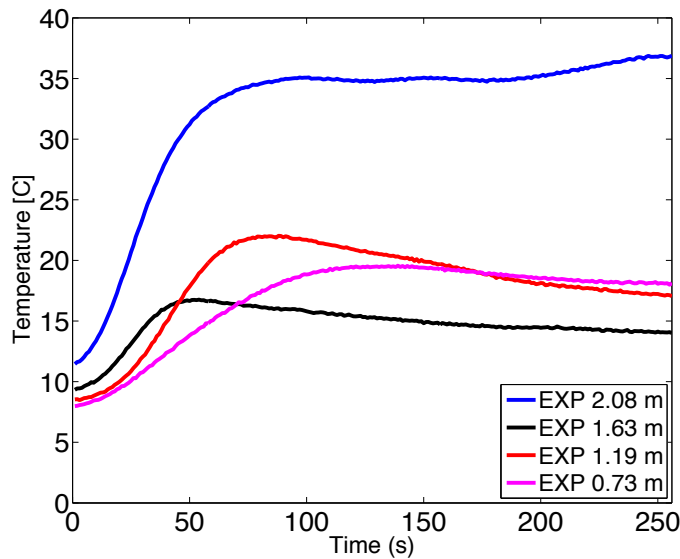
Figure 3.2.5: Standard deviation of temperature as a function of elevation and time for the 8 400 kW experiments. Time equals 0 represents ignition.

Examination of the temperature standard deviation as a function of elevation (Figure 3.2.5) shows that the upper layer value is approximately double that of the lower elevations. This might be expected as the upper layer has the highest temperatures. To better compare the standard deviation across elevations, the standard deviation (°C) as a percentage of the mean temperature (°C) is examined. These values, displayed in Table 3.1, show that the relative standard deviations are consistent through all elevations. To check if the statistics for the 400 kW tests are meaningful for characterizing uncertainty or if there are significantly higher uncertainties for other heat release rates, this same methodology was applied to the 8 300 kW tests that were conducted. Table 3.2.1 shows the relative standard deviations for the 300 kW tests as well.

Table 3.2.1: Time average of the ratio of standard deviation in temperature (°C) to the instantaneous mean temperature (°C) at the 4 thermocouple elevations for 300 kW and 400 kW experimental data sets.

Elevation (m)	Time Average of Standard Deviation to Mean Temperature Ratio	
	300 kW	400 kW
0.73	0.24	0.19
1.19	0.18	0.15
1.63	0.14	0.10
2.08	0.17	0.16

Table 3.2.1 establishes the overall repeatability of the experimental tests and shows that over the length of the tests, the test to test variations are approximately 15 % for the 400 kW tests and approximately 18% for the 300 kW tests. These results show that despite all the possible sources of uncertainty, the experiments show good repeatability. The results also show that uncertainty does not appear to be a large function of experimental fire size. As a check of the level of resolution required in the binning

process to characterize the statistics of the distribution, the standard deviation in temperature calculated by binning resolution used for Figures 3.2.4 is compared to the exact standard deviation calculated using the discrete (unbinned) 48 temperature data samples at each time. Table 3.2.2 shows the average difference between the two standard deviations as well as the maximum difference.

Table 3.2.2: Comparison of percentage error in time averaged standard deviations calculated using binning to the exact standard deviation calculated from the temperature measurement samples for the 400 kW experiments. A positive value indicated that the standard deviation using the samples is larger.

Elevation (m)	Percentage Error in Time Averaged Standard Deviation Difference	Percentage Error in Max Standard Deviation Difference
0.73	0.73	7.7
1.19	0.66	9.7
1.63	0.54	8.9
2.08	0.09	1.9

Table 3.2.2 shows that the methods for calculating standard deviation are nominally the same over the length of the experimental data set. The maximum percentage differences are close to 10 %. The max values of difference between the methods occur within the first few seconds of the experiment. At the start of most experiments, the compartment temperature is cool and temperature distribution is close to uniform. Therefore with a bin size of 5 °C, small variations in temperature may be missed if those variations fall within a one of the bins. Considering the low initial temperatures, a 10% difference between the methods is less than 1 °C.

3.3 COMPARTMENT FIRE MODELING

There are many different ways that the temperature field can be predicted in compartment fires. Depending on the question of interest and the desired level of detail, the computational resources that are available range from low-order zone models (e.g., CFAST) to complex computational fluid dynamics models (e.g., FDS). The computational expense and required expertise in computational science and fire science also vary between the models. Generally, the more complex models are more expensive and expect the user to have higher levels of expertise.

3.3.1 Zone fire model

During the growth stage of a non-vented compartment fire, the interior conditions evolve such that the compartment is thermally stratified. This arises because combustion products fill the compartment from the top down due to buoyancy. This hot upper zone descends with time based on the amount of products being produced (i.e. fire size). As the hot zone descends, it cools, losing heat to the lower zone and the compartment boundaries. The top part of the upper/hot zone remains the hottest as it supplied by hot products from the fire. The lower part of the compartment (lower/cool zone) remains cool, but its temperature rises above ambient due to heat transfer from the compartment walls and hot upper zone. This stratification is evident in the pre-ventilation data from our compartment tests. Figure 3.3.1 shows thermal stratification during a 150kW test.
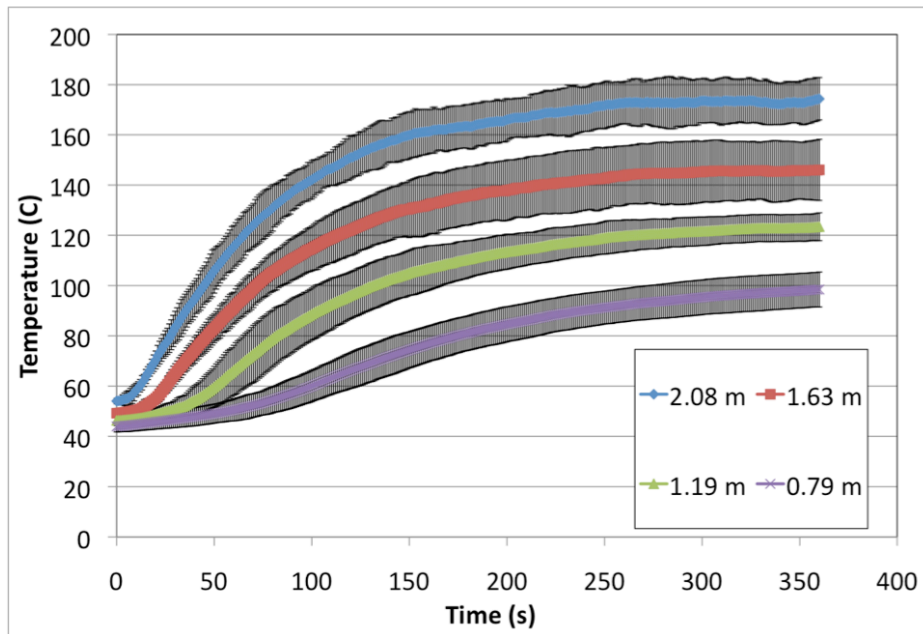
Figure 3.3.1: Spatially averaged temperature at the 4 thermocouples elevations with ± 1 standard deviation for a 150 kW compartment fire test.

Figure 3.3.1 shows spatially averaged temperatures at each of the 4 thermocouple elevations. The plot also includes one standard deviation on both sides of the mean temperature. The temperatures (with standard deviations) appear to go towards steady state values at each elevation, indicating that the gas inside the compartment was stratified. A simplification that is often made for most non-mixed compartment fires is instead of continuously varying temperature; it is assumed that the temperature changes discontinuously between a hot upper zone and a cold lower zone.

Recall that this two layer formulation is used in the low order zone model called Consolidated Model of Fire and Smoke Transport (CFAST) (Jones et al., 2009). As previously mentioned, each compartment is divided into two distinct control volumes or zones. A schematic showing the upper and lower layer as well as orifice flow in CFAST is show in Figure 3.3.2.
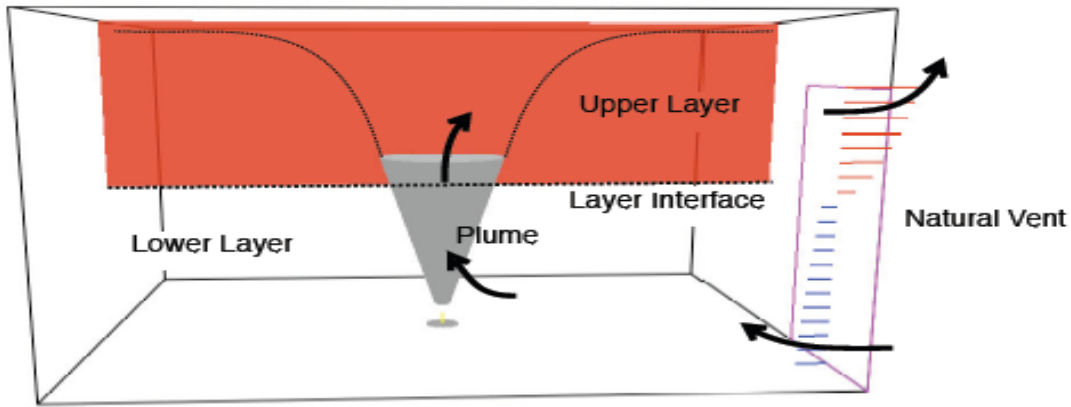
Figure 3.3.2: Schematic showing the two zone model used in CFAST (Jones et al., 2009).

A CFAST model of the burn facility was created based on the geometry and interior wall materials of the experimental structure. In CFAST, fires are controlled by user specified heat release rate (HRR) curves; therefore to accurately model an experiment it is important to know the HRR. To determine the input heat release rate an inversion process developed by Overholt and Ezekoye (Overholt & Ezekoye, 2011) is followed. The goal of this process is to find a HRR curve that matches the upper layer temperature in CFAST to the experimental temperatures at the highest elevation. This is accomplished by iteratively searching for an input HRR to CFAST using a bisection method that matches the CFAST temperature to the experiment temperature within a specified tolerance (Overholt & Ezekoye, 2011). The HRR curve is updated and the process moves forward in time after the tolerance criterion is met. Compartment temperature and layer height predictions from CFAST using the HRR data determined through inversion as an input are compared to the experimentally measured temperatures and calculated layer height to assess the model. The results are shown in Figure 3.3.3.

In experiments and CFD models the temperature dependence on elevation is a continuous function; a distinct delineation between hot gases and cold gases does not

exist. Therefore, to determine an experimental layer height the procedure developed by Janssens (Janssens & Tran, 1992) that is used in FDS is followed. The procedure is based on approximating a compartment into two zones by finding a layer height such that mass flows above and below this height are equal to the mass flow if a continuous temperature profile is used. The following equations, which come from the FDS User's Guide (McGrattan et al., 2010b), indicate how the experimental layer height was determined.

$$(H - z_{\text{int}})T_u + z_{\text{int}}T_l = \int_0^H T(z)dz = I_1$$

$$(H - z_{\text{int}})\frac{1}{T_u} + z_{\text{int}}\frac{1}{T_l} = \int_0^H \frac{1}{T(z)}dz = I_2$$

3.3.1

where H is the compartment height, z_{int}, is the layer interface, T_l is the lower zone temperature assumed to be the lower measured temperature, and T_u is the upper zone temperature defined as:

$$T_u = \frac{1}{(H - z_{\text{int}})} \int_{z_{\text{int}}}^H T(z)dz$$

3.3.2

Equations 3.3.1 and 3.3.2 can be combined and solved for z_{int} to get:

$$z_{\text{int}} = \frac{T_l(I_1 I_2 - H^2)}{I_1 + I_2 T_l^2 - 2T_l H}$$

3.3.3

Differences in the comparisons between the CFAST layer interface height and the experimentally calculated layer height are expected. The experimental value is an estimation of a height that divides the compartment into two zones of different but uniform temperature, however the experimental temperature profile is continuous. Some error in the experimental estimation is expected because of the limited resolution in the vertical direction (only 4 thermocouples).
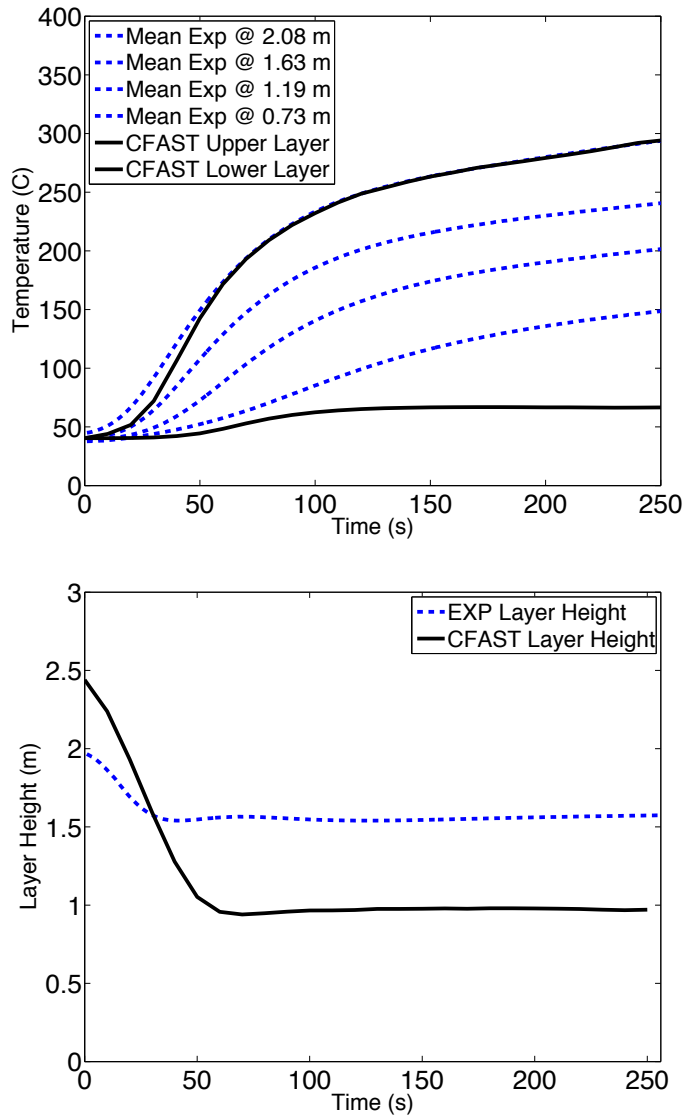
Figure 3.3.3: Comparison of CFAST temperature predictions using a specified input HRR determined from experimental results to the experimental temperatures at 4 elevations (top). Comparison of CFAST layer interface height to experimentally calculated layer height (bottom).

The temperature results show that the upper layer CFAST temperature follows the highest elevation temperature, which is expected based on how the input HRR curve was determined. The layer height plot shows that the CFAST layer interface height drops to 1

m approximately 50 seconds after ignition and remains at that height for the duration of the simulation. The CFAST layer interface height is approximately 0.5 m lower than the experimental layer height but shows similar temporal trends. The experimental results show that between the 2.08 m elevation thermocouples and the 1.19 m elevation thermocouples (slightly above the CFAST layer interface), there is an approximate 100 °C temperature difference that CFAST fails to capture by assuming uniform zones. The CFAST lower zone temperature is under-predicted by approximately 100 °C near the layer interface. The CFAST predictions bound the experimentally determined temperatures. If one is interested in a calculation that simply bounds the compartment temperatures, CFAST is able to meet that requirement. CFAST also shows the ability to predict an approximate layer interface height. When more detailed spatial information is needed, CFD models are often used.

3.3.2 CFD fire model

Similar to the non-reacting experiments, the computational fluid dynamics code Fire Dynamics Simulator (FDS) is used to model the reacting flow experiments. For the discussion in this section, the focus is on the models generated for three experimental configurations: a *No Vent* 400 kW natural ventilation case, a *No Vent* 400 kW PPV case, and an *Open Vent* 400 kW PPV case.

In chapter 1 it was noted that the partial differential equations specifying conservation of mass, momentum, and energy are written in conservative forms and are differenced in space using a second-order central difference scheme and in time using an explicit second order predictor-corrector scheme. An issue with the temporal second-order finite differencing scheme used in FDS is that for cases with coarse grids, sharp gradients cannot be fully resolved (McGrattan et al., 2010a). Sharp gradients can lead to

local (cell value) over-predictions and under-predictions in quantities such as temperature or species mass fractions. This is particularly important in the case of mass fractions as FDS can predict non-physical amounts of mass transfer. To correct this issue, a flux corrected transport scheme is used. This scheme is applied to both the predictor and corrector steps and searches for non-physical values in the domain and corrects them. In the case of mass fractions, non-physical values are corrected by redistributing mass from the surrounding cells. One issue with this method is that it can introduce numerical diffusion. However, the number of cells needing to be corrected at any given time step is small, therefore minimizing the impact of this scheme (McGrattan et al., 2010a).

The computational domain in an FDS simulation is constrained to be composed of rectilinear volumes or meshes. The grid cells are bricks with a preference for a cubic shape. The size of the grid cells plays two roles in FDS. The first being that the size impacts the accuracy and resolution of the calculations; while smaller grid cells increase resolution they also increase computational expense. The grid cells size also govern how solid objects can be placed within the domain.. If the spatial location of the edge of a solid is between the faces of a grid cell, FDS moves the solid edge so that it aligns with the nearest grid cell face. This is particularly important for FDS simulations with large grid cells as the expected position of solid edge can be significantly different than its actual position within the geometric model. For modeling enclosure fires, like the work performed in this study, a failure to recognize this issue could result in a compartment of improper volume or one where the walls may not abut. Input geometry alignment with grid cells is also important for defining holes within structures as discussed with respect to the non-reacting flows. Additionally, solid objects modeled which are smaller than the grid resolution will be increased to a single cell or discarded. Therefore it is necessary to be diligent when defining solid objects in the model by checking in the visualization

software to ensure that what is inputted in the geometry file is the same as how FDS positions it in the mesh.

Turbulence is modeled using a large eddy simulation (LES) model. FDS uses the Smagorinsky form of LES, which is a technique used to model dissipative processes that occur on length scales smaller than those resolved by the user defined grid. Radiative transfer is calculated using a finite volume method, which is applied to the same grid as the flow solver. The default combustion model is a single-step global reaction with an empirical local extinction model.

In the reacting flow simulations, FDS Version 5.5.3 Serial was used with a cubic 10 cm cell mesh (394,912 cells). Grid resolution will be discussed in a later section. While these simulations use a newer version of FDS, compared to the non-reacting flow simulations, the only change to the source code that impacted the results was an improved thermocouple model, which will be discussed in detail in a later chapter. The decision to switch from a parallel implementation to a serial implementation was computationally driven. The FDS models needed to simulate approximately 15 minutes of actual time; using the same grid resolution as the non-reacting cases would have been too expensive. TACC limits active job run times to 24-48 hours, therefore the FDS models were instead completed using the Department of Mechanical Engineering's High Performance Computing (HPC) system which does not limit run-time. Simulations discussed in this chapter range in computational time between 2 hours and 50+ hours. It was important to remain consistent with both the FDS version that was used and the computational system the calculations were being performed on. There was also a goal to avoid having to restart simulations, which would have been necessary had a simulation exceeded the run time using the TACC resources. The HPC uses Dell Poweredge T610s with dual six-core, hyperthreaded 3.33 GHz Xeon processor and 24 GB of shared

memory. The following sections detail the development of the computational models for simulating ventilation tactics applied to a compartment fire. The sections fall into two categories: model calibration and model evaluation.

Calibration: Determination of appropriate HRR

Analogous to the non-reacting PPV simulations in which proper description of the pressure field was required to predict the flow fields, for the reacting flow simulations, it is the proper description of the heat release rate (HRR) given accurate velocity fields that allow accurate predictions of the thermal field. FDS is most commonly used in the form where the HRR is prescribed, not predicted. In FDS a user can explicitly set a desired heat release rate. Defining a heat release rate essentially creates a gas burner where the mass flow rate of fuel from the burner is set by the value of the HRR and the fuel to be burned. When a HRR is defined, FDS automatically uses a 1-step global reaction, mixture fraction based combustion model. FDS will continue to inject fuel (at a default mixture fraction of 1) into domain based on the value of the defined HRR, independent of whether or not combustion can occur in the compartment as determined by the combustion model. The input HRR can be defined to be a function of time where the value of the HRR between any two times is linearly interpolated. As a result, if given some HRR time evolution, this can be used as an input in FDS.

Therefore, to compare to the experimental data, it is important to know the HRR of the experimental fires. While the experiments were shown to be reasonably repeatable (i.e., relatively small standard deviations in temperature), the repeatability does not provide information as to the actual HRR. There is uncertainty associated with the rotamater, pipe flow losses, differences between the burners, and combustion efficiency, which contribute to the estimated HRR. To determine the experimental HRR, an inverse

75

modeling technique developed by Overholt and Ezekoye was used (Overholt & Ezekoye, 2011). As was discussed earlier, the goal of this method is to find a HRR curve that can be used to describe the experimental temperature evolution. This is accomplished by iteratively searching for an input HRR for which the corresponding CFAST temperature matches the experiment temperature within a specified tolerance (Overholt & Ezekoye, 2011). After the tolerance criterion is met, the process is repeated (taking into account the previous times/temperatures) for the duration of the experimental data set. The advantage of using CFAST as opposed to FDS in this fashion is that CFAST is a super real-time computational tool. Super real-time computing is defined by the author to mean that a code produces temporally evolved simulation data faster than it takes for the equivalent amount of clock time to pass (i.e. a 10 minute simulation is produced in 30 seconds). Note that the approximations in CFAST are valid when modeling stratified compartments. One would not expect CFAST to accurately predict thermal fields in compartments with strong mixing (i.e., post ventilation, flashover) (Jones et al., 2009). As such, the inverted HRR was generated prior to ventilation and was then assumed to be constant over the remainder of the simulation. This is a fair assumption as the HRR curves generally reached a steady state value before ventilation. Developed in conjunction with Overholt, Figure 3.3.4 shows the CFAST pre-ventilation time-temperature curve, the discretization of the experimental temperature curve (circles), and the resulting HRR curve for a nominally 400 kW experimental condition. A HRR value was found at each of the circles shown in the left plot of Figure 3.3.4 for the first 400 seconds of temperature data.
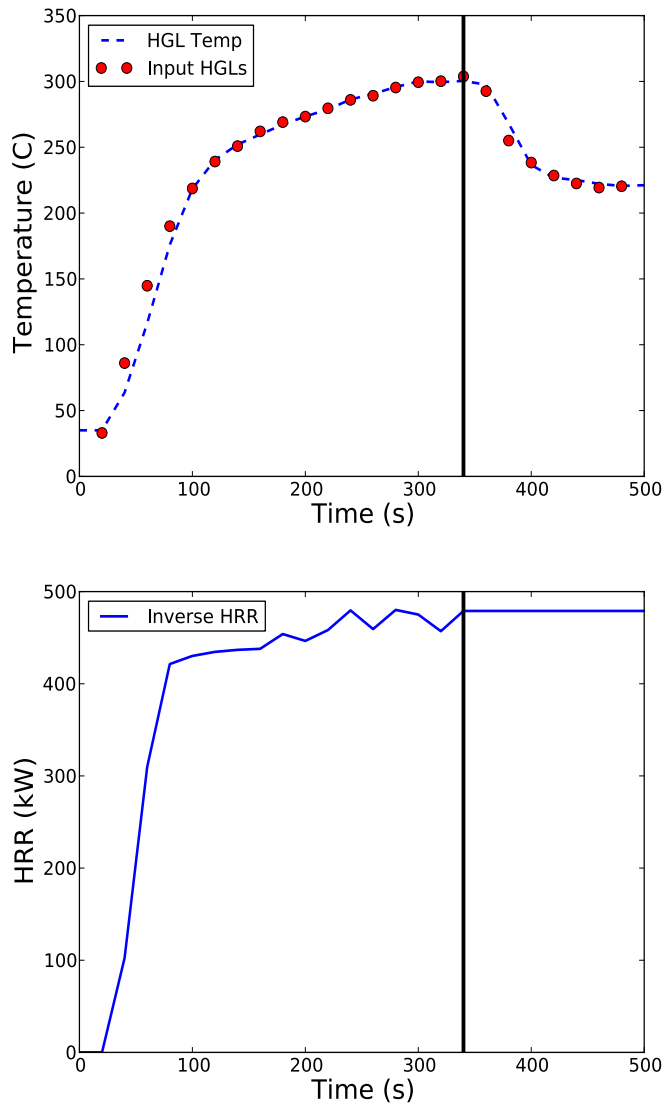
Figure 3.3.4: Plots showing the development of a HHR curve using inverse methods. The dash line represents the CFAST predicted average hot gas layer (HGL) temperature and the circles represent the points at which the experimental data was sampled (top). HRR curve after post process smoothing to get rid of numerical noise (bottom). (Overholt & Ezekoye, 2011) The vertical line in both plots represents the start of ventilation.

77

Calibration: Combustion parameters affecting HRR

After an appropriate HRR input curve was determined, the next step was to ensure that the curve could be accurately modeled in the computational software. As previously noted, a fast chemistry, global single step reaction is used as the combustion model. A mixture fraction conservation equation is solved in the domain. The mixture fraction, Z, is defined to be 1 in the fuel stream and 0 in the oxygen stream. In FDS versions prior to Version 5, a mixed is burned approximation was used. This approximation was adequate for well-ventilated large-scale fires, but failed under several conditions including ventilation-controlled fires (oxygen limited). The new approximation/model uses local oxygen concentration and temperature to model extinction based on the critical flame temperature concept (McGrattan et al., 2010a). This concept relates the energy released by the complete combustion of oxygen within a control volume to the subsequent rise in bulk gas temperature in the control volume assuming adiabatic conditions. A minimum amount of oxygen can be found that is necessary to cause the temperature rise in the control volume to reach the critical value for a reaction to occur, typically ~1400 °C. This value is sometimes referred to as the lower oxygen flammability limit. This concept can also be applied to fuel, in that there is a minimum quantity of fuel needed to react to raise the control volume above the critical temperature needed for a reaction. This value is known as the lower fuel flammability limit. This formulation gives rise to two regions: a burning region and a non-burning region, which are defined by the flame temperature and lower oxygen flammability limit. Figure 3.3.5, from the FDS Technical Reference Guide (McGrattan et al., 2010a) shows the delineation between these zones.
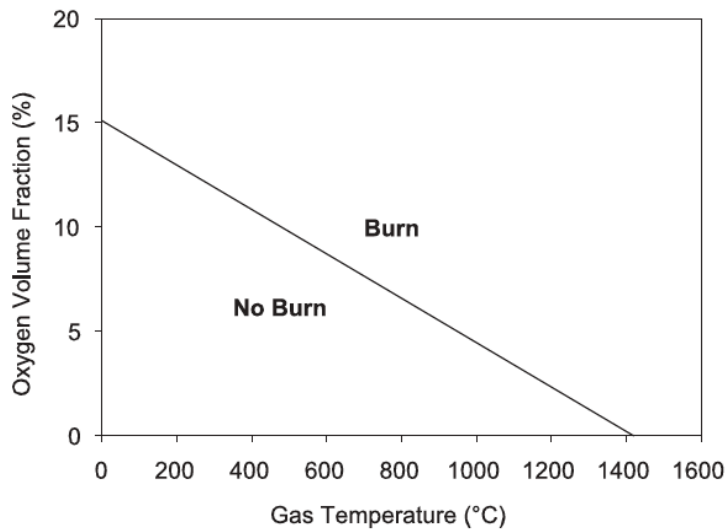
Figure 3.3.5: Plot showing the default oxygen-temperature parameter space the governs the extinction mechanism in FDS (McGrattan et al., 2010a).

Using this formulation fuel and oxygen can mix, react, and generate products or can mix and not react. The non-reacting case is governed by a constant lower oxygen flammability limit and the critical reacting flame temperature. If the combination of the local values for these parameters falls below a threshold value, then combustion does not occur.

The HRR curves used are determined from inversion. The HRR curve governs the mass flow rate of propane into the computational domain. Combustion parameters, specifically the lower flammability limits of fuel and oxygen that govern the reactions, were left as FDS defaults. Note that in FDS, propane is defined as the default fuel and the default values for the lower oxygen flammability limit and lower fuel flammability limit are an oxygen mole fraction (X_{O2}) of 0.15 and fuel mass fraction (Y_{FUEL}) of 0.0 respectively. The lower fuel flammability limit of $Y_{FUEL}= 0.0$ means that in FDS by default, the combustion reaction criteria is based only on oxygen flammability; as long as

the criteria in Figure 3.3.5 are satisfied a combustion reaction will take place if any amount of fuel is present.

Based on Figure 3.3.5, if the local conditions fall in the burn region, then combustion can occur. If a combustion reaction takes place then a HRR per unit volume is calculated in the cell where the reaction occurred. FDS then determines a HRR for the entire domain by multiplying the HRR per unit volume within the cell by the cell volume and then summing over all cells in the domain. Figure 3.3.6 is a plot comparing the prescribed HRR curve to the FDS calculated HRR curve for a *No Vent* 2-burner, 400 kW fire with ignition at 150 seconds and ventilation at 450 seconds.
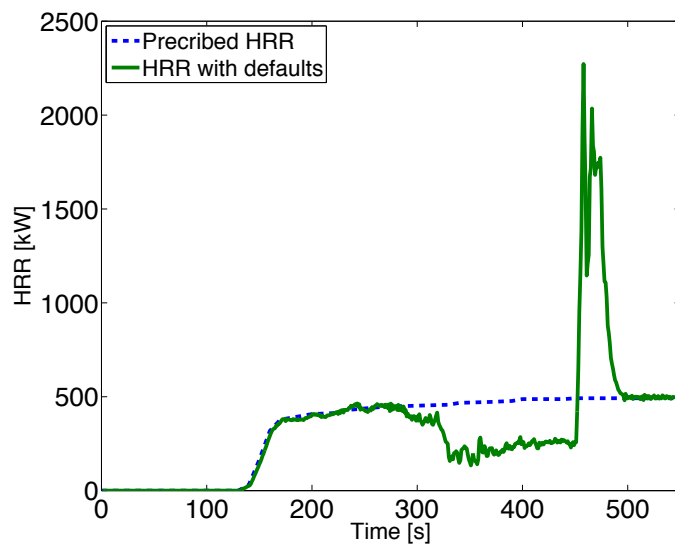
Figure 3.3.6: HRR curves for a 2 burner 400 kW fire. Ignition occurs at 150 seconds and natural ventilation at 450 seconds. The dashed line is the prescribed HRR curve using inverse methods and the solid line is FDS outputted HRR curve.

Over the first 275 seconds of the simulation, the predicted HRR from FDS closely matched the prescribed HRR curve. As the simulation progressed, the FDS HRR decreased from its prescribed value indicating that there was insufficient oxygen in the

compartment. Video from inside the compartment showed that the flames did not globally extinguish from a lack of oxygen. After ventilation occurred at 450 seconds, the FDS curve shows a greater than 2 MW spike in HRR. A HRR of this magnitude is an indicator that the previously unburned fuel in the compartment ignited. Examination of experimental temperature data and video recorded during the experiment revealed that only the gas local to the burners ignited, suggesting an error in the simulation.

From 275 to 450 seconds in Figure 3.3.6, the impact of the lower oxygen flammability limit is evident as the HRR drops due to local extinction within the compartment. This occurs in computational cells where the oxygen concentration is below the lower flammability limit. When ventilation occurs at 450 seconds, there is an instantaneous spike in HRR. The cause of this spike is a combination of both the lower oxygen flammability limit and lower fuel flammability limit. As discussed above an FDS burner injects fuel into the domain based on the prescribed HRR regardless of whether there is sufficient oxygen. For the approximate 175 seconds when the fire was ventilation controlled, fuel continued to flow into the compartment based on the value of the HRR. When ventilation occurred and sufficient oxygen was supplied, any unburned fuel in the compartment combusted because the lower fuel flammability limit was set to a fuel mass fraction of zero. To minimize the spike, the lower fuel flammability limit was set to a mass fraction of 0.021, the value for propane in the SFPE handbook (DiNenno, 2008). By setting the lower fuel flammability limit, a second constraint to the burn/no-burn plot show in Figure 3.3.5 was added. This constraint prevents the combustion reaction from occurring unless there is sufficient fuel (Y_{FUEL}= 0.021) in a control volume (grid cell) that would raise the temperature to above the critical temperature for reaction (~1400 °C).

To limit the premature extinction of the fire, the lower oxygen flammability limit was decreased from the default value of 0.15 mole fraction, allowing combustion to occur

in more fuel rich environments. The lower oxygen flammability limit was initially set to be $X_{O2}=0.115$, as found in the SFPE Handbook (DiNenno, 2008), however as shown in Figure 3.3.7, this still led to early extinction.
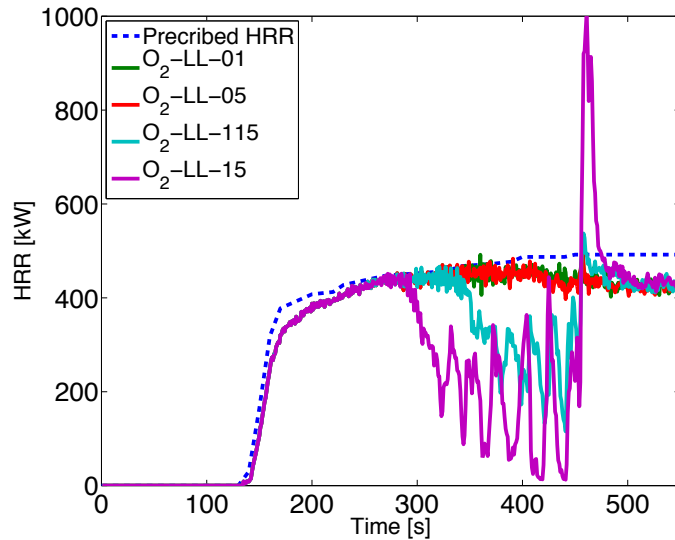
Figure 3.3.7: HRR curves for a 2 burner 400 kW fire. Ignition occurs at 50 seconds and natural ventilation at 450s. The dashed line is the prescribed HRR curve using inverse methods and the solid lines are FDS outputted HRR curves for different lower oxygen limits.

Figure 3.3.7 shows two curves in which the FDS HRR curve drops off from the prescribed HRR curve: $X_{O2}=0.15$ (default) and $X_{O2}=0.115$ (propane specific). The propane specific lower oxygen flammability limit follows the prescribed HRR curve for approximately 75 seconds longer than the default case. Note that the post ventilation spike is not as acute for the default case since all the fuel no longer combusts since the lower flammability on a fuel basis has been imposed as a constraint. For the propane specific lower oxygen limit, a less severe post ventilation spike occurs compared to the default value. Two additional lower oxygen limits were tested: $X_{O2}=0.05$ and $X_{O2}=0.01$. Neither of these values indicates that the fire is becoming oxygen starved as the HRR

curves reach a steady value at approximately 300 seconds. While below experimental values for the lower oxygen flammability limit found in literature (DiNenno, 2008) for propane combustion, $X_{O2}=0.05$ will be used for the simulations in this document as this value best compares the prescribed HRR. Appendix A shows that for vitiated combustion, when the main combustion fuel can be considered to be carbon monoxide, the lower oxygen flammability limit is 0.05 mol/mol.

Calibration: Grid sensitivity

A 10 cm mesh was initially chosen based on characteristic fire diameter, D*, (McGrattan et al., 2010a):

$$D^* = \left(\frac{\dot{Q}}{\rho_\infty c_p T_\infty \sqrt{g}} \right)^{\frac{2}{5}}$$ 3.3.4

where $\dot{Q}$ is simulation heat release rate in kW, ρ_∞ is ambient density in kg/m³, c_p is specific heat in kJ/(kg-K), T_∞ is ambient temperature in K, and g is gravitational acceleration in m/s². Based on recommendations for buoyant flows from the Nuclear Regulatory Commission in 2007, D* divided by the grid cell size, dx, should be between 4 and 16. For the simulations presented in this paper, the D*/dx ratio was 6.65.

As discussed in sections 2.4.1 and 2.4.2, the non-reacting flow FDS models used a grid resolution of 4 cm. Parallelization as well as the fan model drove the level of resolution. The 10 cm cells used for the reacting flow models are over fifteen times larger, ($[2.5]^3$), than the non-reacting flow cells and eight times, ($[2]^3$), larger than the cells for which the fan model was validated. To examine grid resolution affects, simulations were completed using an 8 cm grid, 10 cm grid, and 20 cm grid. The first test was to simulate an enclosure fire (plus leakage). Using the heat release rate determined through inversion along with the appropriate combustion parameters, the results from the

FDS simulations were compared to experimental results. Figure 3.3.8 shows a comparison of the simulated temperatures for the three grid resolutions to experimental data.
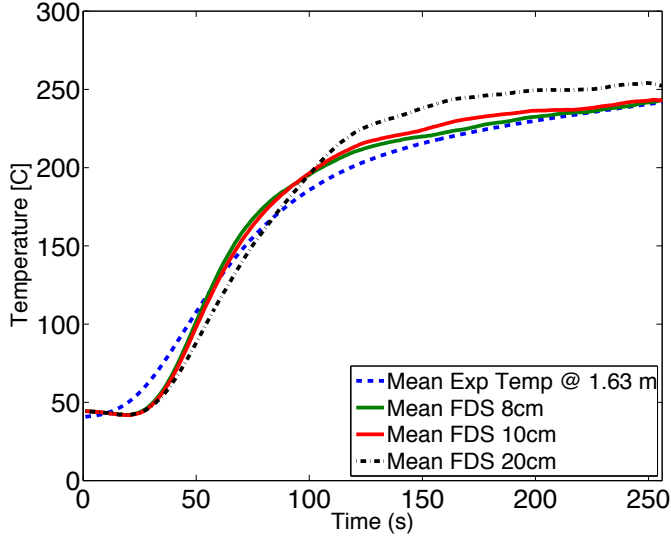
Figure 3.3.8: Comparison of FDS simulated temperatures for three different grid resolution 8 cm, 10 cm, and 20 cm to experimentally measured temperature at an elevation of 1.63 m.

To quantify the differences shown in Figure 3.3.8, the sum of the relative error is defined as:

$$Err(z) = \sum \frac{\left| \overline{T}_{EXP}(z,t) - \overline{T}_{FDS}(z,t) \right|}{\overline{T}_{EXP}(z,t)} \qquad 3.3.5$$

To compare the total relative error for the three grid resolutions, Table 3.3 shows the errors as well as the total computational time for the simulations.

Table 3.3.1: Computational time and total relative error at each elevation for three different computational resolutions for a 256 second simulation of a non-vented compartment fire.

Grid Size (cm)	Computational Time (minutes)	Total Relative Error (%)			
		2.08 m	**1.63 m**	**1.19 m**	**0.73 m**
8	478	15	13	34	62
10	190	20	15	41	84
20	10	25	25	52	115

The table shows that there can be large computational savings depending on the amount of error that is willing to be accepted. The 8 cm and 10 cm resolution show similar total relative errors at the 4 elevations, while the error for 20 cm resolution increases significantly at the lower elevations. The next step is to check the effects of grid resolution for a positive pressure ventilation simulation. For these cases the computational time increased significantly once the fan turn was activated in the model. The 20 cm resolution case took 78 minutes and the 10 cm resolution case took 1592 minutes for 660 seconds of simulation with ventilation occurring 435 seconds into the simulation. To estimate the computational time for the 8 cm resolution model, a simple model for calculating computational time increase is followed. When decreasing cell size, the computational time increase is based on the ratio of the number of cells in the domain for the finer resolution to the current resolution raised to the 4th power (where 4 comes from the three spatial dimensions and time). Therefore, it is expected that a simulation of the ventilation case with 8 cm resolution could take on the order of 7000 minutes (~ 5 days). A simulation of this magnitude becomes expensive.

The reason simulations with ventilation take significantly longer is that the time step in FDS is governed by the Courant-Friedrichs-Lewy (CFL) condition. The CFL condition is a convergence condition imposed on the explicit time-marching scheme in FDS. The CFL conditions prevents a notional particle from crossing entirely through a

single grid cell in one time step (Moin, 2001). For fast moving flow (i.e. PPV fan) with small grid cells the simulation time step becomes very small.

Recall that the original fan model was tested with 5 cm grid cells. The 10 cm and 20 cm cases were compared to the experimental data set to check if the fan model would still be valid with the coarser resolutions (Figure 3.3.9).
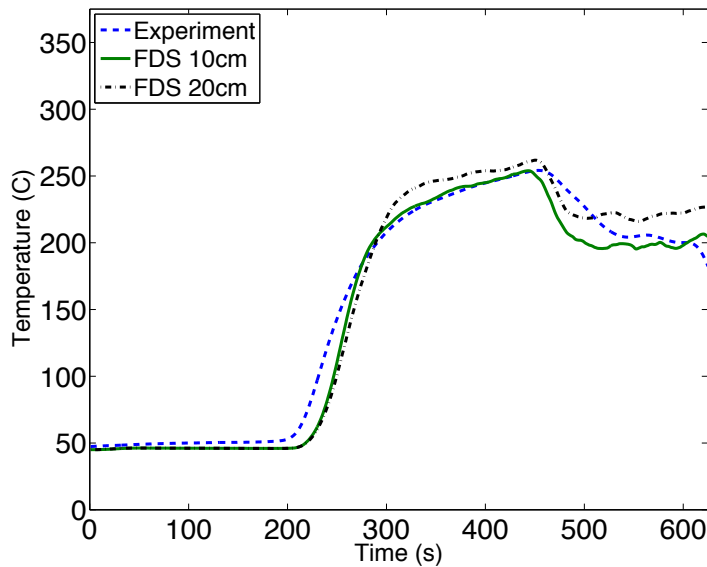
Figure 3.3.9: Comparison of 10 cm and 20 cm resolution FDS simulations to experimental results of a 400 kW *No Vent* PPV experiment at the 1.63 m thermocouple elevation. Ignition occurred at approximately 200 seconds and ventilation at 430 seconds.

Figure 3.3.8 shows the comparison for both resolutions to the pre-ventilation and post-ventilation experimental values. While both resolutions show differences compared to experimental data, the 20 cm showed larger post-ventilation relative error compared to the 10 cm case. Therefore, a 10 cm resolution was chosen for the simulations in this work despite the additional computational expense.

3.3.3 CFD sensor model

The work in this section is largely based on previously published work by this author at the ASME/JSME 8th Thermal Engineering Joint Conference (Weinschenk & Ezekoye, 2010).

With increasing requirements for model validation when comparing computational and experimental results, there is a need to incorporate detailed representations of measurement devices within the computational simulations. Thermocouples are the most common temperature measurement transducers in flames and fire environments. Even for the relatively simple thermocouple transducer, the coupling of heat transfer mechanisms particularly under unsteady flow conditions leads to interesting dynamics. As experimentalists are well aware, the experimentally determined thermocouple values are not the same as the local gas temperatures and corrections are often required (Figure 3.3.10). From the computational perspective, it is improper then to assume that the predicted gas temperatures should be the same as the temperatures that an experimentalist might measure since the thermal characteristics of the thermocouple influence the indicated temperature. The thermal characteristics of simulated thermocouples in unsteady flame conditions are investigated. Validation exercises are presented to test the underlying thermocouple model. Differences are noted between the predicted thermocouple response and expected response. These differences are interpreted from the perspective of what modeling artifacts might drive the differences.
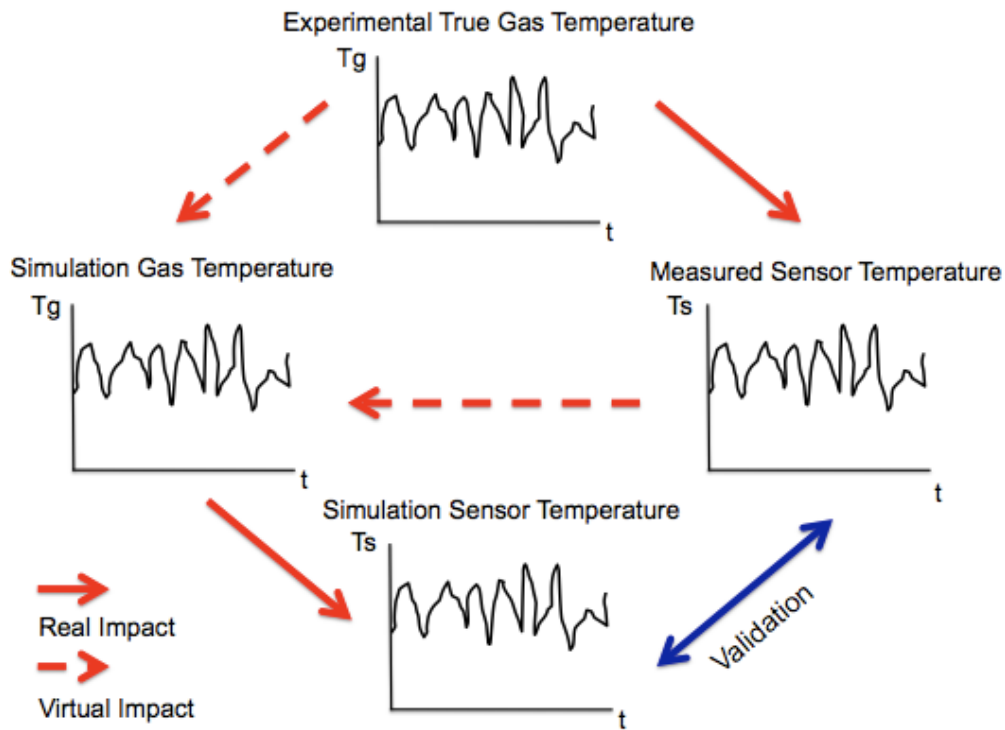
Figure 3.3.10: Flow chart showing the connection between experimental gas temperature to experimental measurements and how simulations results are related. The solid lines represent a real physical impact while the dashed lines represent a virtual impact.

In experiments (top plot in Figure 3.3.10), there exists a true gas temperature time response due to energy inputted into the system from a fire. Knowledge of this true gas temperature response is desired, however a sensor doesn't exist which measures that value. In reality, thermocouples are used to measure temperature versus time (middle right plot of Figure 3.3.10). As the line connecting true gas to measured sensor temperature, the sensor temperature result is affected by environment and thus measures a temperature not equal to the gas temperature. This is primarily due to convective and radiative heat transfer effects. Experimentalists have long corrected for radiation, nominally a 10 % error, using the equation:

88

$$\frac{\Delta T_{rad}}{T_{gas} - T_{ref}} \approx \frac{\sigma \varepsilon_{TC} \left(1 - \varepsilon_{gas}\right) T_{gas}^4}{\left(h + 4\sigma \varepsilon_{TC} T_{gas}^3\right)\left(T_{gas} - T_{ref}\right)} \qquad 3.3.6$$

where T_{gas} is the desired gas temperature, T_{ref} is an experiment specific reference temperature, ΔT is the change in temperature associated with radiation, ε_{TC} is the emissivity of the thermocouple, ε_{gas} is the emissivity of the gas, h is the heat transfer coefficient, and σ is the Stefan-Boltzman constant. The arrow is drawn uni-directional, as the sensor should not have any influence on the experiments.

Using the same experimental structure geometry and energy source, a simulation will produce its own gas temperature (middle left plot Figure 3.3.10), however one cannot accurately compare the simulation temperature to the experimentally measured quantity (sensor temperature) or the corrected gas temperature. Therefore, a model for the sensor in the simulation was developed to interact with the simulation environment in the same fashion as the experimental sensor (bottom plot Figure 3.3.10). If simulation sensor temperatures can be validated through comparison to the experimental sensor temperature, it is believed that the simulation gas temperature predictions can provide insight about the experimental gas temperatures. The remainder of this section will focus on the development of a transient thermocouple model.

Thermocouple modeling background

There is increasingly closer scrutiny of the differences between computational predictions and experimental measurements for a range of applications. With greater reliance on simulations in all aspects of engineering science (e.g., as integral parts of system controllers or as hazard analysis tools) there is a need for greater confidence in the predictive capability of the simulations. A necessary requirement then is that the simulation predictions reliably predict the output of the experiments. It is well known that

skilled experimentalists will generally make every effort to correct for the inconsistencies in their transducers so that the transducers are more likely providing the true value of the measured quantity. That said, in practice, there would be a wide variation in the overall accuracy and care provided in any given literature provided experimental database. In fact, to be of use to a computational researcher, details of the experimental system that may be often considered minor should be provided to the computational researcher to assure that either the transducer system can be simulated or that the reported data are accurate representations of the underlying physical variables. In the case of standard thermal measurements for combustion and fire systems, the thermocouple is ubiquitous and has been central to characterization of many such systems. In spite of its widespread use, it is surprising that most computational codes used to predict the thermal fields within flames and fires do not model the thermocouple within the code, but instead compare the modeled gas temperatures with experimental thermocouple measured temperatures. From a different perspective, the use of a measurement transducer inserted into a computational tool forces the code developer to design subgrid models for the transducers that may challenge and improve the inherent capability of the code models.

In most standard experimental measurement classes, students are taught about the various sources of error in thermocouple measurements. The most common errors are conduction losses associated with conduction heat transfer from the thermocouple junction through the lead wires, radiative losses associated with the thermocouple junction interacting with non-local radiative elements, and transient errors associated with the finite thermal capacity of the thermocouple junction. The ability to incorporate models for thermocouples and other transducers into a CFD code could be extremely useful for experimentalists in terms of being able to design experiments in which unanticipated sources of error can be identified prior to detailed experimental testing.

90

One should recognize that in most large-scale CFD simulations, a typical thermocouple junction of characteristic dimension of a few millimeters will be a subgrid scale feature within the CFD code. As such, there will be errors in the model approximations for these devices, and these modeling errors must be investigated. There is a long history of analyzing thermocouple error (Rizika & Rohsenow, 1952). They primarily analyze the well-known steady conduction fin type error. Previous work in thermocouple modeling comes from Blevens and Pitts in 1999. Their model accounts for radiative losses from the surface of the thermocouple for both bare and aspirated thermocouples but does not include transient effects (Blevins & Pitts, 1999). Other work examining thermocouple errors and associated corrections with respect to computational simulations comes from Hurley and Munguia, though they also did not add in temporal effects (Hurley & Munguia, 2007). Brundage, Nicolette et al. preformed computational and experimental work on sheathed thermocouple and found that a conduction model needs to be included (Brundage, Nicolett, Donaldson, Kearnry, & Gill, 2005). The thermocouples in this study are bare, however a conduction model is being considered. Francis and Yau used a network resistance to model bare and sheathed thermocouples in pre and post flashover fires, however their focus was on quantifying steady state error (Francis & Yau, 2004). Pitts et al. also studied steady state conditions but examined the effects of error in temperatures measurements for bare and aspirated thermocouples (Pitts et al., 2003). Lastly, Yilmaz et al, examined the differences between experimental thermocouple measured temperatures and computational predicted temperatures. Their results say that flame oscillations are a cause for these differences (Yilmaz, Gill, Donaldson, & Lucero, 2008).

In this discussion there is a focus on radiative losses and treatment of transient effects in thermocouples. It is shown through comparisons within an experimental system

that treatment of thermocouple physics within a computer code should be an essential part of the code data reduction plan.

Modeling theory

Modeling the thermal response of a thermocouple begins with a differential equation based on a lumped energy balance for the thermocouple bead. The following is the thermocouple energy equation:

$$\rho c V \frac{dT_{TC}}{dt} = -hA(T_{TC} - T_{gas}) - \varepsilon_{TC} A T_{TC}^4 + \varepsilon_{TC} \int \dot{q}_R'' dA \qquad 3.3.7$$

where $\dot{q}_R''$ is the incoming radiative heat flux, dA is $R^2 d\omega$, R is the thermocouple radius, ω is the solid angle, ρ is the thermocouple density, c is the specific heat of the thermocouple, V is thermocouple bead volume, and A is thermocouple bead surface area. The last term on the right hand side of equation 3.3.7 can be thought of in terms of intensity:

$$\int \dot{q}_R'' dA = \int_{4\pi} \int_{2\pi} s' I R^2 ds' d\omega \qquad 3.3.8$$

where I is the intensity and s' is the direction vector of the intensity. Since R^2 is independent of ds' and $d\omega$, it can be pulled out of the integrals and the order of integration can be switched so that equation 3.3.8 becomes:

$$R^2 \int_{4\pi} \int_{2\pi} s' I ds' d\omega \qquad 3.3.9$$

The definition of average intensity is:

$$\bar{I} = \frac{1}{4\pi} \int_{4\pi} I d\omega \qquad 3.3.10$$

which can be substituted into equation 3.3.8 so that it can be written in terms of average intensity:

$$R^2 \int_{2\pi} 4\pi I s' ds' = 4\pi R^2 \int_{2\pi} s' ds' \qquad 3.3.11$$

where $4\pi R^2 = A$ and $\int_{2\pi} s'ds' = \pi$. Making those substitutions into equation 3.3.11 leads to

$\bar{I}A\pi$. If U is defined as:

$$U = \int_{4\pi} I d\omega \qquad\qquad 3.3.12$$

then combining equations 3.3.10 and 3.3.12 with the simplification of equation 3.3.11 yields:

$$\int \dot{q}_R'' dA = \frac{UA}{4} \qquad\qquad 3.3.13$$

and equation 3.3.7 can now be rewritten as:

$$\rho c V \frac{dT_{TC}}{dt} = -hA(T_{TC} - T_{gas}) - \varepsilon_{TC} A T_{TC}^4 + \frac{1}{4}\varepsilon_{TC} U A \qquad\qquad 3.3.14$$

Equation 3.3.14 shows that the time response of a thermocouple is a balance of convective losses, radiative emission, and integrated intensity. The difficulty with solving equation 3.3.14 is that it is a nonlinear ordinary differential equation that is coupled to the radiative transfer equation. The radiative transfer equation is assumed to be a part of the CFD solution. Various solution techniques are used to solve the radiative transfer equation (RTE) in CFD codes.

Numerical code and quasi-steady thermocouple model

Much has been documented in the literature and also in this dissertation on the underlying methodology of the CFD code used for this study, Fire Dynamics Simulator (FDS) (McGrattan et al., 2010a). Because of the need to complement the work done by experimentalists in fire research, there is a long history of building transducer submodels into FDS. The thermocouple model as it exists in FDS v5.5.0 solves the steady state form of equation 3.3.14 (McGrattan et al., 2010a):

$$\varepsilon_{TC} A\left(\sigma T_{TC}^4 - \frac{1}{4}U\right) + hA\left(T_{TC} - T_{gas}\right) = 0 \qquad\qquad 3.3.15$$

The solution is found using a Newton-Raphson method for root finding where $R(T_{TC})$ is:

$$R(T_{TC}) = \varepsilon_{TC}\sigma T_{TC}^4 + hT_{TC} - \frac{1}{4}\varepsilon_{TC}U - hT_{gas} \qquad 3.3.16$$

and U is the integrated radiative intensity. The derivative of equation 3.3.16 is:

$$R'(T_{TC}) = 4\varepsilon_{TC}\sigma T_{TC}^3 + h \qquad 3.3.17$$

To solve for the thermocouple temperature at each iteration, the temperature is initially assumed to be 95% of the current spatial gas temperature. The thermocouple temperature is then iterated 10 times using equations 3.3.16 and 3.3.17:

$$T_{TC}(i+1) = T_{TC}(i) - \frac{R(T_{TC}(i))}{R'(T_{TC}(i))} \qquad 3.3.18$$

The problem with the current model is that it does not account for the time constant (or thermal lag) associated with heat transfer to a solid. Currently, the thermocouple temperature follows the gas temperature response except that the thermocouple temperature is lower since it accounts for the radiative corrections to the thermocouple bead. However, it is known from heat transfer theory and experiments that the bead at the end of a thermocouple requires a finite time to fully react to changing thermal conditions around it. The response time is known as the time constant, τ, and is defined by:

$$\tau = \frac{\rho c V}{hA} \qquad 3.3.19$$

Density and specific heat are weak functions of temperature while the heat transfer coefficient is a function of temperature and flow conditions. The next section will discuss a direct solution of equation 3.3.20, which includes the time response.

Transient FDS thermocouple model

A transient thermocouple model was implemented into FDS. This model has been incorporated into release 5.5.3 of FDS by the development team. A simple algorithm explicitly integrates equation 3.3.14 using the thermocouple temperature from the previous FDS time step and increments based on FDS' time step:

$$T_{TC}(t) = T_{TC}(t-1) + \frac{A\Delta t_{FDS}}{\rho c V}\left(h\left(T_{gas} - T_{TC}(t-1)\right) - \varepsilon_{TC}\sigma T_{TC}^4(t-1) + \frac{1}{4}\varepsilon_{TC}U\right) \qquad 3.3.20$$

Equation 3.3.20 can be numerically integrated in this fashion because of the small time steps used in FDS. In order to test the applicability of this model, code was implemented into FDS and test simulations were completed. Table 3.3.2 gives the property values used for the thermocouple model.

Table 3.3.2: Physical values used for thermocouple properties

Property	Value	Units
ρ	8908	kg/m^3
C	440	J/kg-K
Σ	5.67x10^{-8}	W/m^2-K^4
d	0.001	m
d	0.003	m
ε	0.85	---

For both thermocouple models (old and new), the bead diameter was initially set to be 1 mm with an emissivity of 0.85. The simulation was designed to find the time response of the thermocouple by using 4 thermocouples in a line at vertical positions of z=0.5 m, 1.0 m, 1.5 m, and 2.0 m. The thermocouples were centered above a 400ºC forced hot airflow source at z=0.0 m that pushed air into an environment of 20ºC. A smokeview rendering of the simulation is included in Figure 3.3.11.
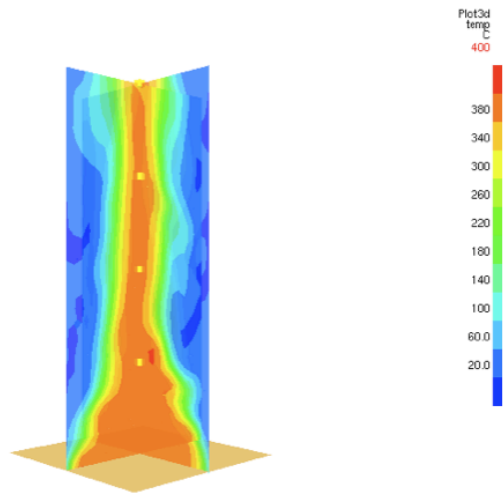
Figure 3.3.11: Smokeview rendering of thermocouple modeling test configuration.

The thermocouple responses were compared to the gas temperature. Time-temperature curves comparing the models at different vertical positions are included in Figures 3.3.12 and 3.3.13.
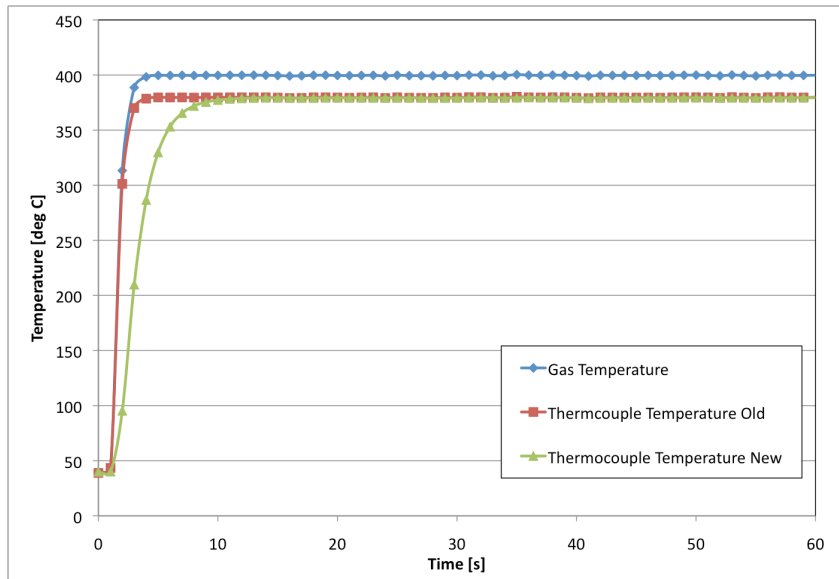
Figure 3.3.12: FDS thermocouple response comparison to FDS gas temperature with a bead diameter of 1 mm at z=0.5 m from a 400ºC hot air source.
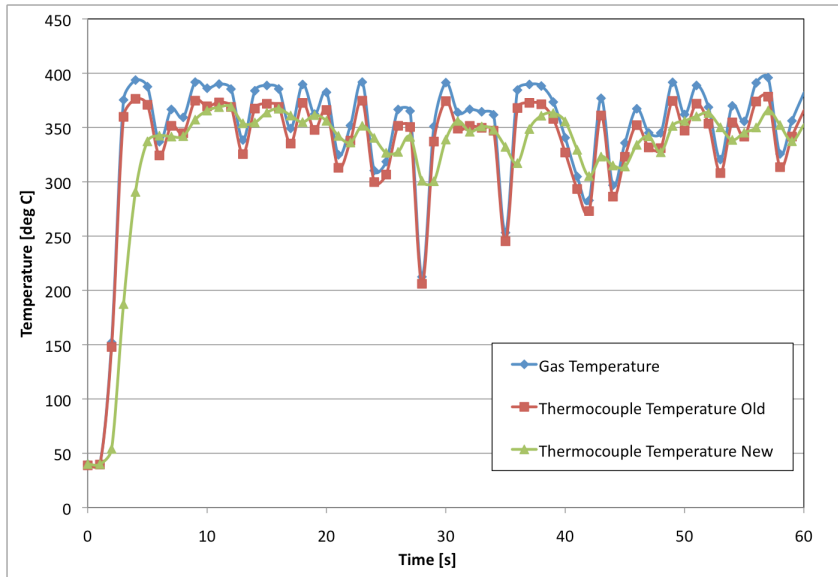
Figure 3.3.13: FDS thermocouple response comparison to FDS gas temperature with a bead diameter of 1 mm at z=1.5 m from a 400ºC hot air source.

Figure 3.3.12 shows that the gas temperature and the old thermocouple model increase to steady state at the same rate (t=4 seconds), and that the thermocouple has a lower steady state temperature, 380ºC, due to radiative losses. The new thermocouple model reaches the same steady state value of the old thermocouple model and lags behind the current model, not achieving steady state until t=10 seconds. Figure 3.3.13 shows a similar trend except the gas temperature at z=1.5 m fluctuates since the environment cools the hot source air. Figure 3.3.13 shows that the old thermocouple exactly follows the gas profile but is consistently lower in temperature. The new thermocouple model shows the local extrema lag behind the gas temperature by 1-2 seconds. The integration of equation 3.6 also acts as a smoothing function to the fluctuations generated from the large eddy simulation (LES) solver in FDS.

Additional simulations were designed to study the impact of bead diameter on temperature response. The same simulation configuration was used, except the bead

97

diameter of the thermocouple was changed from 1 mm to 3 mm. The simulations were conducted for both thermocouple models. Figure 3.3.14 shows responses compared to gas temperature for the two models at z=0.5 m while Figure 3.3.15 shows the responses at z=1.5 m.
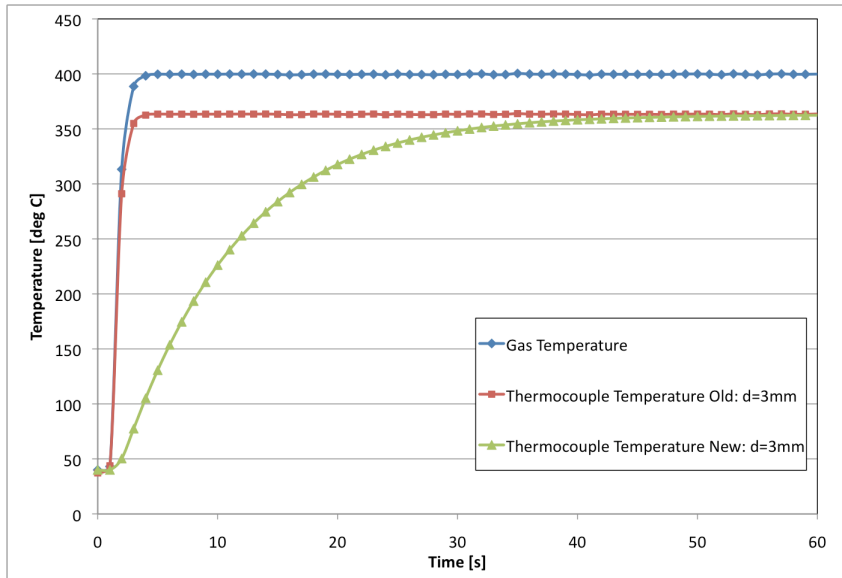
Figure 3.3.14: FDS thermocouple response comparison to FDS gas temperature with a bead diameter of 3 mm at z=0.5 m from a 400ºC hot air source.

Figure 3.3.15: FDS thermocouple response comparison to FDS gas temperature with a bead diameter of 3 mm at z=1.5 m from a 400°C hot air source.

As the diameter increases the old thermocouple model temperature response still has the same time response as the gas temperature, but has lower temperatures compared to the 1 mm diameter bead. The lower temperature makes sense as the heat transfer coefficient, h, is a function of diameter. The new thermocouple model shows that as the diameter increases, the response time becomes longer (as the thermocouple takes longer to heat up). At z=0.5 m the model reaches the same steady state temperature as the old thermocouple model except it takes about 4 times longer. At z=1.5 m, the new model for large diameter thermocouple shows minimal fluctuations to the changing gas temperature around it.

Thermocouple model verification

To ensure that the thermocouple model had the appropriate surface energy balance models, two test cases were conducted. The first case was convection only. In this simulation, the thermocouple bead emissivity was set to zero and the bead was

99

placed in a duct with walls at 600°C and 600°C air (source air) blowing past it. The ambient temperature was initially set to be 20°C. A schematic of the simulation is shown in Figure 3.3.16.
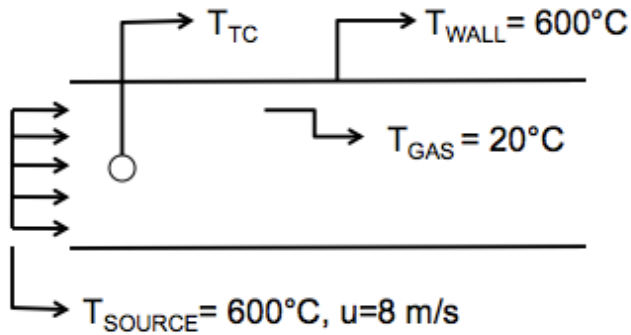
Figure 3.3.16: Schematic of the convection simulation.

For the convection case the analytical model is:

$$\rho c V \frac{dT}{dt} = hA\left(T_{TC} - T_{gas}\right)$$
3.3.21

and the resulting solution to equation 3.3.21 is equation 3.3.22.

$$\frac{T_{TC}(t) - T_{gas}}{T_i - T_{gas}} = \exp\left(-\frac{hA}{\rho c V}t\right)$$
3.3.22

Figure 3.3.17 compares the FDS thermocouple to the analytical solution and gas the temperature.

100
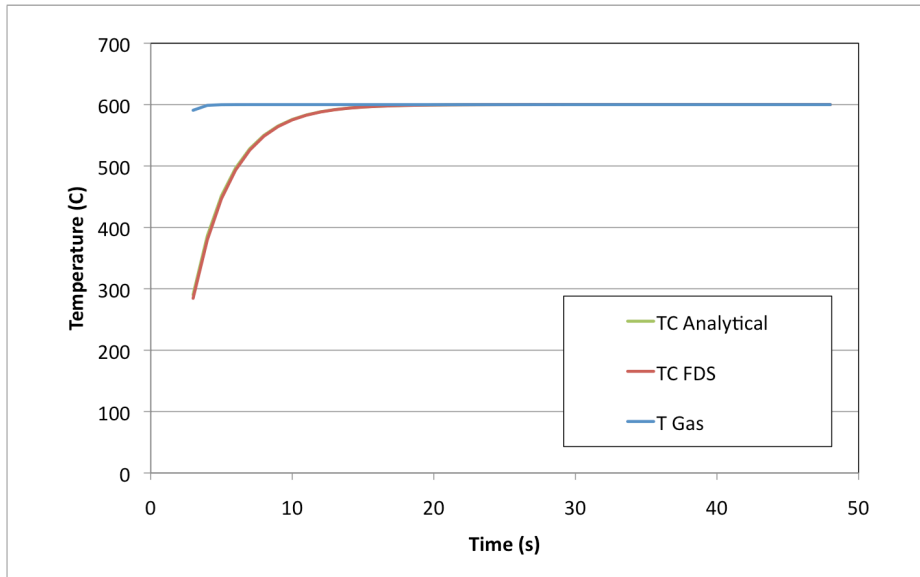
Figure 3.3.17: FDS comparison to analytical model in pure convection.

The gas temperature ramps to the wall/source air temperature. The thermocouple lags behind due to its thermal inertia. The analytical model does a very good job of capturing the FDS response, having a maximum percent difference of approximately 2 percent. These results are expected as the analytical model is solving the same fundamental equation as FDS.

The second case is the pure radiation case. The thermocouple was placed in a box with walls set to 600ºC and gas temperature set to 20ºC. A schematic of the test setup for this simulation is included in Figure 3.3.18.
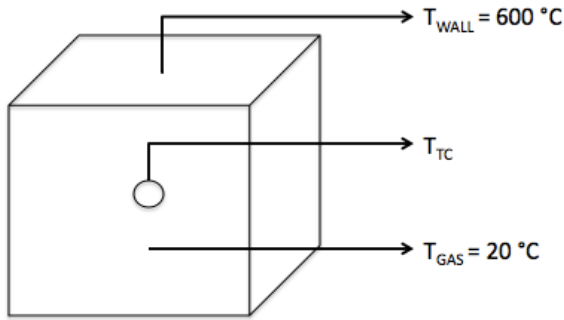
Figure 3.3.18: Schematic of the radiation simulation.

The heat transfer coefficient was set to zero for this simulation. The gas temperature will remain at 20 °C as air is not participating. The lumped analysis form of the energy equation in radiation driven mode is:

$$\rho c V \frac{dT_{TC}}{dt} = \varepsilon_{TC} \sigma A \left(T_{env}^4 - T_{TC}^4 \right)$$

3.3.23

The solution to equation 3.3.23 is:

$$t = \frac{\ln(x+1) - \ln(1-x) + 2\tan^{-1}(x)}{4\beta T_{env}^3} \bigg|_{T_{TC}(0)}^{T_{TC}(t)}$$

3.3.24

where $\beta = \dfrac{\varepsilon_{TC} \sigma A}{\rho c V}$ and $x = \dfrac{T_{TC}}{T_{env}}$. The FDS thermocouple response is again compared to an analytical solution as well as the numerical solution (Figure 3.3.19).
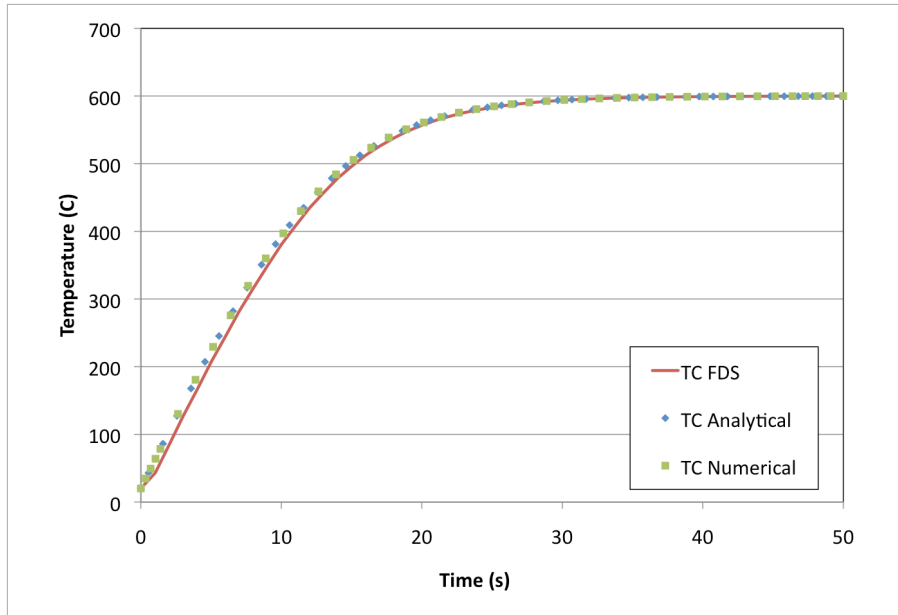
Figure 3.3.19: FDS comparison to analytical model in radiation.

Compared to the convection model where FDS integrates the exact same equation as the analytical solution, the radiation case is more complex. The analytical model is based upon a two surface radiation interaction that is valid in the limit of a small object (i.e., the thermocouple junction) placed within a large cavity. The FDS solution integrates the lumped energy equation in which the radiation interaction is modeled using a discrete transfer solution of the RTE. Often, in combined mode problems involving radiation, the RTE is not solved as frequently as other physics. Obviously, for this verification problem that only has radiation effects, it was necessary to solve the radiative transport equation at each time step of the overall time integration to achieve this level of agreement between the FDS predictions and the analytical result. Figure 3.3.19 shows that the analytical and numerical solutions compare well to the FDS thermocouple model in pure radiation.

Model assessment and experimental comparison

The new model more accurately captures the thermal response of a thermocouple due to the inclusion of temporal effects. The thermal response is a function of tunable material and physical properties of the thermocouple which can be modified based on actual thermocouples. Since the FDS source code was modified, it was important to ensure that there were no additional computational costs associated with its use. Comparison of the output data files showed no change to total computation time for the simulations completed. The model was also examined in the two limiting heat transfer cases (radiation only and convection only). The FDS model compares well to the analytical solution in both the convection and radiation cases. To further test the thermocouple model, results from computational fluid dynamics (CFD) simulations were compared to reacting-flow experiments presented in later in this chapter and in chapter 4.

Thermocouple analysis in a fluctuating fire environment

The next step in understanding the temperature response of a thermocouple is to characterize the coupled influence of gas temperature and wall temperature on the thermocouple bead. This is important in compartment fires because there are situations when a thermocouple response is dominated by radiation (low elevations), dominated by convection (during PPV), and affected by both modes (medium to upper elevations). To evaluate a simple test problem, the gas phase is assumed to be non-participating.

The governing equation for the thermocouple temperature response in a convective and radiative environment is:

$$\frac{dT_{TC}}{dt} = \frac{T_{gas} - T_{TC}}{\tau_{conv}} + \frac{T_{wall}^4 - T_{TC}^4}{T_0^3 \tau_{rad}}$$

$$3.3.25$$

where T_{wall} the surround wall temperature, T_{TC} is the thermocouple temperature, T_0 is some reference temperature of the wall, τ_{conv} is the convective time constant, and τ_{rad} is

the radiative time constant. The convective time constant is defined as $\tau_{conv} = \dfrac{\rho c V}{hA}$.

Similarly the radiative time constant is defined as $\tau_{rad} = \dfrac{\rho c V}{\varepsilon_{TC} \sigma A T_0^3}$. Consider the steady

state case in which equation 3.3.25 becomes:

$$\frac{T_{TC} - T_{gas}}{\tau_{conv}/\tau_{rad}} = \frac{T_{wall}^4 - T_{TC}^4}{T_0^3} \qquad\qquad 3.3.26$$

Equation 3.3.26 provides a relation to determine the thermocouple temperature for known values of the gas temperature and wall temperature. The values of gas and wall temperature can be thought of as distributions due to fluctuations in the temperatures during a compartment fire and uncertainty associated with the sensors. If the driving temperatures (T_{wall} and T_{gas}) are both sampled from distributions, the exercise becomes solving equation 3.25 to determine the resulting distribution for the thermocouple response (Figure 3.3.20). Knowing the thermocouple temperature distribution can provide insight into how each temperature source contributes.

$$\frac{\dfrac{T_{TC} - T_{gas}}{\tau_{conv}}}{\tau_{rad}} = \frac{T_{wall}^4 - T_{TC}^4}{T_0^3}$$
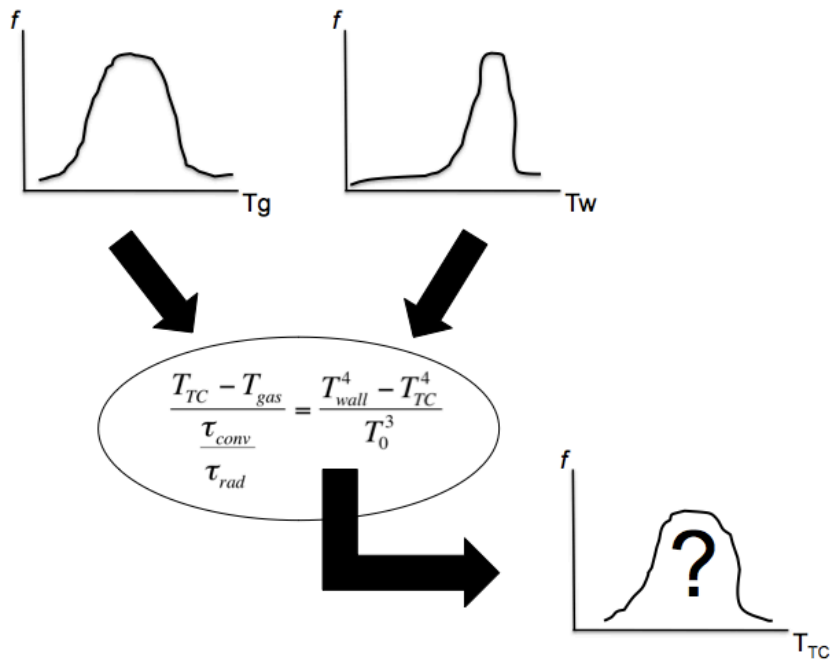
Figure 3.3.20: Representation of PDFs of gas temperature (T_g) and wall temperature (T_w) being combined to find the unknown distribution for thermocouple temperature (T_{TC}).

One way to propagate uncertainty is to use Monte Carlo methods in which randomly sampled values from the gas temperature distribution and wall temperature distribution are propagated through the model to calculate the associated thermocouple temperature. In general, for complex problems with expensive function calls, Monte Carlo methods are computationally expensive. The expense increases for high dimensional problems, as the number of samples needed increases exponentially. In this model problem, the function calls are quite inexpensive, but it is instructive to explore how to analyze the uncertainty propagation with approaches less expensive than Monte Carlo.

An alternative approach to MC is to use the method of moments. To understand how this can be applied, discussion will start from what is desired and work backwards.

Knowing the distribution of the thermocouple temperature, the moments of the distribution can be calculated following equation 3.3.27

$$_{TC}M_k = \int T_{TC}^k n(T_{TC}) dT_{TC} \qquad\qquad 3.3.27$$

which quantitatively describes the thermocouple distribution. The problem is that the thermocouple temperature distribution, $n(T_{TC}) dT_{TC}$ is unknown. The distributions of the gas and wall temperatures are known. For this model problem beta distributions for the gas and wall temperatures are assumed.

A beta distribution is a continuous PDF defined on the interval (0,1) and is characterized by two shape factors: α and β. The PDF of a beta distribution is defined as:

$$f(x;\alpha,\beta) = \frac{1}{B(\alpha,\beta)} x^{\alpha-1}(1-x)^{\beta-1} \qquad\qquad 3.3.28$$

where B is a normalized constant to ensure the PDF integrates to 1. Table 3.3.3 shows the two shape factors chosen for the distributions and the resulting first four moments (M_0-M_3) for the gas and wall temperature distributions. Table 3.3.4 shows the mean temperature and RMS values for the gas and wall based on of moments of the beta distributions used to describe the temperature variations.

Table 3.3.3: Beta distribution shape parameters for the two temperature distributions and the resulting M_1-M_3 moments.

Phase	Shape Parameters	M_0	M_1	M_2	M_3
Gas Temperature	$\alpha=1$; $\beta=1$	1	600	3.9×10^5	2.7×10^8
Wall Temperature	$\alpha=2$; $\beta=0.1$	1	872	7.7×10^5	6.7×10^8

Table 3.3.4: Statistics for gas temperature and wall temperature.

Phase	Mean Temperature [K]	RMS [K]
Gas Temperature	600	173
Wall Temperature	872	68

These values were chosen because they reflect typical values in compartment fires. The gas phase responds quickly to local changes within the compartment so a larger standard deviation is expected. The wall temperature should have a much lower standard deviation as the walls have a large thermal mass and are therefore expected be fairly uniform. From equation 3.3.26 it is known that the thermocouple temperature is a function of the gas and wall temperatures and therefore equation 3.3.27 can be modified to reflect this.

$$_{TC}M_k = \int \int T_{TC}^k\left(T_{gas}, T_{wall}\right) m\left(T_{gas}\right) r\left(T_{wall}\right) dT_{gas} dT_{wall} \qquad 3.3.29$$

Equation 3.3.29 is double integral equation over the distributions of the gas and wall temperatures. This double integral is still not in a form that can be easily solved. Integrating the beta functions is an exercise in numerical integration. An alternative approach is to use the quadrature method of moments (QMOM) (McGraw, 1997). QMOM was developed so that a moment integral (e.g. equation 3.28) can be approximated by n-point Gaussian quadrature. Gaussian qaudrature is a numerical method used to approximate a definite integral by a weighted sum. A description of this method can be found in Upadhyay (Upadhyay, 2006). If a quadrature approximation is applied to equation 3.28, the double integral is replaced by a double sum.

$$_{TC}M_k = \sum_{i=1}^{N_Q}\sum_{j=1}^{N_Q} W_{gas,i} W_{wall,j} T_{TC,ij}^k(\hat{T}_{gas}, \hat{T}_{wall}) \qquad 3.3.30$$

where W_{gas} and W_{wall} are the quadrature weights and $\hat{T}_{gas}$ and $\hat{T}_{wall}$ are the quadrature points of the gas and wall temperature distributions. The quadrature points and weights

for the gas and wall temperatures are found from the moments of their respective distributions. Figure 3.3.21 shows how propagation of uncertainty is handled for this problem using the QMOM framework. In this case, 2 point quadrature is shown. The quadrature points are position along the x-axis, while the quadrature weights are the heights at those positions. As the number of points used to approximate the integral is increased, the accuracy of the approximation improves.
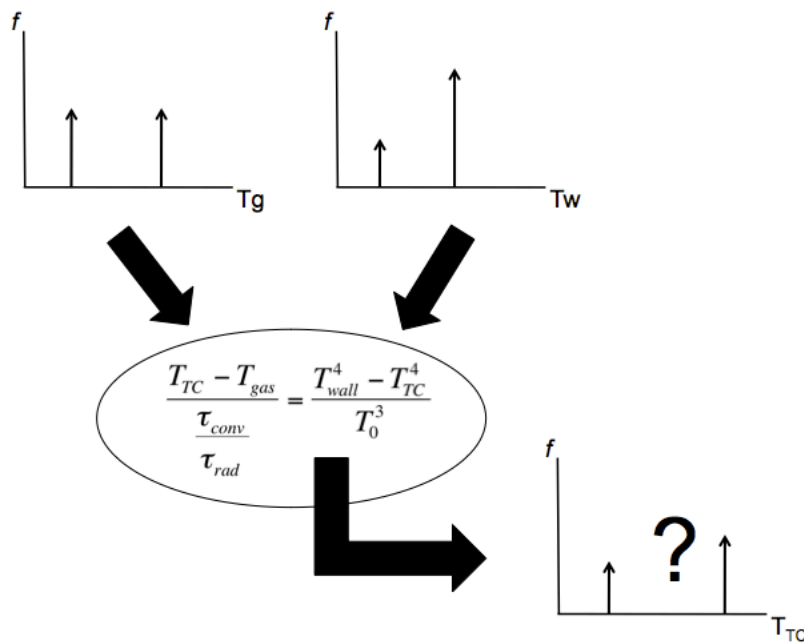
Figure 3.3.21: Representation of the quadrature points and weights of gas temperature (T_g) and wall temperature (T_w) distributions being combined to find the unknown distribution for thermocouple temperature (T_{TC}).

QMOM allows us to find a discrete set of quadrature points and weights that numerically characterize the moments (which describe the temperature distributions). The number of moments, $N_{mom,}$, needed from the experimental temperature data is based on the following equation:

$$N_{mom} = N_Q(d+1)$$ 3.3.31

where N_Q is the number of quadrature points and d is the dimensionality of the problem. Both the gas and wall temperature distributions are assumed to be independent. Thus, each is a univariate analysis. To specify two quadrature points and two weights for each distribution, 4 moments must be specified for each. The first four moments, M_0 through M_3 were calculated from the beta PDF distributions. The two quadrature points and weights can be found by solving for the roots of the following system of non-linear equations:

$$W_1(t) + W_2(t) - M_0(t) = 0$$
$$W_1(t)\hat{T}_1(t) + W_2(t)\hat{T}_2(t) - M_1(t) = 0$$
$$W_1(t)\hat{T}_1(t)^2 + W_2(t)\hat{T}_2(t)^2 - M_2(t) = 0$$
$$W_1(t)\hat{T}_1(t)^3 + W_2(t)\hat{T}_2(t)^3 - M_3(t) = 0$$

$$3.3.32$$

where $\hat{T}_1(t)$ and $\hat{T}_2(t)$ are the two quadrature points and $W_1(t)$ and $W_2(t)$ are the quadrature weights. In practice, this system of equations is very ill-conditioned and direct solution, particularly for problems where N_Q is large, is infeasible.

An alternate way of framing the problem is based on the construction of an orthogonal polynomial sequence to approximate all functions formed by integration weighted with respect to the density function. The final polynomial approximant closes the sequence by assuring that the roots/zeroes exactly close all polynomials of lower order. For the case of a two point approximation, a quadratic equation can be formed whose roots $\hat{T}_1$ and $\hat{T}_2$ are the quadrature points for a distribution whose moment information is contained in the coefficients a,b, and c.

$$a\hat{T}^2 + b\hat{T} + c = 0$$

$$3.3.33$$

Equation 3.3.33 is the quadratic equations and the roots are defined in 3.3.34.

$$a = 1$$

$$b = -\frac{M_3 M_0 - M_1 M_2}{M_2 M_0 - M_1^2}$$

$$c = \frac{M_1 M_3 - M_2^2}{M_2 M_0 - M_1^2}$$

3.3.34

The quadrature weights can be found using the two quadrature points and first two moments:

$$W_1 = \frac{M_1}{\hat{T}_1 - \hat{T}_2} - M_0 \frac{\hat{T}_2}{\hat{T}_1 - \hat{T}_2}$$

$$W_2 = \frac{M_1}{\hat{T}_2 - \hat{T}_1} - M_0 \frac{\hat{T}_1}{\hat{T}_2 - \hat{T}_1}$$

3.3.35

Using equations 3.3.33, 3.3.34, and 3.3.35 two quadrature points and two quadrature weights that satisfy the moments of the temperature distribution can be found. For problems in which N_Q is large, directly computing the roots of the polynomials again is infeasible. The standard way to generate the quadrature points and weights relies on using the three-point recursion relationship for orthogonal polynomials to construct a tridiagonal matrix using the product-difference algorithm (Gordon, 1968). An eigenvalue problem is then solved to find the quadrature points and weights.

Once the quadrature points and weights are known, the last step is to evaluate the thermocouple temperature at the quadrature points of gas and wall temperature distributions. Equation 3.3.26 can be rewritten in terms of quadrature points:

$$\frac{T_{TC,ij} - \hat{T}_{gas,i}}{\tau_{conv}/\tau_{rad}} = \frac{\hat{T}_{wall,j}^4 - T_{TC,ij}^4}{T_0^3} \text{ for i} = 1 \ldots N_Q \text{ \& for j} = 1 \ldots N_Q$$

3.3.36

where $\hat{T}_{gas,i}$ is a gas temperature qaudrature point and $\hat{T}_{wall,j}^4$ is a wall temperature qaudrature point. The number of function evaluations, N_F, (i.e., equation 3.29) is based on

the number of quadrature points, and the dimensionality, d, of the problem by the following equation:

$$N_F = (N_Q)^d \hspace{6cm} 3.3.37$$

For this problem 2-point quadrature is used and operates in 2 dimensions, so the function call in equation 3.3.30 will need to be executed 4 times, 1 for each combination of quadrature points.

The moments of thermocouple temperature distribution can be calculated from equation 3.3.29 using the thermocouple temperatures calculated from equation 3.3.30 and the weights determined from the gas and wall temperature distributions. The statistics of most importance in this case are the mean, M_1, and the standard deviation/RMS, $\sqrt{M_2 - M_1^2}$. The ratio of the convective time constant to the radiative time constant is varied through the heat transfer coefficient, to explore the impact of the statistics of the thermocouple temperature. This convective to radiative time-constant ratio describes which mode of heat transfer is more dominant. Using the same initial temperature statistics shown in Table 3.3.4, the thermocouple temperature distribution was found for four different time constant ratios. These results are included in table 3.3.5.

Table 3.3.5: Thermocouple temperature statistics for 4 different convective time constant to radiative time constant ratios.

τ_{conv}/τ_{rad}	Mean Temperature [K]	RMS [K]
0.0083	615	167
0.017	629	160
0.167	770	86
0.367	819	71

Examination of the data in Table 3.3.5 shows that for τ_{conv} much less than τ_{rad} the thermal environment is convectively dominant. The mean temperature and standard deviation approach the initial values of the gas temperature indicating that the heat transfer process is almost purely convective. For the cases with larger time constant ratios the statistics approach the initial wall values indicating that the problem is radiation dominant. Through the use of QMOM, uncertainty in gas and wall temperature was propagated to the corresponding thermocouple response. Examination of the thermocouple distribution provided insight as to the dominant mode of heat transfer acting on the thermocouple.

3.3.4 Comparing experimental results to model predictions

The previous sections have detailed the calibration of model parameters as well as the development of an improved sensor model. The combination of these factors should lead to a computational model that compares well to experimental results. To evaluate the FDS model results, a 400 kW experiment is compared to an FDS simulation of the same case, using a HRR input determined from the experiment being modeled. Figure 3.3.22 shows experimental thermocouple temperatures and FDS thermocouple temperatures at each thermocouple at the 4 experimental elevations.
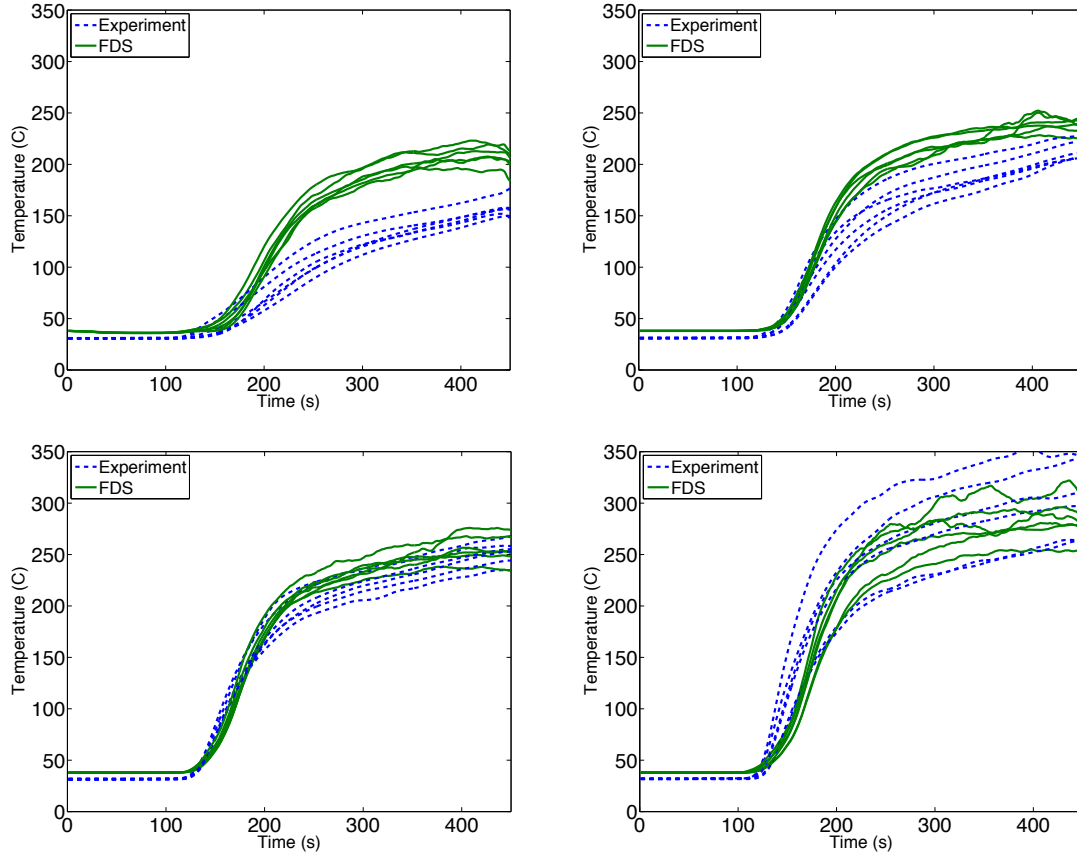
Figure 3.3.22: Experimental thermocouple temperatures (dashed line) and FDS computed
thermocouple temperatures (solid line) with a 400 kW fire at the 4
experimental sensor elevations. The top left plot is 0.73 m, the top right is
1.19 m, the bottom left is 1.63 m and the bottom right is 2.08 m.

A first look at the temperature comparisons shows how the FDS model results
compare to the experimental values. Both sets of results show similar spatial variation
within each of the 4 elevations. Looking at each elevation, there is a better comparison at
the higher elevations and over predictions in temperature from the FDS model at lower
elevations. This is most noticeable at the lowest elevation, 0.73 m. One possibility for the
differences is that in the experiments, the thermocouples were directed away from the
burners and partially shielded by insulation that was used to protect the thermocouple

wiring. This would decrease the shape factor of the thermocouple bead to the flame and lower incident radiation. In FDS, the thermocouple beads were located in the same position as the experimental thermocouples, however the insulation protecting the real thermocouples was not modeled. As a result the FDS thermocouples completely "see" the flames with respect to radiation emission. This issue will be discussed in more detail in a following section.

3.3.5 Towards explaining lower elevation temperature discrepancies

As noted, lower elevations temperatures in FDS are over predicted relative to the corresponding experimental temperatures (Figure 3.3.22). There are several potential sources of this difference, and those sources will be discussed in this section.

At the lower elevations, radiation is the dominant mode of heat transfer. Radiation to the thermocouple beads can come from the flames of the burners, the sooty upper layer, and the surroundings (hot wall, floor, ceiling). Wall/floor/ceiling temperatures were not experimentally measured and therefore cannot be compared to their simulation counterparts at this time. In future tests, however, thermocouples should be imbedded into the gypsum board throughout the compartment interior. In the upper layer, the gas is optically thick due to the presence of soot, which limits thermocouples from "seeing" radiation from other sources beside the gas. In FDS, soot is produced similar to gas phase products with a fractional yield from the carbon in the fuel. There are significant errors in such an approximation, which would subsequently impact gas phase radiation in the model.

A potential source of error in the model that can be checked is incident radiation from the burner flames to the thermocouple beads. In the experiments the thermocouple beads are oriented such that the insulated thermocouple tree supporting the wires also

acts as a radiation shield from the flames. Figure 3.3.30 shows a compartment scale image showing the thermocouple trees orientation with respect to the burners and a close-up of a thermocouple bead protruding from the insulation.

Figure 3.3.23: The image on the left shows a thermocouple tree with insulation with one of the two sand burners behind it. The image on the right shows a thermocouple protruding from the insulation, circled in red.

In the FDS model, there was no explicit modeling of the insulated thermocouple tree. The thermocouple bead was not shielded by the insulation and can "see" in 4π steradians unobstructed. To check the influence of the thermocouple tree shielding on the thermocouple response, solid obstructions of similar size as the insulated trees were added into the geometry model to simulate the trees. The effects of radiation on temperature at the two lower elevations can be seen in the mean fire room temperature plots shown in Figure 3.3.31
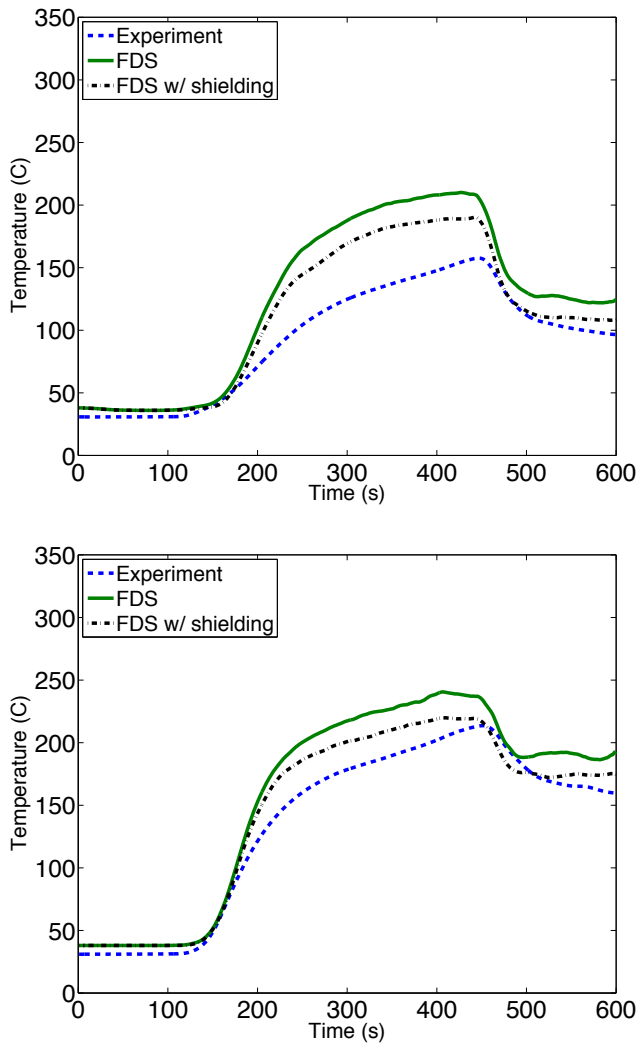
Figure 3.3.24 Examination of radiation shielding in thermocouple temperature in FDS. Both plots compare spatial mean temperatures from FDS without shielding (dashed) and FDS with shielding (dash-dotted) to experimentally measured temperatures (solid) at 0.73 m (top) and 1.19 m (bottom).

Shielding the thermocouples from the flame radiation decreased the average lower elevation temperatures by approximately 20 °C. The results show that blocking flame radiation contributes to correcting the higher FDS thermocouple temperatures. In this experimental and computational scenario, the compartment door was opened at 450

117

seconds to model natural ventilation. The post-ventilation results (time greater than 450 seconds) are encouraging as there was some concern about the radiation shielding obstructions in the FDS model affecting fluid mechanics within the compartment and impacting the convective heat transfer from the thermocouple beads.

The amount and location of structure leakage is another factor that could cause the low elevation temperature discrepancies. The amount of leakage used in the computational models was determined at the outset of fire testing. The large number of fire tests conducted in the structure may have caused additional leakage. Literature shows that in addition to the amount of leakage, shape and elevation also play a role in the thermal evolution of the compartment (Beal et al., 2008). Leakage characteristics also affect the descent rate and steady state value of the hot upper layer gases. Similar to experiments, the computed temperature dependence on elevation is a continuous function; a distinct delineation between hot gases and cold gases does not exist. Recall that the equations to determine layer height were previously discussed in Section 3.3.1 (Equations 3.3.1-3.3.3). Figure 3.3.32 shows the layer height as determined by FDS and the experimentally calculated layer height following the same procedure as the FDS code (McGrattan et al., 2010a).
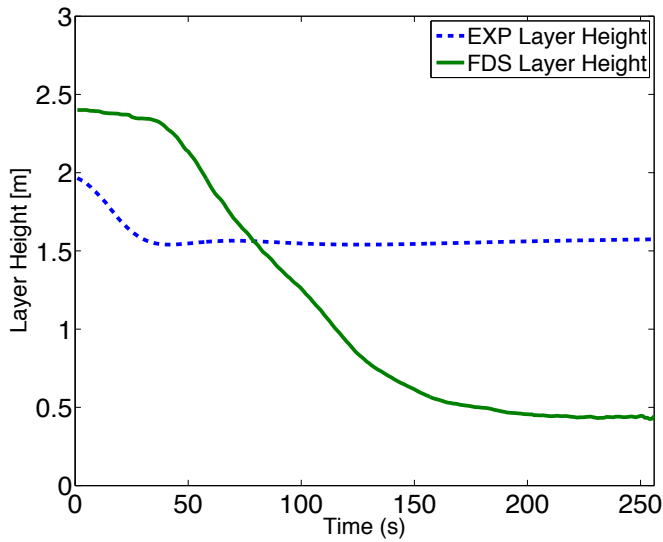
Figure 3.3.25 Comparison of layer height calculated by FDS (solid) to the experimental layer height (dashed) determined by using the same equations as the model.

In the FDS simulation, the layer height descends to about 0.4 m, which is below the lowest thermocouple elevation. In the experiment, the layer height descends to about 1.55 m, just below the second thermocouple elevation. It is believed that with better characterization of structure leakage, the FDS layer height will not descend as far. As a result the lower elevation simulation temperatures will have better comparison to the experimental data. To test this theory, FDS simulations were conducted with the structure door open through the simulation to act as an extreme case of leakage. The door open represents a leakage area of 1.84 m^2. Figure 3.3.26 shows the temperature comparisons with the current model leakage, the door open case, and the experimental data at elevations of 0.79 m and 1.19 m. Figure 3.3.26 shows how the increase in leakage area impacted layer height.
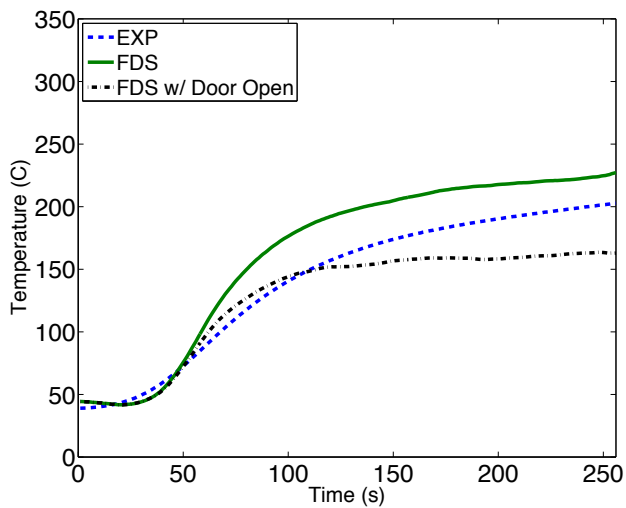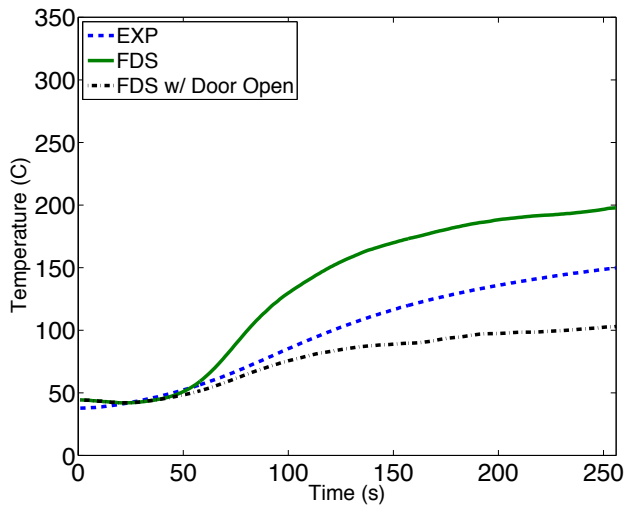
Figure 3.3.26: Comparison of mean experimental temperature (dashed) to mean FDS predicted temperatures using experimentally determined leakage (solid) and an extreme case of leakage (dash-dotted) (e.g., door open) for a 400 kW fire at 0.79 m (top) and 1.19 m (bottom).
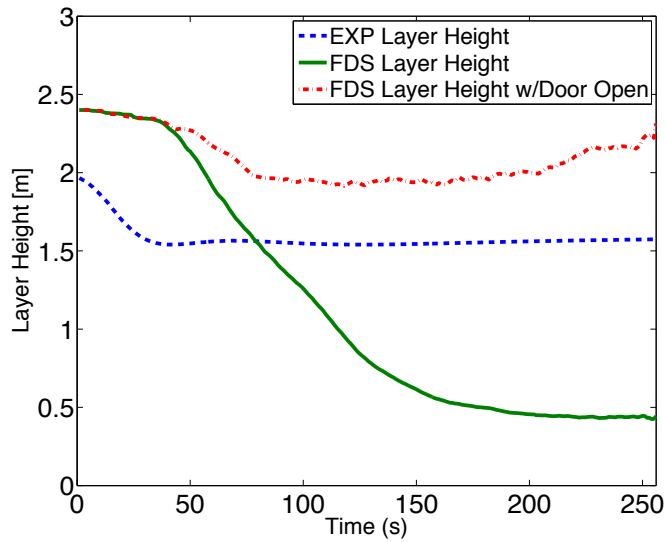
Figure 3.3.27: Comparison of experimentally calculated layer height (dashed) to FDS predicted layer height using experimentally determined leakage (solid) and an extreme case of leakage (dash-dotted) (e.g., door open) for a 400 kW fire.

Figure 3.3.26 shows that with the increased leakage, the FDS thermocouple temperatures under predict the experimental measurements. Figure 3.3.27 shows that the layer height no longer descends below the experimentally calculated layer height. While the actual amount of leakage lies between the current value and area of the door, this simple example illustrates that leakage is another model parameter affecting the lower elevation temperatures. It is important to note that in addition to the lower elevation temperatures decreasing with the increased leakage, the upper elevation temperatures also decreased.

Individually, these model parameters may not completely remedy the lower elevation temperature differences, though the results have shown the proper temperature trends. More likely, with future experimental results and diagnostics these parameters can be applied to combination to better improve the computational model.

3.3.6 Propagation of experimental uncertainty

When using experimental data to validate computer models it is important to recognize uncertainty. Earlier potential sources of experimental uncertainty were detailed and quantified by examining the temperature results for 8 400 kW experiments. Uncertainty is also known to exist within the computer model predictions. Some potential sources computational sources of uncertainty include the numerical approximations of the governing equations, models used to approximate physics that cannot be solved directly such as the radiation model or the sub grid turbulence model, or grid sensitivity affects. Accepting uncertainty inherent to the computational model, the focus of the following discussion is to examine how to propagate experimental uncertainty into the computational model to better compare results.

To determine the input HRRs for the experimental cases studied, the inversion technique developed by Overholt and Ezekoye that was discussed earlier, was used. Each of the 8 400 kW experimental data sets were inverted. We expect there to be a distribution associated with the HRR curves given the variation in the experimental temperature data.

To obtain information about the HRR distribution, one possibility would be to invert each experimental temperature trace to generate a set of HRR curves. For a small number of experiments and an accurate inversion tool this is an acceptable process since there would be no loss of statistical information. However, if there were a large number of experiments or a computationally expensive inversion, this method may not be optimal. QMOM is used to propagate the experimental uncertainty to HRR. A schematic of the procedure for propagating the uncertainty is shown in figure 3.3.23.

122
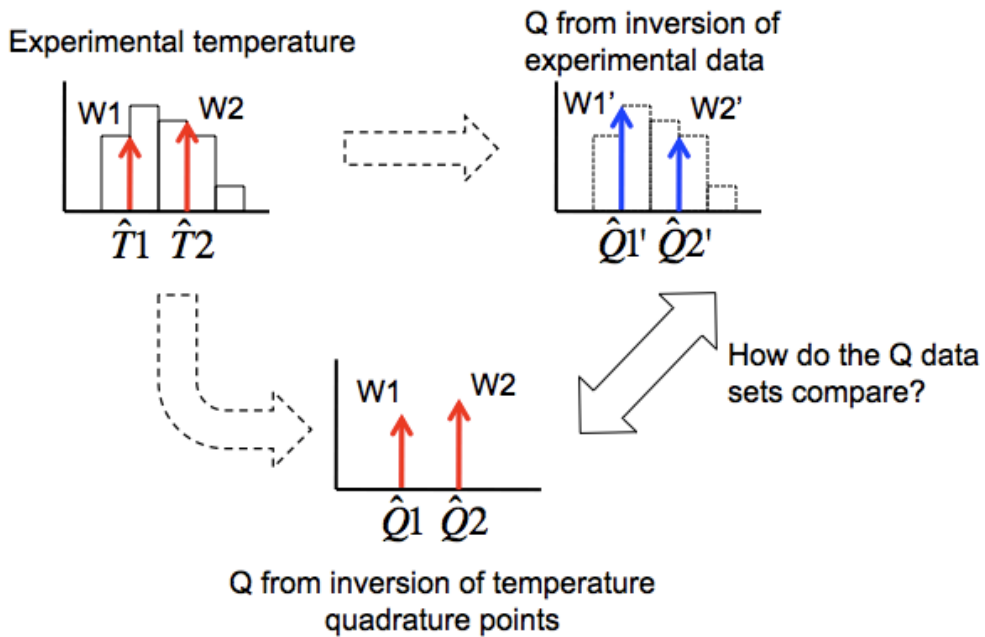
Figure 3.3.28: Schematic detailing the process of propagating experimental uncertainty to HRR. The dashed arrows represent a step that requires an inversion from temperature to HRR. The double ended solid arrow represents a step in which a comparison will take place.

From *section 3.2.2*, histograms of the temperature distribution were constructed to calculate moments of the distribution using equation 3.3. As noted, QMOM allows for a discrete set of quadrature points and weights to be found that numerically characterize the moments (which describe the temperature distribution). The number of moments, N_{mom}, needed from the experimental temperature data is based on the following equation:

$$N_{mom} = N_q(d+1)$$
3.3.38

where N_q is the number of quadrature points and d is the dimensionally of the problem. For this exercise, the problem is 1-dimenstional (temperature) and a two-point quadrature approximation is used. This requires 4 moments to be known to solve for two quadrature points and two quadrature weights. The first four moments, M_0 through M_3 were

123

calculated from the experimental temperature data following equation 3.2.2. The two quarature points and weights can be found solving for the roots of the same quadratic equation that was previously discussed (Eq. 3.3.33).

Using equations 3.3.33, 3.3.34, and 3.3.35 two quadrature points and two quadrature weights were found that satisfy the moments of the temperature distribution. Since the experimental data are functions of time, quadrature points and weights are found for each instant of time for the data set generating, $\hat{T}_1(t)$, $\hat{T}_2(t)$, $W_1(t)$, and $W_2(t)$ (upper left plot in Figure 3.3.28). Figure 3.3.29 shows the plots of the two quadrature points and two quadrature weights as functions of time.
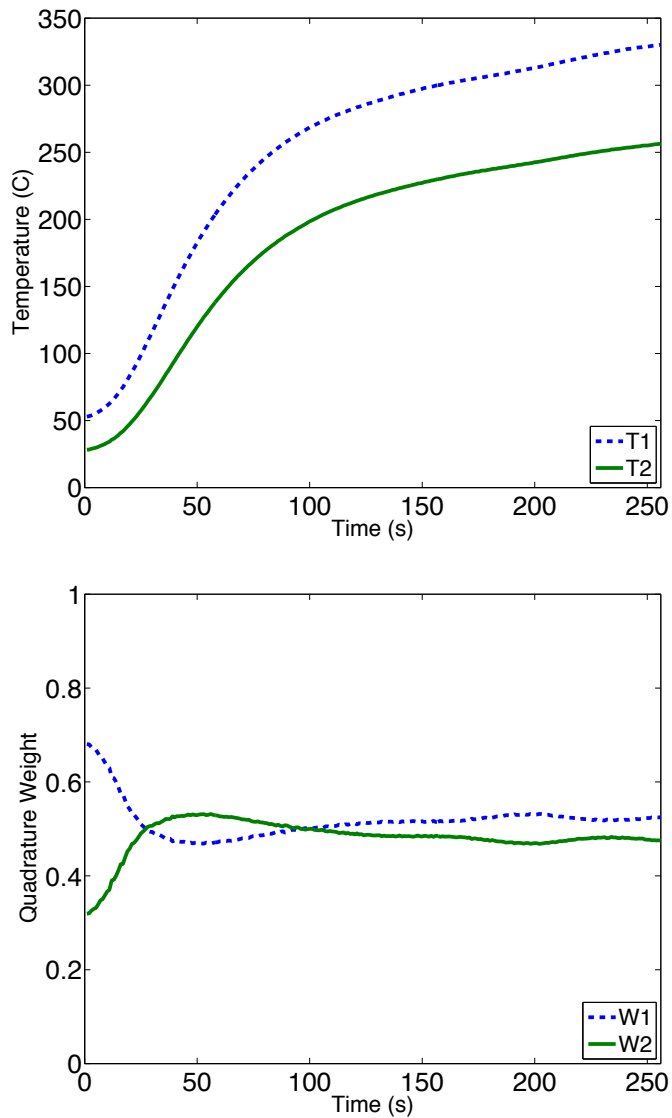
Figure 3.3.29: The two quadrature points in temperature (top) and the two quadrature
weights (botom) that satisfy the first four moments of the experimental
temperature distribution.

Through QMOM, two quadrature points and two quadrature weights are used
toapproximate the moments of the temperature distribution. Using the change in variables
rule for PDFs discussed with respect to QMOM by Updahyay and Ezekoye (Upadhyay &
Ezekoye, 2008), we can invert the quadrature points in temperature to quadrature points

in HRR following the inversion technique developed by Overholt and Ezekoye (Overholt & Ezekoye, 2011). If $\hat{T}_1(t)$ and $\hat{T}_2(t)$ are used as the input temperature curves for the inversion process, then the two HRR curves will be produced are $\hat{Q}_1(t)$ and $\hat{Q}_2(t)$ with the same weights as the temperature quadrature points (bottom middle plot of Figure 3.3.28). Figure 3.3.30 shows the plots of the two quadrature points and two quadrature weights as functions of time
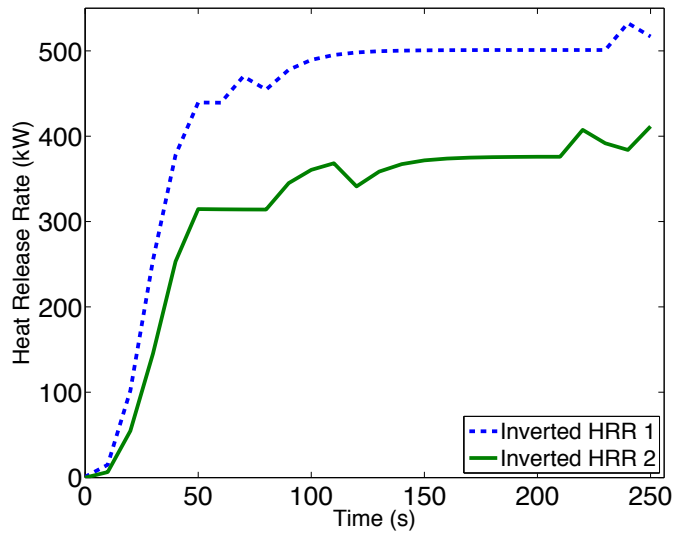
Figure 3.3.30: Heat release rate versus time curves determined from the CFAST inversion of the two quadrature points in temperature that describe the moments of the experimental temperature distribution.

We can use $\hat{Q}_1(t)$ and $\hat{Q}_2(t)$ with *W1(t)* and *W2(t)* to generate the moments of the HRR distribution we want:

$$M_1(t) = W_1(t)\hat{Q}_1(t) + W_2(t)\hat{Q}_2(t)$$
$$M_2(t) = W_1(t)\hat{Q}_1(t)^2 + W_2(t)\hat{Q}_2(t)^2$$

3.3.39

Equation set 3.3.39, describes how the moments of the distribution of HRR can be constructed from the quadrature points in HRR and the quadrature weights. Note that

126

$W_1(t)$ and $W_2(t)$ are known from equation 3.3.35 and the HRR quadrature points were found through the inversion transformation. To examine the statistical information of HRR distribution generated by using QMOM, we compare the results to statistics from inversion of all 8 experiments. Figure 3.3.31 shows the HRR curves inverted from each of the experiments, the mean HRR determined directly from those curves (upper right plot in Figure 3.3.28), and mean HRR determined from QMOM.
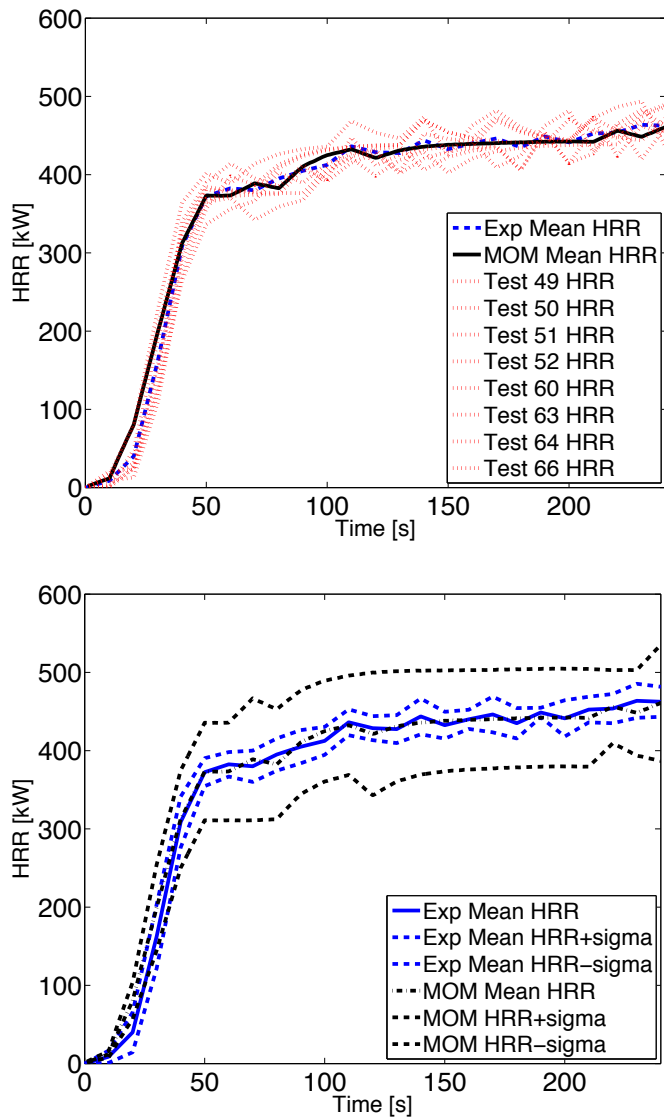
Figure 3.3.31: Top: Comparison of experimental mean HRR (solid) and QMOM mean
HRR (dashed) to the HRR curves from the individual experiments (dotted).
Bottom: Comparison of experimental mean and standard deviation to
QMOM mean and standard deviation HRR. This data is for the 8 400 kW
experiments.

The plot shows that using QMOM, the mean HRR can be reproduced using

inversion on 2 quadrature points compared to using the HRR curves for all 8

experiments. Note that both mean HRRs approach a steady state value of 450 kW, 50 kW

higher than the expected experimental value. While the exact cause of the higher heat release value is unknown, potential causes include uncertainty in the mass flow controller and user error in setting the fuel mass flow rate during experimentation. The standard deviation in the HRR predicted using two quadrature points in the temperatures is significantly different from the true standard deviation calculated using all the experimental data. This likely arises because the mapping between temperature and HRR is nonlinear and as such, the ability to accurately predict the M_0-M_3 in the temperature distribution does not assure one of being able to predict the M_0-M_3 moments in HRR. As an example, if the HRR had a simple power law dependence on temperature (e.g T^2), then M_3 in HRR would correspond to M_6 in temperature. The two point quadrature approximation is only accurate up to M_3 in temperature and would be incapable of predicting the proper M_3 behavior in HRR. An advantage of using moments is that lower moments (e.g. the mean) can be approximated by as few as two quadrature points and two quadrature weights, independent of the number of samples in the distribution. When nonlinear mapping occurs and and higher moments of an inferred quantity are needed, more quadrature points in the propagated variable are necessary for accurate predictions. As the number of experiments is increased, the use of QMOM becomes more advantageous.

The next step is to use the two quadrature points in HRR variable space as inputs that prescribe the HRR for FDS simulations. The temperatures predicted by FDS can then be compared to the original experimental data. Figure 3.3.32 is a schematic describing how the experimental uncertainty can be propagated into FDS.
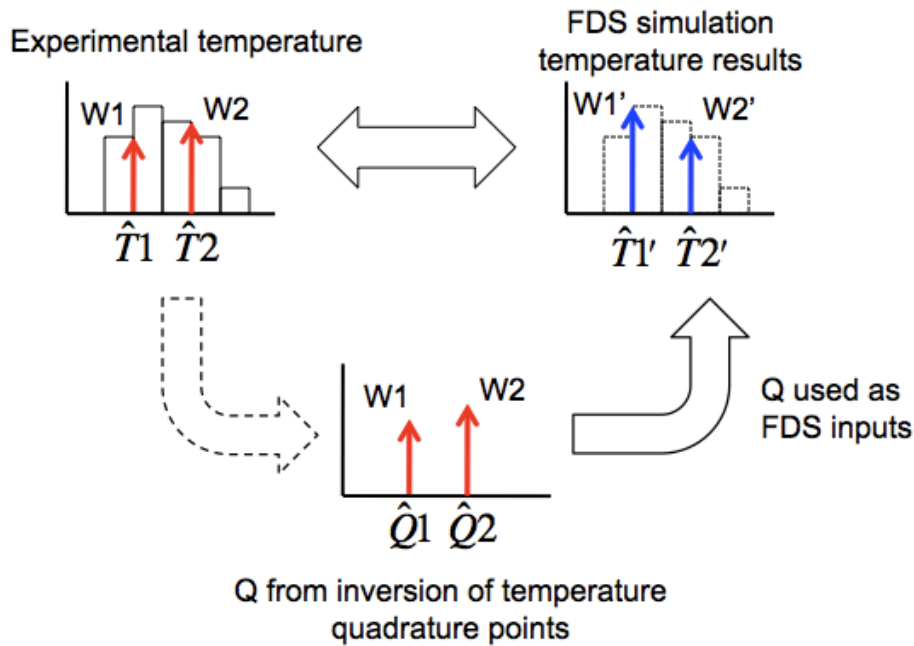
Figure 3.3.32: Schematic detailing the process of propagating experimental uncertainty to FDS. The dashed arrows represent a step that requires an inversion from temperature to HRR. The solid arrow represents a step in where the output data is used as input for the following step. The double ended solid arrow represents a step in which a comparison will take place.

An FDS model of the burn structure (geometry, wall materials, sensor location, etc) was created. Two simulations were completed; each using one of the prescribed HRRs as defined in Figure 3.3.31. From the FDS simulations, there are two quadrature points in temperature: $\hat{T}_1(t)'$ and $\hat{T}_2(t)'$ where the prime differentiates these quadrature points that were generated in FDS from those that determined directly from the experimental data.

From earlier discussion on the evolution of an enclosure fire, the compartment is known to be thermally stratified (i.e. temperature is a continuous function of elevation). Therefore, the experimental and computational quadrature points are both a function of elevation: $\hat{T}_i(z,t)$ and $\hat{T}_i(z,t)'$. Using these quadrature points with their respective

quadrature weights, $W_1(t)$ and $W_2(t)$, we can generate the moments of both temperature distributions at the 4 thermocouple elevations.

The computational moments are compared to the moments from the experimental temperature distribution to examine how uncertainty in experimental data is propagated using QMOM through inversion and a CFD model. Figure 3.3.28 shows the mean temperatures ± 1 standard deviation for the experimental data and simulation data based on the propagated uncertainty for each thermocouple elevation.
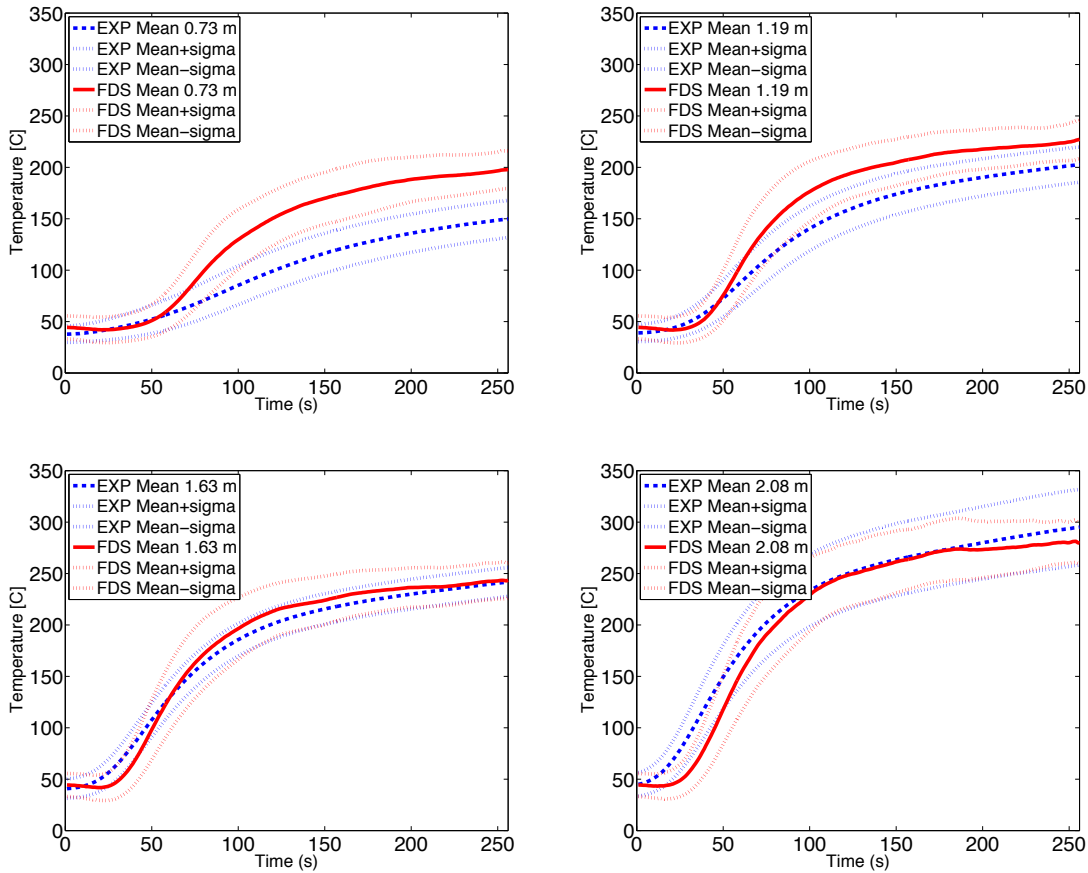
Figure 3.3.33 Comparison of experimental mean temperature with ± 1 standard deviation as a function of elevation (top left 0.73 m, top right 1.19 m, bottom left 1.63 m, and bottom right 2.08 m) to the FDS modeled temperature distribution.

The results from Figure 3.3.33 show that statistical information from an experimental data set can be propagated to a computer model using 2-point quadrature. To better assess the propagation of uncertainty into FDS, the standard deviations in experimental thermocouple temperature to FDS predicted thermocouple temperature (Figure 3.3.34) are compared.
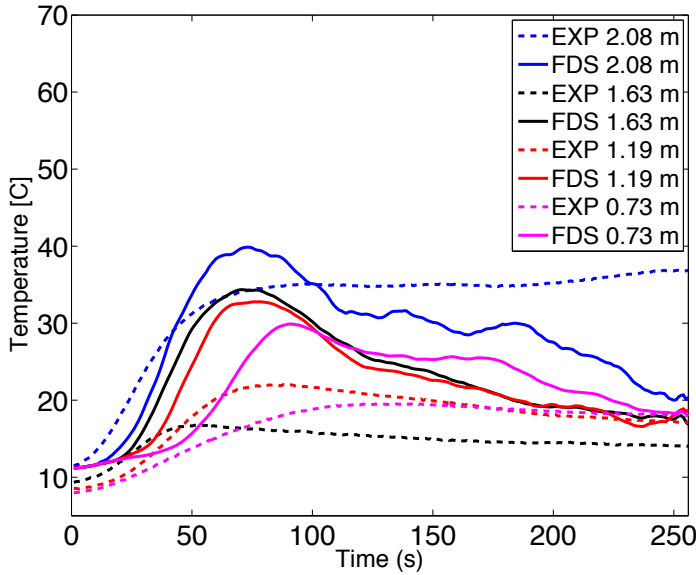
Figure 3.3.34: Comparison of standard deviation in experimental temperature (dashed) to propagated standard deviation in FDS temperature (solid).

Figure 3.3.34 shows that while the time evolution of the thermocouple temperature standard deviation is different between the experimental data and the model data, the magnitudes of the deviations are similar. One notices that the standard deviation in the simulations decays with time while the experimental standard deviation is nearly constant after reaching maximum values. This suggests that there is some mechanism in the experimental system for maintaining the inhomogeneous temperature profiles that does not exist in the simulations. It is possible that some large-scale flow mixing process present in the experiments is not present in the model. In earlier discussions, it was

shown how leakage modeling could affect flow conditions and thermal profiles in the structure. This could be one reason for these differences between the experimental and simulation results. This comparison demonstrates the ability to propagate experimental uncertainty into computer models using QMOM, which could improve future validation work.

3.4 VENTILATION MODELING

The post flashover compartment fire is a dangerous and complex environment for firefighters to operate within as they initiate fire suppression activities. Though most of the fuel within the compartment has been pyrolyzed, it has not fully combusted due to a lack of oxygen within the compartment. By entering the structure, firefighters will likely provide a ventilation path that will markedly increase burning in the compartment. This can happen by firefighters opening a door/window or by initiating firefighting tactics like Positive Pressure Ventilation. Sudden and dramatic changes to the thermal field result when pathways for airflow to reach the fire compartment are made available. Computational fluid dynamics simulations of strongly vent driven flows are useful for understanding the properties of these types of fire scenarios, but these simulations are computationally expensive. Typical zone model tools are inadequate to characterize these types of flows because the underlying assumptions of thermally stratified zones are not valid when strong horizontal flows exist. In this section, to model strongly ventilation flow driven fire-compartment combustion processes, two low dimensional models are explored: a partially stirred reactor (PaSR) and a perfectly stirred reactor (PSR) using both a fast chemistry mixture fraction driven reaction model and a chemical kinetics driven reaction models. A CFD model, FDS, is also compared to ventilation experiments

as a way to validate the CFD model. Finally the low order PaSR model is compared to an FDS simulation.

The need for the development of the PaSR model arises from limitations to CFAST and the computational expense of FDS. Since CFAST is a zone model it is most accurate in modeling compartment fires with weak or zero ventilation and is much less accurate for cases where the compartment is not strongly stratified (e.g. forced ventilation, flashover) (Jones et al., 2009). FDS is able to model the experimental temperature response both pre- and post-ventilation, however it is more computationally expensive and requires detailed knowledge of the specific problem that is being modeled.

To justify using a well-mixed (or stirred reactor) low order model to simulate species and temperature evolution in a post-ventilation compartment, data from a positive pressure ventilation experiment is examined. In particular histograms of experimental thermocouple temperature measurements and a scatter plots of the thermocouple measurements as function of elevation are examined. For this analysis all of the experimental thermocouples (32 measuring temperatures in the compartment) are used, independent of position, to generate the histogram. A bin size of 20 °C is used for the histograms shown in this section. The count in each temperature interval is divided by the total number of thermocouples to display a relative frequency. In this fashion, the histograms provide information as to the level of temperature uniformity in the compartment. The scatter plots are included to show temperature variation as a function of elevation. To characterize how PPV affects the compartment temperature distribution, the compartment is examined before and after ventilation. Figure 3.4.1 shows the temperature data 25 seconds before ventilation.
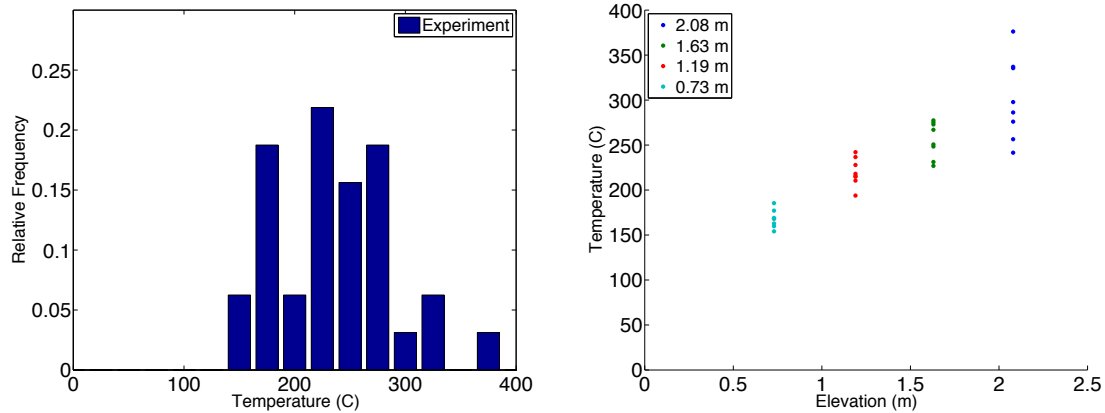
Figure 3.4.1: The plot on the left is a spatial independent histogram and the right is scatter plot of temperature as a function of height. This is 25 seconds before ventilation.

In Figure 3.4.1, 25 seconds before ventilation has occurred, the compartment temperature distribution is primarily driven by buoyancy. The histogram shows a wide temperature distribution of approximately 225 °C (150 °C to 375 °C). The scatter plot shows that the highest temperatures are at the upper elevation and the coolest temperatures are at the lowest elevation. The pre-ventilation temperature dependence on elevation illustrates a justification for using zone models for modeling non-mixed compartment fires. However, both figures show a limitation to that approximation as two distinct zones do not exist and the temperature is better described discretely or as a continuous function of elevation. To examine how the compartment temperature distribution changes due to PPV application, data 35 seconds after ventilation (Figure 3.4.2) is shown.

135
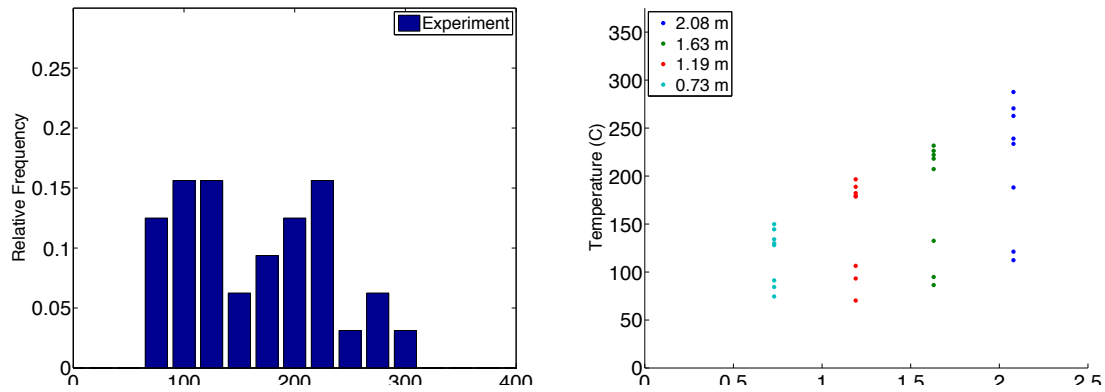
Figure 3.4.2: The plot on the left is a spatial independent histogram and the right is scatter plot of temperature as a function of height. This is 35 seconds after ventilation.

Figure 3.4.2 shows the compartment temperature distribution 35 seconds after ventilation. After ventilation, the width of the temperature distribution is approximately the same at 225 °C. However the entire distribution, now approximately between 75 °C to 300 °C, has shifted to the left indicating that the compartment has cooled. The scatter plot show two groups of temperature at each thermocouple elevation; one group shows similar values to the pre-ventilation case and the other group shows significantly lower temperatures. A more detailed examination of the group of lower thermocouple temperatures indicated that they all belonged to the thermocouple trees inline with the fan and door. Figure 3.4.3 shows the location of these thermocouple trees.
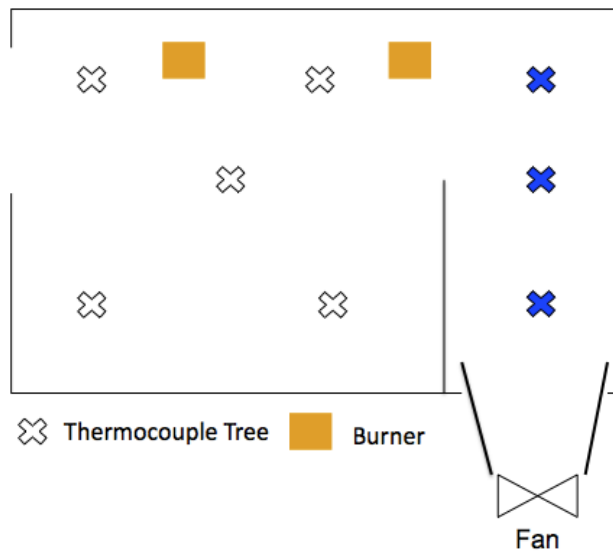
Figure 3.4.3: Plan view of the UT burn facility during a PPV experiment indicating the location of the burners and thermocouple trees. The shaded thermocouple trees are those initially impacted by PPV.

These results are important because they show how PPV initially affects compartment temperatures. There exists significant cooling in the compartment entranceway compared to only slight cooling in the remainder of the structure. Understanding how PPV application affects compartment temperature is critical for the fire service and will be discussed in greater detail in Chapter 4. To see how the compartment changes with continued PPV application, the temperature distribution 75 seconds after PPV (Figure 3.3.4) is examined.
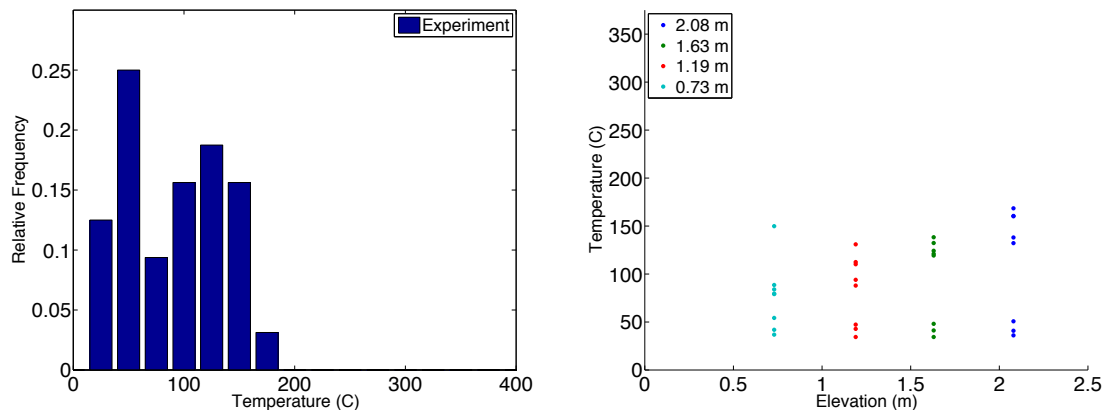
Figure 3.4.4: The plot on the left is a spatial independent histogram and the right is scatter plot of temperature as a function of height. This is 75 seconds after ventilation.

Seventy-five seconds after PPV application, the entire compartment has been cooled as shown the shift to the left of the temperature distribution. The maximum temperatures in the compartment are approximately the same as the lowest temperatures from the pre-ventilation data. Comparing these results to 35 seconds after ventilation (Figure 3.4.2), the temperature difference between the two groups of temperature shown in the scatter plot is smaller. Information about temperature variation with elevation also begins to disappear. This is because the jet from the PPV fan mixes the cool ambient air entering the compartment with products that are being driven out of the compartment. To examine PPV effects as the interior compartment conditions approach steady state, Figures 3.4.5 and 3.4.6 show the compartment temperature distributions at 125 seconds and 175 seconds after ventilation, respectively.
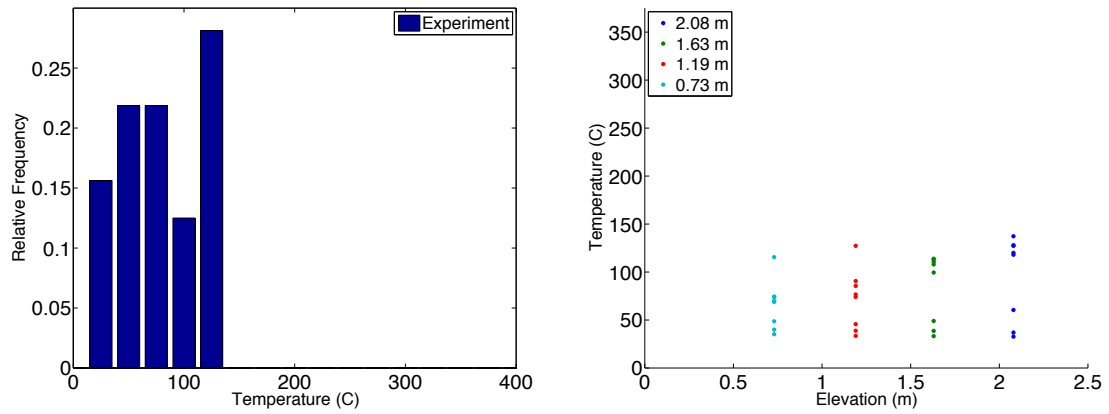
Figure 3.4.5: The plot on the left is a spatial independent histogram and the right is scatter plot of temperature as a function of height. This is 125 seconds after ventilation.
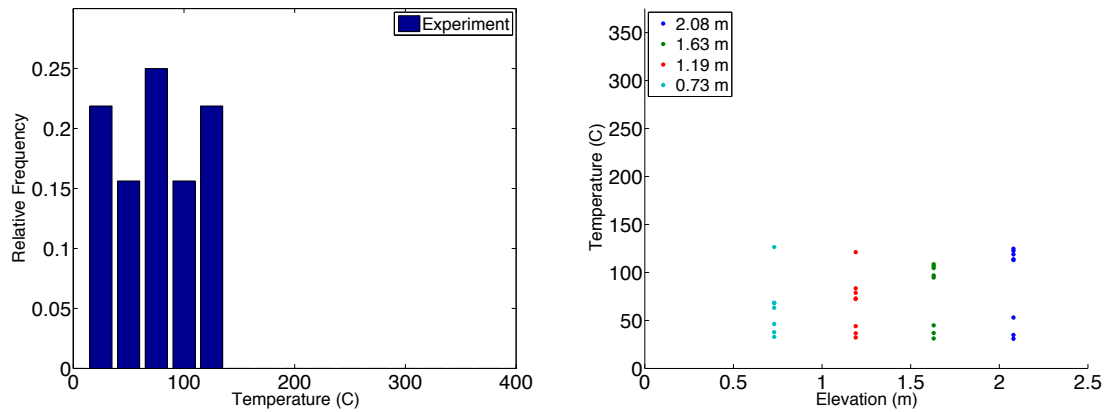
Figure 3.4.6: The plot on the left is a spatial independent histogram and the right is scatter plot of temperature as a function of height. This is 175 seconds after ventilation.

As PPV continues, the compartment becomes cooler and better mixed. This is evident by examination of the widths of the temperature distributions. A narrow temperature distribution with large relative frequencies is an indication of a well-mixed compartment. The scatter plots in Figures 3.4.5 and 3.4.6 also show that temperature is not longer a function of elevation. There is minimal change in compartment temperature

139

distribution between 125 seconds and 175 seconds after ventilation, an indication that the compartment is reaching a post-ventilation steady state. If the compartment were perfectly mixed, the distribution would be represented by a relative frequency of one for a sufficiently narrow temperature interval.

Because one anticipates that there will be no spatial variation in the temperature distribution in a post-PPV compartment, it is reasonable to imagine modeling the compartment with a partially stirred reactor model.

3.4.1 PaSR formulation for strong vent flow enclosure fires

One way to consider an enclosure fire is as a large chemical reactor, where the reaction is a combustion process (Upadhyay, 2006). Chemical reactors have previously been studied in two limiting cases: either fast reactions or fast mixing. A mixture fraction approach is generally used to describe fast reactions, as there is an instantaneous conversion of reactants to products. This method was used in FDS versions prior to Version 5.0. For chemical reactions that are slow relative to the surrounding flow, details quantifying the flow field become relatively unimportant. As a result, the flow in the reactor is generally characterized as plug flow or as continuously stirred (Upadhyay, 2006).

Resolving molecular scale processes becomes intractable in simulations of large scale fluid mechanics such as modeling strong vent flows in an enclosure. Stochastic methods are often used for describing molecular mixing and chemical reactions in these types of problems (Upadhyay, 2006). Molecular scale processes occur at length and time scales that are smaller and faster than the simulation resolution. Consequently, models and in this case stochastic models, are used to obtain information on how these processes evolve. Stochastic methods involve the solution of a PDF transport equation (Upadhyay,

2006). A PDF can carry the desired information such as species concentrations and temperatures. The use a PDF transport equation allows us to evolve the desired information in a higher dimensional space than directly solving equations on the molecular scale. A detailed account of the PDF transport method for turbulent reacting flows is given in Pope (Pope, 1985). As previously discussed using a statistical method such as Monte Carlo can be computationally expensive. Recent innovations in assumed PDF forms such as the Quadrature Method of Moments (QMOM) and Direct Quadrature Method of Moments (DQMOM) can, in principle, predict arbitrarily high moments of the true PDF (Upadhyay, 2006).

In this section the use of Direct Quadrature Method of Moments to simulate mixing and chemical reactions within an enclosure fire is investigated. The mixing and chemical reactions in the compartment are modeled as a partially stirred reactor (PaSR). A PaSR is a reactor that is characterized by perfect macromixing (i.e. no spatial gradients of the scalars) but imperfect micromixing (i.e. mixing is not complete at the molecular scale) (Upadhyay, 2006). As proof of concept, a combustion reaction mechanism that can be described in terms of fast chemistry state relations driven by the mixture fraction is considered. The PaSR results are compared to those from a perfectly stirred reactor (PSR). In a perfectly stirred reactor, the exhaust composition is identical to the internal composition of the reactor and there are no parameter variations in the composition. A PSR is essentially a PaSR with infinitely fast mixing times.

Partially stirred reactor model

It is known that one can describe turbulent combustion using the joint scalar PDF transport equation as described by Pope (Pope, 1985). In this problem, the analysis begins

with a form the equation as discussed in Fox (Fox, 2003) and Upadhyay (Upadhyay, 2006):

$$\frac{\partial f_\phi}{\partial t} + \langle U_i \rangle \frac{\partial f_\phi}{\partial x_i} = \frac{\partial}{\partial x_i}\left[\Gamma_T \frac{\partial}{\partial x_i} f_\phi\right] - \frac{\partial}{\partial \psi_i}\left[\left\langle \Gamma_i \frac{\partial^2 \phi_i}{\partial x_j \partial x_j} \vec{\psi} \right\rangle f_\phi\right] - \frac{\partial}{\partial \psi_i}\left[S_i(\vec{\psi})f_\phi\right] \qquad 3.4.1$$

The second term on the left hand side of equation 3.37 is scalar transport due to the mean flow field. The first term on the right hand side is transport from turbulent velocity fluctuations. The second term is molecular diffusion and the last term a source term for chemical reactions. In equation 3.4.1, the molecular diffusion term cannot be solved directly and therefore needs to be modeled. The Interaction by Exchange with Mean (IEM) model, which says that particle concentrations will relax to their mean values as determined by a mixing time, τ_{mix} (Dopazo, 1975) is used.

Using the IEM model in the joint scalar PDF transport equation (Eq. 3.4.1) gives:

$$\frac{\partial f_\phi}{\partial t} + \langle U_i \rangle \frac{\partial f_\phi}{\partial x_i} = \frac{\partial}{\partial x_i}\left[\Gamma_T \frac{\partial}{\partial x_i} f_\phi\right] - \frac{\partial}{\partial \psi_i}\left[\left(\frac{\psi_i - \langle \psi_i \rangle}{\tau_{mix}}\right) f_\phi\right] - \frac{\partial}{\partial \psi_i}\left[S_i(\vec{\psi})f_\phi\right] \qquad 3.4.2$$

Equation 3.4.2 can be modified to fit the problem of modeling a PaSR by applying the definition that there are no spatial gradients, i.e., f_ϕ is not a function of spatial vector $\boldsymbol{x}$. The lack of spatial gradients in a fire compartment with strong ventilation was shown to be valid in the previous section. Therefore, equation 3.4.2 can be integrated over the compartment volume, to develop equation 3.4.3 (Upadhyay, 2006):

$$\frac{\partial \tilde{f}}{\partial t} = -\frac{\tilde{f}}{\tau_{res}} + \frac{1}{\tau_{res}}\left[P\tilde{f}^{(ox)} + (1-P)\tilde{f}^{(fuel)}\right] - \frac{\partial}{\partial \psi_i}\left[\left(\frac{\psi_i - \langle \psi_i \rangle}{\tau_{mix}}\right)\tilde{f}\right] - \frac{\partial}{\partial \psi_i}\left[S_i(\vec{\psi})\tilde{f}\right] \qquad 3.4.3$$

The first and second terms on the right hand side represent the outflow and inflow at the boundaries of the reactor/compartment. These terms model the large scale mixing (i.e., macromixing). The third term is the micromixing model, which is formulated using

142

the IEM. Following Upadhyay, the mesomixing term is neglected for simplicity (Upadhyay, 2006). This term is usually neglected in PaSR models as it would require the turbulent diffusivity and the spatial gradient of $\tilde{f}$ at the boundaries. For this application of a PaSR model the source fire is a gas burner with a known, constant mass flow rate of fuel. This is typical of experimental compartment fires and is the same technique used in the reacting flow experiments conducted at the UT burn facility. The same fuel (propane) is used for the model as in the experiments. The parameter equations that govern this problem follow those used by Upadhyay (Upadhyay, 2006). The gas exchange time can be considered a residence time $\tau_{res} = \dfrac{m}{\dot{m}_{air} + \dot{m}_{fuel}}$. Here m is the mass of gas inside the reactor/compartment and $\dot{m}_{air}, \dot{m}_{fuel}$ are inlet mass flow rates of the air and fuel respectively. The fuel flow rate fraction is defined by $P = \dfrac{\dot{m}_{fuel}}{\dot{m}_{air} + \dot{m}_{fuel}}$. The inlet flow equivalence ratio is then given by $\phi = \dfrac{P}{P_{st}}$ where P_{st} is the value for which the inflow mixture is in stoichiometric proportions. $\tilde{f}^{(ox)}$ and $\tilde{f}^{(fuel)}$ are the fuel and oxidizer PDFs at the inlet. In this case, it is assumed that there are no fluctuations in the fuel and oxidizer concentrations at the inlet and therefore $\tilde{f}^{(ox)}$ and $\tilde{f}^{(fuel)}$ are defined by delta functions.

$$\tilde{f}^{(ox)} = \delta(\psi_{ox} - \psi_{ox}^{(O)}) \prod_{\alpha \neq ox} \delta(\psi_\alpha - 0)$$

$$\tilde{f}^{(fuel)} = \delta(\psi_{fuel} - \psi_{fuel}^{(F)}) \prod_{\alpha \neq fuel} \delta(\psi_\alpha - 0)$$

3.4.4

where $\psi_{ox}^{(O)}$ is the concentration oxidizer at the inlet oxidizer stream and $\psi_{fuel}^{(F)}$ is the concentration of fuel at the inlet fuel stream. Continuing to follow Upadhyay (Upadhyay, 2006) residence time can be scaled by time, $t^* = t/\tau_{res}$ and 3.4.3 can be written in a form that shows the effect of the chemical, mixing and residence time scales.

143

$$\frac{\partial \tilde{f}}{\partial t^*} = -\tilde{f} + \left[P\tilde{f}^{(ox)} + (1-P)\tilde{f}^{(fuel)} \right] - \frac{\partial}{\partial \psi_i}\left[\left(\frac{\tau_{res}}{\tau_{mix}}\right)\left(\psi_i - \langle\psi_i\rangle\right)\tilde{f} \right] - \frac{\partial}{\partial \psi_i}\left[\tau_{res}S_i(\vec{\psi})\tilde{f} \right] \qquad 3.4.5$$

The mixing can be controlled by varying the mixing time scale τ_{mix} at fixed τ_{res}, the flow rate proportions can be controlled by varying P, and the chemical time scale can be changed by changing the residence time, τ_{res} or the chemical source term, $S_i(\vec{\psi})$. A schematic of a PaSR for this problem is included in Figure 3.4.7.
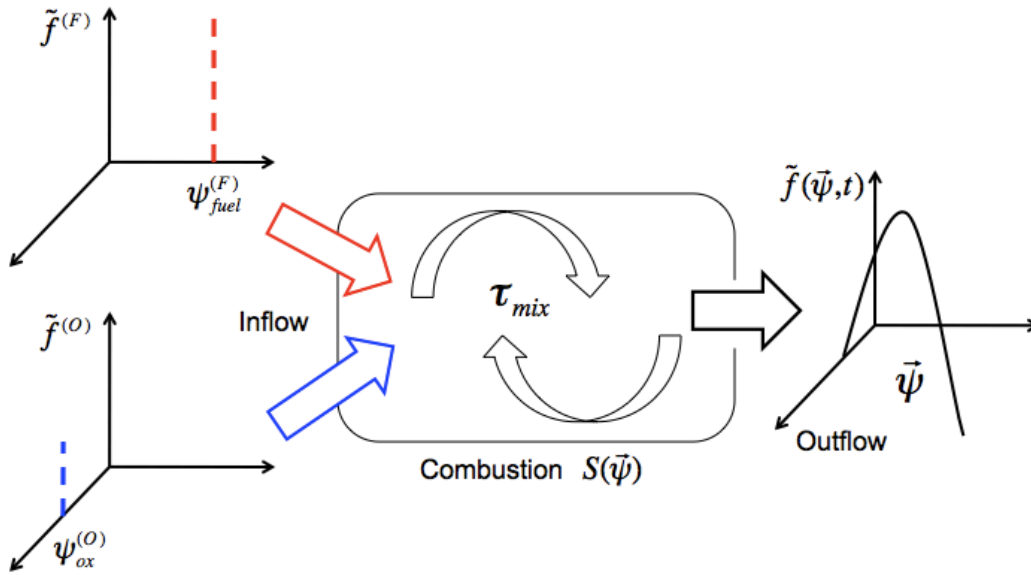
Figure 3.4.7: Schematic of a PaSR showing the delta function fuel and oxidizer inlets (left), mixing and combustion inside the reactor (center) and the reactor/product stream multidimensional distribution of species.

On the left of Figure 3.4.7 are the inflow streams of fuel and oxygen. In this formulation they are represented as delta functions, though they can be distributions. Inside the compartment, the species mix toward their respective mean values based on the defined mixing time to residence time ratio and the combustion reaction is governed by the chemical source term. The outflow is a multivariate distribution based on inflow

species and combustion product species. Since the compartment is well mixed (or partially stirred) the outflow is essentially the same as the compartment composition.

To evolve the governing PDF transport equation of the PaSR (equation 3.41), the direct quadrature method of moments (DQMOM) is used as described by Fox (Fox, 2003). As discussed in Section 1.3, a common issue with using a moment method to solve this type of problem is the closure problem associated with needing moments that are not explicitly defined by the solution. The use of DQMOM avoids this problem by using Gaussian quadrature to determine the unclosed terms. This solution is based on representing the PDF as:

$$f_\phi(\vec{\psi};\vec{x},t) = \sum_{i=1}^{N_Q} W_i(\vec{x},t) \prod_{j=1}^{d} \delta(\psi_j - \hat{\psi}_{j,i}(\vec{x},t)) \qquad 3.4.6$$

where $W_i(\vec{x},t)$ is the *i-th* quadrature weight and $\psi_{j,i}(\vec{x},t)$ is the *i-th* quadrature point of the *j-th* variable. Equation 3.4.6 can be substituted into the governing PDF scalar equation (equation 3.4.5) following Fox (Fox, 2003). Evolution equations are then solved in terms of quadrature weights and the product of the quadrature weights and points.

To solve the PDF scalar equation describing the PaSR, an open source library, libMOM (Upadhyay & Ezekoye, 2011) is used. The libMOM library is designed to solve stochastic differential equations using quadrature-based method of moments. It features functions that if given a PDF, it can determine the moments of a distribution, calculate the points and weights from the moments and evolve the governing PDF transport equation in time.

Chemical reaction model

Propane combustion is used since propane is a frequently used fuel in compartment fire experiments and it was the fuel used in the UT reacting flow experiments. The global one step mechanism for propane is shown below.

$$C_3H_8 + 5O_2 + 18.8N_2 \rightarrow 3CO_2 + 4H_2O + 18.8N_2 \qquad\qquad 3.4.7$$
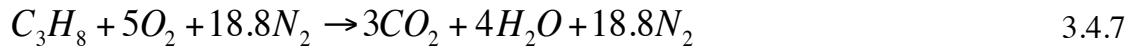
Univariate PaSR with chemical equilibrium

The work in this section is largely based on previously published work by this author at the 7th US National Combustion Institute Meeting (Weinschenk, Upadhyay, & Ezekoye, 2011)

For a typical PPV fan driven compartment fire, the exit window flow velocity is approximately 4 m/s and the exhaust mass flow rate is approximately 2 kg/sec, assuming a 600 K average temperature exhaust. For a compartment of characteristic dimension of 72.5 m^3, this represents an approximate 7-second residence time. A major issue in the implementation of the PaSR model is the specification of a micromixing time. The micromixing time is ideally taken from a CFD simulation of the flow for the problem of interest. To a rough approximation, one might scale the micromixing time in a room through which a 2 m/s door flow takes place as being inversely proportional to a characteristic turbulent velocity (e.g., the square root of the specific kinetic energy) and proportional to a characteristic eddy length scale (e.g., the door width of 1 m). In such a case, an estimate for the micromixing time would be 0.5 sec. One immediately sees that the residence time is 14 times larger than the mixing time. In addition, the other time scale in the problem is the chemical reaction time. Chemical reaction times for adiabatic combustion are considerably faster than either the residence or micromixing time.

In the fast chemistry limit, a mixture fraction approach gives rise to a univariate problem (d = 1). The mixture fraction can be used to describe the evolution of the system. The mixture fraction, Z, is defined to be 0 in air and 1 for pure fuel. The intermediate values represent the various degrees of mixing. Instead of explicitly using a kinetic mechanism to drive the reaction, in this PaSR formulation an equilibrium approach is used. As a result, the chemical source term in equation 3.4.5 is neglected. Since a progress variable is not needed to drive the reaction as is common in the traditional mixture fraction approach with a kinetic mechanism, the problem becomes univariate. To determine the compartment temperature from mixture fraction an equilibrium code, CEA (McBride & Gordon, 1996) is used.

For this model problem a case where the fire compartment is fuel rich and at an elevated temperature prior to ventilation is examined. This type of condition is such that upon ventilation, backdraft or flame-over conditions could occur. Backdraft is extremely dangerous because unburnt products in the compartment when suddenly mixed with air (ventilation) can rapidly burn if exposed to an ignition source. This rapid burning forms a flame front which moves through the compartment toward the exit (lower pressure, oxygen supply) and can result in a fire ball at the vent location (Gorbett & Hopkins, 2007). Flame-over is when sufficient unburned fuel accumulates, typically along the ceiling of an enclosure, and ignites if there is sufficient oxygen (Gorbett & Hopkins, 2007). This can happen without an ignition source if the temperatures are high enough. Flame-over typically happens in under-ventilated compartments where the conditions allow for unburned fuel to accumulate.

Using a residence time of 7 seconds, which is typical for a compartment fire, Figure 3.4.8 shows the temporal evolution of the mean mixture fraction for three different mixing time to residence time ratios, holding the residence time constant.
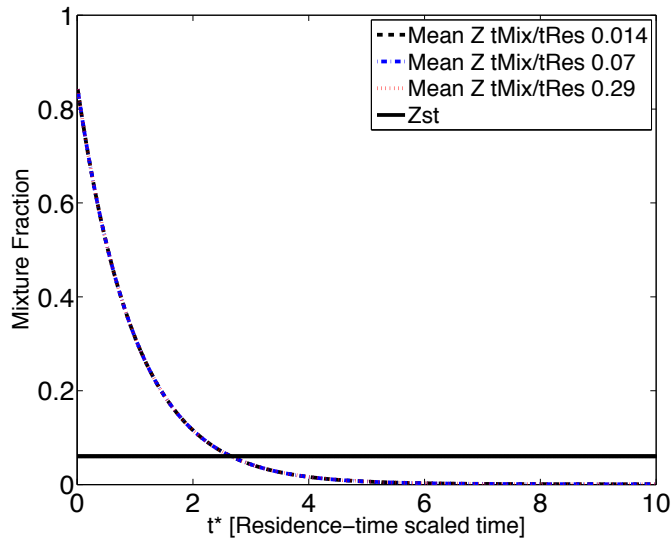
Figure 3.4.8: Mean mixture fraction evolution for three different mixing time to residence time ratios. The horizontal line is the stoichiometric mixture fraction (0.06) based on the propane reaction discussed in section 3.4.2.

The compartment was initially fuel rich, $<Z>=0.85$ where the stoichiometric mixture fraction for propane is 0.06. The initial condition was set to simulate a ventilation-controlled fire (there is more pyrolyzed fuel in the compartment than oxygen available for combustion). At $t^*=0$, a fuel/air mixture with an equivalence ration of 0.012 flows into the compartment. The mean mixture fraction in the compartment drops from fuel rich to a fuel lean mean in approximately 2.5 residence times. By 6 residence times the compartment composition has reached a steady state condition. With a mean mixture fraction of $<Z> = 7x10^{-4}$, this indicates that the compartment is mostly air. It is interesting to note that the mean value of mixture fraction is independent of the mixing

148

time to residence time ratios. Mean values are expected to be the same as this quantity is driven by the problem physics (initial compartment mixture, inflow mixture fraction, and residence time), which were held constant. Higher order moments such as variance/standard deviation, will be different as mixing time changes. To understand how higher order moments may be affected; the evolution of the quadrature points and quadrature points of mixture fraction (Figure 3.4.9) are examined.
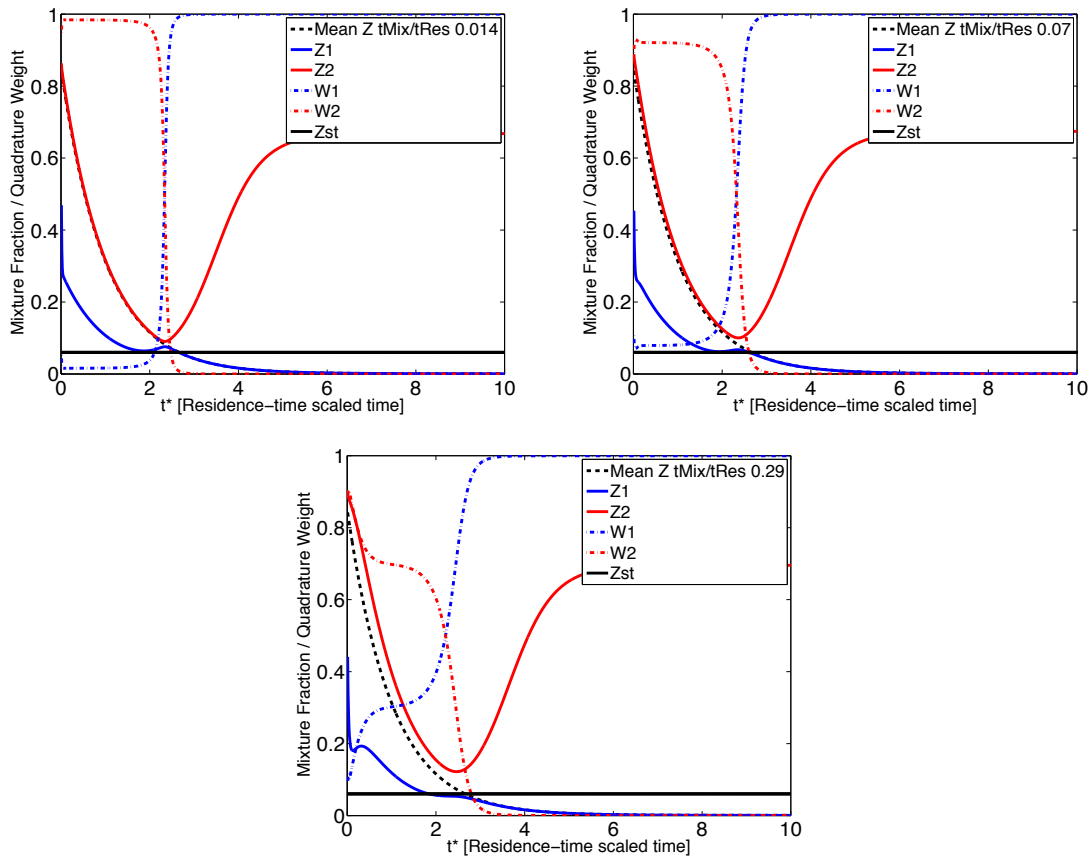
Figure 3.4.9: Quadrature point ($\hat{Z}_1$ and $\hat{Z}_2$), quadrature weight (W_1 and W_2) and mean mixture fraction evolution for three mixing time to residence time ratios: $\tau_{mix}/\tau_{res} = 0.014$ (top left), $\tau_{mix}/\tau_{res} = 0.07$ (top right) and $\tau_{mix}/\tau_{res} = 0.29$ (bottom middle).

Figure 3.4.9 shows the evolution of the quadrature points ($\hat{Z}_1$ and $\hat{Z}_2$) and the quadrature weights (W_1 and W_2) for increasing mixing time to residence time ratios (as the ratio increases, the compartment becomes less mixed). From the definition standard deviation with respect to moments:

$$\sigma = \sqrt{M_2 - M_1^2}$$ 3.4.8

the first two moments are needed. These moments can be found from quadrature points and weights:

$$M_1 = W_1\hat{Z}_1 + W_2\hat{Z}_2$$
$$M_2 = W_1\hat{Z}_1^2 + W_2\hat{Z}_2^2$$ 3.4.9

If M_1 is squared following equation 3.4.9 we get:

$$M_1^2 = W_1^2\hat{Z}_1^2 + 2(W_1\hat{Z}_1)(W_2\hat{Z}_2) + W_2^2\hat{Z}_2^2$$ 3.4.10

For the standard deviation in the compartment to be minimized, W_1 or W_2 needs to approach zero. By definition $W_1+W_2=1$, therefore, if one of the weights becomes very small then the other weight approaches 1 and M_1^2 looks like M_2. This minimizes standard deviation. Standard deviation is also minimized if the weights and points approach the same value. This would mean that the compartment has a uniform distribution.

For the mixing time ratio of 0.014 (upper left plot) the second quadrature weight (W_2) is initially dominant while the first quadrature weight remains small. With a single dominant weight, the compartment composition follows that of the corresponding qaudrature point. This is shown as the second quadrature point sits directly on top of the mean value. If a quadrature point sits on top of the mean value it indicates that the compartment is very well mixed. As the simulation moves forward in time, there is a shift in the dominant weight just after 2 residence times as the mean mixture fraction approaches the stochiometric value. This shift happens as the initial fuel charged compartment becomes overcome by the fuel lean inflow conditions. The shift in weights

150

is sharp and the first quadrature weight approaches 1, becoming the dominant value. The first quadrature point becomes representative of the mean compartment value. The evolution of the weights show that there is minimal variance in the initial mixture fraction and it decreases at long times.

Figure 3.4.9 shows that as the mixing time increases, there is more significant variance in composition. Neither quadrature weight is insignificant and the two quadrature points have different values. For the two slower mixing cases the same long time compartment composition statistics as compared to the fast mixing case. This is because without a chemical reaction term explicitly in the PaSR model the compartment composition is only a function of mixing and the inflow/outflow parameters. For this problem, the inflow is defined by delta functions, meaning no statistical variation. Therefore at long times when the initial mixture has exited the compartment, mixing no longer plays a role, leading to the same values. To better quantify the effects of mixing on composition, Figure 3.4.10 shows standard deviation of mixture fraction as a function of time for several mixing to residence time ratios.
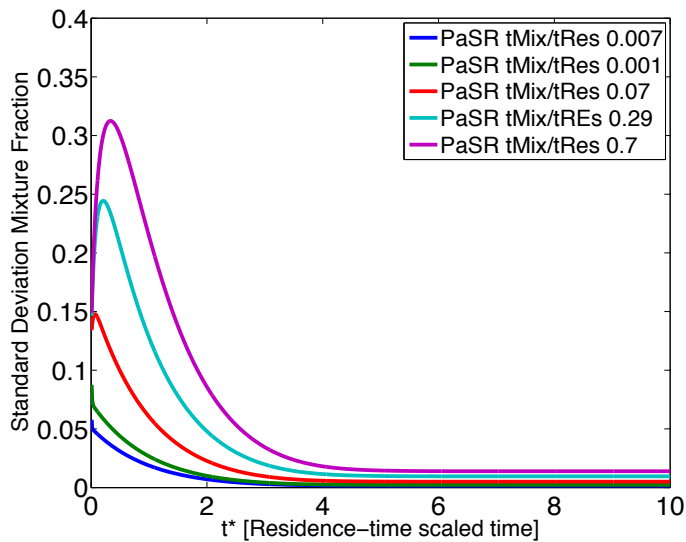
Figure 3.4.10: Standard deviation of mixture fraction versus time for 5 mixing time to
residence time ratios.

From the previous discussion relating mixing time to statistical uncertainty in
compartment composition, Figure 3.4.10 shows how mixture fraction standard deviation
varies. As mixing within the compartment decreases, there is an increase in the peak
standard deviation and a delay in t^*, when that peak occurs. It is important to recognize
the trend in composition uncertainty as a function of mixing time to residence time ratio
because in this formulation temperature is a function of mixture fraction. For example, if
the compartment is not well mixed, $\tau_{mix}/\tau_{res} = 0.7$, an uncertainty in composition leads to
an uncertainty in temperature. This is particularly important for the fire service entering a
poorly mixed, fuel charged structure. Large uncertainties in temperature increase the risk
for those inside the compartment.

To determine temperature from mixture fraction an equilibrium code, CEA is
used. For fuel to air ratios that are greater than stoichiometric ($\phi > 1$) a temperature of
600 K for the equilibrium calculations is used based on an average exhaust temperature

152

from CFD simulations and experiments. For fuel to air ratios that are less than stoichiometric ($\phi < 1$) an ambient temperature of 313 K is used, which is based on the inlet air temperature. Once a map from mixture fraction to temperature was developed, the temperature evolution within the compartment can be examined. Figure 3.4.11 shows the mean temperature evolution and ± 1 standard deviation in temperature for a fast and slow mixing case.
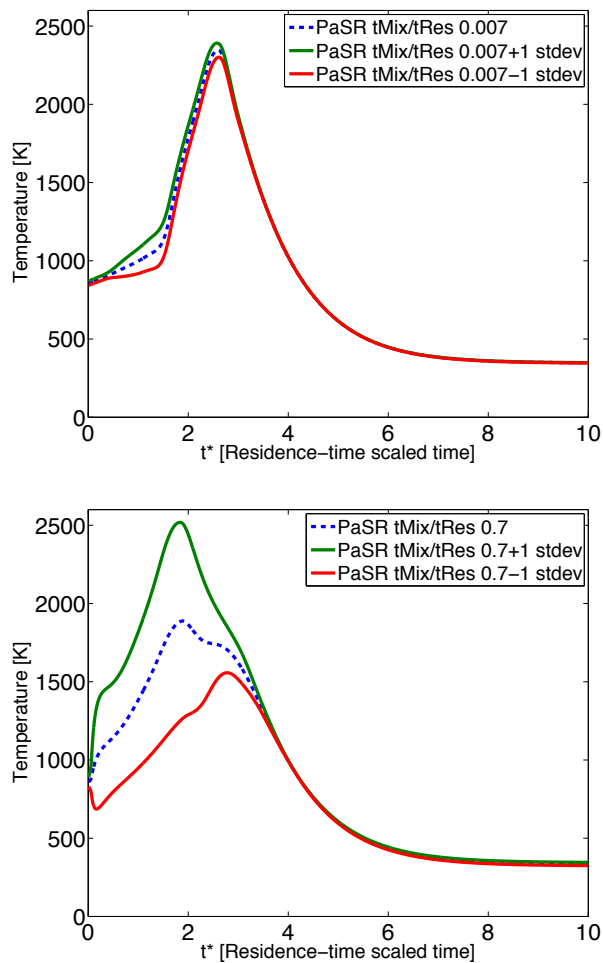
Figure 3.4.11: Time evolution of mean compartment temperature ± 1 standard deviation for a fast mixing time $\tau_{mix}/\tau_{res} = 0.007$ (top) and a slow mixing time $\tau_{mix}/\tau_{res} = 0.7$ (bottom).

As shown previously in Figure 3.4.8, the mean compartment mixture fraction begins at a mean mixture fraction of 0.85. The gas temperature is at a typical enclosure fire exhaust value of approximately 600 K. With the initiation of ventilation, the mixture fraction drops, passing through the stoichiometric value before reaching 7×10^{-4}, the mixture fraction value associated with the inlet mixture equivalence ratio of 0.012. When the compartment mixture fraction is near the stoichiometric value, the temperature increases towards a burned gas temperature. Beyond the stoichiometric value, the average temperature then decreases. Figure 3.4.11 shows two additional curves that indicate the uncertainty in the temperature at one value of the standard deviation. The concern for firefighters is that it is generally not known when an increase in temperature (uncertainty in temperature) will occur or when the temperature will peak. It is interesting to note that with better mixing (more effective PPV), the time and magnitude over which these high temperature excursions occur is reduced. Conversely, with smaller and weaker fans, it is possible that firefighters do not know that a significant temperature rise is impending and thus they could enter the structure and be engulfed in the rapidly reacting mixture.

To better quantify how standard deviation varies with mixing time, the standard deviation is plotted for 5 different mixing time to residence time ratios (Figure 3.4.12). The standard deviation in the temperature is shown to achieve a minimum value at long times, after the compartment mixture becomes a function of only the inlet flow. These results show that the standard deviations are larger for slower mixing times, which makes sense since the compartment is not as well mixed. A problem with slow mixing is that it decreases our confidence in predicting compartment conditions, specifically during the transition from under ventilated fire to an over vented one. This is a common problem encountered by firefighters when assessing changes in fire behavior after implementing a fan.

154
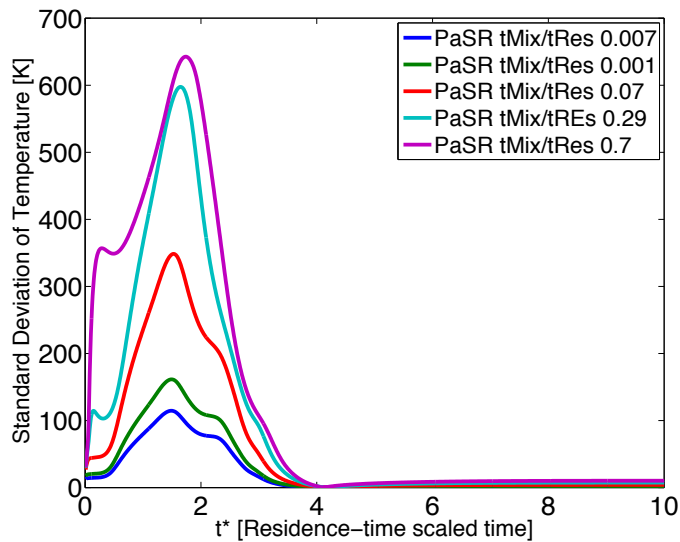
Figure 3.4.12: Time evolution for standard deviation of temperature for varying mixing time to residence time ratios.

To check the accuracy of results from the PaSR model, cross-code validation is performed with a perfectly stirred reactor (PSR). To generate the PSR results we use Cantera, a chemical kinetics software package (Goodwin, 2002). A perfectly stirred reactor is similar to a PaSR except that mixing is infinitely fast, eliminating statistics within the reactor. For slow PaSR mixing times differences are expected between two models, however as mixing is increase in the PaSR model, the results should start to resemble the PSR model.

Using the same reactor parameters, temperature evolutions are shown in Figure 3.4.13, comparing the PSR case to several mixing time to residence time ratios of a PaSR. For both models, the inlet flow fuel-to-air flow rates are governed by an equivalence ratio of 0.012.
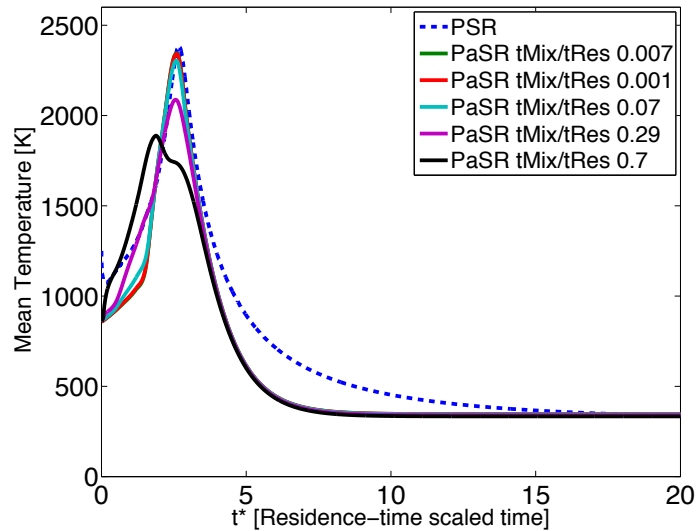
Figure 3.4.13: Temperature evolution comparison for a perfectly stirred reactor to a partially stirred reactor with 5 mixing time to residence time ratios.

Figure 3.4.13 shows that the mixture fraction PaSR model compares well the PSR results. At the fastest mixing time ($\tau_{mix}/\tau_{res} = 0.007$) the PaSR peak mean temperature matches the PSR both in time and temperature magnitude. As the mixing rate is decreased, the peak temperature decreases and at slowest mixing time ($\tau_{mix}/\tau_{res} = 0.7$) the peak temperature occurs earlier than all of the other cases. This illustrates the danger with poor mixing (undersized PPV fans), as the temperature trends no longer follow the same curves of the faster mixing cases. At long times (18-20 residence times) all of the PaSR temperatures and the PSR temperature decrease to the ambient inlet conditions of 313 K. The PSR has initial conditions of 1000 K as compared to the 600 K of the PaSR model. The higher temperature was necessary to provide sufficient energy in the system for the kinetic reactions in the PSR to start. While the heating and cooling of PaSR cases differ from the PSR model, the differences could be improved with a more detailed mixture fraction to temperature map in the PaSR. However, since future iterations of this PaSR

156

will include the chemical sources terms, these differences are acceptable. Overall, the macroscopic comparison of the PaSR model to a PSR model shows that the PaSR formulation can be used for compartment fire modeling.

Multivariate PaSR with one step chemistry

In this section the PaSR model is expanded by including the chemical source terms in the PDF transport equation. A one step kinetic mechanism is used which allows us to examine finite chemistry effects such as ignition and extinction. Propane is again used as the fuel and the one step propane combustion reaction terms come from work conducted by Westbrook and Dryer (Westbrook & Dryer, 1981). Instead of using the mixture fraction to describe the fuel and oxygen concentrations as was used in the univariate case, the mass fractions of the species of interest are tracked. For this problem oxygen ($Y=Y_{02}$), fuel ($Y=Y_{fuel}$), and products ($Y=Y_{prod}$) are considered. For conservation of mass purposes, nitrogen ($Y=Y_{N2}$) is defined as $1-Y_{O2}-Y_{fuel}-Y_{prod}$. The mass fraction of carbon dioxide and water vapor in the product stream can be determined by multiplying the product mass fraction by the respective product species stoichiometric mass fractions. This formulation gives rise to a multivariate problem (*d=3*). By directly using species mass fractions, a chemical source needs to be defined for each of the species being tracked. The chemical source terms are defined as:

$$S_{fuel} = \frac{1000W_{fuel}}{\langle\rho\rangle Y_{fuel}^{(F)}} A[F]^a[O]^b \exp\left(\frac{-E_a}{R\psi_T}\right)$$

$$S_{ox} = \left(\frac{\upsilon_{ox}W_{ox}}{\upsilon_{fuel}W_{fuel}}\right)S_{fuel} \qquad\qquad 3.4.11$$

$$S_{prod} = \left(\frac{\upsilon_{CO_2}W_{CO_2} + \upsilon_{H_2O}W_{H_2O}}{\upsilon_{fuel}W_{fuel}}\right)S_{fuel}$$

where $[F] = \left(\dfrac{\rho Y_{fuel}}{W_{fuel}}\right)$ & $[O] = \left(\dfrac{\rho Y_{ox}}{W_{ox}}\right)$ are molar concentrations of fuel and oxygen

(gmol/cm^3). The reaction parameters are defined as the pre-exponential factor, $A = 8.6 \times 10^{11}$, the activation energy, $E_a = 30.0$ (kcal/mol), and exponents, $a = 0.1$, and $b = 1.65$ (Westbrook & Dryer, 1981). Temperature, ψ_T (K), is defined as:

$$\psi_T = (T_{ad} - T_{init}) \dfrac{Y_{prod}}{Y_{prod.max}} + T_{init} \qquad \text{3.4.12}$$

where T_{ad} is the adiabatic temperature and the maximum products ($Y_{prod,max}$) is defined as the products produced when the reaction is stoichiometric. Note that in the implementation of this formulation, the chemical source terms for fuel and oxygen are negative as they are actually sinks that govern the consumption of the species. The product chemical source term is positive as it governs species production. The equations are also defined such that if the concentration of oxygen or fuel goes to zero the source terms all go to zero, turning off the reaction.

To check the predictions of this PaSR formulation, the species means are compared to results from Upadhyay who examined a PaSR using a mixture fraction – progress variable formulation (Upadhyay, 2006). In this model problem the compartment is initially composed of air and the inflow is a stoichiometric mixture of air and propane. The residence time, τ_{res}, is set at 0.1 second and two different mixing times, τ_{mix}, are examined: 0.1 second and 0.01 second. The inlet temperature is set at 700 K. Figure 3.4.14 shows the model comparisons for the mixing time of 0.1 second and Figure 3.4.15 shows the results for the mixing time of 0.01 second.
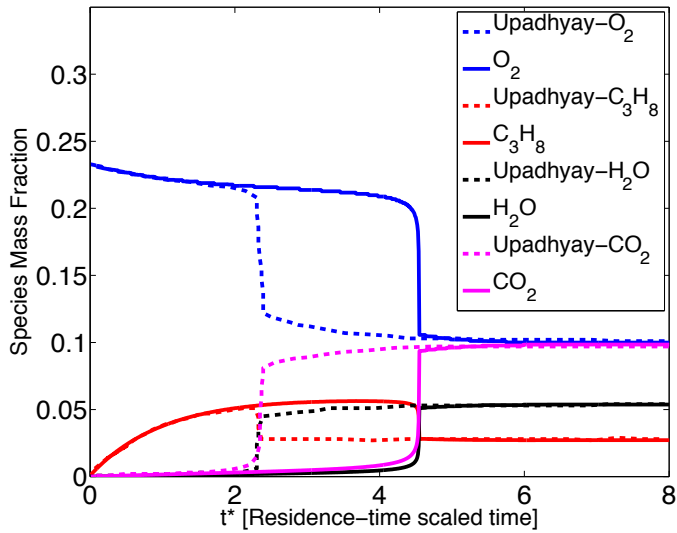
Figure 3.4.14: Comparison of species mean mass fractions from a multivariate single step PaSR (solid) to work conducted by Upadhyay (dashed) (Upadhyay, 2006) with $\tau_{res}=0.1$ second and $\tau_{mix}=0.1$ second.
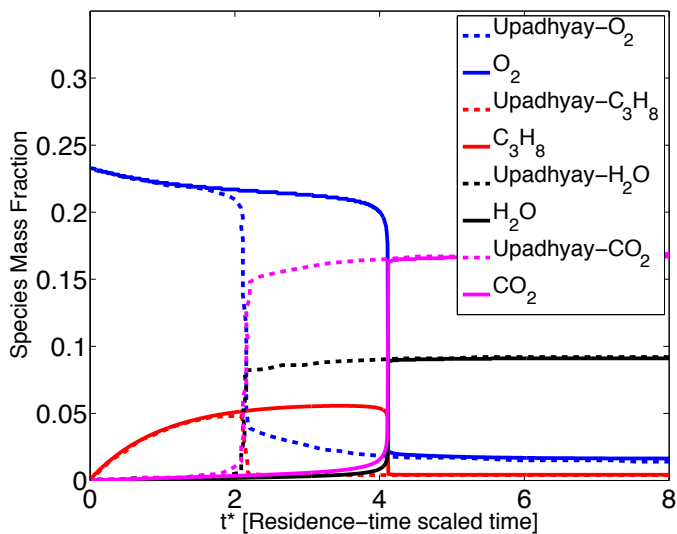
Figure 3.4.15: Comparison of species mean mass fractions from a multivariate single step PaSR (solid) to work conducted by Upadhyay (dashed) (Upadhyay, 2006) with $\tau_{res}=0.1$ second and $\tau_{mix}=0.01$ second.

Looking at Figures 3.4.14 and 3.4.15, the compartment is initially air and as the simulation progresses fuel enters the compartment. The mass fraction of oxygen drops because the compartment is no longer pure air. As the simulation progresses there becomes a point at which there is enough fuel and oxygen at a sufficient temperature for the reaction to occur. This is shown in the plots in the rapid consumption of fuel and oxygen and rapid generation of products. Note that this occurs in Upadhyay's model approximately 2 residence times earlier than in the PaSR formulation developed here. One possible factor for this difference is definition of the temperature function within the model. Temperature is one of the drivers for the reaction to occur. From thermodynamics it is known that temperature is tied to the specific heat of the mixture. In this temperature model, specific heat is set through the specification of the adiabatic temperature. If the adiabatic temperature is increased, the relationship relating temperature to products increases (i.e. increase product generation). A higher compartment temperature leads to an earlier rapid reaction front. The impact of adiabatic temperature is shown in Figure 3.4.16
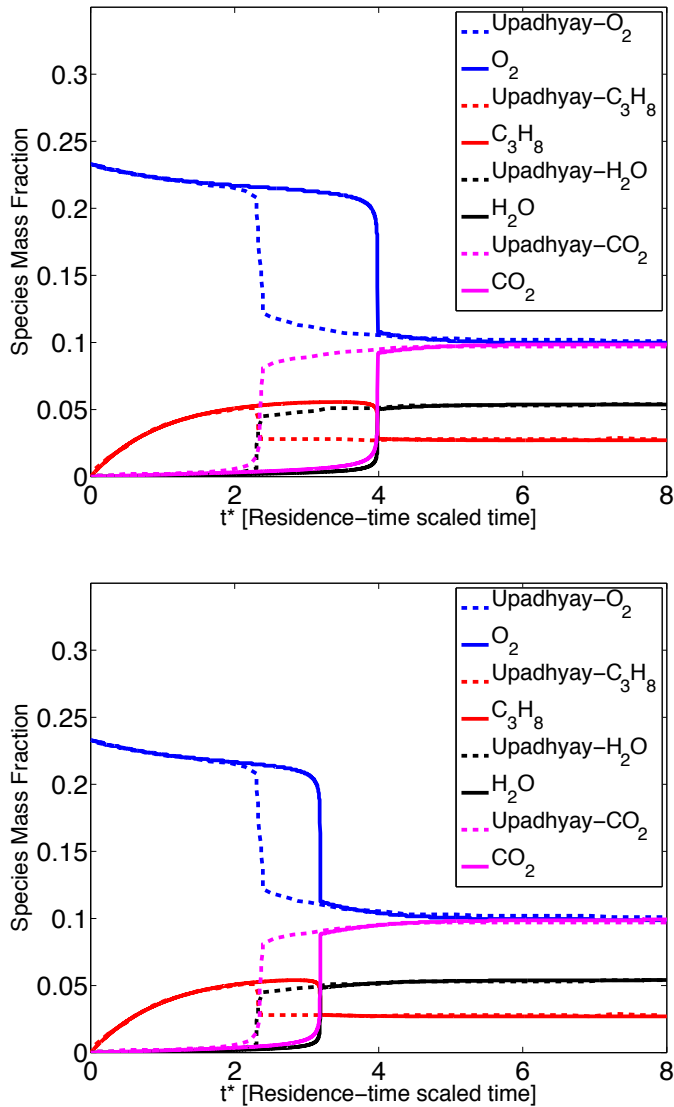
Figure 3.4.16: Comparison of the PaSR model (solid) with increased adiabatic temperature: 100 K (top) and 300 K (bottom) to results from Upadhyay (dashed) (Upadhyay, 2006) with $\tau_{res}=0.1$ second and $\tau_{mix}=0.1$ second.

Comparing the results from Figure 3.4.16 to Figure 3.4.14, the reaction times starts to approach that of Upadhyay (Upadhyay, 2006). There is a limit to this type of modification as there is a finite range of adiabatic temperatures that could be applicable to this problem.

The PaSR mean mixture fraction results for both mixing times compare well to the stationary state results presented in Upadhyay (Upadhyay, 2006). Figures 3.4.14 and 3.14.15 also show how mixing affects compartment composition. The mixing rate affects both the time occurrence of the reaction front and the stationary state compartment composition. For the faster mixing case, the reaction front occurs earlier and more oxygen and fuel are consumed in the reaction. For infinitely fast mixing (e.g., PSR formulation), all the fuel and oxygen would be consumed and converted into products, as the inflow is stoichiometric. However, in both of the cases examined (Figure 3.4.14 and Figure 3.4.15) there is a finite mixing time and therefore variation in compartment composition. Since the PaSR is a stochastic model, predicting and quantifying species variances are equally as important as their mean values. For faster mixing times it is expected that the variation in species will be smaller. To check the species variances in this PaSR model the results are compared to work from Upadhyay. Figure 3.4.17 compares species variance for a τ_{res}=0.1 second and τ_{mix}=0.01 second.
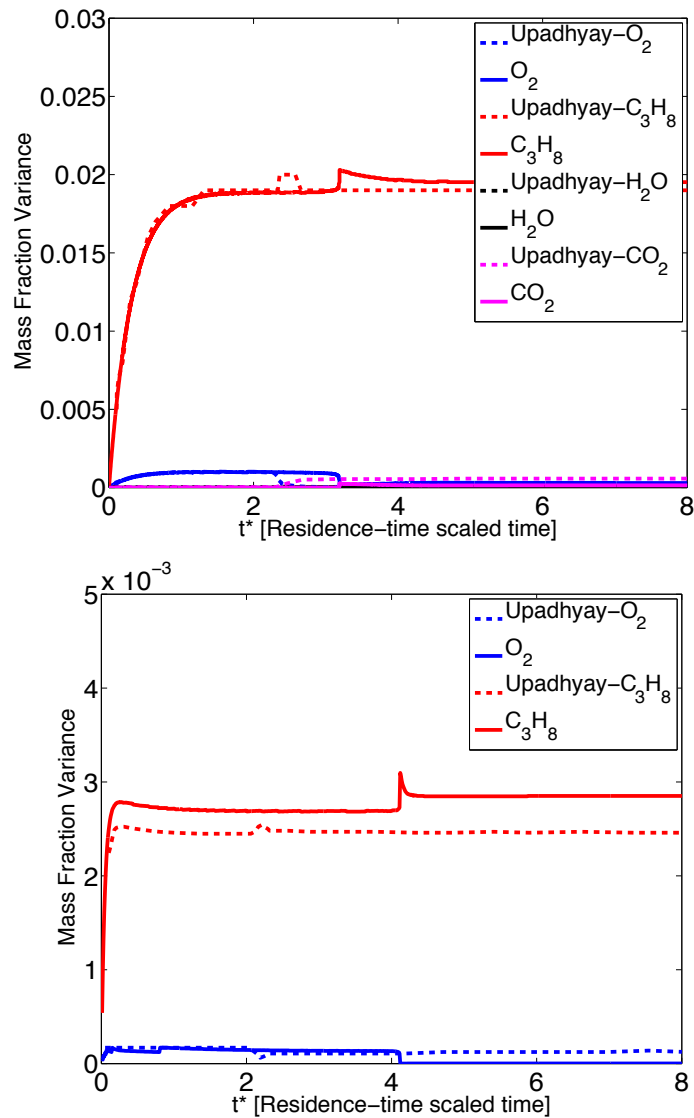
Figure 3.4.17: Comparison of species mass fraction variances from a multivariate single step PaSR (solid) to work conducted by Upadhyay (dashed) (Upadhyay, 2006) with $\tau_{res}=0.1$ second and $\tau_{mix}=0.1$ second (top) and $\tau_{mix}=0.01$ second (bottom).

Experimental work studying PPV has shown that while the forced ventilation mixes the compartment, there is still variation in temperature. Therefore, it is extremely important for this model to be able to characterize the variation or standard deviation of

163

species. Species mass fraction variances compare well to the previous work conducted by Upadhyay for both mixing times (Figure 3.4.17). For the faster mixing time, the species variation decreases by an order of magnitude. This is important because smaller variations lead to greater confidence in predicting compartment composition using this model.

A final element of this analysis is to examine how temperature is affected by mixing time. Based on equation 3.4.12, temperature is a function of the mass fraction of products. For fast mixing times when more products are produced higher temperatures are expected. Figure 3.4.18 shows the mean temperature evolution with standard deviations for the two mixing times discussed above.
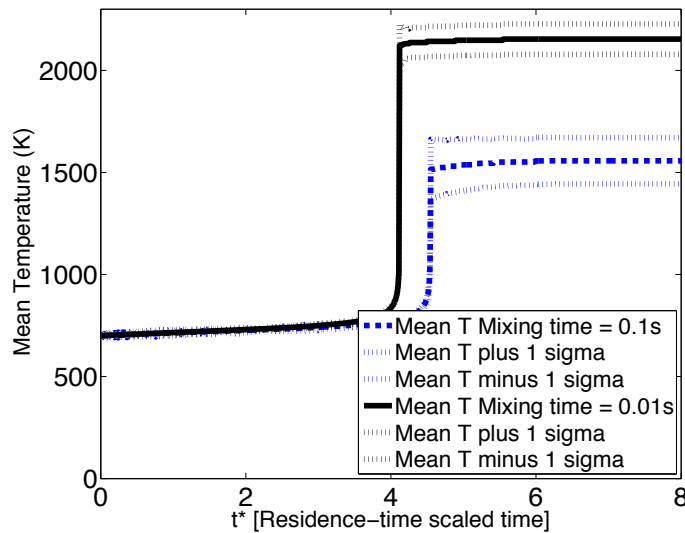
Figure 3.4.18: Comparison of mean compartment temperature with ± 1 standard deviation as a function of mixing times (τ_{mix}=0.1 second and τ_{mix}=0.01 second) with constant τ_{res}=0.1 second.

The temperature plot shows that for the faster mixing time there is a higher temperature and a smaller standard deviation. This response was expected based on examination of species mass fractions and that temperature is tied to the mass fraction of

products. In both cases the temperature starts at the inlet 700 K and gradually increases indicating that some fuel and oxygen are being consumed and products are being produced. A rapid increase in temperature is seen when there is sufficient fuel, oxygen, and products to fully drive the reactions defined by the chemical source terms. The temperature remains constant as the inflow remains in stoichiometric proportions.

Comparing FDS to PaSR

The next step to analyzing the PaSR model is to compare PaSR results to FDS results for a model problem. For this example a 0.125 m^3 compartment is used (0.5 m by 0.5 m by 0.5 m) that is initially filled with air. Fuel and air flow into compartment in stoichiometric proportions with mass flow rates that set a 1 second residence time. Based on the mass flow rates, the local Reynolds number at the incoming jet is approximately $3\text{x}10^4$, making the flow turbulent. In the FDS model, nine spatial point measurements of temperature and species mass fraction (fuel, oxygen, water vapor, and carbon dioxide) are taken in the exhaust stream so that statistics of the exhaust composition can be found. The compartment walls are defined to be adiabatic in the model so that the reflect those of the PaSR model.
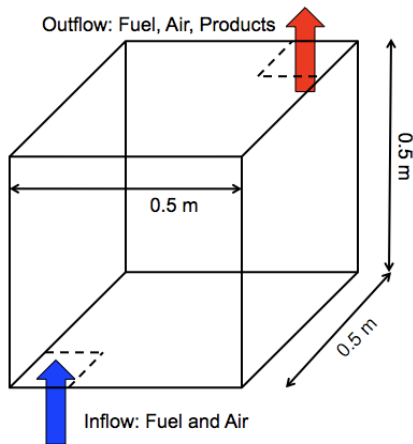
Figure 3.4.19: Schematic of finite rate FDS and PaSR enclosure simulation. Fuel and air enter at the bottom, mix, combust and exit at opposite top corner. Volume is 0.5 m x 0.5 m x 0.5 m.

In the FDS models discussed earlier in this chapter, specifying a HRR determines ignition, fire size and extinction. However, in this execution of FDS a governing HRR is not specified. Rather the mass flow rates of fuel and oxygen are specified and finite rate kinetics determine if/when a reaction will occur within the compartment. Similar to the PaSR model, the FDS finite rate kinetics model is based on a one-step Arrhenius kinetics. The fuel (propane), oxidizer (air), pre-exponential, activation energy, reaction stoichiometric coefficients, and finite rate reaction exponents must be specified. The parameters were defined to be the same for both the PaSR model and FDS model.

The FDS *Technical Reference Guide* recommends that when using the finite rate model, the DNS solver should be used instead of the LES solver (McGrattan et al., 2010a). This is because the LES solver may predict lower temperatures due to smoothing within the computational cells and will not accurately model micro scale mixing of species. To run a DNS simulation in FDS, computational cells smaller than millimeter scale are necessary. That size resolution would result in a minimum of 125 million grid cells, making the problem too computationally expensive. As a result, the finite rate

166

model in this problem is used with the default LES solver and 1 centimeter grid resolution. This results in a potential for decreases in local temperature and inefficient mixing. Therefore, to ensure that a reaction occurred, the inlet fuel and air temperatures are set at 1400 K for 1 second before ramping down to a 700 K inflow temperature.

The PaSR model is run following the same residence time, compartment composition, and inflow composition as the FDS model. Since the mixing time is unknown, the PaSR model is run for varying mixing times until the mean compartment temperatures are in agreement (Figure 3.4.20). Outflow species mass fractions and variances are subsequently compared.
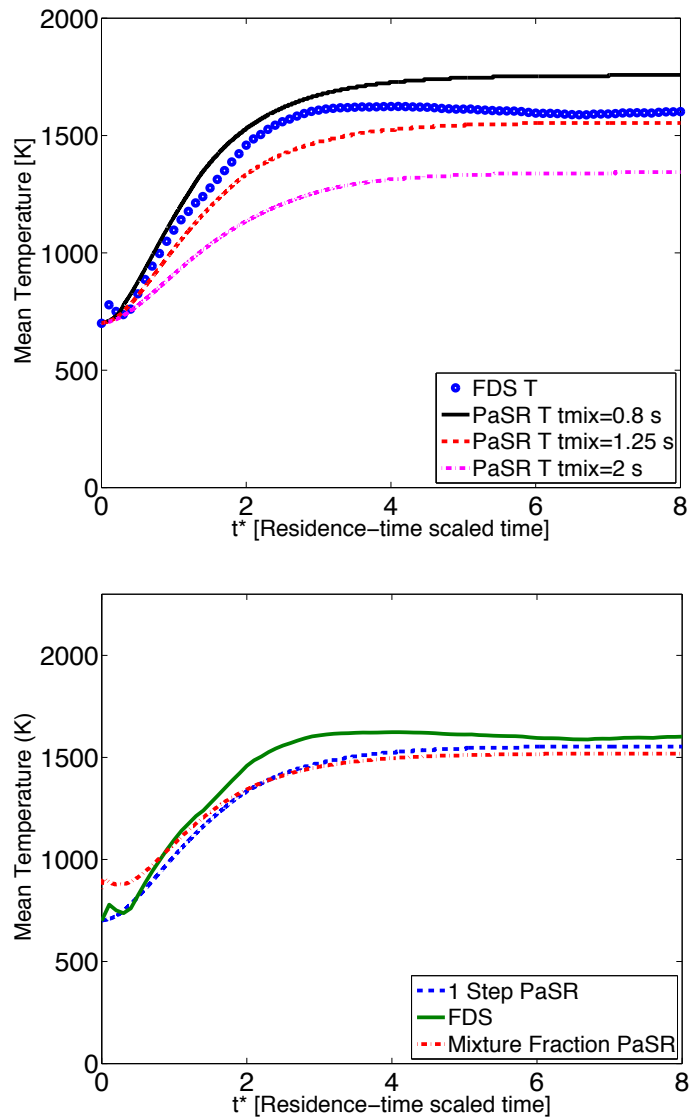
Figure 3.4.20: Comparison of finite rate FDS mean temperature to PaSR mean
temperature with varying mixing times (top) and comparison of 1 step PaSR
and mixture fraction PaSR with 1.25 second mixing time to FDS (bottom).

Figure 3.4.20 (left) shows three mixing times (τ_{mix}=0.8 s, 1.25 s, and 2 s)
compared to the results from the FDS model using finite rate combustion. An
approximate mixing time was found by initially guessing a mixing time of 2 seconds
based on using FDS with the LES solver. The resulting PaSR mean temperature was low

compared to FDS so the 0.8 second mixing time was run. This mixing time produced a mean temperature that had better comparison, but the mean temperature was over predicted. Based on the results from the 2 second mixing time and 0.8 second mixing time, a 1.25 second mixing time was run. The 1.25 second mixing time showed good comparison to the FDS mean temperature. Figure 3.4.20 (right) shows a comparison of the mixture fraction PaSR to the 1-step reaction PaSR both with a mixing time of 1.25 seconds to the finite rate FDS simulation. Both PaSR models show good steady state comparison, as the composition is the same for both models. Initially, the mixture fraction model shows higher temperatures because there is a lower limit to initial mixture fraction value that the libMoM library can generate a solution for. The problem becomes singular as the mixture fraction approaches either extreme (0 or 1). The exhaust species mass fractions using a mixing time of 1.25 seconds (Figure 3.4.21) are compared with the 1-step reaction model in FDS.
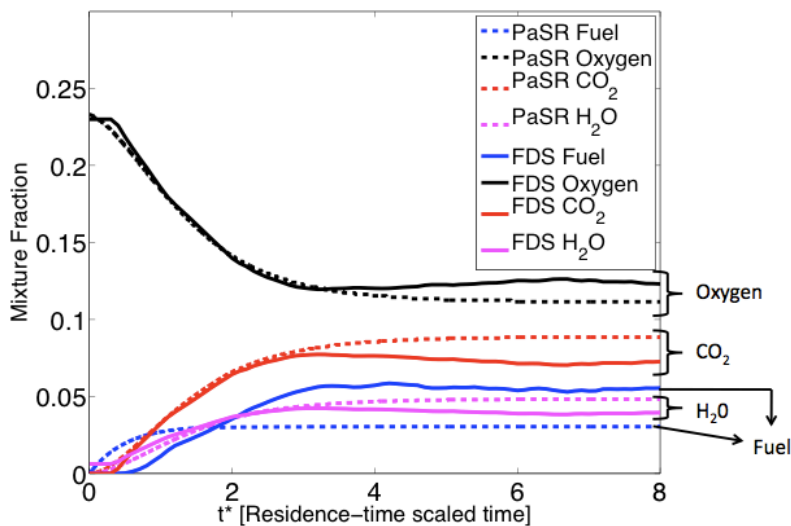
Figure 3.4.21: Comparison of species mean mass fractions for an FDS simulation (solid) using finite rate chemistry to a PaSR model (dash) with a mixing time of 1.25 seconds.

The PaSR model and FDS model results are compared over the length of the simulations. The models show similar time evolution trends but differences in the stationary state mass fractions. FDS shows more fuel and oxygen in the outflow and therefore lower products. These comparisons may improve with a closer tolerance in matching temperatures as well as finer grid resolution in the FDS model. In addition to comparing the mean values, it is important to compare the standard deviation within the exhaust flow as the PaSR is a stochastic modeling tool. Figure 3.4.22 shows the standard deviation for oxygen, fuel, and temperature for the PaSR and FDS models.
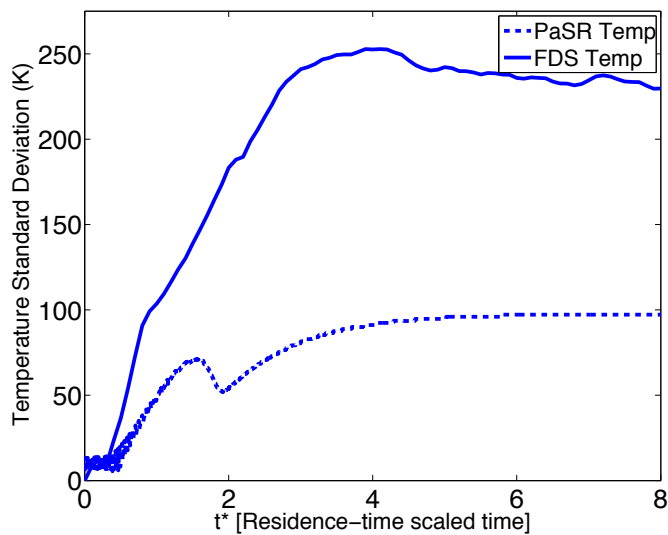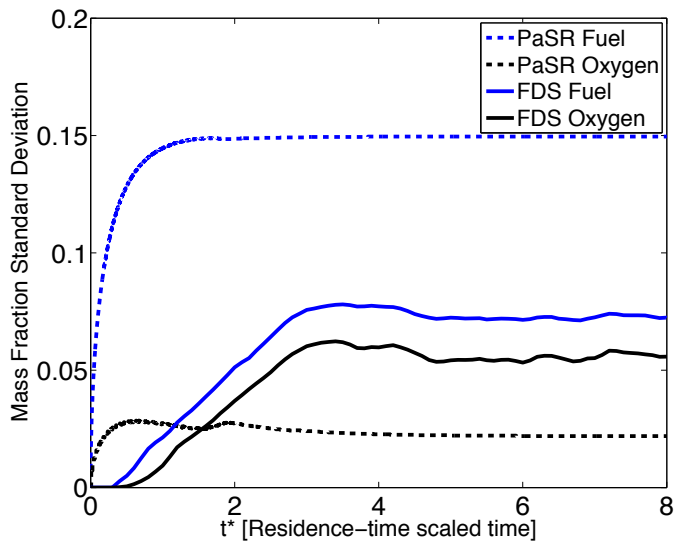
Figure 3.4.22: Comparison of mass fraction standard deviation of oxygen and fuel (top) and temperature (bottom) for the PaSR model (dash) and FDS (solid).

The two models show significant differences in the outflow reactant variances. The PaSR over predicts the fuel variance and under predicts the oxygen variance. In the temperature comparison FDS model variance is approximately 2.5 times the PaSR temperature variance. While these values differ it is important to recognize that there

could be significant error in the FDS model do to the nature in which the model was being run.

Overall, this comparison shows the potential of using a low order PaSR model to predict species and temperature evolutions in well-mixed, strong vent flow compartments. The PaSR offers computational savings as it took approximately 1 hour to complete the simulation versus > 2 hours for the finite rate FDS model. An advantage of the PaSR is that its computational time is independent of flow speed (residence time), where as the CFL number limits FDS for fast moving flows.

Multivariate PaSR with two step chemistry

To track carbon monoxide generation, the PaSR compartment fire model is expanded using a more sophisticated two-step chemical reaction. The evolution of moments of the mass fractions as governed by the PDF transport equation (Equation 3.4.5) is solved using the libMOM library (Upadhyay & Ezekoye, 2011). In this section a two-step finite rate reaction from Westbrook and Dryer is used to track oxygen (Y_{O2}), fuel (Y_F), nitrogen (Y_{N2}), water vapor (Y_{H2O}), carbon dioxide (Y_{CO2}), and carbon monoxide (Y_{CO}) (Westbrook & Dryer, 1981). Similar to the one step mechanism nitrogen is used for conservation of mass; therefore this 2-step formulation becomes a 5 dimensional problem ($d=5$). The governing chemical reactions for the 2-step propane combustion becomes:

$$C_3H_8 + 3.5O_2 + 18.8N_2 \rightarrow 3CO + 4H_2O + 18.8N_2$$
$$CO + \frac{1}{2}O_2 \leftrightarrow CO_2$$

3.4.13
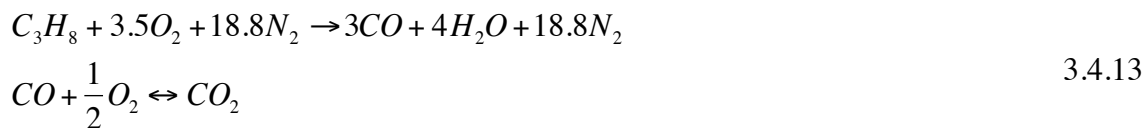
where the first reaction governs propane combustion and the second reaction governs the production and destruction of carbon dioxide and carbon monoxide. Note that in the second reaction the arrow is double sided, which indicates that there is a forward and

reverse reaction that occurs. The two reactions give rise to three chemical reaction terms, which govern species evolution:

$$R_1 = A_1[F]^a[O]^b \exp\left(\frac{-E_{a1}}{R\psi_T}\right)$$

$$R_2 = A_2[CO]^c[H_2O]^d[O]^e \exp\left(\frac{-E_{a2}}{R\psi_T}\right)$$ \hfill 3.4.14

$$R_3 = A_3[CO_2]^f \exp\left(\frac{-E_{a2}}{R\psi_T}\right)$$

where the molar concentrations (gmol/cm^3) are defined in same fashion as Equation 3.4.11. The pre-exponential values are defined by $A_1=1x10^{12}$, $A_2=10^{14.6}$, and $A_3=5x10^8$. The activation energies are defined as $E_{a1}=30.0$ and $E_{a2}=40.0$ (kcal/mol). The reaction rate exponents are defined as $a=0.1$, $b=1.65$, $c=1.0$, $d=0.5$, $e=0.25$, $f=1.0$ (Westbrook & Dryer, 1981). Temperature is determined the same as Equation 3.4.12. The resulting chemical source terms for each of the five species are:

$$S_{fuel} = -\left(\frac{1000W_{fuel}}{\langle\rho\rangle}\right)R_1$$

$$S_{ox} = -\left(\frac{3.5W_{O2}}{W_{fuel}}\right)\left(\frac{1000W_{fuel}}{\langle\rho\rangle}\right)R_1 + \left(\frac{500W_{O2}}{\langle\rho\rangle}\right)(R_3 - R_2)$$

$$S_{CO2} = \left(\frac{1000W_{CO2}}{\langle\rho\rangle}\right)(R_2 - R_3)$$ \hfill 3.4.15

$$S_{H2O} = \left(\frac{4W_{H2O}}{W_{fuel}}\right)\left(\frac{1000W_{fuel}}{\langle\rho\rangle}\right)R_1$$

$$S_{CO} = \left(\frac{3W_{CO}}{W_{fuel}}\right)\left(\frac{1000W_{fuel}}{\langle\rho\rangle}\right)R_1 + \left(\frac{1000W_{CO}}{\langle\rho\rangle}\right)(R_3 - R_2)$$

To check the results for this formulation, the evolution of mean species mass fractions and variances are compared to mixture fraction-progress variable work

173

conducted by Upadhyay (Upadhyay, 2006). Figure 3.4.23 shows the comparison between the two models for mean mixture fraction for a fast mixing case.
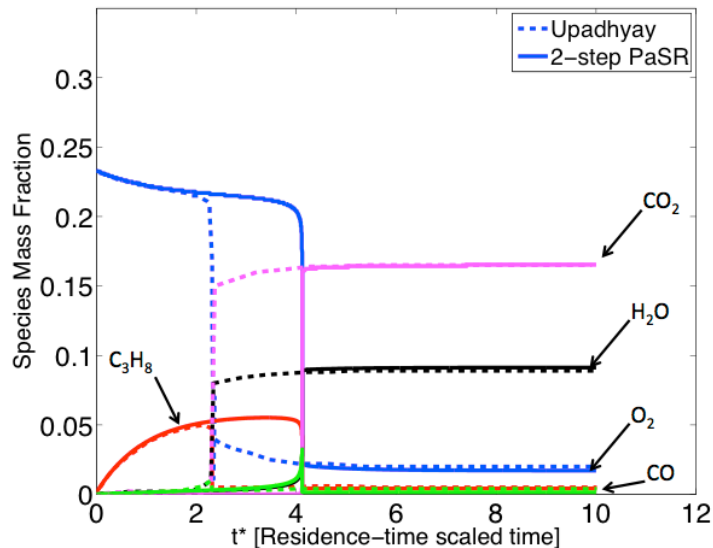
Figure 3.4.23: Comparison of species mean mass fractions from a multivariate two-step PaSR (solid) to work conducted by Upadhyay (dashed) (Upadhyay, 2006) with $\tau_{res}=0.1$ second and $\tau_{mix}=0.01$ second.

Figure 3.4.23 shows similar trends to the 1-step reaction, with respect to the reaction occurring earlier compared that shown by Upadhyay (Upadhyay, 2006). The figure also shows that both models show the same stationary state values verifying the two-step PaSR model equations above. At long times, both fuel and carbon monoxide go to approximately zero because the compartment is initially air, the inflow is a stoichiometric fuel and air mixture, and the mixing time is fast compared to the residence time. With slower mixing or fuel rich combustion, fuel and carbon monoxide would both be expected in the output stream. The 2-step reaction mass fraction variances of fuel and oxygen are again compared to results from Upadhyay (Figure 3.4.24).

174
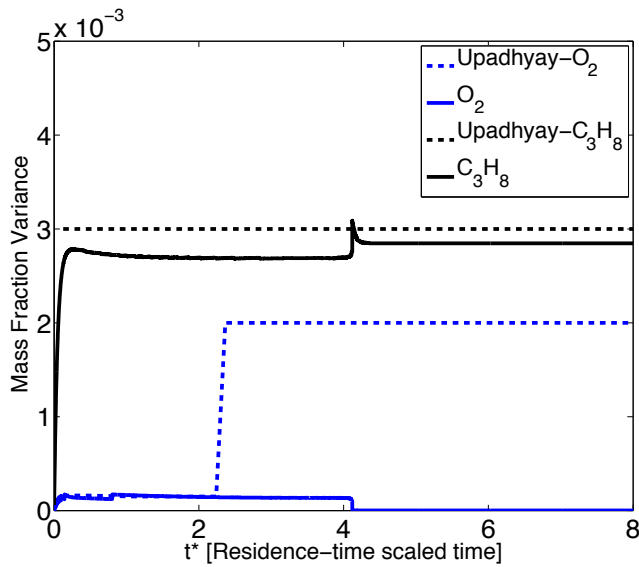
Figure 3.4.24: Comparison of species mass fraction variances from a multivariate two-step PaSR (solid) to work conducted by Upadhyay (dashed) (Upadhyay, 2006) with $\tau_{res}=0.1$ second $\tau_{mix}=0.01$ second.

The fuel variances show similar trends for the fast mixing case as shown previously in Figure 3.4.17 (left). The oxygen in two-step PaSR model is also similar to the single step reaction, however in Upadhyay's work there is an increase in oxygen variance associated with the two-step reaction. Additional validation cases will need to be conducted to better determine the evolution of oxygen variance.

3.4.2 Towards validating ventilation FDS models using experiments

Validation of reacting flow models followed a similar framework as discussed in *Chapter 2* with the non-reacting PPV model. As discussed in *section 3.3*, an experiment specific HRR was found which acts as the driver for the time evolution of the thermal environment within the compartment. Corrections/improvements were made where necessary to model parameters (flammability limits), computational parameters (grid resolution) and sensor models (transient thermocouple model). In this section the changes

175

made in the FDS model are coupled to the fan model used in the non-reacting flow model to simulate the application of PPV to a compartment fire. For the discussion in this section, the focus is on the models generated for three experimental configurations: a *No Vent* 400 kW natural ventilation case, a *No Vent* 400 kW PPV case, and an *Open Vent* 400 kW PPV case.

For the reacting flow ventilation simulations, the focus is on accurately capturing three phases of the experimental data: the initial ramp of temperature, the pre-ventilation peak/steady state temperatures, and the decrease in temperature as a result of ventilation. FDS' capabilities to model the pre-ventilation compartment temperature evolution were discussed in *section 3.3*. The importance of experimental uncertainty was also previously discussed, however for these comparisons one experimental data set is compared to one FDS simulation. Due to the uniqueness of the three ventilation tactics studies, there is not sufficient post-ventilation experimental data to quantify the uncertainty. For the simulations discussed below, the prescribed FDS HRR was found for the specific experiment being modeled following the inversion process discussed earlier.

The first tactic examined is a *No Vent* 400 kW natural ventilation case. This is an important case to model because it tests FDS' ability to model thermally driven buoyant flows. Figure 3.4.25 shows the mean interior compartment temperature for the four thermocouple elevations.
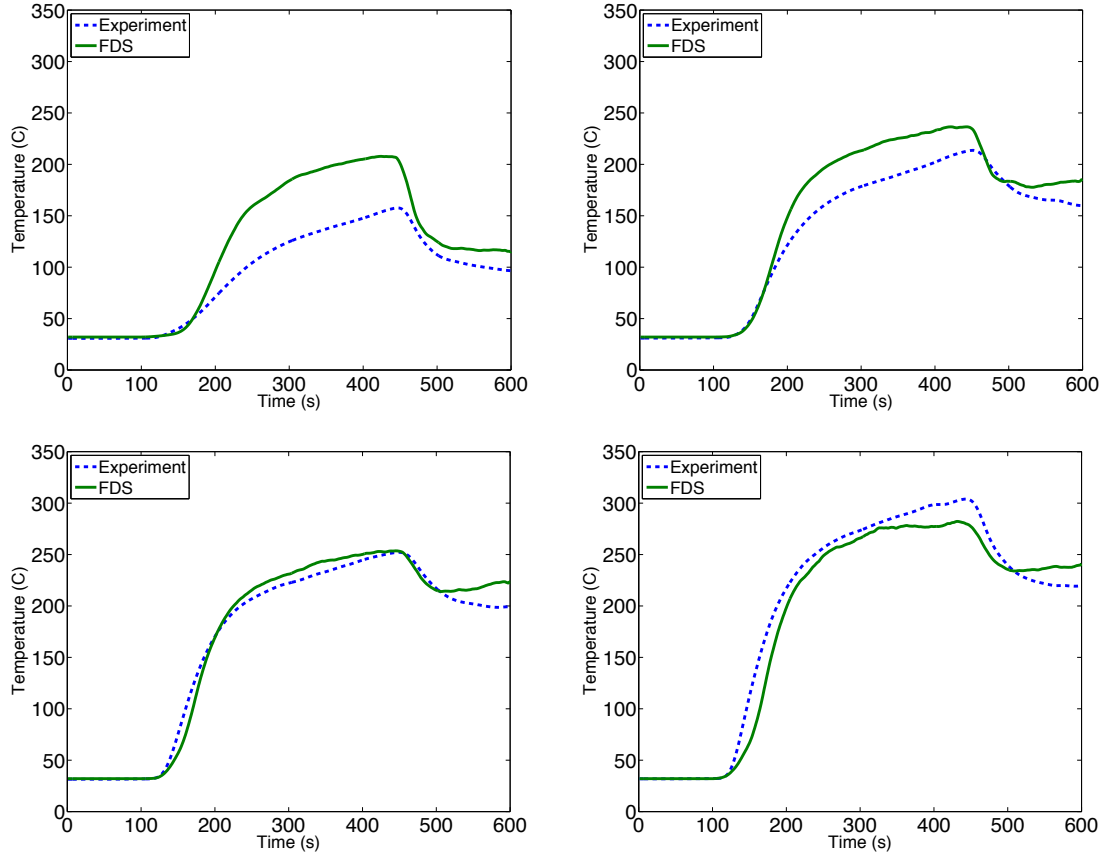
Figure 3.4.25: Spatially averaged temperatures for experiment (dashed line) and FDS simulation (solid line) for a *No Vent* 400 kW natural ventilation case at varying elevations. The top left plot is 0.73m, the top right is 1.19 m, the bottom left is 1.63 m and the bottom right is 2.08 m.

The plots in Figure 3.4.25 shows that the FDS simulation compares well to the experimental data set for the natural ventilation case. To best compare with the experiment, the compartment temperature is initialized to the average pre-ignition compartment temperature. The timeline for the experimental ventilation is followed as the structure door in the model is opened at 450 seconds. The plots show that FDS over predicts the mean experimental post-ventilation compartment temperature at each of the four thermocouple elevations. To better quantify the differences between the model and

experiments the relative error at each thermocouple at the 4 elevations is examined. The relative error is defined as:

$$Err(x,y,z,t) = \frac{T_{EXP}(x,y,z,t) - T_{FDS}(x,y,z,t)}{T_{EXP}(x,y,z,t)}$$ 3.4.16

where T_{EXP} is the experimental thermocouple temperature measurement and T_{FDS} is the computationally modeled thermocouple temperature from FDS both in °C. Figure 3.4.26 shows the relative error for each thermocouple at the 4 elevations for the duration of the experiment to see pre- and post-ventilation error.
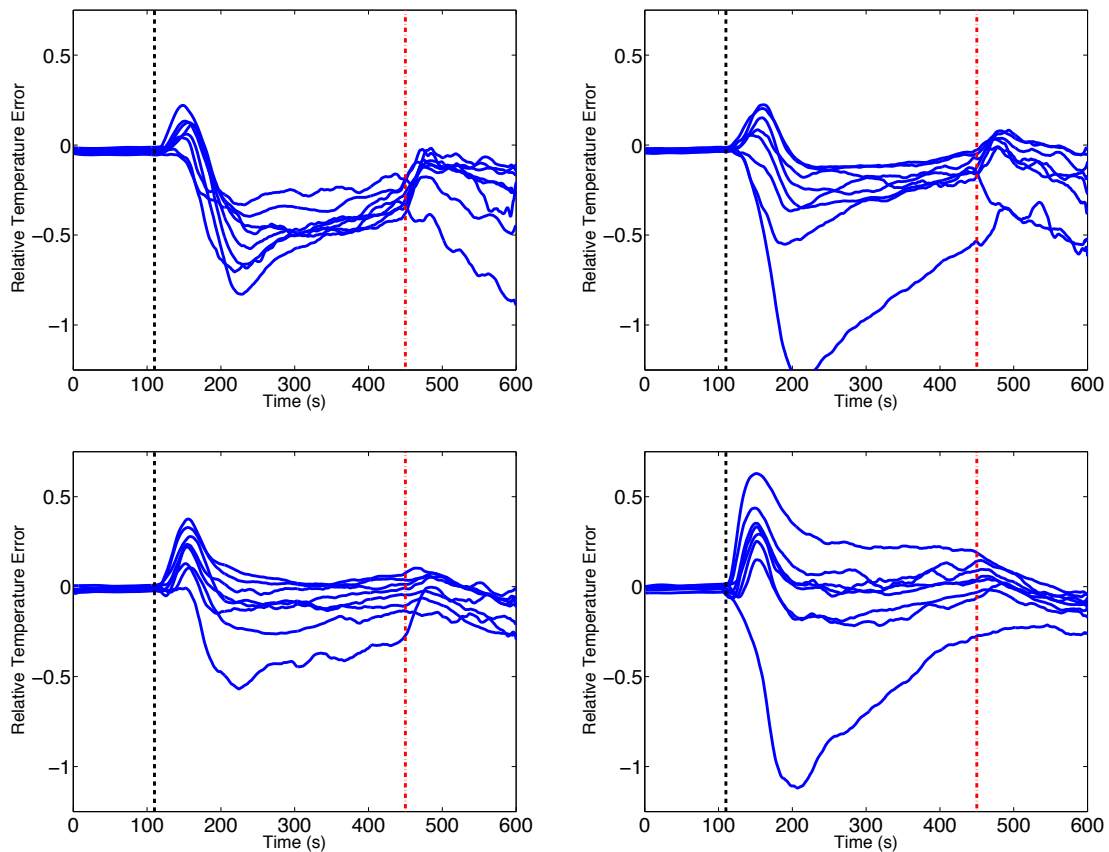
Figure 3.4.26: Relative error comparing experimental thermocouple temperature to FDS modeled thermocouple temperature for a *No Vent* 400 kW natural ventilation case. The first vertical line (dashed) indicates ignition time and the second (dash-dotted) represents ventilation. Negative values indicate model over prediction. The top left plot is 0.73 m, the top right is 1.19 m, the bottom left is 1.63 m and the bottom right is 2.08 m.

The relative error is shown for the length of the experiment in order to see how well FDS can model ventilation as compared to the enclosure fire. Vertical lines on the plot indicate ignition (left) and ventilation (right). Significant change in relative error are not seen with the application of ventilation with an approximate relative error between any experimental thermocouple and model thermocouple of 25%. This shows that the

ventilation modeling is similar to the enclosure modeling in predicting experimental results.

Figure 3.4.26 shows that at 200 seconds into the test most notably at the 1.19 m and 2.08 m elevations, FDS is over predicting the temperature measurements by > 100%. Examination of these thermocouples shows that they were located in the thermocouple tree at the doorway. It is known that there is leakage around the doorway; however, the amount of leakage has not been quantified. Therefore the amount of leakage is approximated from experimental observations. Leakage around the doorway is also susceptible to environmental effects such as wind, which was not accounted for in the model.

The error plots also show a spike in error after ignition that increases with elevation. To better visualize this error, the time derivative of temperature for the experiment and model at the highest elevation (Figure 3.4.27) is examined.
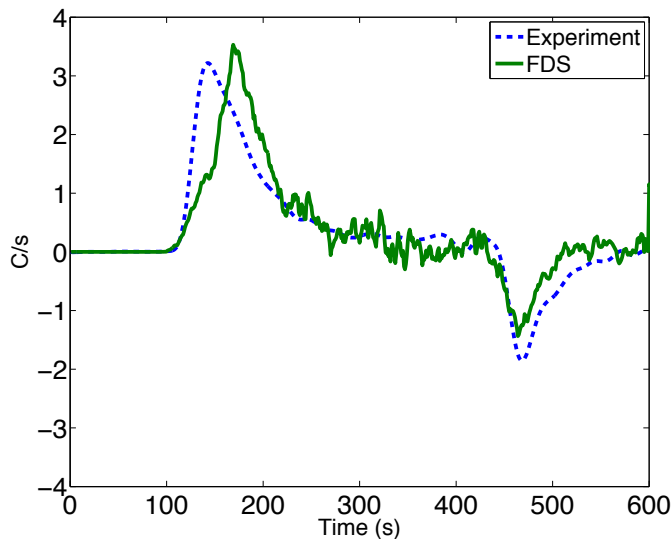
Figure 3.4.27: Time derivative of spatially averaged temperatures for experiment (dashed) and FDS simulation (solid) at 2.08 m for *No Vent* natural ventilation case.

180

In Figure 3.4.27, data above zero represents an increase in temperature while anything below zero is a decrease in temperature. Ignition occurred at 100 seconds and the data spike indicates a rapid rise in temperature. While the rate of change temperature spikes are similar in width and peak, the model spike is skewed to the right. This indicates that either the model thermocouple responds slower than its experimental counterpart or that prescribed HRR ramp needs to ramp faster. Both the experiment and model temperature derivatives fluctuate around zero as the 2.08 m elevation approaches a steady pre-ventilation temperature. Ventilation occurred at 450 seconds, shown by the negative peak. The negative spike shows better comparison between the two data sets, which is reflected in the post-ventilation error plots. The experimental ventilation does have a higher peak decrease in temperature and extended cooling compared to the FDS results.

The next step is to couple the PPV fan model the reacting flow model to examine forced ventilation. The PPV cases should show similar pre-ventilation trends as compared to the natural ventilation cases. More importantly, is to examine the ability of the FDS model to simulate the more complex forced ventilation. Figures 3.4.28 and 3.4.29 show the FDS comparison to experimental data for average temperature for *No Vent* and *Open Vent* 400 kW PPV tests respectively.
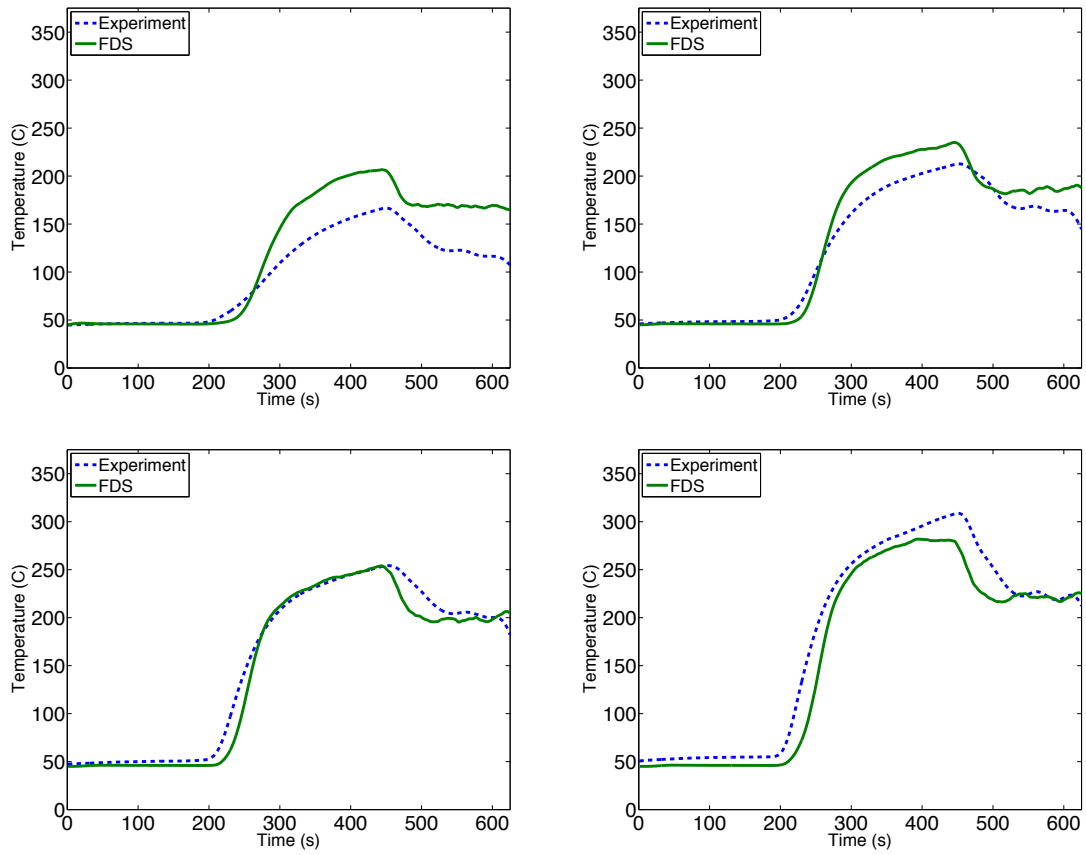
Figure 3.4.28: Spatially averaged temperatures for experiment (dashed) and FDS simulation (solid) for a *No Vent* 400 kW PPV case at varying elevations. The top left plot is 0.73m, the top right is 1.19 m, the bottom left is 1.63 m and the bottom right is 2.08 m.

182
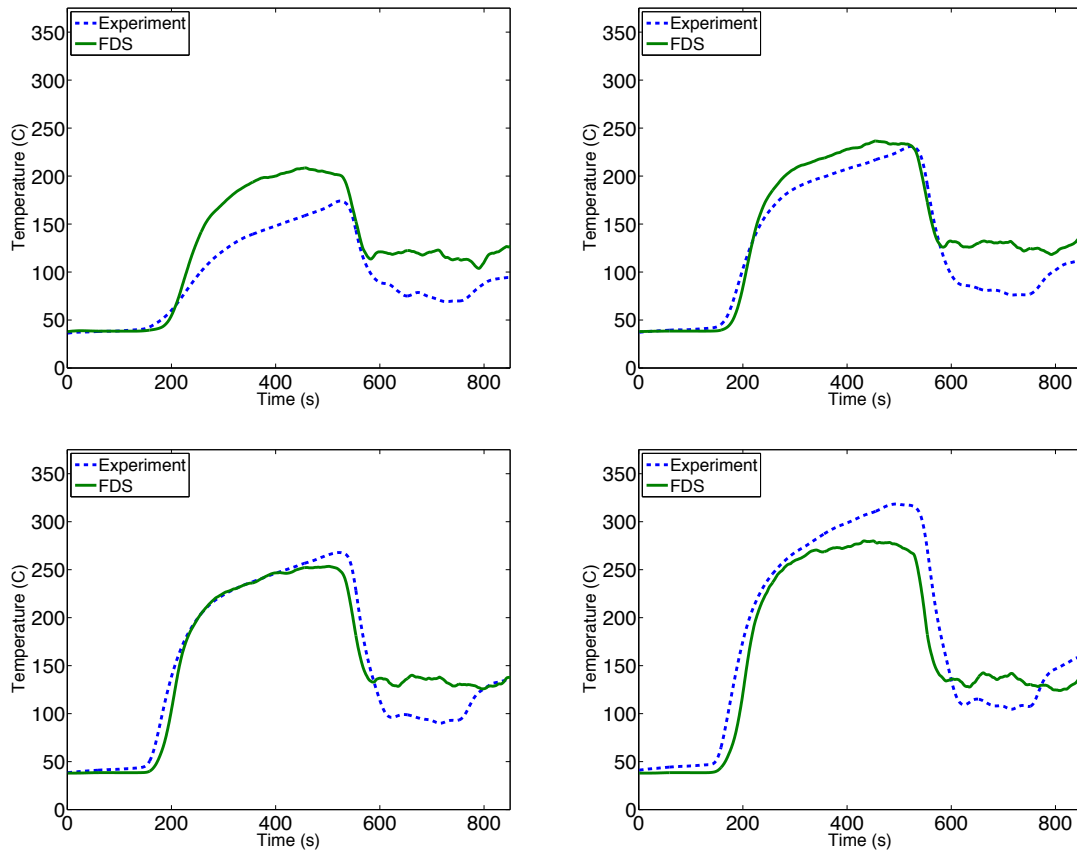
Figure 3.4.29: Spatially averaged temperatures for experiment (dashed) and FDS
simulation (solid) for an *Open Vent* 400 kW PPV case at varying elevations.
The top left plot is 0.73m, the top right is 1.19 m, the bottom left is 1.63 m
and the bottom right is 2.08 m.

For the *No Vent* PPV case (Figure 3.4.28), the temperature drop is not as
significant as compared to the *Open Vent* PPV case (Figure 3.4.29). This is expected as
Table 2.3 and Table 2.4 show a factor of 12 increase of mass flow rate through the
doorway for the *Open Vent* case compared to the *No Vent* case. The increased mass flow
rate of ambient air through the structure forces more hot combustion products out,
lowering compartment temperature. Post ventilation temperatures compare well for the
No Vent PVV case, especially at the two upper elevations. In the *Open Vent* case,

however FDS consistently over predicts the experimental post ventilation temperature. Similar to the natural ventilation analysis the relative error between the experiment and model are examined to quantify the differences (Figure 3.4.30 and Figure 3.4.31).
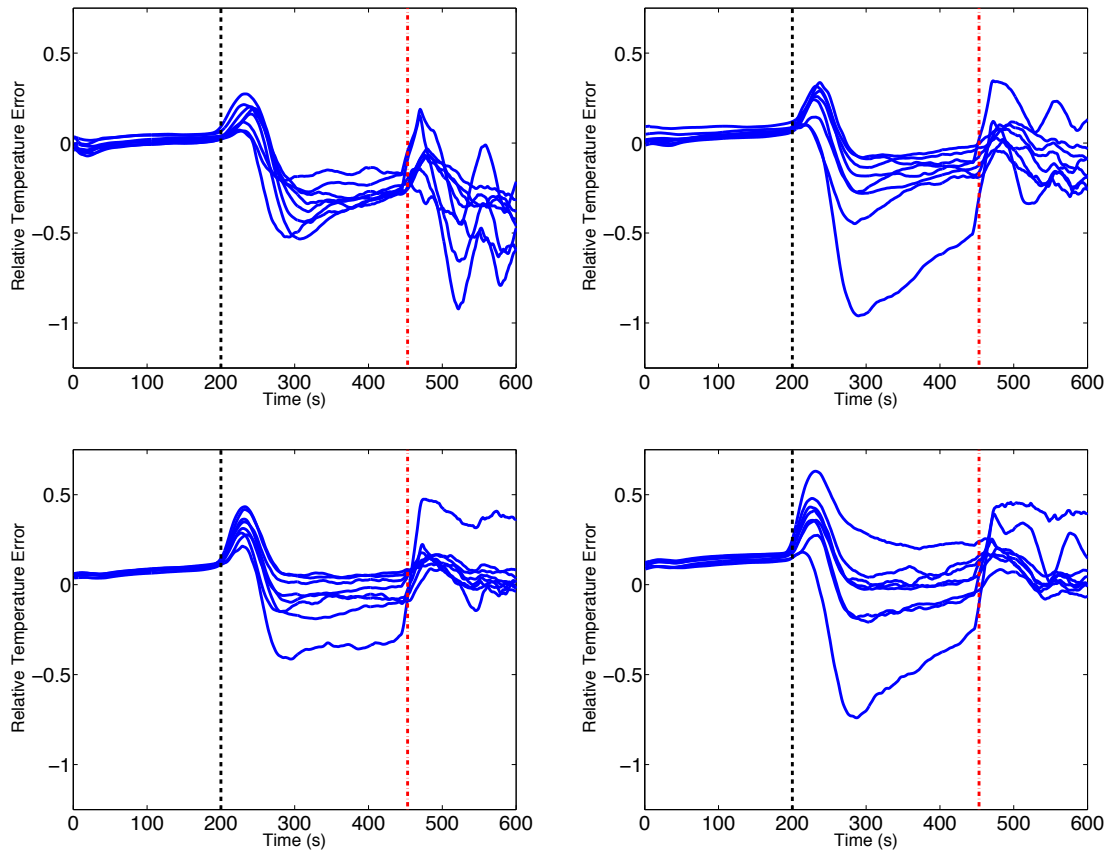
Figure 3.4.30: Relative error comparing experimental thermocouple temperature to FDS modeled thermocouple temperature for a *No Vent* 400 kW PPV case. The first vertical line (dashed) indicates ignition time and the second (dash-dotted) represents ventilation. Negative values indicate model over prediction. The top left plot is 0.73 m, the top right is 1.19 m, the bottom left is 1.63 m and the bottom right is 2.08 m.
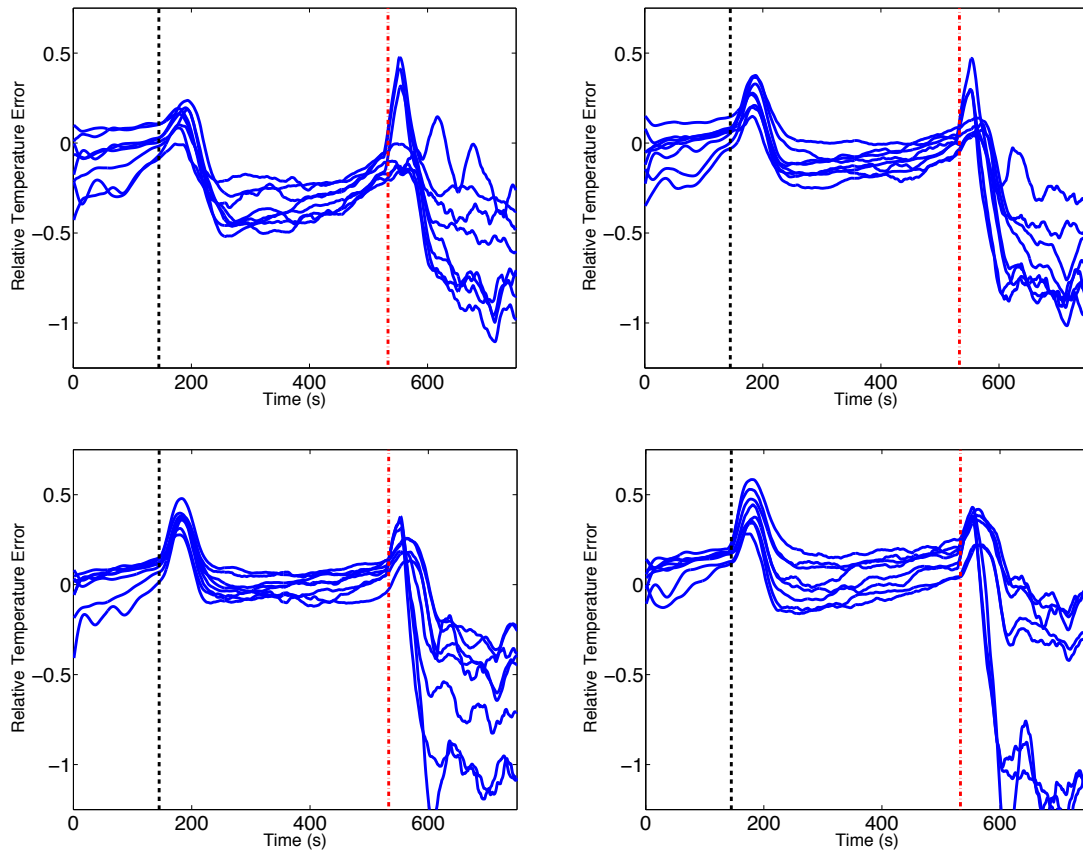
Figure 3.4.31: Relative error comparing experimental thermocouple temperature to FDS modeled thermocouple temperature for an *Open Vent* 400 kW PPV case. The first vertical line (dashed) indicates ignition time and the second (dash-dotted) represents ventilation. Negative values indicate model over prediction. The top left plot is 0.73 m, the top right is 1.19 m, the bottom left is 1.63 m and the bottom right is 2.08 m.

Similar pre-ventilation trends are shown in the two PPV cases (Figures 3.4.30 and 3.4.31) as expected. Both cases show the error spike that may be associated with the initial temperature ramps in FDS being less acute than the experiment temperature rise or temperature sensors. The plots show that prior to ventilation in the *No Vent* PPV case (Figure 3.4.30) the error is spatially consistent except for 1 outlying thermocouple. This means that while FDS is generally predicting temperatures greater than the experiment,

the model is able to capture the variation in each layer similar to the variations that occur in the experiments. The one thermocouple that had significant error (>50%) was again to found to be on the thermocouple tree near the doorway. More work may need to be done to better seal the doorway of the experimental structure, as this error is possibly caused by leakage to/from the environment.

Note that in Figure 3.4.31 there is noticeable pre-ignition error and variation of the error across the 4 elevations. In the FDS model the compartment temperature was initialized to be one uniform temperature: the average of the pre-ignition experimental thermocouple temperatures. This approach is good for modeling the first in a series of consecutive experiments, however after a test is completed the compartment temperature remains stratified due to heat transfer from the walls to the thermocouples. Figure 3.4.31 shows that after ignition, the error associated with initial conditions is minimal.

Post-ventilation, there are different trends between the errors associated with the two PPV cases. The *No Vent* case shows error comparable to the pre-ventilation values, however there are several sensors where the model under predicts the thermocouple temperature. The thermocouples with under predicted temperature are on the three-thermocouple trees that are aligned with the fan. In the *Open Vent* case, there are significant over predictions of compartment temperatures; those thermocouples are located on the same three thermocouple trees as the under predictions in the *No Vent* case. These types of errors are not surprising considering the highly turbulent nature of the mixing (Reynolds number of fan jet $\sim 1\text{x}10^6$) that is occurring in the entrance to the structure. Also consider that the post-ventilation temperatures are generally 100 °C cooler than the pre-ventilation temperature so higher percent differences are expected. The actual temperature differences are 50 °C or less. From experimentation, it was observed that the application of PPV causes vibrations to the thermocouples closest to the door.

186

These physical fluctuations are not possible to model in FDS and may contribute to some of the error. As more ventilation experiments are conducted in the future, post ventilation compartment statistics can be determined which would provide a better data set for validation. However, as an initial comparison with a single experimental set and coarsely resolved PPV fan, the results show that FDS can be used to model natural and forced ventilation of a compartment fire.

3.5 CONCLUSIONS

The computational methods used to predict the thermal environment of an experimental enclosure fire exposed to ventilation represent a significant improvement towards understanding the relevant parameters that govern the problem. A framework was developed to characterize strong vent flow enclosure fires using experimental measurements and computational modeling. The framework required calibration of relevant modeling parameters, quantification of propagation of uncertainties, and improvements of submodels.

To experimentally characterize enclosure fires and subsequently ventilation, the UT burn facility needed to be upgraded from its condition following the non-reacting flow experiments. This required adding fire protection to the structure interior, installing instrumentation, setting up the data acquisition system, and constructing the fuel supply system for the burners. Over 70 reacting flow experiments have been conducted to study the thermal environment of an enclosure fire. Fifty-seven of these experiments included ventilation: 30 positive pressure ventilation tests and 27 natural ventilation tests. Within this testing set, fire size and compartment openings were varied; the focus of the experiments in this study were 8 400 kW tests using natural and forced ventilation with and without an open compartment window. Recognizing that there is uncertainty

associated with the experiments, relevant statistics of the experimental temperature distributions are calculated by finding the moments of the distributions. Standard deviations in thermocouple temperature were found to be consistent at each of the sensor elevations and to be consistent for both 300 kW and 400 kW experiments.

Computational analysis of the ventilation experiments was divided into enclosure fire modeling (pre-ventilation) and ventilation modeling. For the enclosure fire modeling a low-order model (CFAST) and a full CFD model (FDS) were examined with a focus on the CFD model. In using FDS to model the enclosure fire experiments, it was necessary to calibrate certain governing model parameters. The first parameter was to best determine the HRR of the burners in the experiments. While the mass flow rate of fuel into the compartment is set based on a desired HRR, there is error in the use of the mass flow controller and in the physical controller. Therefore an inversion technique that finds HRR as a function of time was used. This HRR controls the flow rate of propane into the model. Using this HRR to govern fire growth in the FDS simulations it was found that the model compartment transitioned to a ventilation-controlled environment while experiments did not indicate that this was occurring. This led to a deeper analysis of the governing combustion criteria in the model. As a result the lower oxygen flammability limit was changed from a default value of 0.15 mol/mol to 0.05 mol/mol and the lower fuel flammability limit was changed from 0.0 kg/kg to 0.021 kg/kg. Using these parameters, FDS was able to best follow the prescribed HRR.

The FDS thermocouple submodel was also modified as part of this analysis. A transient thermocouple model was developed and implemented into FDS. Verification and validation work was performed and the model has since been accepted into the current public release of FDS.

After the appropriate model parameters and submodels were modified the FDS predicted thermocouple temperatures were compared to experimentally measured thermocouple temperatures. FDS results showed similar spatial variations to the experimental data at each thermocouple elevation, however the computational temperatures were over predicted at the lowest elevation. Potential causes for this error include a difference in radiation from the burners to the thermocouples in the model versus the experiment and a difference in the amount of leakage in the computational model to actual experimental structure. Correcting for these error sources showed the appropriate temperature trends in the model. In the future, leakage tests need to be conducted again to determine the impact the repeated thermal stresses from fire testing have had on the compartment. Knowing the current leakage and the impact of that leakage area on the simulation results can help in finding other potential sources of error in the simulation.

The last step in characterizing the enclosure fires was to propagate the experimental error into the FDS model as a way to better compare results. The error propagation was completed using QMOM along with the HRR inversion method. QMOM allowed statistical information to be carried in the form of two quadrature points and two quadrature weights, which is computationally efficient. Quadrature points and weights are found based on the experimental temperature distribution, converted to quadrature points in temperature to HRR through inversion, and FDS simulations were run based on the two quadrature points in HRR. The moments of the experimental distribution are compared to those generated from FDS. Examination of the results revealed that considering fluctuations in both the experimental data and computational models is a good way to compare the data sets.

Computational modeling of ventilation was divided into two sections: the development and application of a lower order model for strong vent flow fires and CFD comparison of experimental results using FDS. In the post ventilation experimental compartment, it was shown that temperature is not a function of spatial location, mainly as a result of mixing. Therefore the PaSR, which assumes that there are no spatial gradients within the reactor/control volume, is an appropriate model for this situation. The PaSR model was built and results was analyzed for a series of problems using a library developed for solving stochastic differential equation with DQMOM. A fast chemistry mixture fraction driven reaction process was compared to a PSR for a fuel rich compartment exposed to ventilation. The impact of mixing time on the statistics of compartment composition and temperature was shown. For fast mixing times the PaSR, variations decreased and the results resembled the PSR formulation. A PaSR with a one-step finite rate reaction tracking individual species mass fractions was developed and compared to results from a model problem with a PaSR that used one-step chemistry with mixture fraction-progress variable. Finally the PaSR was compared to a FDS simulation using finite rate chemistry instead of a traditional prescribed HRR. The PaSR model was shown to be able to model a wide range of problems with varying compartment residence times, mixing times, and composition. The PaSR model is able to provide statistics on the time evolution of compartment composition. The future of this model is continue to work with the 2-step reaction in order to predict CO with the intent to use this model to augment the current CO production model in FDS.

Finally FDS model predictions were compared to the experimental results for three ventilation tactics. Comparing mean thermocouple temperatures at each of the elevations, FDS was shown to model the post ventilation trends associated with ventilation, however the FDS model temperatures tended to be high relative to

experiments. Examination of the relative error between the simulations and experimental temperatures showed individual thermocouples with large relative errors. This was most notable for the PPV cases as the use of the fan creates a highly turbulent environment, which is difficult to accurately model. More experiments using the same ventilation tactics are needed to characterize the post-ventilation experimental uncertainty.

Chapter 4: Application of Enclosure Fire Experiments and Models

One of the main motivations for this work has been to increase understanding of how ventilation impacts the thermal environment of enclosure fire, so that this information can be disseminated to the help the fire service to improve its tactics. Previous discussions have mainly focused on the computational tools, the applications and limitations of those tools, and the comparison of computational results to experimental results. The focus of this chapter is the discussion of relevant experimental and computational results as they relate to the application of ventilation as a firefighting tactic.

4.1 EXAMINATION OF COMPARTMENT TEMPERATURE EVOLUTION FOR DIFFERENT VENTILATION TACTICS

The primary functions of ventilation as a fire firefighting tactic are to remove the hot combustion products from the fire room and to improve tenability for firefighters to make entry to the structure for fire attack. Therefore, it is important to examine how the different ventilation tactics affect temperature at the structure entrance and if FDS can be used to model the same trends. Temperature from the first thermocouple tree inside of the doorway (*attack corridor*) was plotted against the mean thermocouple temperatures in the interior of the compartment (*interior)* to see how the entrance and core of the structure changed as a result of ventilation. Figure 4.1.1 shows how the *attack corridor* and *interior* are defined in this analysis.
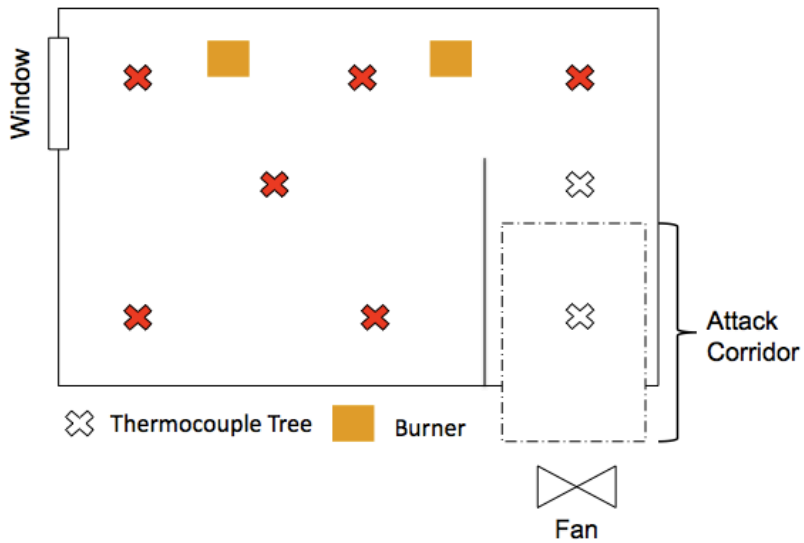
Figure 4.1.1: A plan view of the UT burn facility. The shaded thermocouple tress whose average represents the *interior*. The thermocouple tree closest to the door is used to represented the *attack corridor*.

Figure 4.1.2 shows the comparison of experimental data to FDS results for the *No Vent* natural ventilation configuration at the lowest (0.73 m) and highest (2.08 m) thermocouples.
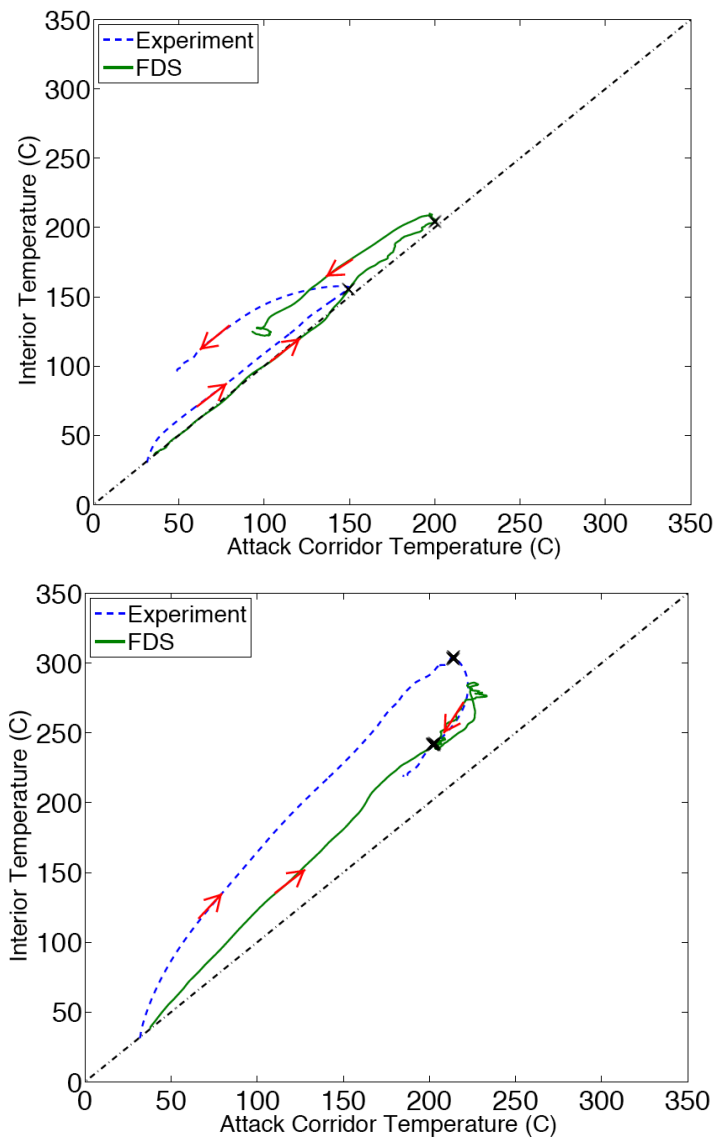
Figure 4.1.2: Mean *interior* temperature versus a*ttack corridor* temperature for experiments (dashed) and FDS (solid) at 0.73 m (top) and 2.08 m (bottom) for *No Vent* natural ventilation. In these plots the black line (dash-dotted) represents equal temperature for the two parts of the structure. The arrows (->) represent an increase in time and the X indicates ventilation.

To understand the effects of ventilation shown in the plots in Figure 4.1.2, it is first important to explain the plots. The dash/dotted diagonal line (-.-) represents equal temperature in the *interior* and *attack corridor; y=x*. If the temperature change has the

194

same slope as this line, the compartment is heating uniformly. Unless the temperature curve is on this line, the compartment temperature is not uniform. The arrows represent progression in time and the X indicates ventilation. If temperature increases on the left side of the equal temperature line, the *interior* is heating up faster than the *attack corridor*. This is expected as the burners were placed in the *interior* of the compartment. If the temperature changes along a horizontal line, *y= constant*, this represents a change in *attack corridor* temperature and a constant *interior* temperature. A vertical line, *x=constant*, represents a change in the *interior* temperature and a constant *attack corridor* temperature. Lines that fall between these two bounds represent changes in both parts of the compartment.

For the natural ventilation case, the lower elevation heated up uniformly throughout the compartment. After ventilation, the experiment and FDS show that the *attack corridor* initially cooled faster than the *interior* but then both cool at an equal rate. At the upper layer, both curves show more dominant *interior* heating compared to the lower elevation. After ventilation, there is an increase in *attack corridor* temperature for both FDS and the experimental data before both temperatures decrease. This result is expected because in the *No Vent* case, the exit path with least resistance for the hot upper layer gases is the doorway. Since the *interior* temperatures were hotter than the *attack corridor*, the exiting gases heat the thermocouples as they flow past them. Once sufficient ambient air has entered the compartment and mixed with the combustion gases therefore lowering the temperature, then temperature in the *attack corridor* will cool. Figures 4.1.3 and 4.1.4 show how forced ventilation affects compartment temperature evolution.
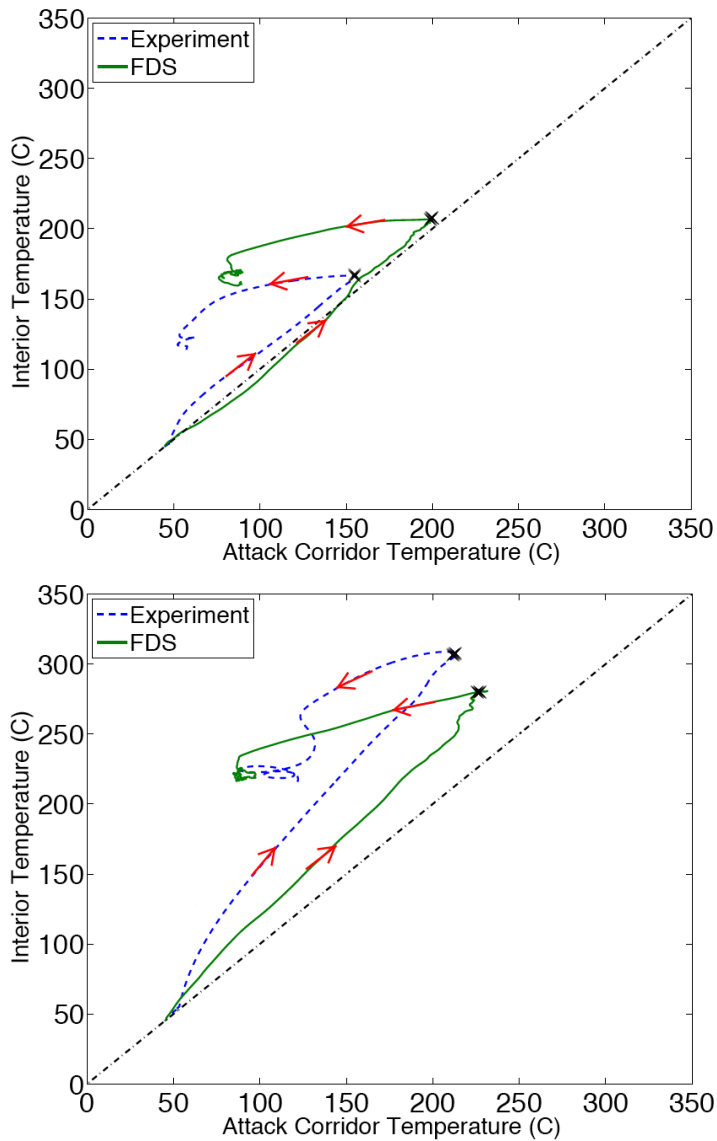
Figure 4.1.3: Mean *interior* temperature versus *attack corridor* temperature for experiments (dashed) and FDS (solid) at 0.73 m (top) and 2.08 m (bottom) for *No Vent* PPV. In these plots the black line (dash-dotted) represents equal temperature for the two parts of the structure. The arrows (->) represent an increase in time and the X indicates ventilation.

As expected at both elevations for the *No Vent* PPV case the same pre-ventilation trends exist as seen in the natural ventilation case. Post ventilation at the lower elevation for the *No Vent* case, there is a significant drop in *attack corridor* temperature compared

196

to a small change in the *interior* temperature. This is more severe than natural ventilation as PPV forces cool ambient air into the compartment at a much higher rate than natural ventilation. While the temperatures are different for the experiment and FDS, both cases show the same trend for PPV, indicating that model captures the ventilation effects. The higher elevation also shows the *attack corridor* cooling significantly more than the fire room.
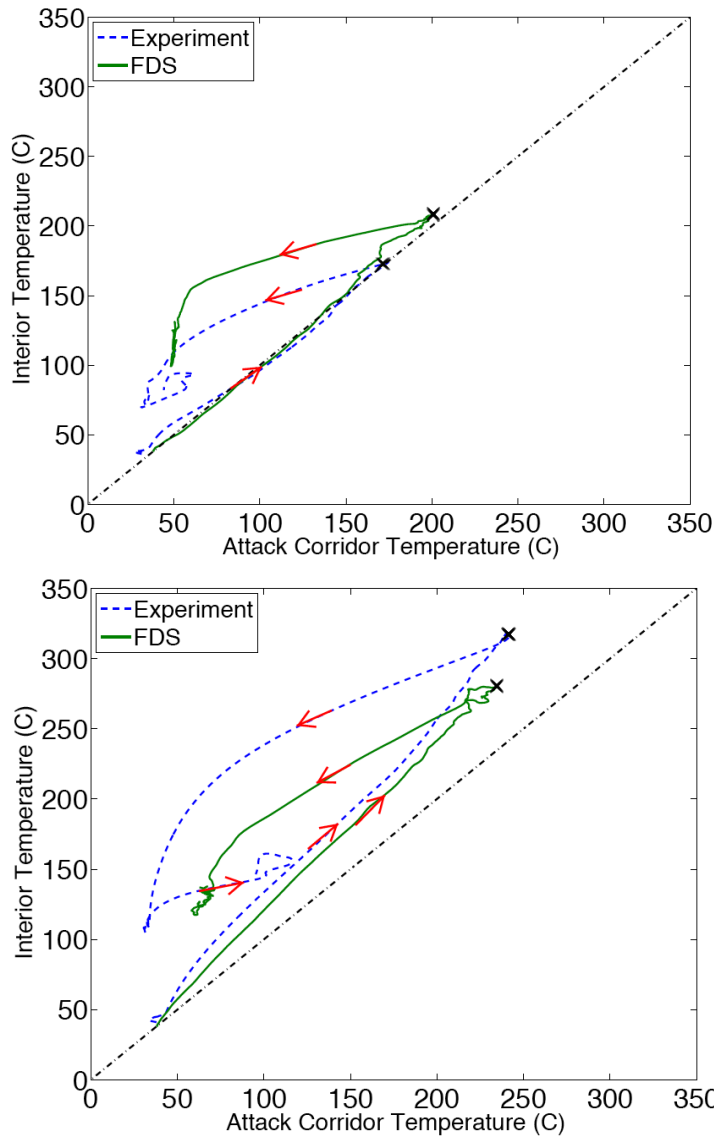
Figure 4.1.4: Mean *interior* temperature versus *attack corridor* temperature for experiments (dashed) and FDS (solid) at 0.73 m (top) and 2.08 m (bottom) for *Open Vent* PPV. In these plots the black line (dash-dotted) represents equal temperature for the two parts of the structure. The arrows (->) represent an increase in time and the X indicates ventilation.

The *Open Vent* PPV case is similar to the *No Vent* case except that there is significantly more cooling in the both the *attack corridor* and *interior*. This shows the advantage of providing sufficient exit area for PPV to push the combustion gases out of

the compartment. One risk however is that vent provides another orifice which is susceptible to environmental effects. After the upper layer experimental temperatures minimize with an approximate *attack corridor* temperature of 25 °C and *interior* temperature of 100 °C, the data shows an increase in both the *interior* and *attack corridor* temperature. Wind effects are believed to cause the increase in temperature and will be discussed in greater detail in the following section.

Note that in both PPV cases, the increase in upper layer temperature discussed in the natural ventilation case is not present as the PPV fan causes significant mixing with the combustion products and incoming ambient air.

Figures 4.1.2-4.1.4 show that while the temperature values may be different, FDS is able to model the trends associated with the application of the three ventilation tactics. Smokeview, the visualization tool packaged with FDS, is used to produce contour plots of temperature just after ventilation to see the evolution of the entire compartment. Figures 4.1.5-4.1.7 show temperature contours of a plan view of the compartment at an elevation of 1.5 m (middle of window) and temperature contours in a vertical plane that bisects the fan and doorway.
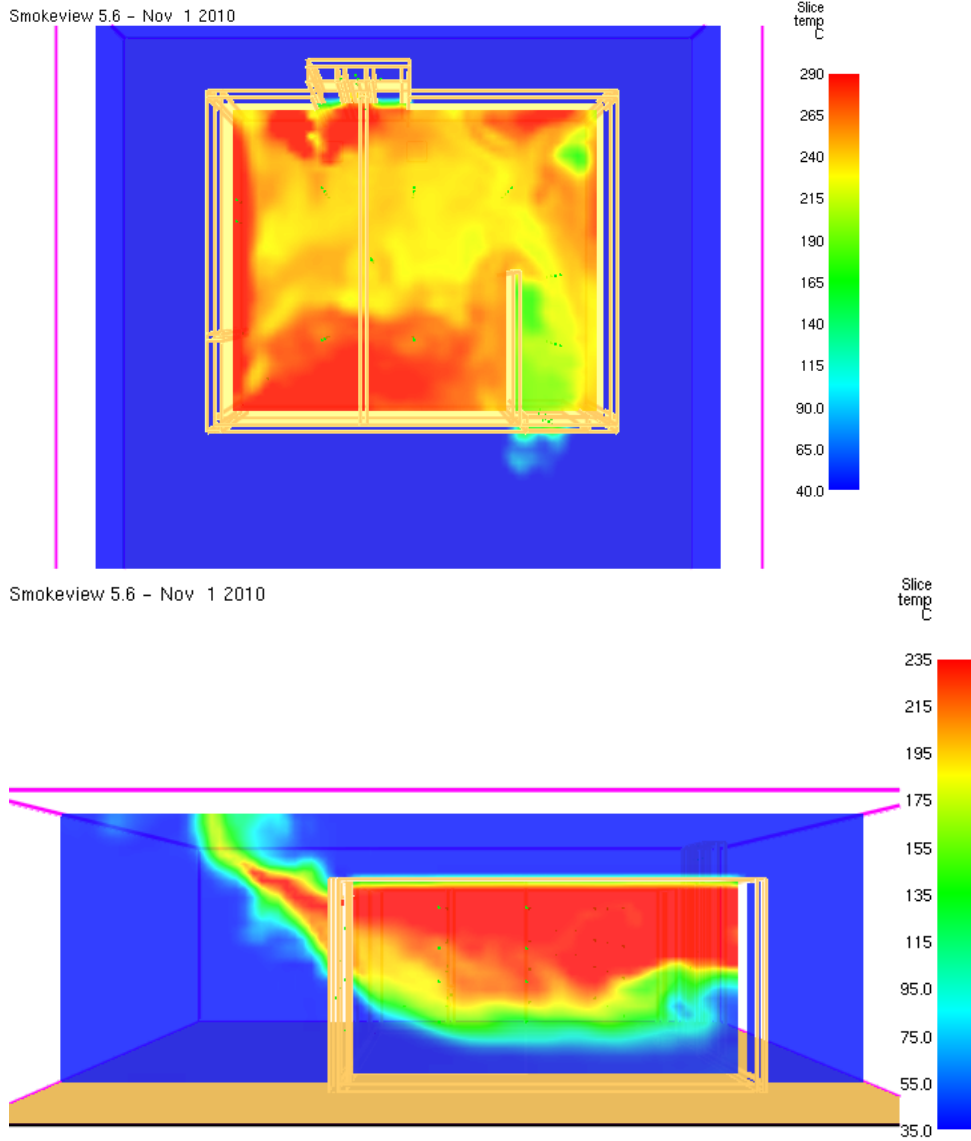
Figure 4.1.5: Post-ventilation temperature contours of the compartment in *x-y* plane (top) at an elevation of 1.5 m (middle of window) in the vertical plane (bottom) that bisects the fan and doorway for the *No Vent* natural ventilation case.
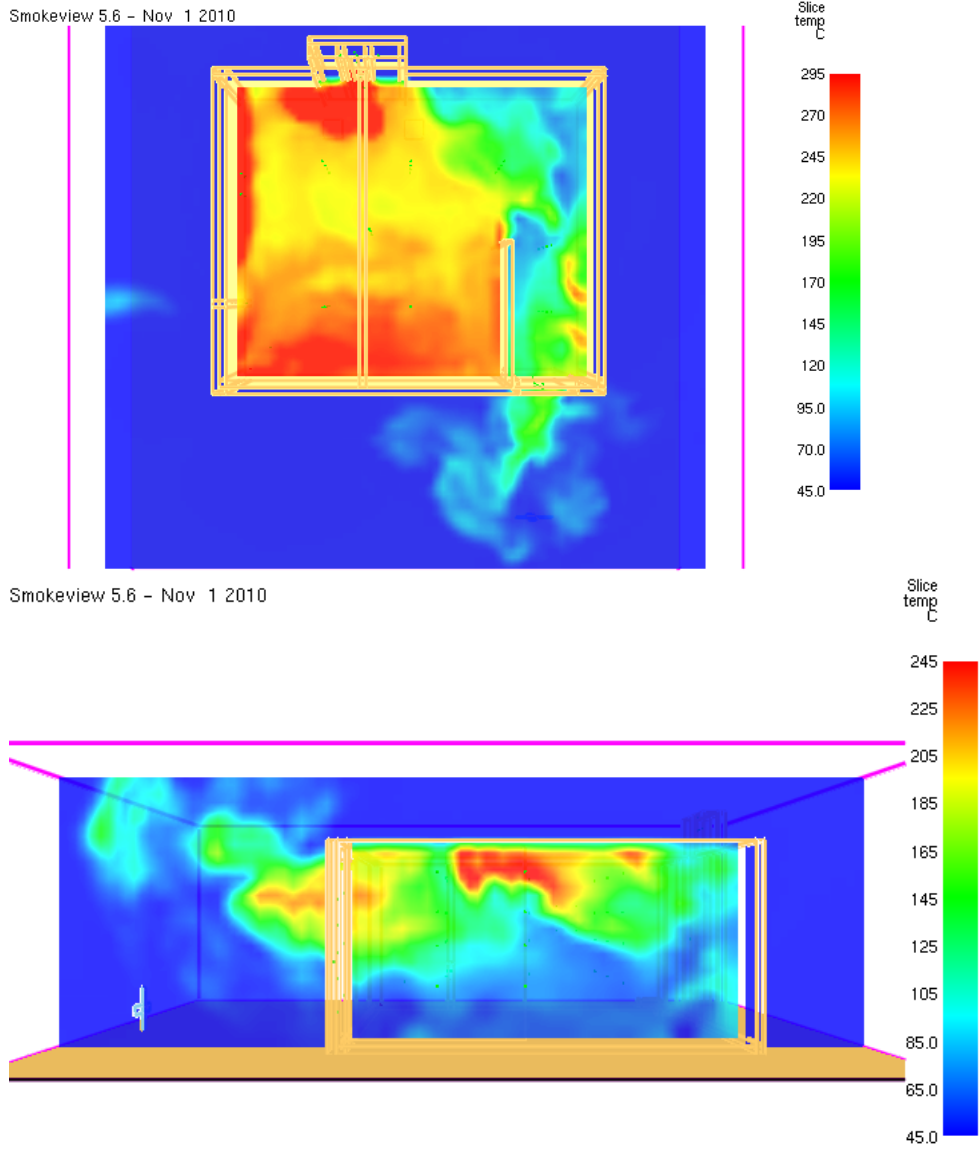
Figure 4.1.6: Post-ventilation temperature contours of the compartment in *x-y* plane (top) at an elevation of 1.5 m (middle of window) in the vertical plane (bottom) that bisects the fan and doorway for the *No Vent* PPV case.
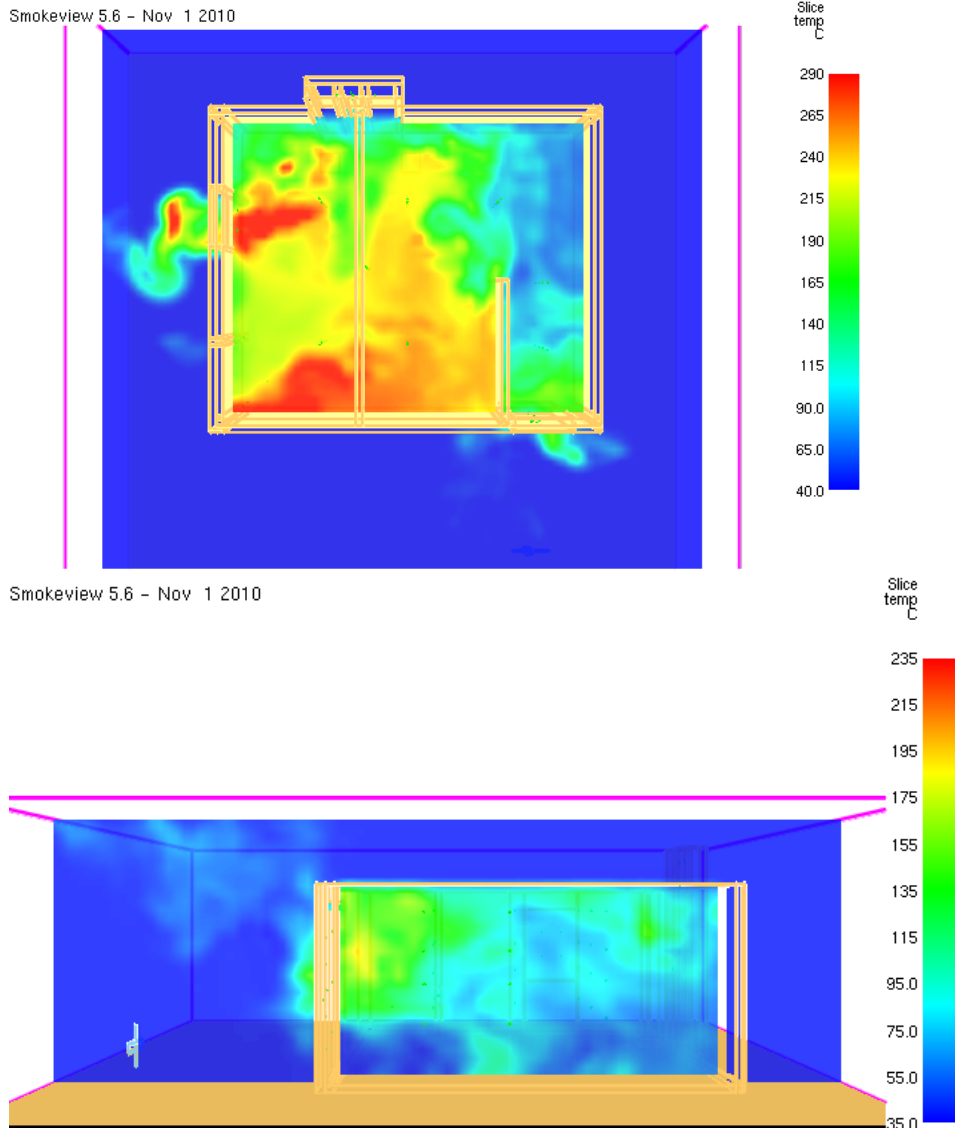
Figure 4.1.7: Post-ventilation temperature contours of the compartment in *x-y* plane (top)
at an elevation of 1.5 m (middle of window) in the vertical plane (bottom)
that bisects the fan and doorway for the *Open Vent* PPV case.

Examination of the temperature profiles of the plan view of structure (top) in
Figures 4.1.5-4.1.7 shows the impact that PPV has on the entranceway to the
compartment compared to natural ventilation. There is further penetration of the affects
of the cooler ambient air entering the structure with two forced ventilation cases. The

Open Vent PPV simulation shows the coolest throughout the entire compartment as the vent provides a low resistance pathway for combustion products to exit. The temperature profiles that bisect the doorway to the compartment (Figures 4.1.5-4.1.7 bottom) also illustrate the affects of forced ventilation on the compartment entrance. In the natural ventilation case (Figure 4.1.5) the entrance hallway remains stratified, similar to pre-ventilation compartment conditions. Temperatures at the ceiling range up to 235 °C. For the two PPV simulations (Figures 4.15 and 4.1.6), mixing eliminates temperature stratification in the hallway. In the *Open Vent* case we see noticeably lower temperatures. Specifically, there are no longer elevated temperatures exiting the compartment through the doorway.

4.2 EXAMINING THE IMPACT OF WIND DURING VENTILATION

Previous work as well as firefighter close calls and line of duty deaths (LODDs) have elicited the need for research into the impact of wind on fire growth and fire spread (NIOSH, 2008, 2010). Wind driven fire studies have primarily focused on characterizing how wind increases the hazard level in multi-family and commercial structures and the firefighter tactics which can be used to mitigate the effects (S. Kerber & Madryzkowski, 2009a, 2009b). These tactics include the use of wind control devices and floor below nozzle attachments to fire hoses, which can be used concurrently with positive pressure ventilation. The studies concluded that each of the tactics improved the conditions (decreased temperature and heat flux) in the attack corridor, however independently these tactics did not significantly improve conditions such that the corridor would be tenable even if firefighters were in full personal protective equipment. The range of wind speeds in the studies that caused the increased hazard was 10 m/s to 20 m/s.

In the *Open Vent* PPV experiment discussed in *section 3.4*, an increase of approximately 50 °C occurred at all elevations post ventilation 3 minutes and 35 seconds after ventilation was initiated. The experimental mean temperatures at each of the thermocouple elevations (Figure 4.2.1 left) show this temperature rise.
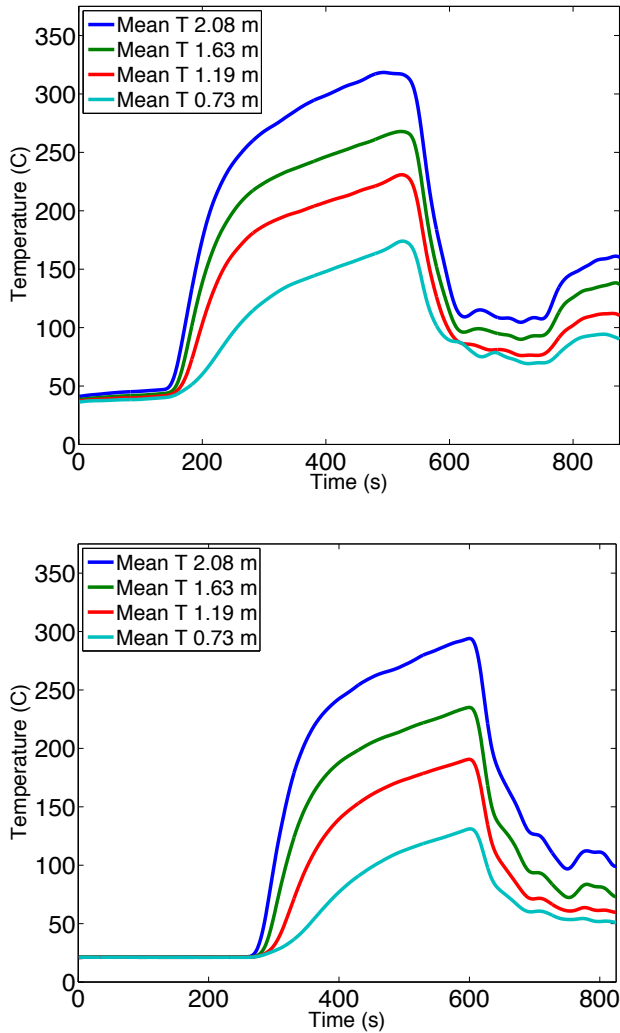
Figure 4.2.1: Spatial mean temperatures for a 400 kW *Open Vent* PPV experiment showing a rise in post ventilation temperatures (top) and an experiment without a post ventilation temperature rise (bottom).

Figure 4.2.1 shows a rise in mean temperature at each of the elevations, with the upper layer having the largest temperature increase. It is suspected that wind speeds normal to the exit vent were sufficient enough to affect the ability of the fan to push the combustion gases through the compartment. Wind speed is measured at the structure using a bi-directional probe mounted above the roofline. Bi-directional probe results are susceptible to error for airflow non-normal to the probe, however the probe was aligned in the direction of the wind at the beginning of testing. The average wind speed during the time interval where temperatures were elevated ventilation was 6.6 m/s, which according to Figure 2.5.6 is significant enough to reduce exit mass flow of combustion products. As a check of the bi-directional probes, wind speed data was taken from two nearby weather stations, KTXAUSTI129 and KTXAUSTI47. Both stations recorded sustained gusts of 7.15 m/s (Weather-Underground, 2010a, 2010b). The stations indicated a northern wind, which meant the wind was blowing north to south, into *Vent 1* (cf. Figure 2.1). This is opposite of the general trend for wind direction at the structure location. To understand how the compartment temperature was spatially affected, the 8 thermocouples at the 2.08 m elevation are shown (Figure 4.2.2).
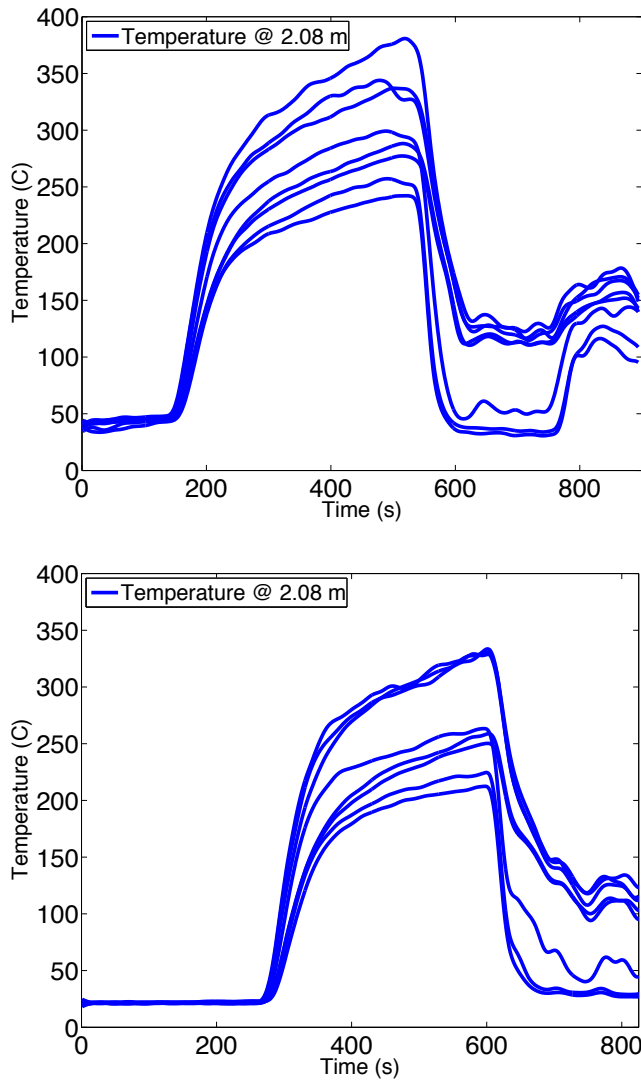
Figure 4.2.2: Experimental thermocouple temperatures for the 8 thermocouples at 2.08 m for a 400 kW *Open Vent* PPV experiment (top) and an experiment without a post ventilation temperature rise (bottom).

Figure 4.2.2 shows that post ventilation, three thermocouples are cooled to significantly lower temperatures. These thermocouples are located on the three trees that are inline with the fan and doorway. When the wind speed increases there is a rise in all of the temperatures, most significantly at the three trees that were initially cooled the

most. This shows that some of hot combustions gases that were initially being pushed out of the compartment through the open vent due to PPV are remaining in the compartment or being pushed out of the doorway (against the PPV fan) by wind.

High wind speeds can restrict the mass flow of combustion products leaving the compartment through the open vent. Figure 4.2.3 shows the experimentally measured window velocities.
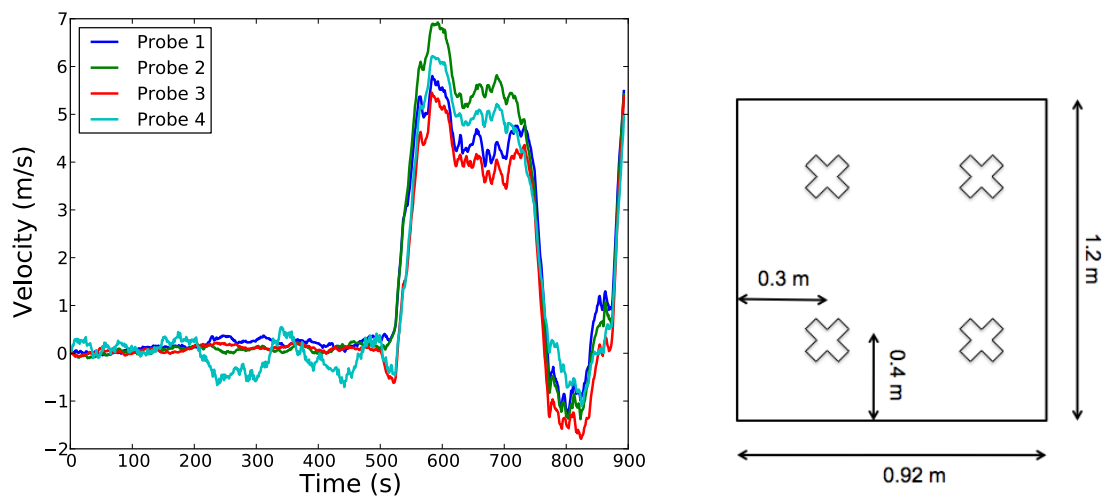
Figure 4.2.3: Experimentally measured velocities from 4 bi-directional probes positioned at the open vent (left). Positive velocities indicate flow exiting the compartment and negative velocities indicate flow entering the compartment. The locations of the probes in the window (right) are indicated by Xs and numbered clockwise from the upper left.

Figure 4.2.3 shows that when PPV is initiated, there is a rapid increase in velocity out of the window. There is significant flow exiting the compartment through the window, as the exit velocity is approximately 5 m/s. When the wind speed increases there is a rapid decrease in window velocity to approximately -1 m/s indicated that flow in entering the structure. At the end of the experiment, the wind calms down and the window velocities increase to values representative of PPV.

207

This rapid change in velocities can be particularly dangerous for entering firefighters or victims if the wind overcame PPV and changed the interior condition without warning. To better visualize the effect of wind on the fire, consider the series of still images taken from video inside the compartment during this test.

Figure 4.2.4: Still images from *Open Vent* PPV experiment. Top left: prior to ventilation. Top right: during PPV application. Bottom: PPV application during the time interval with increased wind speeds.

Figure 4.2.4 shows three images from the *Open Vent* PPV experiment which show the influence of wind. The top left image is pre-ventilation and the flames are both vertical, similar to free burning. The second image, top right, is taken just after ventilation was applied. PPV knocked over the flames, pushing them toward the open

window. In the bottom image, both flames have been pushed back to vertical but are noticeably lower than the pre-PPV flames. This lower height is most likely caused by the high turbulence inside the compartment. The fact that the flames are no longer pushed over indicates that the wind was sufficient enough to flow through the window and into the compartment, overcoming the pressure created by the fan.

4.3 Using FDS to Predict Compartment Thermal Environment for Fires Larger than Experiments

The experimental work conducted in Chapter 2 (non-reacting experiments) and Chapter 3 (reacting experiments) has led to the creation of a virtual representation of the UT burn facility in FDS. This model has been compared to experimental compartment pressure and flow rates for the non-reacting experiments and thermocouple temperatures in the reacting flow experiments. Currently, the model results are compared to experiments by recreating the experimental conditions within the model. This involved using appropriate experimental parameters such as fan flow rate and burner HRR. Due to safety concerns and limitations on the thermal protection of the interior of the burn facility, experiments were limited to HRRs ≤ 400 kW. In the remainder of this section, larger HRR fires are simulated in FDS based on the validation work conducted for the 400 kW experiments.

One reason to simulate larger fires is that a compartment the size of the test facility can have a large range in fire loads depending on the contents of the room. The fire load is the measure of the total energy released by combustion of all fuel items in an enclosure; this is essentially the integral of a HRR curve over the length of time that combustion occurs. The rate of fire growth, peak energy release, and fuel load are factors that influence tactics decisions and firefighter safety. For comparative purposes, the same HRR curves used in the 400 kW simulations are followed, except the values of the HRR

will be increased to represent larger fires: a 500 kW fire and a 1 MW fire. The same three testing configurations used in the 400 kW experiments are also followed: *No Vent* natural ventilation, *No Vent* PPV, and *Open Vent* PPV.

Following ASTM E 1355: *Standard Guide for Evaluating the Predictive Capability of Deterministic Fire Models*, it cautions that while a model can be validated for one scenario, there is no implication that the validation applies to different scenarios (ASTM, 2005). Results from the 500 kW simulations are compared to 400 kW simulations. Figure 4.3.1 shows mean compartment temperature at the 2.08 m thermocouple elevation for the three ventilation tactics that were studied.
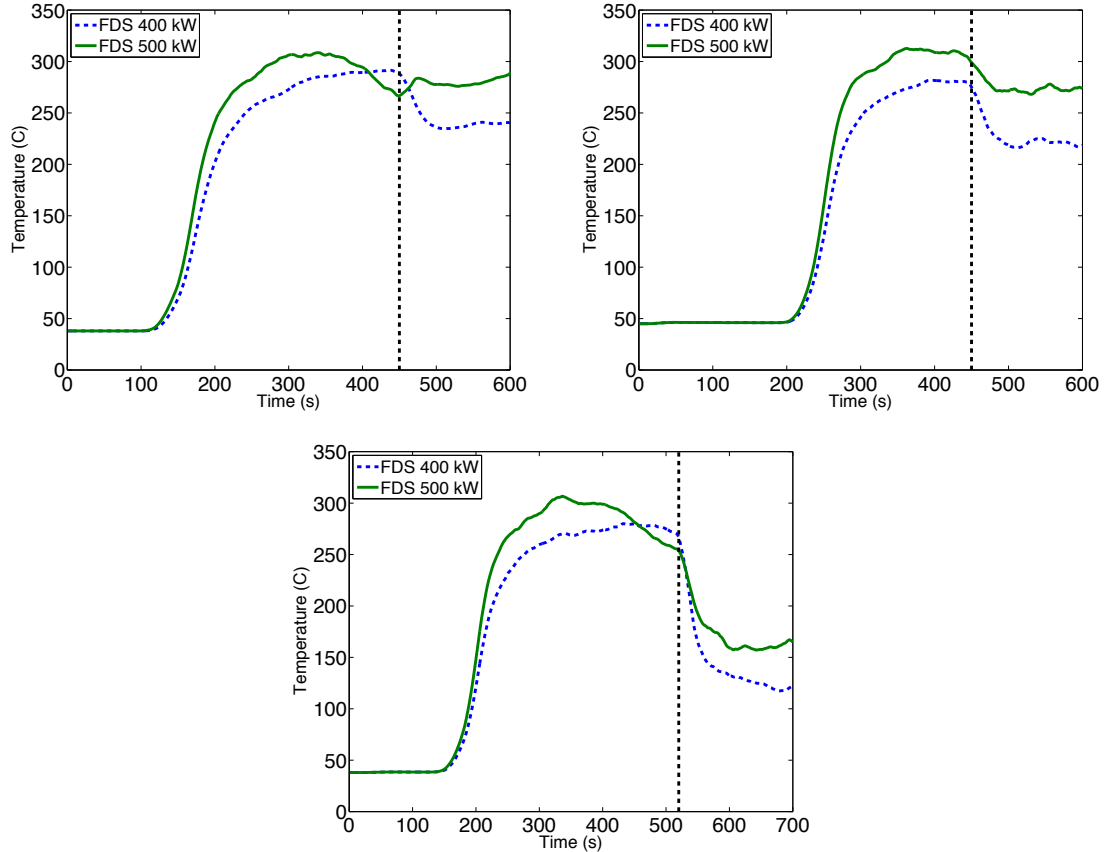
Figure 4.3.1: Comparison of mean temperatures for 400kW simulations (dashed) to 500 kW simulations (solid) at the 2.08 m thermocouple elevation for a *No Vent* natural ventilation (upper left), a *No Vent* PPV (upper right), and an *Open Vent* PPV (bottom) case. The vertical line (dash-dotted) indicates ventilation.

Figure 4.3.1 shows that while there are generally higher temperatures for the 500 kW fires, the temperatures begin to drop as the compartment becomes ventilation-controlled. A ventilation-controlled fire (or oxygen-limited) means that combustion is limited by the amount of oxygen present in the compartment or in a computational cell with respect to FDS. Without a continuous supply of oxygen, local extinction within the compartment can occur resulting in a drop in temperature. The pre-ventilation local extinguishment is more obvious in the *No Vent* natural case (top left) and *Open Vent* PPV

case (bottom) as their ignition to ventilation times were 340 seconds and 385 seconds respectively. For the *No Vent* PPV case (top right), with an ignition to ventilation time of 250 seconds, the temperature drops about 10-20 seconds before ventilation. The HRR in FDS is specified for the length of the simulation, so even though the combustion reaction starts to consume all of the oxygen, fuel will continue to flow into the compartment. This type of behavior can happen in real compartment fires as upper layer temperatures can be hot enough to continue to cause fuel to off-gas despite a lack of oxygen for combustion. This type of under-ventilated compartment behavior can be dangerous for firefighters because by venting this system, they introduce air to a compartment that accumulated unburned fuel at elevated temperatures. The rapid change from oxygen-controlled to fuel-controlled can be very dangerous for firefighters applying the ventilation or making entry because of the unpredictability of how the compartment will react.

Experiments were not conducted for the 500 kW case; therefore it cannot be definitively claimed that the burners in the 500 kW case causes the compartment to become ventilation controlled. If the assessment of the lower flammability limit $Y_{02}= 0.5$ is appropriate for propane combustion in FDS and the constraints on the burn/no burn extinction model are valid, then there is confidence in the results shown in Figure 4.3.1.

Post-ventilation there are similar trends in the two PPV simulations compared to the 400 kW experiments. The upper elevation temperatures drop; yet remain above the 400 kW results. In the natural ventilation simulation there is a rise in upper elevation temperature post ventilation. A similar temperature rise for natural ventilation exists that was shown and discussed relative to Figure 4.1.2. As a result, the thermocouple temperatures were examined at each elevation. The same temperature trends exist at the 1.63 m elevation and 2.08 m elevation. The two lowest elevations (1.19 m and 0.73 m) did not show a post ventilation temperature rise. In the natural ventilation case, the

compartment remains well stratified and a cooling trend in the lower elevation is expected. In the upper elevation, hot combustion products exit the structure. There may also be unburned fuel in the upper layer that combusts when mixing with oxygen that causes the rise in temperature.

From the three plots, despite indications that the compartment was ventilation controlled, there was not significant unburned fuel in the compartment to have drastic post ventilation temperature changes. The next step is to compare the set 1 MW simulations to the 400 kW simulations (Figure 4.3.2).
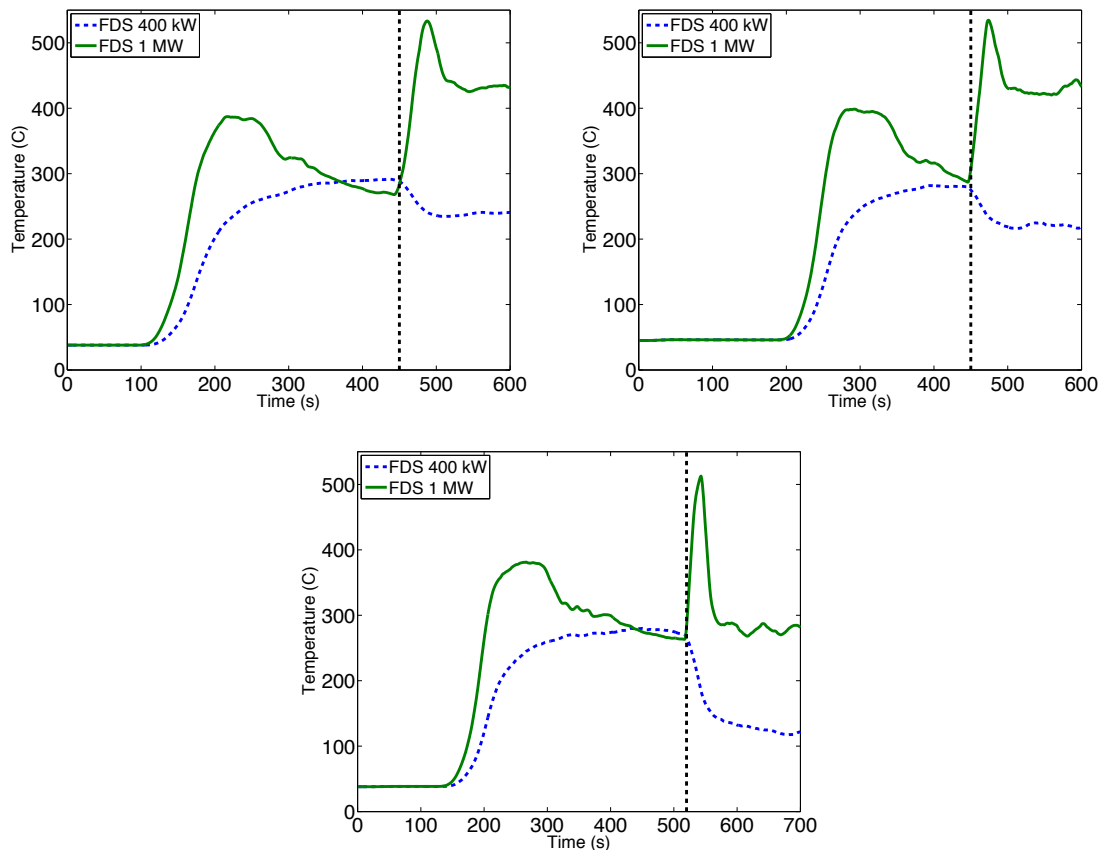
Figure 4.3.2: Comparison of mean temperatures for 400kw simulations (dashed) to 1 MW simulations (solid) at the 2.08 m thermocouple elevation for a *No Vent* natural ventilation (upper left), a *No Vent* PPV (upper right), and an *Open Vent* PPV (bottom) case. The vertical line (dash-dotted) indicates ventilation.

Similar to the 500 kW simulations, but to a more significant degree, the compartment becomes ventilation controlled in the 1 MW simulations. Prior to ventilation, a significant amount of unburned fuel in the compartment is expected compared to the 400 kW and 500 kW cases. After ventilation, the 1 MW simulations show a significant spike in temperature with the *Open Vent* PPV simulation showing the fastest response. This type of rapid temperature response as a result of ventilation is usually an indicator of backdraft (Gorbett & Hopkins, 2007). Backdraft is very difficult

214

to predict and dangerous for firefighters. While it cannot definitively concluded that backdraft occurred, the models do show the effects of ventilation on large ventilation controlled fires: > 200 °C mean temperature change in ~35-45 seconds. What can be taken away from these simulations is that for large fires in a compartment of this size, the compartment could transition to a ventilation-controlled state within several minutes of ignition. Ventilation of ventilation-controlled fires leads to a rapid change in compartment composition. This rapid change can lead to the combustion of unburned fuels and significant increases in temperature.

4.4 CONCLUSIONS

The use of ventilation on the fireground is an important tool for firefighters; however there are factors that firefighters should consider to best use these tactics. It was shown through the tests conducted in the experimental facility and subsequent models of the experiments that there is increased mixing resulting in lower entranceway temperatures through the use of forced ventilation compared to natural ventilation. The results also showed that for the forced ventilation cases where an additional exit path was provided (open window) lower temperatures were observed in both the *attack corridor* and the *interior* of the compartment.

While the results show that compartment temperatures are cooler for the experiment with the additional open vent during PPV application, the open vent also made the compartment more susceptible to environmental affects. Specifically, strong winds were shown to have adverse effects on the compartment conditions during ventilation. Initially PPV dropped the temperature in the compartment, however due to strong winds the flow direction in the compartment was reversed. Instead of PPV forcing combustions products out through the open window, wind was able to overcome the

pressure generated by the fan. Velocities through the window were reversed and a temperature rise in the compartment occurred. The most significant rise was in the entranceway to the compartment indicating that combustions products were being forced out of the compartment through the doorway. Wind conditions can change rapidly and without warning, therefore it is important for firefighters to recognize local wind conditions when applying ventilation.

Lastly, the 400 kW models developed through comparison to experimental data were used to simulate larger HRR fires that experiments could not be conducted for. A 500 kW and a 1 MW fire were examined. It was found that for the 500 kW the compartment, the compartment transitioned to ventilation-controlled compartment at approximately 250 seconds. For the 1 MW a more rapid transition to ventilation controlled occurred, at approximately 150 seconds. It is important to recognize that the pre-ventilation conditions for these fires represent a higher risk for firefighters venting the compartment.

Chapter 5: Conclusions and Future Work

5.1 SUMMARY OF MAIN CONCLUSIONS

This research has been motivated by the coupling of engineering sciences (fluid mechanics, heat transfer, and thermodynamics) to practical fireground problems with a goal to disseminate the findings to improve firefighter tactics. The objective of this research was to experimentally and computationally characterize strong vent flow enclosure fires. To accomplish this task a compartment scale burn facility was constructed on the J.J. Pickle Research Campus of The University of Texas at Austin. Characterization was divided into non-reacting and reacting experiments and computational models to initially decouple the fluid mechanics of ventilation from the buoyancy driven flows of an enclosure fire. A framework was developed to computational characterize strong vent flow enclosure fires by developing the appropriate models, improving submodels, and calibrating model parameters. While the level of modeling detail presented in this dissertation is probably too expensive to directly apply to every unique fire scenario encountered by firefighters, this framework does allow for the development of highly detailed simulations of specific cases that can be used aid current training.

The non-reacting, mechanically driven flow experiments and computational models discussed in Chapter 2 showed that two important factors for obtaining valid results are the flow source (PPV fan) and quantification of the effective leakage area in the structure. With accurate characterization of those two factors, the FDS model of PPV simulated mass flow rates through exit vents within the experimental uncertainty for the

non-reacting flow results and pressure within the structure was matched within 5% for the ventilation cases studied. The analytical resistance model produced pressure and bulk flows through structure outlets to within 16% of the experimental results for the same venting conditions. The resistance model reiterated the importance of the initial fan flow rate and inclusion of leakage in developing accurate predictions. The ability of the analytical model to predict bulk flow values similar to FDS showed that choosing the correct model based on required level of flow detail is important because the most complex model is not always needed.

Similar to the non-reacting experiments, the reacting experiments discussed in Chapter 3 showed the importance of correctly specifying particular model parameters. Analogous to the PPV fan which was the source for the non-reacting flow models was the HRR for the reacting flow experiments. Tied to the specified HRR are the oxygen and fuel lower flammability limits. These parameters need to be specified appropriately within the FDS model to ensure the combustion model is appropriate for the specific case that is being modeled. Additionally a transient thermocouple model was developed and implemented into FDS as it was found that the previous quasi-steady model did not capture the thermal lag that occurs in experimental thermocouples.

After applying these reacting flow model parameters, the reacting flow FDS computational results were compared to the experimental results before and after ventilation. In the pre-ventilation comparison, the FDS model was able to capture the spatial variance in thermocouple temperature that was present at each of the experimental thermocouple elevations. Comparison of temperatures at each elevation show that FDS was able to better predict the upper elevation temperatures. At the lowest elevation, the FDS model was shown to consistently over predict thermocouple temperature. Over the duration of the fire testing, the leakage characteristics of the compartment have increased

from the value determined during the non-reacting flow experiments. As a result, the current models do not have representative leakage, which was shown to be a contributing factor to the temperature over-prediction. Comparing the post-ventilation model predictions FDS showed the same trends as the experiments. The FDS model generally over-predicted post-ventilation mean compartment temperatures. Examination of the relative error for individual thermocouples showed larger error for the two PPV cases compared to the natural ventilation case. The highly turbulent entrance way to the compartment showed the largest errors.

The lack of a current low order model for strong vent flow enclosure fires led us to examine the application of a PaSR model to this problem. A fast chemistry mixture fraction driven reaction process, a one-step finite rate reaction, and a two-step finite rate reaction were considered. The results the fast chemistry implementation were compared to a PSR formulation and the results from the one-step finite rate reaction implementation were compared to FDS. The two-step reaction results were compared to results from a model problem found in literature. Both formulations were able to model the compartment evolution for a range of mixing time to residence time ratios.

In Chapter 4 the experimental and computational results were examined with respect to the influence of ventilation tactics on temperature response. PPV was shown to have a more significant influence on cooling the entranceway to the compartment compared to natural ventilation. The *Open Vent* PPV cases showed the most significant drop in entranceway and compartment interior temperatures. The *Open Vent* case however was influenced by strong wind gusts, which were able to reverse the flow through the open window. This resulted in a rise in compartment temperature, most significantly at the entrance to the compartment. It was found that for simulations of larger HRR in the same enclosure, the results indicate that the compartment becomes

oxygen-limited prior to ventilation. This type of compartment behavior is dangerous to firefighters who may vent the structure as the application of ventilation can lead to backdraft or flame-over conditions.

5.2 RECOMMENDATIONS FOR FUTURE WORK

Based on discussion from the previous chapters, there are two areas where future work can help improve the analysis of strong vent flow enclosure fires: experimental work and computational work.

5.2.1 Experimental recommendations

There were previous discussions that the current that leakage area being used to quantify leakage in the compartment may be too low compared to what the actual value may currently be. A re-characterization of structure leakage would be beneficial toward improving FDS simulation comparisons to experimental results. Additional experimental measures can also provide a future modeler more information to assist in validation work. This would be to include wall, ceiling, and floor temperature measurements so that the contributions to thermocouple temperature and heat flux measurements from the compartment interior can be found. Finally, there are been exploratory work using heat flux gages to determine layer height in experiments. More work in this area could provide additional insight into compartment temperature evolution and another parameter to compare to models.

5.2.2 Computational recommendations

In the current release of FDS, version 5.5.3, a two-step combustion model can be used to simulate fire progression and compartment gas composition for under-ventilated compartment fires. While this model offers improvement in CO prediction compared to previous models used in FDS, research shows that the CO production model returns

significantly lower values of CO compared to experimentally measured values. This is an important issue as a significant portion of the user base uses this code for life safety analysis. FDS has been developed and improved with the side constraint that it should be computationally inexpensive so that the user base can run simulations on inexpensive desktop machines. Any future candidate submodels introduced into FDS should strive to achieve this goal of being relatively computationally inexpensive.

In the work conducted, it was shown that a PaSR model could be used to model enclosure fires with less cost than a comparable FDS model. There is a need for exploration into coupling PaSR volumes at varying length scales to model CO and soot production within FDS. The next step then is to continue to validate the two-step reaction model in the PaSR formulation including comparing results to experimental work and FDS simulations where CO is known.

Appendix A

For an under ventilated, vitiated compartment fire, the combustion reaction can be modeled as a carbon monoxide reaction:

$$CO + \frac{1}{2}(O_2 + 3.76N_2) \rightarrow CO_2 + 1.88N_2 \qquad \text{A.1}$$

From literature that carbon monoxide has an upper flammability limit of 0.74 mol/mol (DiNenno, 2008). This means that if the concentration of carbon monoxide is above this level in a control volume, the resulting reaction will not be sufficient to reach the critical temperature needed for combustion. Therefore, the left hand side of equation A.1 becomes:

$$CO + \lambda(O_2 + 3.76N_2) \rightarrow \qquad \text{A.2}$$

where lambda is an unknown coefficient representing the fractional amount of air in the reaction. If we perform a molar balance of A.2 based on the upper flammability limit of CO as 0.74:

$$\frac{1}{1+4.76\lambda} = 0.74 \qquad \text{A.3}$$

lambda is found to be 0.074. The resulting mole fraction of oxygen is 0.05 mol/mol, which is the lower oxygen flammability limit for oxygen in a carbon monoxide combustion reaction. This value has been shown in literature to be 5.5% (DiNenno, 2008).

Bibliography

Anzalone, R. (2010). *A toolkit for characterizon uncertainties in hypersonic flow-induced ablation*. Masters, The University of Texas at Austin, Austin, TX.

ASHRAE. (1988). Air leakage performance for detached single-family residential buildings (Vol. 119). American Society of of Heating, Refrigerating, and Air Conditioning Engineers.

ASTM. (2005). Standard guide for evaluating the predictive capability of deterministic fire models (Vol. E 1355, pp. 1-8).

ASTM. (2008). Standard test method for room fire test of wall and ceiling materials and assemblies (Vol. E 2257-03).

Averill, J. D., Moore-Merrell, L., Barowy, A., Santos, R., Peacock, R., Notarianni, K. A., & Wissoke, D. (2010). Report on residential fireground field experiments. In B. Robinson (Ed.), *NIST Technical Note 1661*. Gaithersburg, MD: NIST.

Awbi, H. (2003). *Ventilation of buildings* (Second ed.). London, UK: Spon Press.

Aynsley, R. (1997). A resistance approach to analysis of natural ventilation airflow networks. *Journal of Wind Engineering and Industrial Aerodynamics, 67-68*, 711-719.

Beal, C. (2008). *Computational studies of parameters affecting positive pressure ventilation in compartment fires and cold flow experiments in a one room burn structure*. Master of Science, The University of Texas at Austin, Austin, TX.

Beal, C., & Ezekoye, O. A. (2008). *Effects of exit vent location of fire room conditions during ppv*. Paper presented at the ASME Heat Transfer Conference 2008, Jacksonville, FL.

Beal, C., Fakhreddine, M., & Ezekoye, O. A. (2008). Effects of leakage in simulations of positive pressure ventilation. *Fire Technology, 45*(3), 257-286.

Blevins, L., & Pitts, W. (1999). Modeling of base and aspirated thermocouples in compartment fires. *Fire Safety Journal, 33*(4), 239-259.

Brundage, A., Nicolett, V., Donaldson, A., Kearnry, S., & Gill, W. (2005). A joint computational and experimental study to evaluate inconel-sheathed thermocouple performance in flames. Albuquerque, NM: Sandia National Lab.

Burnett, J., Bojic, M., & Yik, F. (2005). Wind-induced pressure and external surfaces of a high-rise residential building in hong kong. *Building and Environment, 40*(6), 765-777.

Casey, K. D., Gates, R. S., Wheeler, E. F., Xin, H., Liang, Y., Pescatore, A. J., & Ford, M. J. (2008). On-farm ventilation fan performance evaluations and implications. *Journal of Applied Poultry Research, 17*(2008), 283-295.

Chen, H., Lui, N., & Wanki, C. (2009). Wind effects on smoke motion and temperature of ventilation-controlled fire in a vent compartment. *Building and Environment, 44*(12), 2521-2526.

DiNenno, P. (2008). *Sfpe handbook of fire protection engineering* (Vol. 4th Edition). Bethessa, MD: National Fire Protection Association.

Dopazo, C. (1975). Probability density function approach for a turbulent axisymmetric heated jet. Centerline evolution. *Physics of Fluids, 18*(4), 397-404.

Dwyer Instruments. (2011). Series rm (rma/rmb/rmc) rate-master® flowmeter. from http://www.dwyer-inst.com/Product/Flow/Flowmeters/VariableArea/SeriesRM-RMA-RMB-RMC-

Ezekoye, O. A., Lakshminarasimhan, K., Seers, P., & Nicks, R. (2005). Effects of ppv attack on thermal conditions in compartment downstram of a fire. *Fire Technology, 41*(3), 193-208.

Fox, R. O. (2003). *Computational models for turbulent reacting flows*: Cambridge University Press.

Francis, J., & Yau, T. (2004). On radiant network models of thermocouple error in pre and post flashover compartment fires. *Fire Technology, 40*(3), 277-294.

Goodwin, D. (2002). Cantera: Object-oriented software for reacting flows: California Institute of Technology.

Gorbett, G., & Hopkins, R. (2007). *The current knowledge & training regarding backdraft, flashover, and other rapid fire progression phenomena*. Paper presented at the National Fire Protection Association World Fire Safety Conference, Boston, Massachusetts.

Gordon, R. G. (1968). Error bounds in equilibrium statistical mechaics. *Journal of Mathematical Physics, 9*, 655-663.

Higuera, F. J., & Martinez, M. (1993). An incompressible jet in a weak crossflow. *Journal of Fluids Mechanics, 249*, 73-97.

Hurley, M. J., & Munguia, A. (2007). Analysis of fds thermal detector response prediction capability. Gaithersburg, MD: National Institute of Standards and Technology.

Ingason, H., & Fallberg, R. (2002). Positive pressure ventilation in single medium-sized premises. *Fire Technology, 38*(3), 213-230.

Janssens, M. L., & Tran, H. C. (1992). Data reduction of room tests for zone model validation. *Journal of Fire Sciences, 10*(6), 528-555.

Jones, W. W., Peacock, R. D., Forney, G. P., & Reneke, P. A. (2009). Cfast - consolidated model of fire growth and smoke transport (version 6). Gaithersburg, MD: National Institute of Standards and Technology.

Kerber, S. (2010). Impact of ventilation on fire behavior in legacy and contemporary residential construction. Northbrook, IL: Underwriters Laboratories.

Kerber, S., & Madryzkowski, D. (2009a). Fire fighting tactics under wind driven conditions: 7-story building experiments. Gaithersburg, MD: National Institute of Standards and Technology.

Kerber, S., & Madryzkowski, D. (2009b). Fire fighting tactics under wind driven conditions: Laboratory experiments. Gaithersburg, MD: National Institute of Standards and Technology.

Kerber, S., & Walton, W. (2003). Characterizing positive pressure ventilation using computational fluid dynamics. Gaithersburg, MD: National Institute of Standards and Technology.

Kerber, S., & Walton, W. (2005). Effect of positive pressure ventilation on a room fire. Gaithersburg, MD: National Institute of Standards and Technology.

Ko, N. W. M., & Chan, W. T. (1978). Similarity in the initial region of annular jets: Three configurations. *Journal of Fluids Mechanics, 1*(84 part 4), 641-656.

Kokel, P. (2008). *Modeling of directional flame thermometer for real-time incident radiation measurements in room fire testing*. Master of Science, The University of Texas at Austin, Austin, TX.

Liu, C. Y., Wong, Y. W., Chan, W. K., & Can, T. C. (1990). Note on the robust bidirectional low velocity probe. *Experiments in Fluids, 9*(6), 354-356.

McBride, J., & Gordon, S. (1996). Computer program for calculation of complex chemical equilibrium compositions and applications ii. User's manual and program description. Cleveland, OH: National Aeronautics and Space Administration.

McCaffrey, B., & Heskestad, G. (1976). A robust bidirectional low-velocity probe for flame and fire application. *Combustion and Flame, 26*(1), 125-127.

McGrattan, K., McDermott, R., Hostikka, S., & Floyd, J. E. (2010a). Fire dynamics simulator (version 5) technical reference guide. Gaithersburg, MD: National Institute of Standards and Technology.

McGrattan, K., McDermott, R., Hostikka, S., & Floyd, J. E. (2010b). Fire dynamics simulator (version 5) user guide. Gaithersburg, MD: National Institute of Standards and Technology.

McGraw, R. (1997). Description of aerosol dynamics by the quadrature method of moments. *Aerosol Science and Technology, 27*(2), 255-265.

Moin, P. (2001). *Fundamentals of engineering numerical analysis*. New York, NY: Cambridge University Press.

NIOSH. (2008). Career fire fighter dies in wnd driven residential structure fire - virginia. *Death In the line of duty*. from http://www.cdc.gov/niosh/fire/reports/face200712.html

NIOSH. (2010). Career probationary fire fighter and captain die as a result of rapid fire progression in a wind-driven residential structure fire – texas. *Death In the line of duty*. from http://www.cdc.gov/niosh/fire/reports/face200911.html

Overholt, K., & Ezekoye, O. A. (2011). *Inverse fire modeling for heat release rate characterization*. Paper presented at the 7th U.S. National Combustion Meeting, Atlanta, GA.

Pitts, W., Braun, E., Peacock, R., Mitler, H., Johnson, E., Reneke, P., & Blevins, L. (2003). Temperature uncertainties for bare-bead and aspirated thermocouple measurements in fire environments. *ASTM Special Technical Publication*(1427), 3-15.

Pope, S. B. (1985). Pdf methods for turbulent reacting flows. *Progress in Engery and Combustion Science, 11*, 119-192.

Rizika, J., & Rohsenow, W. (1952). Thermocouple thermal error. *Industrial & Engineering Chemistry, 44*(5), 1168-1171.

Sherman, M. (1995). The use of blower-door data. *Indoor Air, 5*(3), 215-224.

Sherman, M., & Dickerhoff, D. (1998). Air-tightness of u.S. Dwellings: Lawrence Berkley Lab.

Svensson, S. (2001). Experimental study of fire ventilation in fire-fighting operations. *Fire Technology, 37*(1), 69-85.

Tempest-Technology. (2010). Positive pressure ventilation (ppv). from http://www.tempest-edge.com/ppv/index.htm

Upadhyay, R. (2006). *Simulation of population balance equations using quadrature based method of moments*. Ph.D., The University of Texas at Austin, Austin, TX.

Upadhyay, R., & Ezekoye, O. A. (2008). Treatment of design fire uncertainty using quadrature method of moments. *Fire Safety Journal, 43*, 127-139.

Upadhyay, R., & Ezekoye, O. A. (2011). Libmom: A library for stochastic simulations in engineering using statistical moments. *Engineering with Computers*. doi: 10.1007/s00366-011-0219-9

Vettori, R. L., Madryzkowski, D., & Walton, W. (2002). Simulation of the dynamics of a fire in a one-story restaurant, texas, february 14, 2000. Gaithersburg, MD: National Institute of Standards and Technology.

Weather-Underground. (2010a). History for ktxausti47. from http://www.wunderground.com/weatherstation/WXDailyHistory.asp?ID=KTXAUSTI47&month=10&day=28&year=2010

Weather-Underground. (2010b). History for ktxausti129. from http://www.wunderground.com/weatherstation/WXDailyHistory.asp?ID=KTXAUSTI129&month=10&day=28&year=2010

Weinschenk, C. (2007). *A study of firefighter compliance to ventilation standad operating guidelines and development of a computational model of a ventilation fan*. Master of Science, The University of Texas at Austin, Austin, TX.

Weinschenk, C., Beal, C., & Ezekoye, O. A. (2011). Modeling fan-driven flows for firefighting tactics using simple analytial models and cfd. *Journal of Fire Protection Engineering, 21*(2), 85-114.

Weinschenk, C., & Ezekoye, O. A. (2010). *Analysis of thermocouple response to turbulent radiating environments*. Paper presented at the ASME/JSME 8th Thermal Engineering Joint Conference, Honolulu, Hawaii.

Weinschenk, C., Upadhyay, R., & Ezekoye, O. A. (2011). *Comparison of a partially stirred reactor model and a perfectly stirred reactor model for large vent flow fires*. Paper presented at the 7th US National Combustion Institute Meeting, Atlanta, Georgia.

Westbrook, C., & Dryer, F. (1981). Simplified reaction machanisms for the oxidation of hydrocarbon fuels in flames. *Combustion Science and Technology, 27*(1), 31-43.

Yilmaz, N., Gill, W., Donaldson, A., & Lucero, R. (2008). Problems encountered in fluctuating flame temperature measurements by thermocouple. *Sensors, 8*.

Zeisler, P. S., Gunnerson, F. S., & Williams, S. K. (1994). Advances in positive pressure ventilation: Live fire tests and laboratory simulation. *Fire Technology, 30*(2), 269-277.

Vita

Craig Weinschenk was born on September 7, 1984 in New Brunswick, NJ to Carl and Louise Weinschenk. Craig has one older brother, Robert Weinschenk, who is an Intellectual Properties Lawyer. Craig graduated from South River HS in 2002 and earned his B.S. in Mechanical Engineering from Rowan University in 2006. Craig earned his M.S. in Mechanical Engineering from The University of Texas at Austin in 2007.

Permanent address: 17 Essex Street, South River, NJ 08882

This dissertation was typed by Craig Weinschenk.